A key role for BID-mediated mitochondrial damage in oxidative cell death

Dissertation

zur

Erlangung des Doktorgrades

der Naturwissenschaften

(Dr. rer. nat.)

dem

Fachbereich Pharmazie

der Philipps-Universität Marburg

vorgelegt von

Anja Maria Jelinek

aus Gießen

Marburg, 2018

A key role for BID-mediated mitochondrial damage in oxidative cell death

Dissertation

zur

Erlangung des Doktorgrades

der Naturwissenschaften

(Dr. rer. nat.)

dem

Fachbereich Pharmazie

der Philipps-Universität Marburg

vorgelegt von

Anja Maria Jelinek

aus Gießen

Marburg, 2018

Erstgutachter: Prof. Dr. Carsten Culmsee

Zweitgutachter: Prof. Dr. Moritz Bünemann

Eingereicht am 04.01.2018

Tag der mündlichen Prüfung am 16.02.2018

Hochschulkennziffer: 1180

Meiner Familie

E R K L Ä R U N G

Ich versichere ehrenwörtlich, dass ich die dem Fachbereich Pharmazie Marburg zur Promotionsprüfung eingereichte Dissertation mit dem Titel

„A key role for BID-mediated mitochondrial damage in oxidative cell death“

selbständig ohne unerlaubte Hilfe angefertigt, alle vollständig oder sinngemäß übernommenen Zitate als solche gekennzeichnet und mich dabei keiner anderen als der von mir ausdrücklich bezeichneten Quellen bedient habe.

Die Dissertation wurde in der jetzigen oder einer ähnlichen Form noch bei keiner anderen in- oder ausländischen Hochschule anlässlich eines Promotionsgesuchs eingereicht und hat noch keinen sonstigen Prüfungszwecken gedient.

Marburg, den 04.01.2018

.....

(Anja Maria Jelinek)

Table of contents

1 Introduction

1.1 Neuronal cell death mechanisms

Regulated cell death (RCD), a well-defined sequence of genetically encoded or biochemically determined events for the elimination of cells, is a central aspect of cellular homeostasis, tissue sculpting during embryogenesis, maturation of the immune system and disease control. In 1842, Carl Vogt was the first to describe primal features of programmed cell death [198] and since then *apoptosis*, coined in 1972 [96], became the best-characterized form of regulated cell death. RCD has expanded from simple descriptive microscopic characterization to genetic and biochemical definition, giving rise to a variety of well-defined heterogeneous cell death pathways, for instance apoptosis, autophagy or regulated necrosis (Figure 1). Despite significant efforts to determine the unique characteristics on a genetic and biochemical basis *in vitro*, cell death pathways *in vivo* should be regarded as an interconnected network rather than individual mechanisms as they are mostly found in parallel or in succession [50,58,59,221]. Over the past decades, RCD comprising massive accumulation of reactive oxygen species (ROS) and disturbed calcium homeostasis [69] has been implicated in a variety of chronic neuropathologies such as Alzheimer's disease (AD) [28,166], Parkinson's disease (PD) [181,187], Huntington's disease (HD) [108,197], and in acute brain injury induced by cerebral ischemia [128,176], hemorrhagic insults [76,145] or brain trauma [70,119,149].

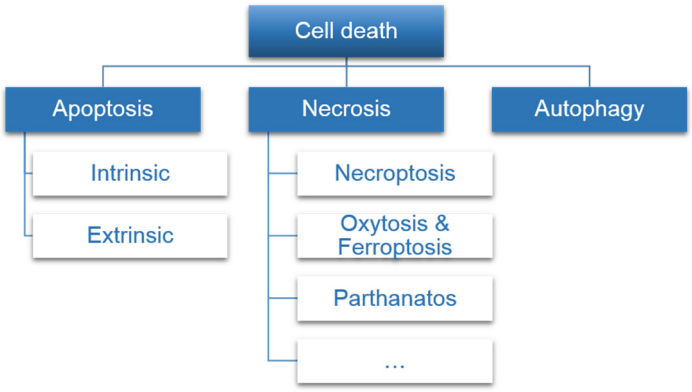

Figure 1. Cell death mechanisms

Cell death mechanisms can be subdivided into three major classes of regulated apoptosis, necrosis and the "recycling" mechanism autophagy. These major classes itself include a variety of subgroups, such as intrinsic and extrinsic apoptosis or necroptosis, oxytosis, ferroptosis parthanatos and many others.

Mounting evidence has linked imbalanced calcium signaling and the accumulation of ROS, such as lipid peroxides, hydrogen peroxide or hydroxyl and nitric oxide radicals, to excessive mitochondrial damage, and hence is considered to provoke impairments of mitochondrial morphology and function [109]. Since the brain relies on a high metabolic turnover, it crucially depends on a functional energy metabolism by mitochondrial respiration and glycolysis, thus, rendering it vulnerable to oxidative stress and mitochondrial dysfunction.

Moreover, recent findings suggest that inflammation severely contributes to mitochondrial dysfunction and neurodegenerative cell death [139,193]. In this regard, strong microglial activation has been demonstrated to affect mitochondrial dynamics and impair mitochondrial energy metabolism, thus, provoking neurodegenerative processes. *Vice versa*, harmed mitochondria of microglia amplify the inflammatory response by ROS production and release of damage-associated molecular patterns (DAMPs) [139]. Despite that several events, which are attributed to apoptotic or necrotic events, were found to underlie neuronal degradation, the exact biochemical mechanisms of cell death in neurons remain to be elucidated for the precisely targeted and ideally curative therapy of neuronal diseases.

1.1.1 Apoptosis

The best-studied molecular cell death pathway is apoptosis and occurs not only in pathological conditions upon cell damage but also during tissue development, homeostasis and ageing [47,156]. Typical hallmarks include cytoplasmic shrinkage, chromatin condensation, DNA degradation, nuclear fragmentation and membrane blebbing with the formation of apoptotic bodies, and caspase-dependency as a biochemical feature [75,79,96]. Apoptosis is further subdivided depending on its initiation by either intracellular (intrinsic) or extracellular (extrinsic) stimuli (Figure 2).

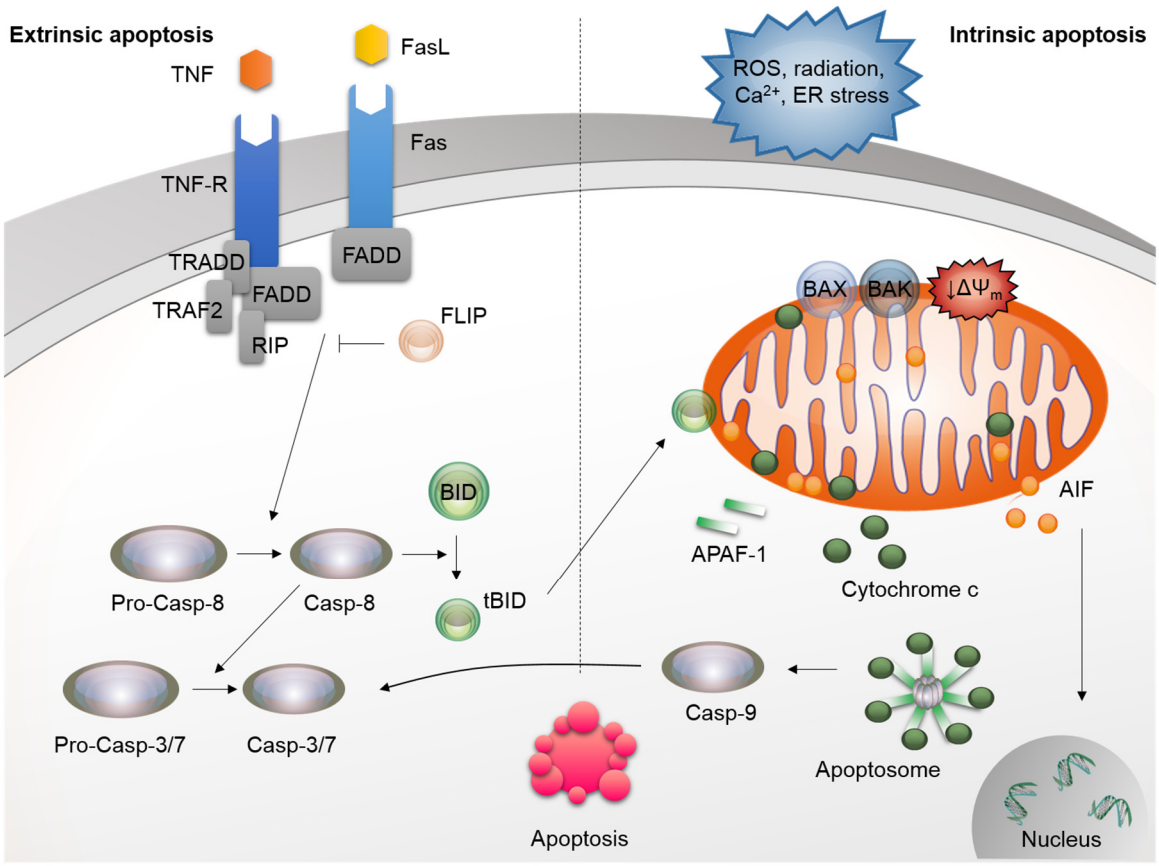

Figure 2. Apoptosis

Extrinsic apoptosis (left) induced by extracellular death ligands (TNF, FasL) leads to the rapid activation of the initiator caspase-8 and effector caspases-3/7 causing cell death. Caspase-8 links extrinsic to intrinsic apoptosis via cleavage of full-length BID to truncated BID, which translocates to the mitochondria. Intrinsic mitochondria-dependent apoptosis (right) is activated upon harsh intracellular stimuli, e.g. ROS, radiation, calcium overload or ER stress, and results in detrimental mitochondrial damage. BAX/BAK and BID/tBID provoke MOMP (mitochondrial outer membrane permeabilization) thereby releasing AIF and cytochrome C into the cytosol. Cytc, APAF-1 and caspase-9 form the so-called apoptosome, which triggers a caspase activation cascade finally executing cell death.

Extrinsic apoptosis requires external death signaling *via* death receptors at the plasma membrane, such as FAS/CD95, tumor necrosis factor (TNF)-related apoptosis-inducing ligand receptor (TRAIL1/2) or TNF receptor 1 (TNFR1) [7]. After ligand binding, death receptors form oligomers and death domains to activate the initiator caspase-8, thereby activating a cascade of effector caspases and provoking rapid cell death [160]. Caspase-8 is also capable of cleaving and activating the pro-apoptotic B-cell-lymphoma-2 (BCL-2) protein BID (BH3 interacting-domain death agonist) to truncated BID (tBID) [48,74,104,111], thereby connecting extrinsic and intrinsic apoptotic pathways [177].

In contrast to death receptor signaling, intrinsic apoptosis is induced by a wide array of intracellular stimuli including oxidative stress, radiation, hypoxia, DNA damage, endoplasmic reticulum (ER) stress or increased intracellular calcium concentration [58].These diverse stimuli converge at the level of mitochondria where they trigger mitochondrial outer membrane permeabilization (MOMP)[57] by pore formation [12,57,154] through the recruitment of the pro-apoptotic BCL-2 family proteins BCL-2 associated x protein (BAX) [73,206] and BCL2 antagonist killer 1 (BAK) [202] to the mitochondrial outer membrane (OMM). Upon mitochondrial permeabilization, pro-apoptotic factors such as Apoptosis-inducing-factor (AIF), Endonuclease G (EndoG), high temperature acquired protein A2 (OMI/HrtA2) or second mitochondria-derived activator of caspases (SMAC/DIABLO) and cytochrome c (Cytc) [74,111,153,154] are released from the mitochondrial intermembrane space (IMS). Released Cytc, APAF-1 (apoptotic protease-activating factor 1) [110,229] and caspase-9 [105] activate a caspase cascade in the cytosol *via* formation of the so-called apoptosome ternary-complex [134,188], whereas SMAC/DIABLO [46] and OMI/HtrA2 [78] promote caspase activation through neutralizing the inhibitory effects of IAPs (inhibitors of apoptosis proteins). Eventually, the apoptosome initiates the auto-activation of caspase-9 and subsequent activation of caspase-3 [105,229].

Over the past decades a caspase-independent form of intrinsic apoptosis has been introduced where mitochondrial damage is regarded as *the point of no return* in the cell's commitment to die [127,177,223]. Alterations in mitochondrial morphology and function ultimately result in disruption of the mitochondrial membrane potential and energy supply, ROS formation and sudden opening of the mitochondrial permeability transition pore (mPTP). This mPTP, is observed at the inner mitochondrial membrane rendering it permeable for small molecules and proteins with less than 1500 Da [16]. Finally, nuclear DNA fragmentation occurs through interaction of AIF with phosphorylated cyclophilin A (CypA) and histone H2AX [6,11,43,163] or the nuclease macrophage migration inhibitory factor (MIF) [200]. Owing to increasing research recognizing significant morphological overlap with necrosis, this form of cell death should rather be allocated to regulated necrosis than to apoptosis [182].

1.1.2 Regulated necrosis

Necrosis, which was originally defined as random and irreversible rapid death forced by harsh mechanical, chemical or temperature stimuli, is recently accepted as genetically controlled and, consequently, is termed *regulated necrosis* [30,196]. Necrosis is an acute form of cell death morphologically characterized by cytoplasmic swelling, early plasma membrane rupture, cellular leakage, and dilatation of cellular organelles causing inflammation in surrounding regions [58]. Additional aspects, such as ROS formation, mitochondrial damage, necrosome formation or inhibition by several pharmacological inhibitors, define a number of distinct subclasses of regulated necrosis, for instance necroptosis, parthanatos, oxytosis or ferroptosis [59] which all have been implicated in various age-related and/or neurodegenerative diseases.

1.1.2.1. Oxytosis

In immortalized mouse hippocampal HT22 cells, a model system to study regulated oxidative neuronal cell death has been established which is known as *oxytosis* [185]. A special feature of these HT22 cells, originally derived from neural HT4 cells [34,123], is their deficiency in ionotropic NMDA (N-methyl-D-aspartate) receptors. Consequently, upon exposure to millimolar glutamate concentrations, oxidative cell death occurs independently of excitotoxic NMDA receptor-activated calcium overload or caspase activation (1.1.3) [54]. Independence of caspases, calpains and cathepsins is further confirmed by the fact that neither the pan-caspase inhibitor z-VAD-FMK, caspase-8 inhibitor IETD-FMK nor calpain or cathepsin inhibitors are protective in this paradigm of cell death [54,103]. Instead, oxytosis is induced through direct inhibition of the cystine/glutamate antiporter system (X_C^-) at the cell surface [9,125] which consists of the disulfide bond-linked cell surface antigen heavy chain (4F2) and the solute carrier family 7 member 11 (xCT or SLC7A11) light chain [155].

Physiologically, X_C^- transports glutamate out of the cell in exchange for cystine [155] (Figure 3). However, upon high extracellular glutamate concentrations or direct inhibition of the transporter, this exchange is shut off thereby reducing cysteine pools required for glutathione (GSH) synthesis as part of the cell's redox defense [2,184]. GSH depletion in turn leads to compromised function of glutathione peroxidase 4 (GPX4), which is essentially responsible for the maintenance of a proper redox state by reduction of hydrogen peroxide, organic hydroperoxides as well as lipid peroxides as products of 12/15 lipoxygenases (LOX) (e.g. oxidized polyunsaturated fatty acids: PUFA-OOH and phospholipids: PL-OOH) at the expense of reduced glutathione [4,45,114]. In addition, GPX4 inhibition is correlated to enhanced 12/15-LOX activity through accumulated ROS giving rise to a chain reaction of massive soluble and lipid ROS production [162], which can be blocked using the antioxidants vitamin E [159], Trolox and the LOX inhibitors baicalein or PD146176 [106,186]. Subsequent to increased ROS formation, the dynamin-related protein 1 (DRP1) and the pro-apoptotic BCL-2 family protein BID translocate to the OMM, where they mediate fission of the mitochondrial network, mitochondrial ROS production, and loss of mitochondrial membrane potential and ATP production through electron leakage from the electron transport chain [103,186]. Notably, depending on their subtype and differentiation state, neurons exclusively inherit an alternatively spliced, BH3 domain-only form of BAK (N-BAK) with strong translational arrest of the mRNA, thus not being a substitute for BAX or a target for BID at the mitochondrial site during oxidative cell death [86,189]. Sequential release of pro-apoptotic proteins, for instance the mitochondrial flavoprotein AIF anchored at the inner mitochondrial membrane, mediate final cell death execution upon translocation to the nucleus [72,186], nuclear condensation and DNA cleavage [163] presumably through interaction with cytosolic CypA [43] or MIF nuclease [200]. Despite this pro-death signaling upon mitochondrial release, AIF is believed to play an important role in the regulation of mitochondrial morphology and mitochondrial energy metabolism [163]. In this context, AIF was shown to stabilize mitochondrial complex I and *vice versa*. Interestingly, AIF depletion-induced complex I degradation resulted in protection against glutamate toxicity through preconditioning effects, such as reduced mitochondrial membrane potential and enhanced mitochondrial stability [23,24,133].

Despite a lack of initial calcium overload as found in excitotoxicity, during oxytosis calcium enters the cell in a delayed manner through the calcium release-activated calcium channel protein 1 (ORAI1) [80]. Therefore, glutamate toxicity in HT22 cells is considered as an adequate model system to study oxidative neuronal cell death *in vitro* as it combines oxidative stress, mitochondrial BID-transactivation, mitochondrial damage, AIF release and enhanced intracellular calcium levels.

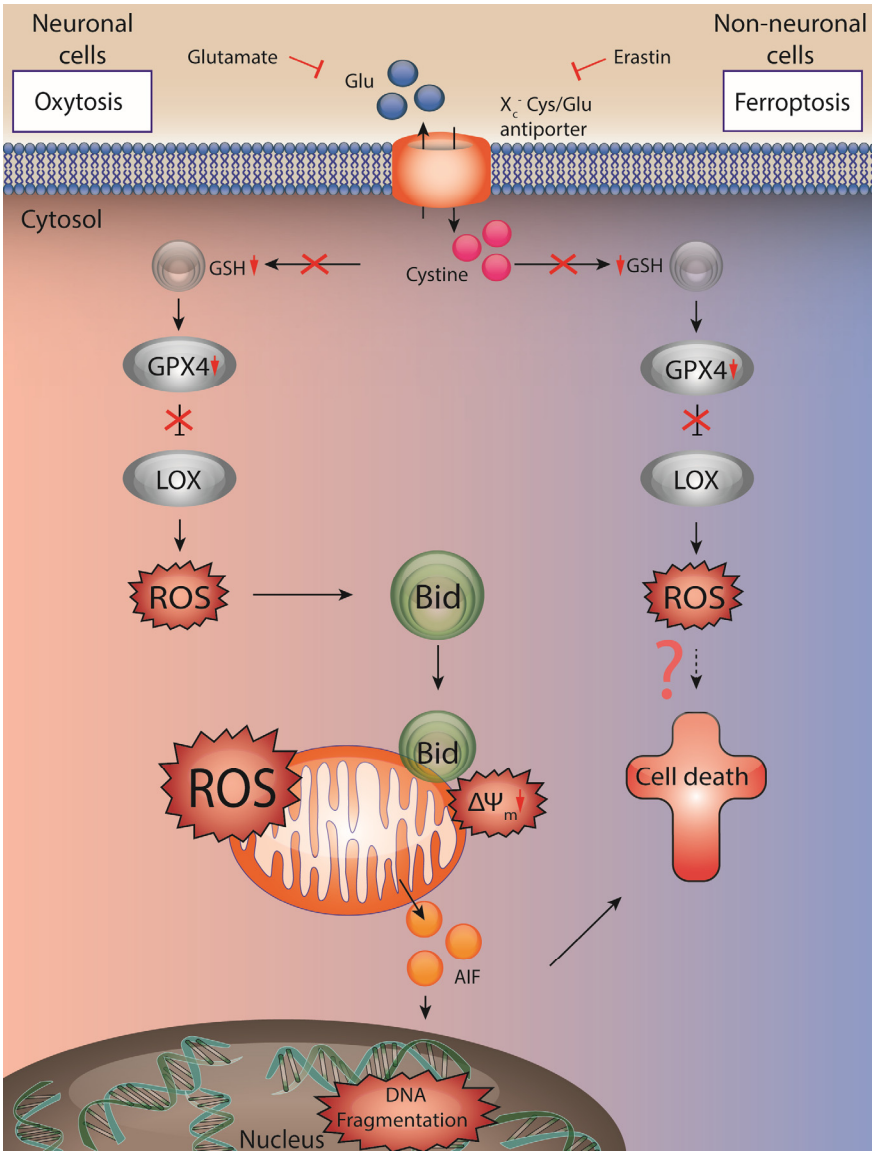

Figure 3. Oxytosis and ferroptosis

Glutamate and erastin inhibit the X_c^--antiporter at the cell's surface in paradigms of oxytosis and ferroptosis, respectively, resulting in decreased cystine and GSH levels. Subsequently reduced GPX4 activity and correlated activation of 12/15-LOX mediate significant formation of reactive oxygen species (ROS). In erastin-induced ferroptosis cell death is defined to be induced through oxidative stress and independently of mitochondrial demise. In neuronal HT22 cells, oxytosis-induces transactivation of BID to the mitochondria and causes mitochondrial ROS formation that is associated with irreversible morphological and functional damage, e.g. loss of membrane potential, decline of ATP levels and release of apoptosis inducing factor (AIF), which mediates final cell death.

1.1.2.2. Ferroptosis

Recently, an iron-dependent form of regulated oxidative cell death attracted much attention. The term *ferroptosis* is derived from the word *apoptosis* to emphasize the strict regulation of this type of cell death, and *ferrum*, the Latin word for "iron" due to the biochemical contribution of iron metabolism and iron-containing enzymes to impaired redox homeostasis [38]. Iron is crucial to a variety of redox enzymes involved in respiration, which use iron-sulfur (Fe-S) clusters as cofactors, for instance nicotinamide adenine dinucleotide (NADH) dehydrogenase and coenzyme Q (Cytc reductase). Heme iron is used in oxygen transport as hemoglobin and myoglobin, and by catalase and superoxide dismutases (SODs) for detoxification of ROS [49].

Death from ferroptosis has been defined as the fatal combination of iron toxicity, antioxidant depletion due to disruption of GPX4 and membrane damage through autoxidation of polyunsaturated phospholipids (PU-PLs) [38,41,90,180] and enhanced 12/15-LOX activity, and, as such, is implicated in several human pathological conditions [30]. In this regard, one of the best-studied pathologies is neurodegeneration. To date, GPX4 impairment and lipid peroxidation as key features of ferroptosis have been described in models of traumatic brain injury [204], cerebral ischemia [175], AD [21,88,115,205], PD [35,77,217], Friedreich's ataxia [1] and HD [29,137]. In addition, ferroptosis is emerging in acute renal failure, hepatic and heart ischemia/reperfusion injury, in T-cell immunity and as a curative therapeutic mechanism in tumor pathology [49,207,219]. In this regard, NAD phosphate (NADPH) abundance was proposed as a biomarker for ferroptosis sensitivity useful for predictions about cancer cell sensitivity towards chemotherapy using novel ferroptosis inducing-compounds [168,169].

Mechanistically, oxidative cell death by ferroptosis can be induced by either indirect disturbance of redox homeostasis through inhibition of system X_c^-, subsequent cysteine and GSH depletion and reduced GPX4 activity by erastin [42,185], or in a direct manner through RSL3-induced covalent GPX4 binding and inactivation [211] (Figure 3). In the following, increasing 12/15-lipoxygenase activity gives rise to excessive PEBP1-dependent enzymatic [170,204] and iron-catalyzed non-enzymatic lipid peroxide formation (mostly oxidized arachidonic [20:4] and adrenic [22:4] phosphatidylethanolamines, Figure 4) [162,195,213], which changes lipid bilayer architecture and rapidly leads to cell death.

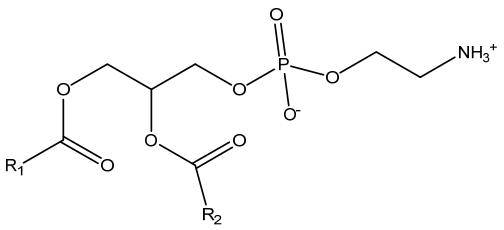

Figure 4. Phosphatidylethanolamine scaffold

For the synthesis of polyunsaturated phospholipids, the fusion of polyunsaturated fatty acids with CoA is required, which is catalyzed by the enzyme acyl-CoA synthetase long chain family member 4 (ACSL4) thus facilitating their esterification into phospholipids accomplished by LPCAT3 (lysophospholipid acyltransferase 5) [40,90]. In MEF and Pfa1 cells genetic deletion or pharmacological inhibition of ACSL4 by triacsin C were both effective in protecting against ferroptosis at an early stage before lipid ROS occur [41,90,90]. In this paradigm of oxidative death, inhibition of iron supply, ROS formation and LOX inhibition provides therapeutic potential against neuronal loss. At the level of iron metabolism, chelators such as deferoxamine and the lipid ROS scavenger liproxstatin aim to reduce iron-dependent ROS formation and prevent downstream ferroptotic cell death *in vitro* and in *in vivo*, e.g. in models of acute renal failure and hepatic ischaemia/reperfusion injury [38,53]. Another encouraging strategy is the pharmacological inhibition of lipid peroxidation through inhibitors of lipid autoxidation, so-called radical-trapping antioxidants (RTAs), for instance liproxstatin-1 [53] and ferrostatin-1 [38,171,227], which were identified using high-throughput screens; or recently described diarylamines derived from petroleum degradation inhibitors [164]. Despite a considerable increase in studies on oxidative cell death, the exact chronological and molecular pattern of the events accompanying ferroptosis and the final cell death execution following lipid peroxidation particularly in neurons remains elusive.

1.1.3 Excitotoxicity

During ischemic and hypoglycemic episodes, presynaptic neurons massively release the excitatory neurotransmitter glutamate up to millimolar concentrations in the synaptic cleft (Figure 5) resulting in overstimulation of postsynaptic NMDA or AMPA (α-amino-3-hydroxy-5-methy-4-isoxazole propionic acid) glutamate receptors and subsequent excitotoxic cell death initially proposed by Olney et al. in 1969 [129].

Upon rapid calcium influx and secondary activation of voltage-gated calcium channels as well as calpain-mediated cleavage of the plasma membrane Na^+/Ca^{2+} exchanger (NCX), homeostatic mechanisms are inactivated and calcium levels dramatically rise. Mitochondria are massively overloaded with calcium causing permeability transition, ATP depletion, ROS generation, such as superoxide and nitric oxide, and release of AIF and Cytc. In addition, the activation of cathepsins, calpains and caspases is observed orchestrating the final steps of cell death [3,25,142,143,201]. Regardless of unique biochemical features it is still under debate whether the paradigm of excitotoxicity should be considered as a sole form of cell death as it has been linked to both the activation of apoptosis and regulated necrosis [116].

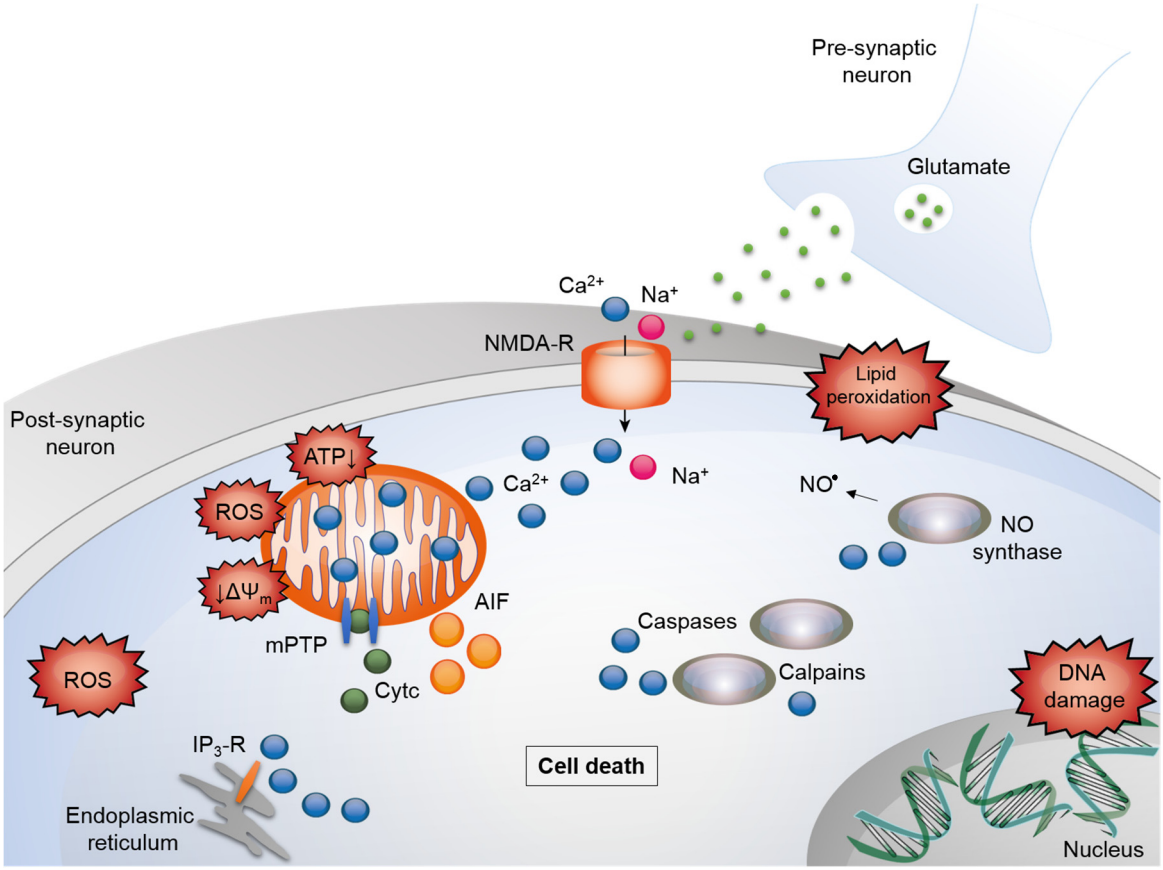

Figure 5. Excitotoxicity

Excitotoxicity is initiated upon massive glutamate release from pre-synaptic neurons. This neurotransmitter binds to post-synaptic glutamate receptors, e.g. NMDA and AMPA receptors, provoking excessive calcium influx. Mitochondria take up a significant amount of calcium leading to ROS formation, disturbed ATP synthesis and membrane depolarization. Upon opening of the mitochondrial permeability transition pore, Cytc and AIF are released, which leads to caspase-activation, nuclear DNA damage and cell death. The ER contributes to calcium overload by release of stored calcium thereby promoting caspase and calpain-cleavage induced detrimental effects. Inside the cell calcium-induced ROS formation through NO synthase (NOS) and lipid peroxidation further harms the cell and leads to the disruption of membranes at the cell surface and at the mitochondria driving the neuron to death.

1.2 BCL-2 family proteins

The family of BCL-2 proteins plays a major regulatory role in mitochondrial permeabilization and thereby promote pro- and anti-apoptotic events in the cytosol and in mitochondria. As such, BCL-2 protein activity is implicated in the regulation of mitochondrial morphology and metabolism such as carbon substrate utilization, electron transport and metabolite import [66]. Moreover, BCL-2 family proteins are involved in tumor pathology, neurodegenerative and autoimmune diseases as well as in tissue development and maturation of blood cells [62,118]. In mammalian cells, at least 12 core BCL-2 proteins are known which are subdivided in three classes according to their properties of either promoting or inhibiting cell death and their BCL-2 homology (BH) domains (Figure 6). The first group includes all pro-survival BCL-2 proteins (BCL-2, BCL-XL, BCL-W, MCL-1, A1), whereas the apoptosis initiators are subdivided in multi-domain (BAX, BAK, BOK) and BH3-only proteins (BID, BIM, BIK, BAD, PUMA, NOXA). Pro-apoptotic signaling can be achieved by either direct activation of cell death, known as *activators* (BID, BIM) or by antagonizing anti-apoptotic proteins, the so-called *sensitizers* (NOXA, BIK) [101,218]. The multi-domain pro-apoptotic proteins BAX and BAK most prominently mediate MOMP by their incorporation into the OMM once truncated BID is translocated to the OMM and mediates BAX/BAK oligomer pore formation. At the MOM, the pores release Cytc and other pro-apoptotic factors which can be circumvented by direct interaction with prosurvival BCL-2 proteins [138]. In turn, a caspase cascade is activated and the apoptosome is formed representing the *point of no return* in intrinsic apoptosis (1.1.1.).

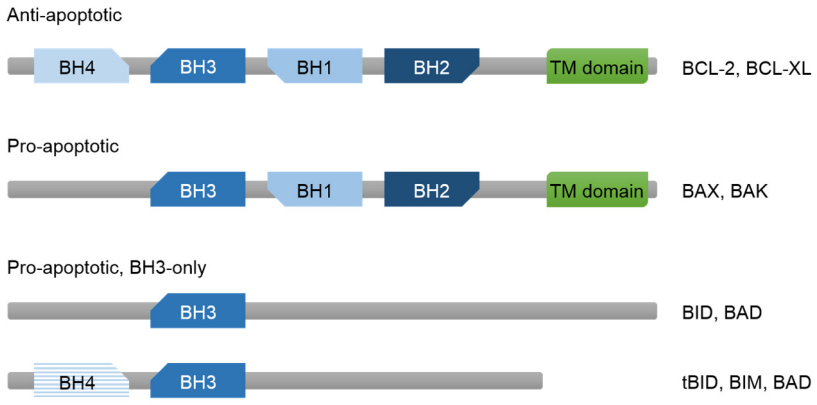

Figure 6. BCL-2 family proteins
BCL2-family proteins are subdivided into three major groups according to their anti-apoptotic or pro-apoptotic properties and their BH domains.

1.2.1 The BH3-only protein BID

Among the BCL-2-family proteins the cytosolic 22 kDa BH3-only protein BID is a key regulator of mitochondrial apoptosis by activating BAX and BAK to promote MOMP, thereby linking extrinsic to intrinsic apoptosis pathways [199]. In contrast to other BH3-only proteins, BID appears as a highly structured protein with conserved regions of sequence homology and similar predicted secondary structure to the core multi-BH3 domain BCL-2 family members (Figure 7). According to the NMR spectroscopy structural 3D models [26,120], BID contains eight α-helices, two of which build a hydrophobic core (α6 and α7), an unstructured N-terminus and an intramolecular unstructured loop with several distinct cleavage sites for caspases, calpains, cathepsins, granzyme B and c-Jun N-terminal kinases (JNK) activated protease [18]. As suggested by Kvansakul et al. [102], BID may contain a redefined BH4 region at the N-terminus, which was originally found in anti-apoptotic BCL-2 proteins. Further attempts to clarify the 3D structure included generation and purification of novel recombinant mouse Bid constructs lacking unstructured parts of the protein to facilitate crystal growth for X-ray crystal analysis, however, reproducible crystallization could not be achieved so far[132].

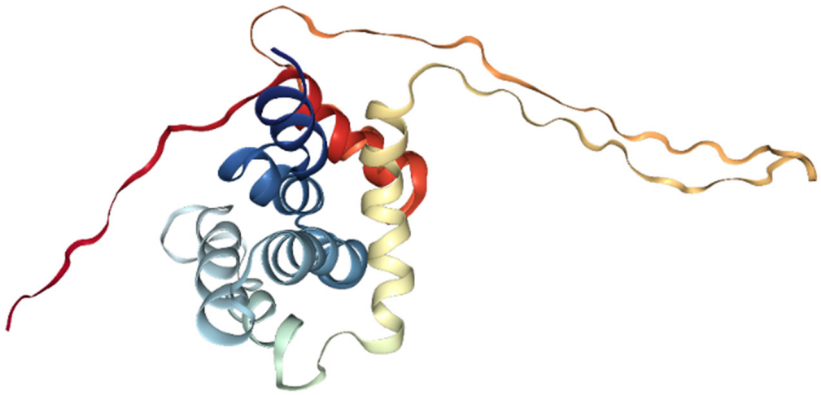

Figure 7. NMR mouse BID protein structure (1DDB)
The NMR solution structure of mouse BID [112] depicts eight α-helices, two of which build a core unit, an unstructured N-terminus and an intramolecular unstructured loop

In response to apoptotic stimuli, the full-length protein is proteolytically cleaved by caspase-8 (or by granzyme B, calpains, cathepsins and more rarely other caspases) into an N-terminal p7 fragment, so-called nBID and a C-terminal p15 fragment, so-called truncated BID (tBID or cBID) containing the BH3 domain (amino acids 90-98) (Figure 8) [74,104,111].

```
Human:    MDCEVNNGSSLRDECITNLLVFGFLQSCSDNSFRRELDALGHELPVLAPQWEG--YDELQ
Mouse:    MDSEVSNGSGLGAEHITDLLVFGFLQSSG--CTRQELEVLGRELPVQA-YWEADLEDELQ

 58       TDGNRSS-HSRLGRIEADSESQEDIIRNIARHLAQVGDSMDRSIPPGLVNGLALQLRNTS
 57       TDGSQASRSFNQGRIEPDSESQEEIIHNIARHLAQIGDEMDHNIQPTLVRQLAAQFMNGS
          ▲                                  ▲       ▲
          Casp-8                             BH3 domain
          RSEEDRNRDLATALEQLLQAYPRDMEKEKTMLVLALLLAKKVASHTPSLLRDVFHTTVNF
          LSEEDKRNCLAKALDEVKTAFPRDMENDKAMLIMTMLLAKKVASHAPSLLRDVFHTTVNF

          INQNLRTYVRSLARNGMD 195
          INQNLFSYVRNLVRNEMD 195
```

Figure 8. Human/mouse BID protein sequence alignment

When still bound, the fragment-complex (also termed cBID: cleaved BID) is masking the BH3 domain and translocates to the mitochondria. At the mitochondria, the BID-complex breaks apart, adopts an extended conformation [55] and tBID helices α4-α7 associate with the OMM [165] (Figure 9) thereby recruiting BAX [73,206] and BAK [202][203] with its unmasked hydrophobic BH3 domain.

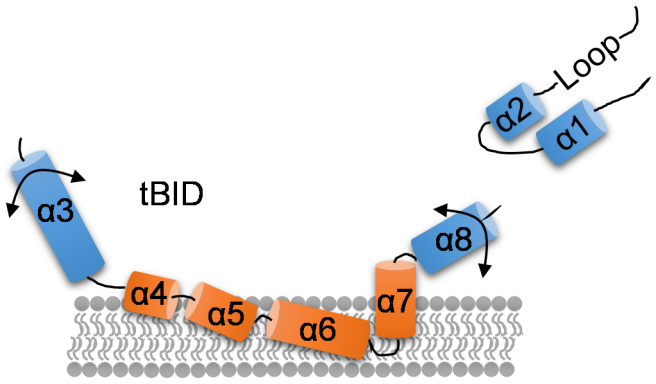

Figure 9. Proposed tBID association with mitochondrial membranes

BAX and BAK, in turn, insert and form oligomers mediating MOMP to release pro-apoptotic proteins such as Cytc [12,74,111,154,202] and AIF [5] from the IMS. The presence of a mitochondria specific negatively charged phospholipid at the IMM, namely cardiolipin, was demonstrated to be required for tBID binding and BAX oligomerization [68,112]. In addition, the presence of mitochondrial carrier homolog 2 (MTCH2) at the mitochondria has been shown to further increase tBID recruitment and is discussed as a second *tBID receptor* [71,92,146,222]. Apart from direct pro-apoptotic function, BID is also able to bind and inhibit anti-apoptotic BCL-2 family proteins such as BCL-2 and BCL-XL, thus indirectly promoting apoptosis [199]. Moreover, BID is upregulated by the tumor suppressor and apoptosis initiator p53 and promotes p53-regulated apoptosis [157]. Additionally, BID is located in the nucleus where it is known to participate in a mitosis checkpoint and maintenance of genomic stability possibly functioning as a sensor of DNA damage through ATM (ataxia-telangiectasia mutated serine/threonine kinase)-mediated phosphorylation [91,228].

Functional studies on BID deficiency *in vitro* found significant protection against oxidative stress in neuronal HT22 cells [103], oxygen-glucose deprivation (OGD) in neurons [117,140] and against MNNG-induced necroptosis in $BID^{-/-}$ MEFs (mouse embryonic fibroblasts) [19]. In mice, loss of BID has little effect on developmental apoptosis but provokes resistance to Fas-induced hepatocyte apoptosis [215]. A study on middle cerebral artery occlusion (MCAO) as a model of cerebral ischemia confirmed BID-cleavage by caspase-8 *in vivo* and revealed BID-deficient mice to obtain attenuated infarction size [140,216] and reduced inflammation [117] suggesting BID to contribute to nerve cell demise upon ischemia. Improved outcome of BID-deficient mice was additionally demonstrated in a model of renal ischemia reperfusion injury where *Bid* knockout ameliorated renal failure [203].

The BCL-2 family protein BID was also found to be a mediator of astrocyte activation in neuroinflammation through NF-κB signaling analyzed in wildtype (WT) and BID-deficient mice [100]. In a controlled cortical impact (CCI) model for traumatic brain injury, BID-deficient mice showed decreased early posttraumatic brain cell death and tissue damage, however, their functional outcome deficits were not reduced [15]. Finally, excitotoxic BID cleavage was detected in a rat model of seizures evoked by kainic acid injection into the amygdala [81] and in human temporal lobe epilepsy [209].

1.2.2 The BID-inhibitor BI-6c9

One of the best-studied inhibitors of oxytosis is the BID inhibitor BI-6c9 [13,14] (Figure 10), which was developed in order to provide neuroprotection in conditions of BID-mediated mitochondrial cell death. The molecular design of BID inhibitors was based on the mouse BID NMR structural data from 1999 (1DDB) [120] which indicated a hydrophobic groove at the surface of the protein and led to the lead structures BI-11A7 and BI-6c9 being protective *in vitro* [13,14,72,98,103,186]. However, further optimization of small-molecule BID inhibitors requires improved affinity and water solubility for increased bioavailability upon oral application and would be facilitated by high-resolution crystal BID structures for 3D modeling of lead structures.

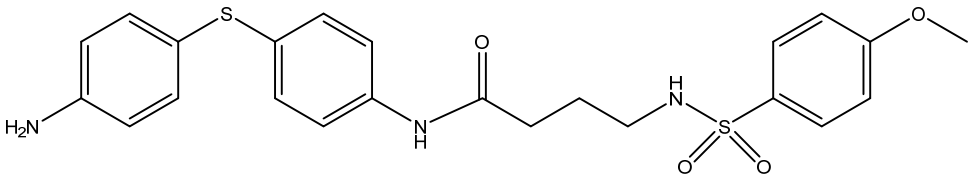

Figure 10. BID inhibitor BI-6c9

1.3 CRISPR/*Cas9* genome engineering

Genetic abnormalities are responsible for a variety of neurodegenerative disorders as they often result in the accumulation of mutated and/or misfolded proteins as found in for instance AD, HD or PD [17]. Latest research has established CRISPR (Clustered Regularly Interspaced Short Palindromic Repeats)/*Cas9* (CRISPR-associated protein) gene editing as a versatile tool [63,87] to knock out or repair certain genetic material providing new therapeutic options for the treatment of genetic neurological diseases lacking effective treatment options. Editing genomic DNA using CRISPR marks the beginning of a new era and may be used to reduce or even halt disease progression but has to be tightly controlled for precise gene manipulation in the affected area. Due to the complexity of editing human genomes, CRISPR is also widely established for the generation of animal models [210] for investigating the pathogenic mechanisms underlying neurodegenerative processes and to reveal novel treatment strategies. So far, various other gene editing tools, for instance TALEN (transcription activator-like effector nucleases) [89] and zinc finger nucleases (ZFNs) [190] have been established, however, the CRISPR/*Cas* technology seems most promising being faster and more efficient [56].

CRISPR/*Cas* editing techniques have evolved from a microbial adaptive immune mechanism to fend off foreign nucleic acids upon viral invasion (Figure 11) [122,144]. A CRISPR locus contains a sequence encoding the endonuclease *Cas* and unique so-called *spacer motifs* derived from viral nucleic acids delineated by short, repeated, palindromic sequences. Upon transcription and translation of the bacterial CRISPR-DNA, the spacers, which are homologous to the viral nucleic acids, become guide RNAs leading the endonuclease *Cas9* to the target viral sequences for degradation. In case of reinfection, bacteria utilize this system to destroy pathogenic viral nucleic acids.

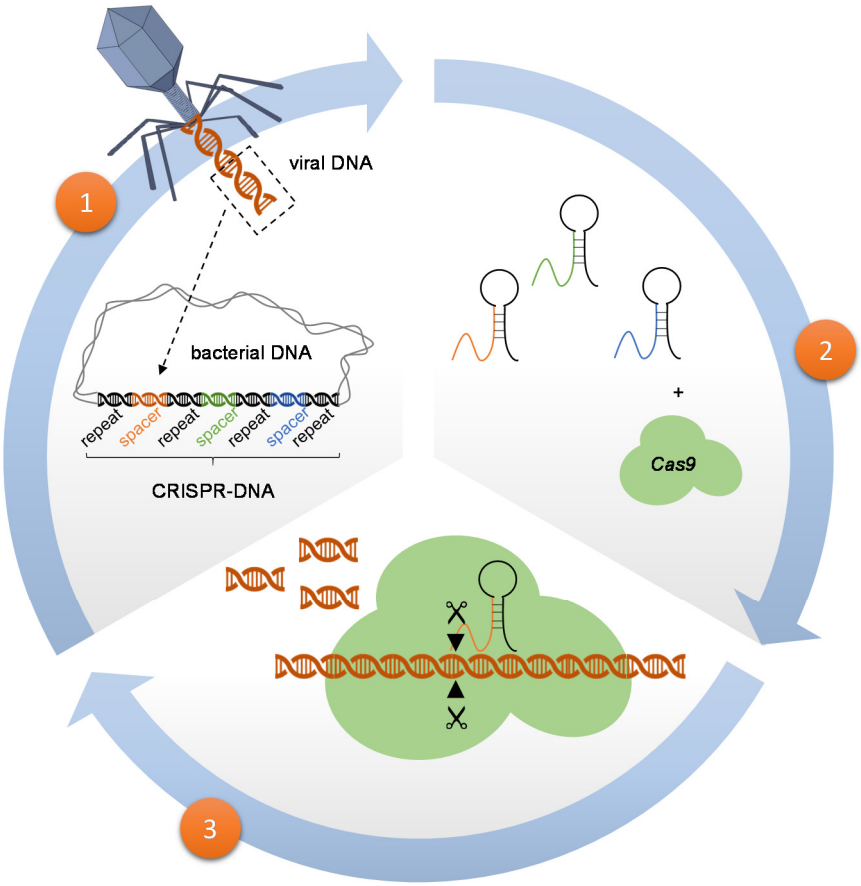

Figure 11. CRISPR/Cas process

(1) Infection of a bacterial cell and release of bacteriophage nucleic acids leads to the incorporation of viral DNA/RNA in the bacterial genome delineated by short repeated sequences (CRISPR-DNA). (2) Transcription and translation of bacterial CRISPR DNA results in various guide-RNA/tracr-RNA sequences targeting the original viral DNA by *Cas9*. (3) Bacterial CRISPR-RNA and *Cas9* eliminate invading viral genomic material.

Since the early discovery of CRISPR sequences in 1987 [85] and viral defense mechanisms in 2005 [122,144], the system has been adapted for use as gene editing tool in eukaryotes in 2012 (Figure 12) [63,87]. Meanwhile, the number of new applications and improved gene editing protocols increased dramatically [56]. One of the most applicable gene editing techniques using CRISPR/*Cas9* is simple gene knockout by frameshift or stop codon mutation. Here, a target-specific guide RNA including a PAM (protospacer adjacent motif, mostly NGG for *S. pyogenes* derived *Cas9*) sequence combined with *Cas9* is exploited to perform double-strand breaks (DSB) in the genomic DNA. Subsequently, DNA repair mechanisms are activated in an attempt to repair DNA strand breaks by non-homologous end joining (NHEJ) or homology-directed repair (HDR) [83]. The predominant repair mechanism NHEJ, however, is error-prone leading to addition or deletion of nucleotides named *indel mutations* ultimately resulting in non-sense protein mutation or knockouts. In contrast, HDR results in full DNA restoration but requires a homologous DNA sequence for insertion. This rare repair mechanism can be taken advantage of if targeted introduction of specifically mutated genetic material is desired (knock-in) although the successful mutation rate is as little as ~8-10 % [8] if not enhanced by suppressing NHEJ using for instance KU70 knock down [191].

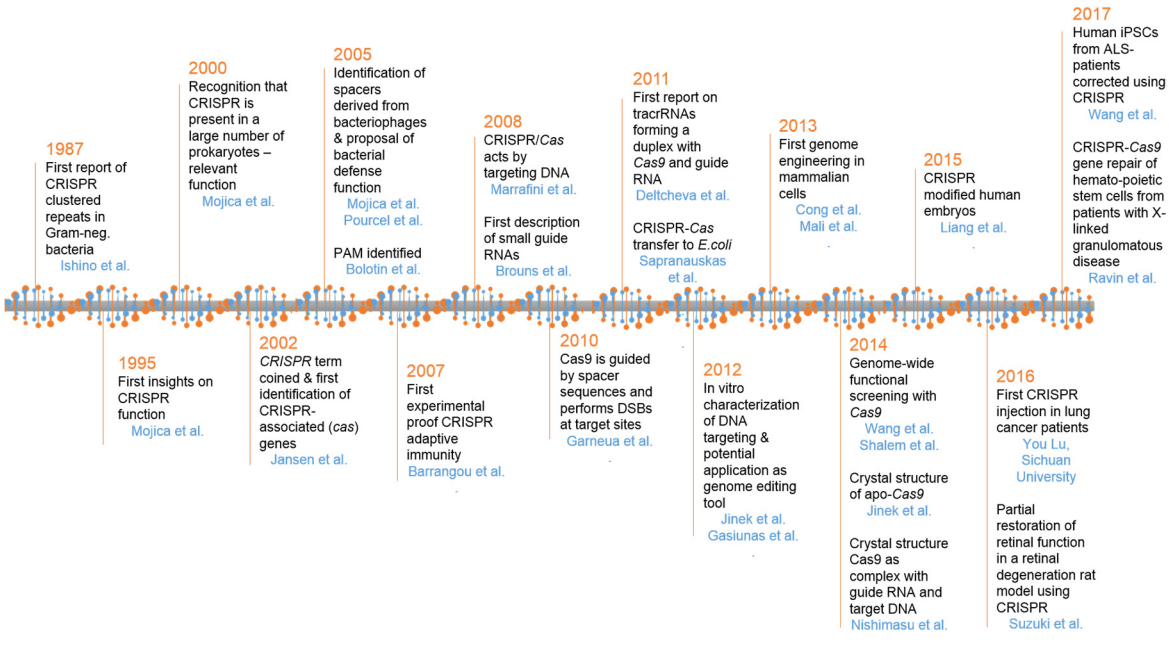

Figure 12. CRISPR timeline

CRISPR/Cas9 is not only useful to permanently alter genetic material but is also applicable for gene regulation purposes [64]. To do so, an enzymatically inactive *Cas9* (*dCas9*) is employed to repress or activate gene transcription when combined with a proper guide RNA and repressor or activator proteins. Variations of *dCas9* can also be targeted to the transcriptional promoter regions of specific genes to activate or block their transcription initiation or elongation [51].

Current attempts in the development of CRISPR-based therapy in neurodegenerative diseases address, for instance, AD and PD. In particular, early-onset familial AD is genetic in origin leading to accumulation of amyloid β plaques (Aβ). Mutations were found in genes encoding for proteins that enhance the accumulation of Amyloid beta (Aβ) protein such as presenilin 1/2 (PSEN1/2) or amyloid precursor protein (APP), and alterations in apolipoprotein E (APOE) which increase the risk for late-onset AD. In order to study AD, human induced pluripotent stem cells (iPSCs) have been created, which display certain phenotypes according to their genotype (CRISPR-derived APP and PSEN mutations [135]). Further, CRISPR applications might be enhancing pathogenic Aβ-clearance or repressing mutant APP production. Moreover, animal models of CRISPR can be used to predict therapeutic and/or adverse effects of pharmacological drugs by repression of certain enzymes targeted by pharmacological inhibitors and to halt detrimental neuronal loss by the identification of key proteins involved in nerve cell death.

A major concern in the field of CRISPR research remains the precise control for off-target effects as gRNAs are limited to 17-24 base pairs length often targeting genetic sequences other than the target site [158]. The chance for off-target effects depends on the succession and number of mismatched nucleotides [83,84,113]. For example, mismatches at the 5' end and at gRNA sequences with high GC content are more likely to be tolerated. Thus, gRNAs should be chosen carefully and CRISPR knockout attempts should be controlled for off-target effects. In addition, nickases are useful to reduce off-targets. Here, *Cas9* is altered in a way, that it is only capable of cleaving one DNA strand and requires a second guide RNA to bind at the opposite side of the target sequence to achieve a complete DSB [97]. Additional approaches are reducing the *Cas9* concentrations and limiting the half-life by using *Cas9* protein delivered *via* cell-derived membrane vesicles (CMV) instead of *Cas9* plasmid DNA [82,192].

1.4 Aims of the thesis

Over the last decades, the crucial involvement of BID-mediated mitochondrial damage in various cell death paradigms involved in neurodegeneration has become evident. Upon activation through excessive (lipid) ROS formation, BID translocates to mitochondria where it fatally harms mitochondrial morphology and function thereby disrupting the bioenergetic homeostasis. As neuronal computation is energetically expensive, loss of the brain's limited energy supply and mitochondrial damage-associated release of pro-death factors drive neurons to death. Based on this fatal contribution to neuronal loss by mediating mitochondrial death signaling, impeding BID function as a novel therapeutic strategy should be a promising chance to protect brain tissue in neurodegenerative diseases.

In the first part of this thesis the precise biochemical mechanisms and time-dependent progression underlying ferroptotic oxidative cell death by erastin were analyzed. Assuming mechanistic similarity to already existing cell death paradigms, for instance oxytosis, the pathways of ferroptosis in neurons downstream of lipid peroxidation and potential mitochondrial involvement at *the point of no return* in the cell's commitment to die were elucidated. The study focused on the role of BID in linking oxidative stress to mitochondrial injury. Therefore, genetic (CRISPR/Cas9 knockout) and pharmacological BID inhibition (BI-6c9) were exploited to evaluate the role of BID on erastin- and RSL3-induced ferroptotic cell death processes.

In the second part of the thesis, novel targeted antioxidant treatment options for neurodegenerative disorders were addressed with respect to mitochondrial protection. For this purpose, the mitochondria-targeted ROS scavenger MitoQ was assessed for potential neuronal protection against RSL3-induced GPX4 inhibition and subsequent ferroptotic cell death in order to elucidate mitochondrial damage in the context of ferroptosis. Due to the fact that MitoQ is already commercially available as a dietary supplement, potential interference with mitochondrial energy metabolism were investigated.

Finally, neuroprotective approaches could be assisted by structure-guided ligand design demanding high-resolution protein structures of the target protein. To date, two NMR structures for BID have been published [26,120] but no high-resolution X-ray data are available. In previous attempts [132], different constructs of recombinant mouse BID were expressed and purified in high amounts by GSH-affinity and size exclusion chromatography. In an attempt to crystallize these, promising experimental conditions could already be identified as a basis for further optimization. Hence, the primary aim of this part of the study was to optimize BID crystallization by creating and purifying appropriate protein constructs followed by identifying optimal crystallization conditions for an optimal elucidation of the structure of BID using X-ray analysis.

2 Materials and methods

2.1 Chemicals, reagents and kits

2.1.1 Standard chemicals and reagents

All standard chemical reagents commercially available were acquired from Sigma-Aldrich (Taufkirchen, Germany) or Roth (Karlsruhe, Germany) if not stated differently. All buffers and solutions were prepared with demineralized, ultrapure water that was obtained from the SG Ultra Clear UV plus pure water system (VWR, Darmstadt, Germany). Ultrapure, demineralized water for aseptic preparation of solutions and for media used in the cell culture was sterilized either using a steam autoclave (Systec V-40, Systec GmbH, Wettenberg, Germany) or by filtration using 0.22 µm filter sets (Sarstedt, Nümbrecht, Germany). All Kits used in this study (Table 1) were applied according to the manufacturer's protocol:

Table 1. Kits

Kit	**Purpose**	**Company**
Annexin-V-FITC Detection Kit	Apoptosis/Necrosis detection	Promokine, Heidelberg, Germany
Attractene Transfection Reagent	Plasmid transfection	Qiagen GmbH, Düsseldorf, Germany
BODIPY (581/591 C11)	Measurement of lipid peroxidation	Invitrogen, Karlsruhe, Germany
Bradford	Determination of protein content	AppliChem, Darmstadt, Germany
CM-H_2DCFDA	Measurement of soluble ROS	Invitrogen, Karlsruhe, Germany
GSH Assay Kit	GSH detection	Cayman Chemical, Ann Arbor, US
InviTrap® Spin Universal RNA Mini Kit	DNA/RNA extraction	Stratec Molecular GmbH, Berlin, Germany
Lipofectamine RNAiMax Transfection Reagent	siRNA transfection	Life Technologies, Carlsbad, US
ZymoPURE™ Plasmid	Plasmid DNA isolation	Zymogen, Irvine USA
MitoPT™ TMRE Kit	Mitochondrial membrane potential detection	Immunochemistry Technologies, Hamburg, Germany

Kit	Purpose	Company
MitoSOX™	Mitochondrial ROS detection	Invitrogen, Karlsruhe, Germany
Pierce BCA Kit	Determination of protein content	Perbio Science, Bonn, Germany
REDTaq® ReadyMix™ PCR Reaction Mix	PCR	Sigma-Aldrich, Taufkirchen, Germany
SelenoMet *Dream*™ Media Kit	Recombinant protein expression with heavy atom exchange	Molecular Dimensions, Suffolk, UK
SuperScript III One Step RT-PCR System with Platinum® Taq	RT-PCR	Invitrogen, Karlsruhe, Germany
ViaLight™ ATP Plus-Kit	ATP detection	Lonza, Verviers, Belgium
Wizard® SV Gel and PCR Clean-Up System	DNA Gel extraction	Promega, Madison, US
XF Cell Mito Stress Kit	Measurement of respiratory function	Seahorse Biosciences, North Billerica, US

2.1.2 RSL3 synthesis

The four RSL3 diastereoisomers were synthesized by the group of Prof. W.E. Diederich (Philipps-University, Marburg, Germany) according to Yang et al. [211] as depicted in Figure 13 for the *1S, 3R*-RSL3 isomer. Analytical data were in agreement to those published before. Reaction of 3a, an advanced intermediate in the RSL3 synthesis, with acetyl chloride afforded the des-chloro derivative *1S, 3R*-RSL3-Cl in 45% yield.

Reagents and conditions: a, b: [211]; c: acetyl chloride, $NaHCO_3$, CH_2Cl_2, 0 °C - RT, 45 %.

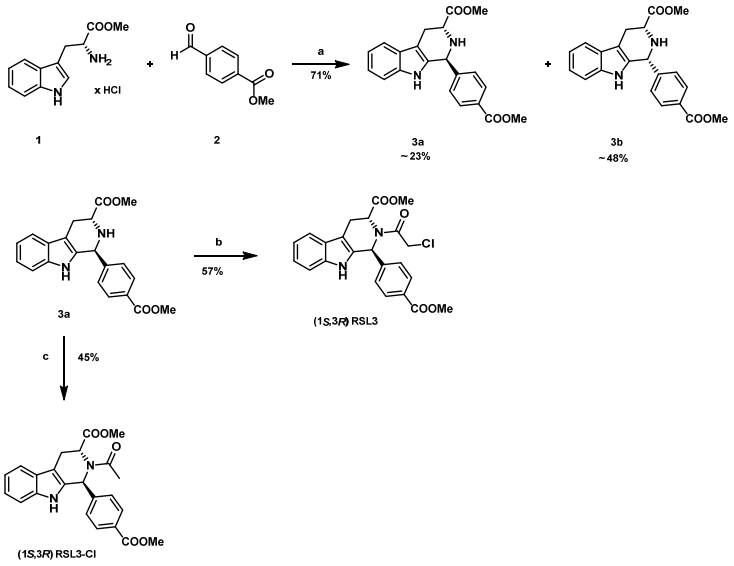

Figure 13. RSL3 synthesis

2.2 Cell culture

2.2.1 HT22 and MEF cell system

2.2.1.1. Cell culture plastic ware:

Cell culture sterile plastic ware was used as listed in Table 2:

Table 2. Cell culture: Sterile plastic ware

Plastic ware	**Company**
T75 flasks	Greiner, Frickenhausen, Germany
T175 flasks	Greiner, Frickenhausen, Germany
6-well plates	Greiner, Frickenhausen, Germany
24-well plates	Greiner, Frickenhausen, Germany
96-well plates	Greiner, Frickenhausen, Germany
96-well plates for BCA	Greiner, Frickenhausen, Germany
96-well plates (white) for ATP	Greiner, Frickenhausen, Germany
96-well xCELLigence E-plates	Roche, Applied Science, Penzberg, Germany
XF96-well microplates and cartridges	Seahorse Biosciences, North Billerica, MA
IbiTreat 8-well plates	Ibidi, Munich, Germany
6 cm dishes	Sarstedt, Nümbrecht, Germany
10 cm dishes	Sarstedt, Nümbrecht, Germany
15 mL tubes	Greiner, Frickenhausen, Germany
50 mL tubes	Greiner, Frickenhausen, Germany
0.2, 0.5, 1.5, 2.0 mL Eppendorf tubes	Sarstedt, Nümbrecht, Germany
0.22 µm Whatman Puradisc™ sterile filter	Whatman, Dassel, Germany
0.45 µm filter	Whatman, Dassel, Germany
Cell scraper	Sarstedt, Nümbrecht, Germany
1, 5, 10 mL syringes	Braun, Melsungen, Germany
Cannulae	Braun, Melsungen, Germany
Nalgene Rapid-Flow Bottle-Top Filter 0.2 µm filter	ThermoFisher Scientific, Schwerte, Germany
Pipette tips	Gilson, Middleton, USA
	StarLab, Hamburg, Germany

2.2.1.2. Cultivation of HT22 and MEF cells

HT22 cells were derived from Gerald Thiel (Homburg/Saar, Germany) with kind permission of David Schubert (Salk Institute, San Diego, US). HT22 cells are derived from parent HT4 cells that were originally immortalized from primary mouse hippocampal neuronal culture with a temperature-sensitive SV40 T-antigen [34,123]. MEF cells were a kind gift from Prof. Axel Methner (Johannes-Gutenberg University, Mainz, Germany).

HT22 and MEF cells were cultured in Dulbecco's modified Eagle medium from Capricorn (DMEM, Ebsdorfergrund, Germany) supplemented with 10 % heat-inactivated fetal calf serum (Biochrom, Berlin, Germany), 100 U/mL penicillin, 100 µg/mL streptomycin and 2 mM L-Alanyl-L-glutamine (Capricorn, Ebsdorfergrund, Germany). For standard cultivation cells were kept in 75 cm^2 culture flasks (T75) in a standard unified incubator at 37 °C and 5 % CO_2. Cells were split twice per week in a ratio of 1:10-1:20.

Splitting of cells was performed as follows: Growth medium was removed and cells were washed once with 10 mL phosphate buffered saline (1x PBS, Table 3) to fully remove the growth media and FCS. For detachment of cells from the bottom of the flasks, 2 mL of trypsin/EDTA solution (Table 4) was added and cells were incubated 2-5 minutes at 37 °C. After detachment of the cells, the protease activity was stopped by adding the 5-fold amount of DMEM growth medium (Table 5). Thereafter, the cell suspension was centrifuged at 1,000 rpm for 5 minutes and the cell pellet resuspended in fresh growth medium. For the quantification of cell numbers, a counting chamber (Neubauer Zählkammer, Brand, Wertheim, Germany) was utilized. Afterwards, cells were seeded into the appropriate culture dishes with a cell density of 6 $x10^3$–6 $x10^4$ cells per well or 5 $x10^5$–1.5 $x10^6$ cells per dish depending on the respective experiments (Table 6).

Table 3. Phosphate buffered saline (PBS), pH 7.4

NaCl	9 g
Na_2HPO_4	0.527 g
KH_2PO_4	0.144 g
HCl (0.1 M)	q.s. for pH 7.4
Aqua demin.	up to 1 L

Table 4. Standard Trypsin/EDTA solution (TE)

Trypsin 7,500 U/mg	100 mg
Ethylene diamine-tetra-acetic acid (EDTA)	40 mg
1x PBS	up to 200 mL

Table 5. HT22 and MEF standard growth medium

DMEM medium with 4.5 mg/L glucose and 110 mg/L sodium pyruvate	440 mL
Heat-inactivated fetal calf serum (FCS)	50 mL
L-Alanyl-L-glutamine 200mM	5 mL
Penicillin 10,000 U/mL, Streptomycin 10,000 µg/mL (Pen/Strep)	5 mL

Table 6. Cell densities for HT22 and MEF cell seeding

Format	**Cell density [~ cells per well or dish)**
96-well plate	6,000-10,000
24-well plate	40,000-60,000
6-well plates	100,000-200,000
Ibidi 8-well plate	12,000-16,000
6 cm dish	500,000
10 cm dish	1,000,000-1,500,000
XF96-well microplates	6,000-10,000
96-well xCELLigence E-plates	5,000-10,000

2.2.2 Primary mouse and rat embryonic neurons

Primary cortical neurons were cultured in PEI-coated dishes. Therefore, cell culture dishes were coated with 5 % polyethylenimine (PEI, Table 7). Coating was achieved by incubation of the dishes with 5 % PEI for 2-3 hours at 37 °C. Afterwards the dishes were washed three times with sterile bidest. water and allowed to dry for 30 minutes under UV-light exposure.

Table 7. Polyethylenimine 5% (PEI)

Boric acid	3.1 g
Borax	9.0 g
PEI 5 %	1 mL
Aqua demin.	ad 0.8 L

Cortices were obtained from embryonic day 14-16 wild type C57BL/6 mice (Charles River Laboratories, Sulzfeld, Germany) and split by trypsinization and trituration as follows: Isolated cortices were incubated in Hank's balanced salt solution (HBSS, diluted from 10x HBSS, Invitrogen, Karlsruhe, Germany, Table 8) containing 1 mg/mL trypsin (Sigma- Aldrich, Taufkirchen, Germany) for 15 minutes at 37 °C. Afterwards, DNAse was added for 30 seconds and the cortices were washed with HBSS and then mixed with HBSS containing 2 mg/mL trypsin inhibitor (Sigma-Aldrich, Taufkirchen, Germany). The cell suspension was then incubated for a further 2 minutes at room temperature. Afterwards, the cortices were washed once with HBSS, and triturated. The triturated cells were centrifuged at 2,000 rpm for 5 minutes at room temperature and the supernatant was removed, and the cells cultured in neurobasal medium supplemented with 2 % (v/v) B-27 (Table 9). Afterwards, the cells were counted in a cell counting chamber (Neubauer Zählkammer) and seeded into 96-well plates with a density of 5.5 $x10^4$ cells. On day 5 and 7 after seeding of cells, half of the medium was exchanged with fresh neurobasal medium, respectively. As cultures of primary neurons develop functional NMDA receptors after 6 to 8 days in culture and therefore are sensitive to glutamate-induced excitotoxicity, experimental treatments were performed with 7 to 9 day old cultures. All media were obtained from Invitrogen (Karlsruhe, Germany) and chemical substances were obtained from Sigma-Aldrich (Taufkirchen. Germany) if not specified differently.

Primary rat embryonic cortical neurons were obtained from wild type Sprague–Dawley rats (Charles River Laboratories) at embryonic day 18 and cultured similarly to primary mouse neurons.

Table 8. Hank's balanced salt solution (HBSS), pH 7.2

10x HBSS	50 mL
HEPES	1.2 g
Pen/Strep 1 % (v/v)	5 mL
Aqua demin.	up to 500 mL

Table 9. Neurobasal medium

Neurobasal medium (Gibco®)	480 mL
B-27 (Gibco®) 2 % (v/v)	10 mL
L-glutamine 1 % (v/v)	5 mL
Pen/Strep 1 % (v/v)	5 mL

2.2.3 DNA/RNA transfection

Transfection of HT22 and MEF cells was performed in either 96-well, 24-well, 6-well, ibidi 8-well plates or in 6 or 8 cm^2 dishes according to which experiment was carried out. Plasmids were transfected 24 hours after cell seeding, whereas siRNA was applied prior to cell seeding (reverse transfection).

2.2.3.1. Transfection reagents

For the formation of DNA transfection complexes of plasmid vectors with Attractene transfection reagent (Qiagen, Hilden, Germany), Opti-MEM I medium (Invitrogen, Karlsruhe, Germany) was utilized.

For siRNA transfection, Lipofectamine RNAiMax transfection reagent (Invitrogen, Karlsruhe, Germany) was used in antibiotic-free Dulbecco's modified Eagle medium (DMEM, Invitrogen, Karlsruhe, Germany) supplemented with 10 % heat-inactivated fetal calf serum and 2 mM L-Alanyl-L-glutamine (all from PAA Laboratories GmbH, Germany).

2.2.3.2. Plasmid transfection

For the purpose of plasmid transfection, HT22 or MEF cells were seeded as stated in Table 10 24 hours in advance and grown under normal growth conditions (37 °C, 5 % CO_2). Prior to transfection, the normal growth medium was replaced completely by fresh standard growth medium and enriched with pre-treatment substances as may be necessary at given time points.

The plasmids were dissolved in Opti-MEM I and Attractene transfection reagent was added. To allow for complex formation, the solutions were incubated for 15 to 20 minutes at RT before the transfection mixture could be finally added to the cell's growth medium. Afterwards, cells were cultivated under normal conditions for 24 to 48 hours until further experimental steps were performed.

Table 10. Plasmid transfection

Format	Cells/well seeded	DNA/well	Attractene/well	Opti-MEM I/well
96-well	5,000-8,000	100-200 ng	0.75 µL	up to 15-20 µL
24-well	30,000-40,000	400 ng-2 µg	1.5-4.5 µL	up to 60 µL
6-well	100,000-150,000	500 ng-5 µg	4.5-8 µL	up to 200-250 µL
Ibidi 8-well	16,000	1 µg	1 µL	up to 50 µL

2.2.3.3. Plasmid vectors

In this thesis the following plasmid vectors (Table 11) were used:

Table 11. Plasmid vectors

Gene/Purpose	Vector names	Company/Origin
Control vector	pcDNA 3.1$^{(+)}$	Invitrogen (Karlsruhe, Germany)
Control vector eGFP	pIRES-EGFP	PT3267-5, #60296-1 BD Biosciences Clontech (US)
Mouse tBid	pcDNA3 Bid p15 or pcDNA3 tBid	Plasmid #8808, Addgene (Cambridge, US)
Mouse full-length Bid	pcDNA3 Bid p22 or pcDNA3 Bid	Plasmid #8774, Addgene (Cambridge, US)
Mouse full-length Bid	pcDNA3 Bid p22 mut	Mutated from Addgene Plasmid #8774
Mouse tBid, eGFP	pIRES-tBid-EGFP	Previously described in [93]
Mouse Bid CRISPR/Cas9	U6-gRNA/CMV-Cas9-GFP target: GTCAGCAACGGTTCCGGCCTGG	Sigma-Aldrich (Taufkirchen, Germany)
Mouse full-length Bid	pET15b Bid p22	Plasmid #8784, Addgene (Cambridge, US)
Mouse tBid	pET15b Bid p15	Plasmid #8782, Addgene (Cambridge, US)

All plasmids were amplified in either self-made DH5α-competent *E.coli*, supercompetent DH5α and isolated using the ZymoPURE™ Plasmid kit according to the manufacturer's protocol. Prior to use, the DNA concentration was quantified using the NanoPhotometer™ (Implen, Munich, Germany). All plasmids cloned were verified by sequencing afterwards (EurofinsGenomics, Ebersberg, Germany).

2.2.3.4. SiRNA transfection

SiRNA transfection was performed in a reverse way immediately before seeding of cells. For transfection, Lipofectamine RNAiMax transfection reagent was used according to the manufacturer's protocol.

The respective siRNA and Lipofectamine RNAiMax were diluted in antibiotic-free growth medium to a concentration appropriate to yield a final concentration of 20 to 80 nM siRNA and 2 µL/mL transfection reagent in the cell culture plate or dish, and were then allowed to equilibrate for 10 minutes at RT. Afterwards, the siRNA solution was combined with the Lipofectamine RNAiMax solution and mixed gently. For normal siRNA transfection the cell's growth medium was exchanged for antibiotic-free growth medium and after 20 minutes of incubation at RT the prepared siRNA mixture was added dropwise. For reverse transfection, the siRNA mixture was filled into the cell culture plates or dishes where it was allowed to form siRNA complexes for 20 minutes at RT prior to addition of antibiotic-free cell suspension. Controls were treated similarly with either control siRNA or transfection reagent in antibiotic-free growth medium exclusively. Gene silencing was verified by RT-PCR and Western blot analysis after 24 and 48 hours, respectively.

2.2.3.5. SiRNAs

For the deletion of BID, two siRNAs and a non-functional control siRNA were acquired from Sigma-Aldrich (Taufkirchen, Germany) according to Table 12:

Table 12. SiRNAs

siRNA	Sequence
SASI_Mm01_00115198 "Bid siRNA #1"	5´-GAGUGUAUCUAAGAGUUU[dT][dT]-3´
SASI_Mm01_00115200 "Bid siRNA #2"	5´-AAACUCUUCAGAUACACUC[dT][dT]-3´
MISSION® siRNA Universal Negative Control #1 (SIC001)	Not specified
siAIF 2.2	5´-AUGUCACAAAGACACUGCA-3´
Eurofins control siRNA	5´-AAGAGAAAAAGCGAAGAGCCA-3´

2.2.4 Induction of cell death

Induction of cell death was performed 24 to 48 hours after seeding of HT22 or MEF cells with either glutamate, erastin, H_2O_2, RSL3, tBID or staurosporine when the cells had reached 70 to 80 % confluency.

2.2.4.1. Glutamate, erastin, RSL3and staurosporine induced toxicity

Glutamate was applied at a final concentrations of 1 to 10 mM, erastin at 0.25 to 2 µM, RSL3 at 0.001-100 µM and staurosporine at 0.1 to 5 µM to initiate cell death. For the preparation of the glutamate stock solution, *D, L*-glutamic acid monohydrate (Sigma-Aldrich, Taufkirchen, Germany) was dissolved in DMEM (PAA Laboratories GmbH; Cölbe, Germany) to a stock concentration of 1 M and the pH was subsequently adjusted to pH 7.2 with sodium hydroxide solution of 1 or 5 M, respectively. The stock aliquots were stored at -20 °C until use. Erastin, RSL3 and staurosporine were dissolved in DMSO to a stock concentration of 1 mM.

For treatment, the stock solutions were diluted in normal growth medium prior to use. Cell growth medium was removed and replaced with the prepared glutamate/erastin/RSL3/ staurosporine solution. For the investigation of neuroprotective effects of several inhibitors, these inhibitors were additionally applied to the glutamate/erastin/RSL3/staurosporine solution either before the treatment (pre-treatment, 1-7 hours), simultaneously (co-treatment) or after the treatment (post-treatment, 1-8 hours). Four to 24 hours after treatment cells were analyzed according to the indicated protocols for RNA, DNA or protein analysis, cell viability, flow cytometry, epi- and confocal microscopy, immunoprecipitation, ATP, Seahorse or GSH assay.

2.2.4.2. H_2O_2 induced cell death

H_2O_2 was used to provoke oxidative stress induced cell death independent of oxytosis or ferroptosis. Therefore, H_2O_2 was applied to HT22 cells at a final concentration of 1 mM and incubated over-night.

2.2.4.3. TBID induced toxicity

TBID mediated cell death was initiated 24 hours after seeding of 5,000-8,000 HT22 cells per well in a 96-well format according to *2.2.3.1* with 0.25 to 0.75 µg plasmid/well, and 0.75 µL Attractene/well or in 24-well format with 2 µg plasmid/well and 4.5 µL Attractene/well. Seventeen to 24 hours after transfection cell viability, morphology or other cell parameters were assessed.

2.2.5 Inhibition of cell death

2.2.5.1. BID inhibitor BI-6c9

For the inhibition of oxidative cell death during oxytosis in HT22 cells, the BID inhibitor BI-6c9 (Sigma-Aldrich, Taufkirchen, Germany; Figure 14) was dissolved in DMSO to a stock concentration of 10 mM and stored at -20 °C until further use. With final concentrations of 10 µM in normal growth medium as co-treatment a complete protection can be achieved.

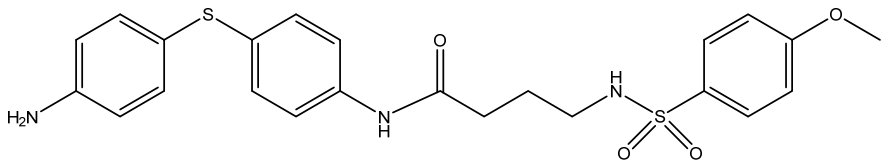

Figure 14. BID inhibitor BI-6c9; Mw: 471.59 g/mol

2.2.5.2. Liproxstatin-1 (Lip-1)

For the inhibition of oxidative cell by lipid peroxidation during ferroptosis [53], the small molecule liproxstatin-1 (a kind gift of Marcus Conrad, Helmholtz-Zentrum Munich, Germany; Figure 15) was used dissolved in DMSO (stock concentration of 100 µM) and was further diluted in growth medium to a final concentration of 1 nM to 2 µM (co- or post-treatment) depending on the respective purpose.

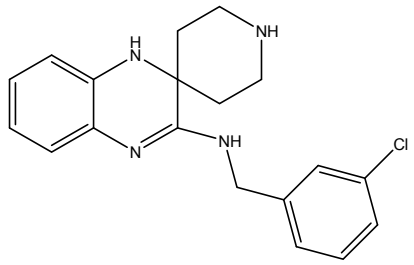

Figure 15. Liproxstatin-1, Mw: 340.85 g/mol

2.2.5.3. Ferrostatin-1 (Fer-1)

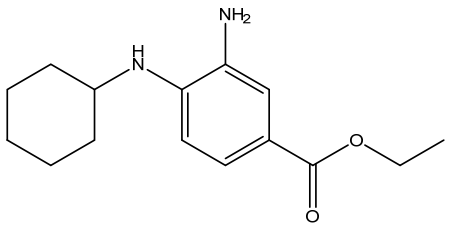

Figure 16. Ferrostatin-1, Mw: 262.35 g/mol

Ferrostatin-1 (Sigma-Aldrich, Taufkirchen, Germany; Figure 16) was used as an inhibitor of oxidative cell death during ferroptosis to control lipid soluble ROS [227]. Therefore, ferrostatin-1 was dissolved in DMSO to a stock concentration of 10 mM and diluted to a final concentration of 10 µM in normal growth medium to protect against ferroptotic cell death.

2.2.5.4. Iron chelator deferoxamine

Deferoxamine (Figure 17) was used as an iron chelating ferroptosis inhibitor [38,53] dissolved in DMSO to a stock concentration of 10 mM and stored at -20 °C until usage. Prior to use deferoxamine was diluted in normal growth medium to a final concentration of 10 µM.

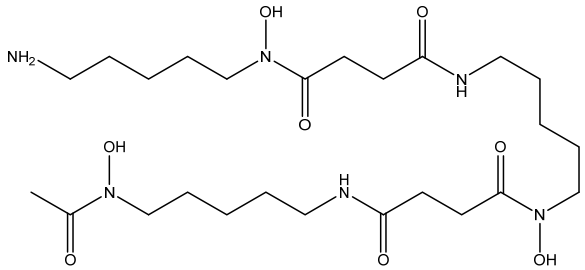

Figure 17. Deferoxamine

2.2.5.5. Mitoquinone (MitoQ)

In order to specifically block mitochondrial ROS formation the mitochondria-targeted ubiquinone derivative mitoquinone (MitoQ; Figure 18) was used [94,95]. MitoQ was diluted in DMSO to a stock concentration of 10 mM and stored at -20 °C. Prior to use MitoQ was diluted in normal growth medium to final concentrations of 0.1-2 µM.

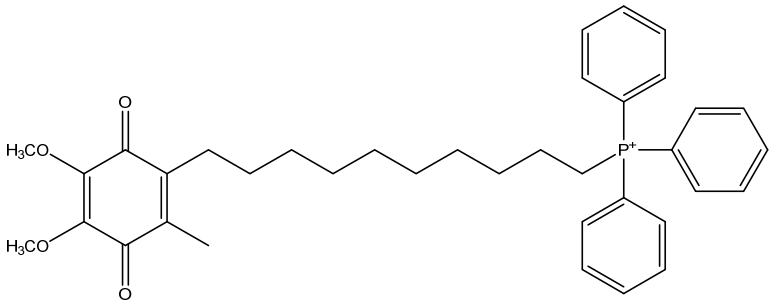

Figure 18. MitoQ

2.2.6 CRISPR/Cas9 Bid gene knockout

2.2.6.1. Plasmid transfection

HT22 *Bid* KO cells were generated using a ready-to-use *Bid* CRISPR plasmid (U6gRNA-Cas9-2A-GFP; MM0000220718, Sigma Aldrich, Germany). As control, the ordered plasmid was digested with XbaI to ensure working with the correct plasmid. The following reaction mix was prepared:

Table 13. XbaI digest

CRISPR plasmid DNA	1 µg
Tango buffer 10x	2 µL
XbaI enzyme	1 µL
Bidest. H_2O	ad 20 µL

The mix was incubated at 37 °C for 1.5 hours and, together with an undigested sample, loaded on a 1 % agarose gel to check for the correct size of cleaving products.

In order to achieve knockout, cells were seeded in 6-well plates with a density of 1.0 x10^5 cells per well and incubated for 24 hours under normal growth conditions (37 °C, 5 % CO_2). 5 µg DNA was diluted in OptiMEM I and mixed with Attractene as stated in section 2.2.3.1 and given into the respective well. Cells were transfected for 48 hours before harvesting with trypsin. To do so, cells were washed once with PBS and incubated with trypsin until floating. After centrifugation at 1,000 rpm for 3 minutes cells were re-suspended in PBS and kept on 37 °C for FACS sorting.

2.2.6.2. FACS sorting

In order to increase CRISPR efficacy successfully transfected GFP-positive cells were sorted by FACS. For elimination of dead cells, cells were stained with DAPI (200 µg/mL). Afterwards, cells were filtered through an 80 µm filter to exclude cell clusters. GFP-positive and DAPI-negative cells were automatically seeded in 96-well plates with either 1, 2 or 5 cells per well, respectively, and grown in HT22 standard growth medium (Table 5).

2.2.6.3. Mutation detection

Growing cell colonies from single wells were picked and allowed to proliferate in either 6-well plates or T75 flasks in HT22 standard growth medium for genomic DNA analysis or Western blot.

For Western blot analysis, cells were trypsinized, centrifuged at 1,000 rpm and washed once with PBS. After a second centrifugation step, cells were lysed in Western blot lysis buffer and put in liquid nitrogen. After thawing on ice cells were centrifuged at 10,000 rpm for 15 min at 4 °C to eliminate cell debris. The supernatant containing proteins was either stored at -20 °C or directly used for BCA protein amount determination (542.8.2). For Western blot analysis 50-80 µg protein were loaded on a 12.5 % 1.5 mm SDS-gel and blotted onto a PVDF-membrane (2.8.4). Incubation with primary anti-BID antibody (Cell signaling, US) was performed overnight at 4 °C. After incubation with a secondary HRP-labeled anti-rabbit antibody (Vector Laboratories, US), Western blot signals were detected *via* chemiluminescence with Chemidoc software (Bio-Rad, Germany).

For genomic DNA sequencing, cells were trypsinized, centrifuged at 1,000 rpm and washed once with PBS. After a second centrifugation step cells were put in liquid nitrogen and either stored at -80 °C or directly used for genomic DNA extraction using InviTrap® Spin Universal RNA Mini Kit. The cell pellet was lysed in 700 µL Lysis buffer containing 1:100 β-mercaptoethanol and immediately put onto a DNA-Binding Spin Filter. After incubation for 1 minute at room temperature and DNA binding to the filter, the filter was centrifuged for 2 minutes at 11,000 rpm. Afterwards, the filter was washed once with Wash buffer 1 and twice with Wash buffer 2 and allowed to dry by centrifugation for 4 minutes at maximum speed. Finally, genomic DNA was eluted using 40 µL of Elution buffer and DNA amount was determined at 260 nm using a NanoPhotometer™ (Implen, Munich, Germany) (2.9.3). For PCR amplification of the CRISPR target region the following reactions were prepared:

Table 14. Genomic DNA PCR

DNA	200 ng
Primer fwd/rev (Table 40)	1 µL each
REDTaq® ReadyMix™ PCR Reaction Mix	6 µL
RNAse free H_2O	ad 20 µL

For genomic DNA PCR the following protocol was used:

Table 15. Genomic DNA PCR cycler program

Initial denaturation	94°C	3 min	
Denaturation	94°C	30 sec	
Annealing	62°C	30 sec	40 x
Elongation	72°C	30 sec	
Final elongation	72°C	5 min	
Cooling	4°C	∞	

After PCR amplification according to section 2.9.4, the PCR samples were loaded onto a 1 % agarose gel stained with ethidium bromide and electrophoresis was performed at 80 V for 30-45 minutes. Under UV light for visualization of the respective PCR products, the 1028 bp band was cut out and DNA purified using the Wizard® SV Gel and PCR Clean-Up System Kit. After determination of DNA amount, 150 ng purified DNA were mixed with 1 µL of forward primer and filled up with RNAse-free water to 15 µL and send for DNA sequencing to Eurofins Genomic (Ebersberg, Germany).

2.2.6.4. Off-target analysis

Most potential off-targets were calculated with web-based tools from the Zhang group [225] and the University of Heidelberg (Germany) [178,179].

Table 16: Genomic DNA PCR program Off-target analysis

Initial denaturation	94°C	3 min	
Denaturation	94°C	30 sec	
Annealing		30 sec	40-45 x
Elongation	72°C	30 sec	
Final elongation	72°C	5 min	
Cooling	4°C	∞	

Table 17. Off-target primer

Primer	Sequence forward/reverse	PCR product size
Trpc4	5' GTCAGCACCTAACGTGTC 3'	707 bp
	5' CGTGGGGCTTAAGTCATAG 3'	
Grm3	5' CACTGTGACAGGAAGCTTC 3'	587 bp
	5' GTGAGCCACACATCACAG 3'	
Syngr1	5' GGAACTCCTTTGGGGTATG 3'	666 bp
	5' GTACCAGAAGAGCAAGTCTG 3'	
Hprt "new"	5' AATCCTCTGGGAGACGAC 3'	728 bp
	5' GCCTGATCCTTCCTGAAG 3'	
Kcne1	5' TGCTGGAATTAGCCAATCAG 3'	593 bp
	5' GGTGCCCCTACAATAAAGAC 3'	
Hivep3	5' CTCTACAAGCACAGGAAGTC 3'	721 bp
	5' GATCTCACTGGTGTCCAC 3'	

Table 18. CRISPR Off-target PCR annealing temperatures

Primer	Annealing temperature
Trpc4	51 °C
Grm3	59 °C
Syngr1	59 °C
Hprt "new"	54 °C
Kcne1	54 °C
Hivep3	54 °C

After PCR amplification of the respective genomic DNA, an ExoSAP digest (USB® ExoSAP-IT® PCR Product Cleanup kit, affymetrix) was performed according to the manufacturer's protocol to remove unused PCR primers and nucleotides for better sequencing results. In brief, 5 µL of the respective PCR product was mixed with 1 µL of ExoSAP reagent and incubated at 37 °C for 30 minutes. Afterwards, the mixture was heated to 80 °C for 15 minutes in order to inactivate the ExoSAP reagent. For sequencing, 1 µL of the respective forward primer was added and sent for sequencing (EurofinsGenomics, Ebersberg, Germany).

2.3 Cell viability assays

2.3.1 Cell morphology analysis

Cell morphology for the analysis of cell death was assessed using a Leica DM6000 epi-fluorescence microscope (Leica, Wetzlar, Germany) and light was collected through a 20 x objective. Images were acquired using phase contrast and were processed with ImageJ Software 1.48v (Maryland, USA). Before imaging, cells were fixed with 4 % paraformaldehyde for 20 minutes at room temperature and washed once with PBS.

2.3.2 MTT assay

Metabolic activity as a measure of cell death was determined using the MTT assay. Here, the reduction of a yellow salt, 3-(4,5-Dimethylthiazol-2-yl)-2,5-diphenyltetrazolium bromide, to an insoluble purple formazan (Figure 19) is exploited to determine activity of NAD(P)H-dependent enzymes of the endoplasmic reticulum and mitochondria (Berridge, M.V., Tan, A.S., McCoy, K.D. & RUI WANG. BIOCHEMICA_96_4_p14-19) and thus metabolic activity or cell viability, respectively.

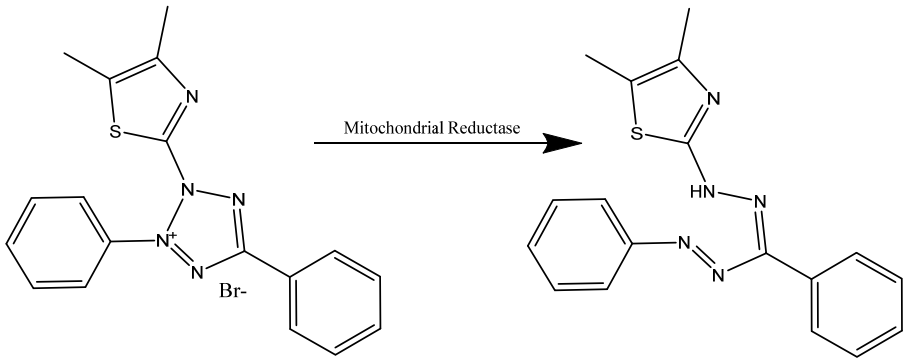

Figure 19. MTT assay

Cells were seeded in 96-well plates and 24 hours later treated as indicated before. 20 µL MTT were added to the culture medium at a concentration of 2.5 mg/mL (in PBS; final concentration: 0.5 mg/mL). After incubation for 1 hour at 37 °C the medium was removed and plates were frozen at -80 °C for at least 1 hour. The purple formazan was then dissolved in 70 µL DMSO and incubated at 37 °C on a shaker for another hour before 570 nm absorbance was measured using FluoStar OPTIMA (BMG Labtech, Offenbach, Germany). Background signals at 630 nm were subtracted for background correction. Absorbance of control conditions was set as 100 % and metabolic activity was displayed relative to controls.

2.3.3 XCELLigence system

The xCELLigence system RTCA SP (Roche, Penzberg, Germany) is a real-time cell analysis tool employing non-invasive gold microelectrodes implanted in a multi-well plate. Here, electrical impedance is increasing upon proliferation of viable cells and drops with detachment of dying cells, and is utilized for real-time monitoring of cell proliferation, cell size/morphology, cell attachment quality, and cell invasion/migration upon specific stimuli. The changes in impedance are represented as cell index (CI) as a function of time by RTCA Software 1.2 (Roche Diagnostics, Penzberg, Germany). After background analysis with pure culture medium, cells were seeded into 96-well E-plates according to Diemert et al. [36]. Having reached a CI of ~ 1.0, cells were treated with the indicated cell death inducers and/or inhibitors, respectively, and impedance was recorded for 14-24 hours. For subsequent presentation and comparability of the respective graphs, the cell index was normalized to 1.0 before treatment. After the experiment E-plates were re-used by removing the medium and washing with sterile bidest. H_2O followed by incubation with trypsin for 15-30 min. After removal of trypsin the plate was washed three times with bidest. H_2O and sterilized 30 minutes under UV light.

2.4 Glutathione assay

The measurement of glutathione is based on the enzymatic recycling reaction of GSH converting Ellman's reagent (5,5'-dithio-bis-(2-nitrobenzoic acid): DTNB) into the yellow colored 5-thio-2-nitrobenzoic acid (TNB). TNB production is directly proportional to the concentration of GSH and therefore provides an accurate estimation in the sample. The enzymatic reaction is as follows:

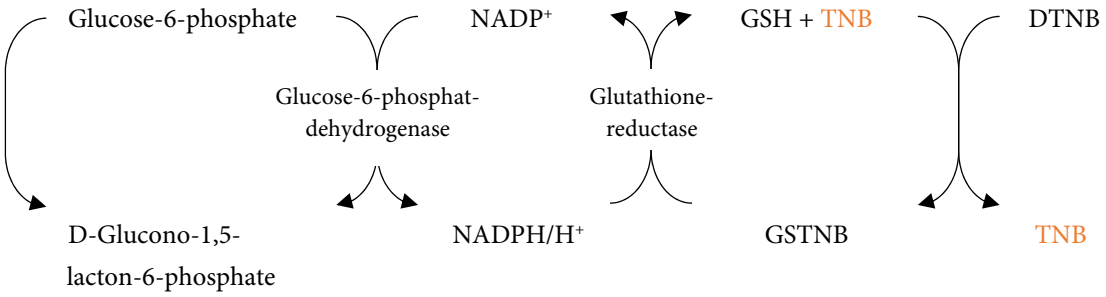

Figure 20. GSH assay

Intracellular glutathione levels were determined according to the Glutathione Assay Kit (Cayman Chemical Company, Ann Arbor, US). Cells were seeded in 6-well plates at a density of 2 x10^5 or in 10 cm dishes at a density of 1 x10^6 and after 24 hours treated with cell death inducers and/or inhibitors. After the indicated amount of time, cells were scratched with a cell scraper and harvested by centrifugation at 1,000 rpm for 3 minutes. After washing the cell pellet once with PBS cells were centrifuged again and stored at -80 °C until the experiment.

For the measurement of GSH levels, cell pellets were thawed on ice and assay reagents warmed up to room temperature. Cell pellets were re-suspended in 100 µL 1x MES-buffer (0.4 M 2-(N-morpholino) ethanesulphonic acid, 0.1 M phosphate, 2 mM EDTA, pH 6.0) and homogenized by sonication. Cell debris was removed by centrifugation at 10,000 g for 15 minutes at 4 °C. 80 µL of the supernatants were transferred into another Eppendorf tube and deproteinated *via* addition of 80 µL of metaphosphoric acid (MPA, 1.25 M) and incubation for 5 minutes at room temperature. The remaining supernatant was used for determination of protein amount using BCA assay (2.8.2). After deproteination the mixture was centrifuged again (17,000 g, 10 minutes, 4 °C). 100 µL of the supernatant was transferred into another tube and mixed with 5 µL of a 4 M triethanolamine solution to increase the pH.

For measuring a calibration curve, GSH standards were diluted as stated in the manufacturer's protocol and 50 µL of each sample and GSH standard was pipetted into a 96-well plate and mixed with 150 µL of a freshly prepared assay cocktail containing 1x MES-buffer, co-factors ($NADP^+$ and glucose-6-phosphate), enzymes (glutathione reductase and glucose-6-phosophate dehydrogenase) and Ellman's reagent. Afterwards, the plate was incubated and shaken for 20 minutes at room temperature protected from light and absorbance was measured at 405 nm using the EL_X808 Ultra Microplate Reader (Bio-Tek Instruments, Bad Friedrichshall, Germany). Total GSH amount was calculated *via* the standard curve and normalized to protein content after BCA assay. Data are displayed as percent GSH of control, which was set to 100 %.

2.5 Mitochondrial morphology and respiratory function

2.5.1 Analysis of mitochondrial morphology

In order to visualize mitochondria and analyze their morphology, mitochondria can be stained using MitoTracker® DeepRed FM (Invitrogen, Karlsruhe, Germany). MitoTracker is a cell-permeant far red-fluorescent dye containing a mildly thiol-reactive chloromethyl moiety for labeling mitochondria and can be excited at ~644 nm under emission of ~665 nm light. MitoTracker was dissolved in DMSO to a stock concentration of 50 µM and stored at -20 °C in the dark.

For counterstaining of nuclei the DNA-binding blue-fluorescent dye DAPI (4', 6-diamidin-2-phenylindol; Sigma Aldrich, Taufkirchen, Germany) was used (excitation at ~358 nm, emission at ~461 nm).

For the analysis of mitochondrial morphology, cells were seeded in 8-well ibidi-slides at a density of ~1.6 $x10^5$ and 24 hours later stained at 37 °C for 30 minutes with a working solution in normal growth medium of 200 nM (1:250) MitoTracker and 1 µg/mL DAPI, which was freshly prepared. After removing the medium, cells were treated with the indicated cell death inducers and/or inhibitors and fixed with 4 % paraformaldehyde for 20 minutes protected from light. After washing with PBS twice, ibidi slides were stored at 4 °C for further experiments.

Images were acquired using a Leica DM6000 epi-fluorescence microscope (Leica, Wetzlar, Germany) collecting light through a 63x or 100x objective. Images were acquired using band pass filters for 633 nm (MitoTracker) or 360 nm (DAPI) excitation and emission filters at 640 nm (MitoTracker) and 470 nm (DAPI), respectively, and were processed with ImageJ Software 1.48v (Maryland, USA).

2.5.1.1. Manual mitochondrial morphology classification system

In order to examine changes in mitochondrial morphology during treatment with specific stimuli, ~500 MitoTracker-stained cells of each condition were counted blinded to treatment and categorized in three different classes according to their mitochondrial morphology as previously described [72]. Briefly, healthy elongated mitochondria localized throughout the whole cell were assigned to category I, whereas highly fragmented mitochondria accumulating around the nucleus were classified as category III. Mitochondria which already underwent fission but were still evenly distributed in the cytoplasm were defined as category II.

2.5.1.2. Automated mitochondrial morphology analysis by ImageJ

Automated quantification of the average perimeter of mitochondria as a measure of mitochondrial fragmentation was performed employing a custom macro for NIH ImageJ software (version 1.48) as described previously by Ruben K. Dagda (University of Nevada School of Medicine) and Charleen Chu (University of Pittsburgh) [33].

2.5.2 ATP bioluminescent assay

For the quantitative analysis of whole cell ATP as a measure of mitochondrial respiratory function, the bioluminescent ViaLight™ ATP Plus-Kit (Lonza, Verviers, Belgium) was used according to the manufacturer's protocol. The bioluminescent method utilizes an enzymatic reaction, where luciferase catalyzes the formation of light from ATP and luciferin according to the following reaction:

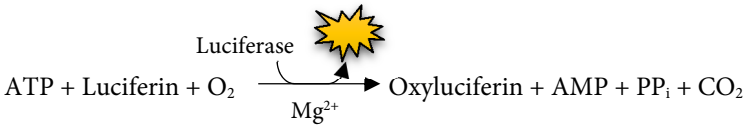

Figure 21. ATP assay

The emitted light is linearly proportional to the ATP content in the respective sample and was measured using the FluoStar OPTIMA (BMG Labtech, Offenbach, Germany).

For the analysis of cellular ATP content, 6,000-8,000 cells were seeded in white 96-well plates and 24 hours later treated with the indicated substances. All reagents of the ViaLight™ ATP Plus-Kit were warmed to room temperature and ATP was extracted by application of 50 µL Cell Lysis Reagent to the culture medium. After 10 minutes of incubation in the dark, 100 µL of ATP monitoring reagent plus (AMR) were added to generate the luminescent signal. After 2 more minutes of incubation luminescence was measured using the FluoStar OPTIMA. Signals were corrected for background noise and depicted as percent of control which was set to 100 %.

2.5.3 Seahorse measurements

Understanding mitochondrial alterations and energy metabolism in oxidative cell death is key to develop new strategies to protect the cells. The Seahorse XF96 system (Agilent Technologies, Santa Clara, US) provides vital information on mitochondrial respiration and glycolytic activity in a real-time manner and is used to detect even small changes in bio-energetic profile during induction of cell death.

2.5.3.1. Oxygen consumption rate (OCR)

For measuring oxygen consumption rate (OCR) the *Mito Stress Test* (Agilent Technologies, Santa Clara, US) was utilized to detect respiratory parameters. The *Mito Stress Test* uses injection of different modulators of specific components of the electron transport chain (ETC). The compounds oligomycin, FCCP, and a mix of rotenone and antimycin A, and in some experiments also 2-desoxyglucose (2-DG), were serially injected to measure basal and ATP-linked respiration, maximal respiration and non-mitochondrial respiration, respectively. Proton leak and spare respiratory capacity can be calculated using basal respiration and the above-mentioned parameters as shown in Figure 22:

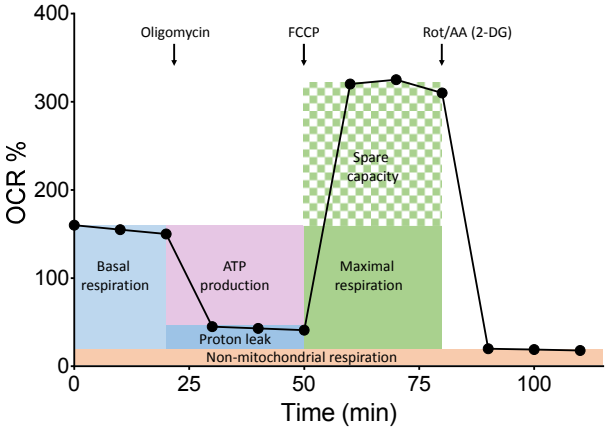

Figure 22. Representative OCR measurement

The modulators of electron chain components show the following effects:

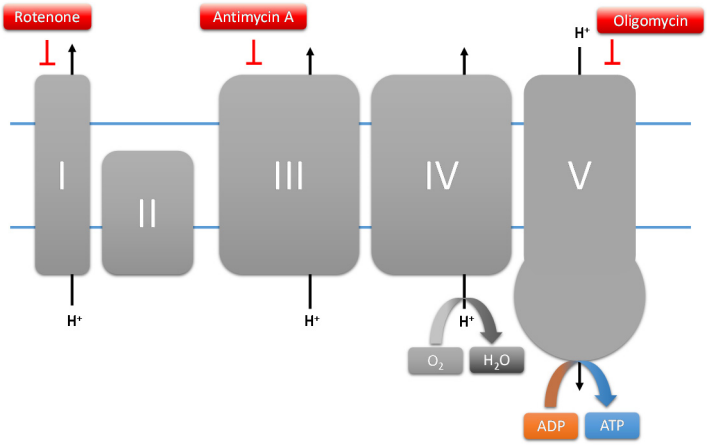

Figure 23. Respiratory chain modulators

Oligomycin inhibits ATP synthase (complex V) by blockage of the proton channel and thereby causes an increased proton gradient, loss of electron transport and drop in oxygen consumption. Carbonyl cyanide-4-(trifluoromethoxy) phenylhydrazone (FCCP) acts as a mobile ion carrier and uncoupler of the mitochondrial respiratory chain by transporting hydrogen ions through the membrane before they can be used to provide energy for oxidative phosphorylation. Thereby, MMP breaks down and ATP synthesis is disrupted leading to an immediate increase in OCR. The final application of rotenone as an inhibitor of mitochondrial complex I and antimycin A as an inhibitor of complex III completely shuts down mitochondrial respiration indicated by rapid decline in OCR.

2.5.3.2. *Extracellular acidification rate (ECAR)*

Measurement of extracellular acidification rate (ECAR) in parallel with OCR during the *Mito Stress Test* is an indicator of glycolysis as glycolysis-derived lactate is exported from the cell together with protons thus decreasing pH. Acidification rate is used to calculate glycolytic capacity, glycolytic reserve and non-glycolytic acidification after serial injection of the above-mentioned modulators:

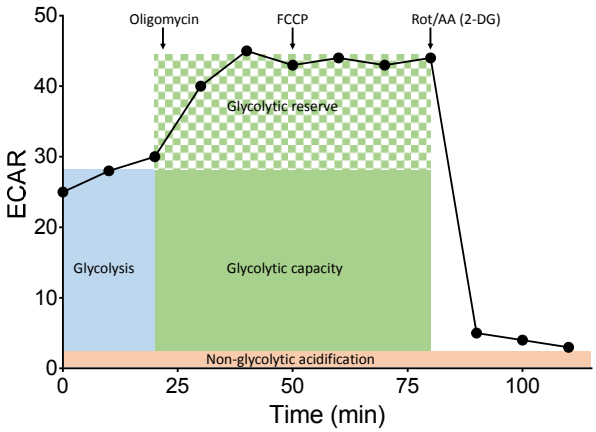

Figure 24. Representative ECAR measurement

2-Desoxyglucose is used to shut down glycolysis as it lacks the 2-hydroxyl group and competitively inhibits production of glucose-6 phosphate from glucose:

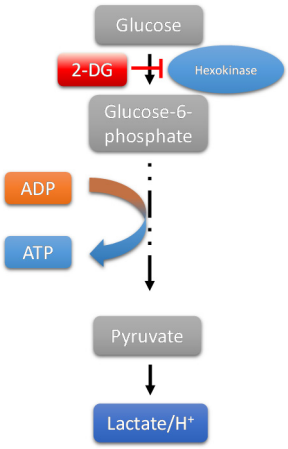

Figure 25. Glycolysis modulator 2-desoxyglucose

For the measurement of CRISPR *Bid* KO cells 8,000 HT22 or HT22 *Bid* KO cells were seeded in 96-well XF-plates and kept at 37 °C for 24 hours. Cells were treated with glutamate (2 mM) or erastin (0.25 µM) over night (16 hours) and culture medium was washed once with 100 µL and then replaced with 180 µL of Seahorse assay medium (DMEM containing 4.5 g/L glucose, 2 mM L-Alanyl-L-glutamine, 1 mM Na-pyruvate, pH 7.35) and kept at 37 °C -CO_2 for 1 hour. The cartridge was prepared as follows:

Table 19. Cartridge design CRISPR Bid KO

Port	Substance	Volume	Stock concentration	Final concentration
Port A	Oligomycin	20 µL	30 µM	3 µM
Port B	FCCP	22.5 µL	5 µM	0.5 µM
Port C	Rot./AA	25 µL	1 µM/10 µM	0.1 µM/1 µM
Port D	-		-	-

After calibration of the cartridge three baseline OCR/ECAR measurements were recorded before successively injecting port A-C followed by three measurements after application of each substance (3 min mixing followed by 3 min measuring).

For RSL3 seahorse measurements 12,000 HT22 cells per well were seeded in 96-well XF-plates and kept at 37 °C for 24 hours. Culture medium was washed once with 100 µL and then replaced with 175 µL of Seahorse assay medium (DMEM containing 4.5 g/L glucose, 2 mM L-Alanyl-L-glutamine, 1 mM Na-pyruvate, pH 7.35) and kept at 37 °C -CO_2 for 1 hour. 25 µL of the EC modulators were pipetted into the cartridge as follows:

Table 20. Cartridge design RSL3

Port	Substance	Stock concentration	Final concentration
Port A	RSL3	8 µM	1 µM
Port B	Oligomycin	27 µM	3 µM
Port C	FCCP	5 µM	0.5 µM
Port D	Rot./AA/2-DG	1.1 µM/11 µM/550 mM	0.1 µM/1 µM/50 mM

After calibration of the cartridge three baseline OCR/ECAR measurements were recorded before applying port A. OCR/ECAR were measured for 6 hours before port B-D was injected successively followed by three measurements after application of each substance (3 min mixing followed by 3 min measurement).

2.6 Flow cytometric measurements (FACS)

Fluorescence-activated cell sorting (FACS) provides an objective and quantitative method for analyzing a heterogeneous mixture of cells based upon their individual light scattering and fluorescent characteristics. For FACS measurements the microcapillary Guava Easy Cyte 6-2 L system (Merck Millipore, Darmstadt, Germany) was used. Cells were seeded in a 24-well format at a density of 35,000-70,000 cells and were kept at 37 °C until further treatment. After 8 to 16 hours of treatment cells were analyzed for specific parameters and data collected from at least 4,000 cells per sample. For quantitative analysis the GuavaSoft Software package was used.

2.6.1 BODIPY staining: Lipid peroxidation

BODIPY 581/591 C11 (Figure 26) (Invitrogen, Karlsruhe, Germany) is a fluorescent lipid peroxidation sensor for FACS analysis.

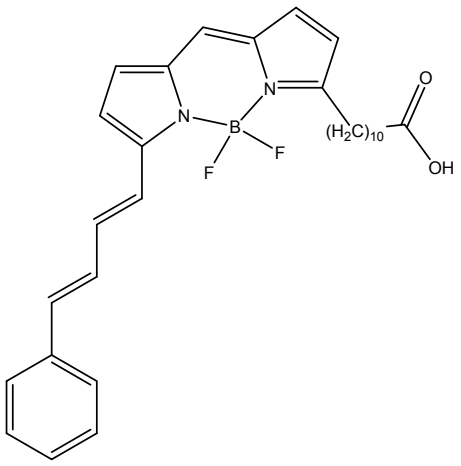

Figure 26. BODIPY 581/591 C11

BODIPY was used to detect reactive lipid species in cells and membranes as oxidation of the polyunsaturated butadienyl portion of the dye results in a shift of the fluorescence emission peak from red (~590 nm) to green (~510 nm). For BODIPY FACS analysis fluorescence was excited with a 488 nm laser (blue) and emission recorded with a 525/30 nm filter (green) and a 690/50 nm filter (red). For FACS analysis, after the indicated treatment, cells were stained with 0.5 µL/well of BODIPY solution (final concentration 2 µM) for 30 minutes at 37°C and harvested with trypsin after washing once with PBS. The cell pellet was re-suspended in 130-200 µL of PBS and was put on ice for the measurement.

2.6.2 DCF staining: Soluble ROS

CM-H_2DCF (Figure 27) (Invitrogen, Karlsruhe, Germany) is a fluorescent soluble ROS indicator used in FACS experiments.

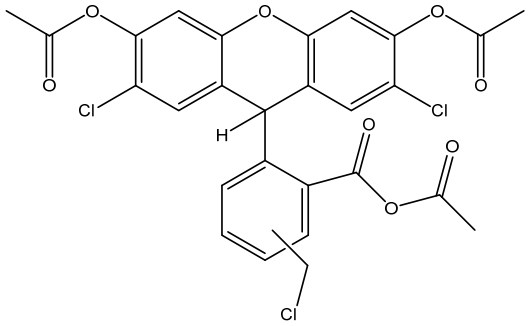

Figure 27. CM-H_2DCF

DCF passively diffuses into the cytoplasm, where its acetate group is cleaved by intracellular esterases and its thiol-reactive chloromethyl group reacts with intracellular glutathione and other thiols. The oxidation-derived fluorescent adduct is now trapped inside the cell and facilitates long-term analysis. Oxidation of DCF results in an increase in emission at ~517–527 nm. For DCF FACS analysis fluorescence was excited with a 488 nm laser (blue) and emission recorded with a 525/30 nm filter (green). For FACS analysis, after the indicated treatment, medium was exchanged by serum-free medium to avoid deacetylation and cells were stained with DCF solution (final concentration 2.5 µM) for 30 minutes at 37°C. Afterwards, cells were incubated another 30 minutes in serum-containing medium without DCF and harvested with trypsin after washing once with PBS. The cell pellet was re-suspended in 130-200 µL of PBS and was put on ice for the measurement.

2.6.3 TMRE staining: Mitochondrial membrane potential

Tetramethylrhodamin ethyl ester (TMRE) (Figure 28) (Immuno Chemistry Technologies, Bloomington, USA) is a lipophilic fluorescent FACS dye (orange, ~574 nm) accumulating in negatively charged mitochondria due to a delocalized positive charge. Upon collapse of the mitochondrial membrane potential, TMRE is dispersed throughout the cytosol thus fluorescence levels of the measured cells instantly drop. Detection of the loss of fluorescence of TMRE stained cells is a reliable method to quantify loss of mitochondrial membrane potential during mitochondrial damage.

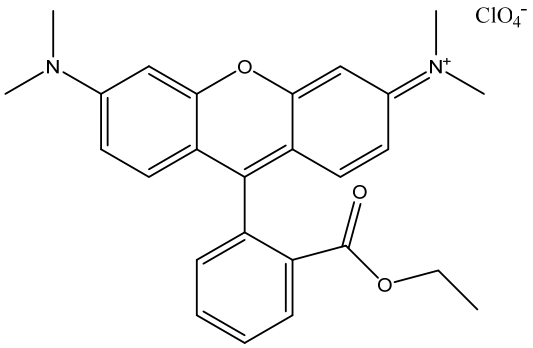

Figure 28. TMRE

TMRE was utilized to differentiate between those cells with healthy mitochondria and others with an acute loss of mitochondrial membrane potential upon mitochondrial damage. For TMRE FACS analysis fluorescence was excited with a 488 nm laser (blue) and emission recorded with a 690/50 nm filter (red).

For FACS analysis, after the indicated treatment, cells were stained with 1 µL/well of TMRE solution (final concentration 400 nM) for 30 minutes at 37°C and harvested with trypsin after washing once with PBS. The cell pellet was re-suspended in 130-200 µL of PBS and was put on ice for the measurement.

2.6.4 MitoSOX staining: Mitochondrial ROS

MitoSOX (Figure 29) (Invitrogen, Karlsruhe, Germany) is a live-cell permeant fluorescent mitochondrial ROS sensor for FACS analysis.

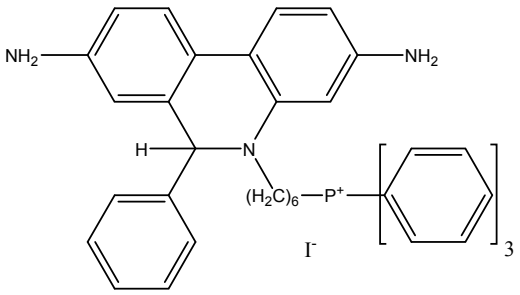

Figure 29. MitoSOX

MitoSOX was used for detection of reactive oxygen species in mitochondria. MitoSOX selectively localizes to the mitochondria and upon oxidation by superoxide shows increased light emission of ~580 nm wavelength. For MitoSOX FACS analysis fluorescence was excited with a 488 nm laser (blue) and emission recorded with a 690/50 nm filter (red).

For FACS analysis, after the indicated treatment, cells were stained with 0.5 µL/well of MitoSOX solution (final concentration 2.5 µM) for 30 minutes at 37°C and harvested with trypsin after washing once with PBS. The cell pellet was re-suspended in 130-200 µL of PBS and was put on ice for the measurement.

2.6.5 Annexin V and PI staining: Apoptosis and necrosis

In order to detect early apoptosis and late necrosis as a measure of cell death Annexin V FITC and PI (propidium iodide) staining and subsequent FACS analysis were used. In early apoptotic cells, phosphatidyl serine (PS) is exposed to the extracellular space by translocation to the outer leaflet of the plasma membrane thereby facilitating calcium-dependent binding of Annexin V FITC as illustrated in Figure 30. PI is used for the detection of late necrotic cells, which became permeable upon membrane disruption and allow PI to pass through and bind to nucleic acids.

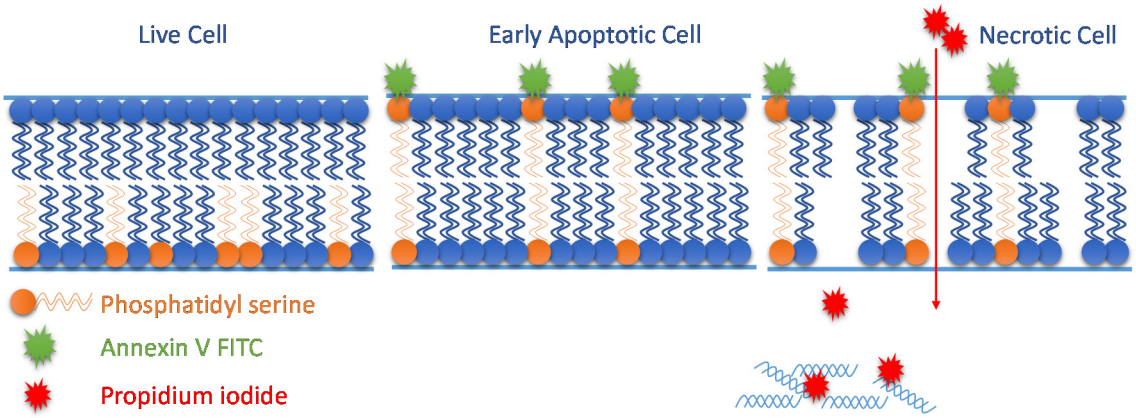

Figure 30. Annexin V/PI staining

Annexin V FITC/PI staining was utilized to detect cell death and fluorescence was excited with a 488 nm laser (blue) and emission recorded with a 525/30 nm filter (green) and a 690/50 nm filter (red).

For FACS analysis, after the indicated treatment, cells were harvested with trypsin and washed once with PBS. The cell pellet was re-suspended in 130-200 µL of Annexin V FITC/PI-binding puffer containing 0.5-1 µL Annexin V FITC and 0.5-1 µL PI per well and was incubated in the dark for 5 minutes at room temperature and afterwards put on ice for the measurement.

2.7 Microscopy

2.7.1 Epifluorescence microscopy

For the analysis of cellular morphology, cells were seeded in 8-well ibidi slides, incubated at 37 °C for 24 hours and treated with the indicated substances. After the indicated time-points cells were either instantly imaged at 37 °C or fixed with 4 % PFA for 20 minutes protected from light and washed with PBS twice. Ibidi slides were then stored at 4 °C for further experiments.

Images were acquired at a Leica DM6000 epi-fluorescence microscope (Leica, Wetzlar, Germany) collecting light through a 20x objective using bright field illumination and were processed with ImageJ Software 1.48v (Maryland, USA).

2.7.2 Confocal laser scanning microscopy (CLSM)

Confocal microscopy was performed on living cells using an LSM800 inverted microscope (Zeiss, Jena, Germany) equipped with an incubation chamber for temperature and CO_2 control and coupled with ZEN blue software(2.3, Zeiss, Jena, Germany). For imaging, cells were seeded in 6-well plates at a density of 200,000 cells and for 24 hours transfected with 0.5 ng Life-Act-GFP plasmid using Attractene transfection reagent (Qiagen, Hilden, Germany) and OptiMEM I medium (Invitrogen, Karlsruhe, Germany). Afterwards, cells were re-seeded in 8-well ibidi slides at a density of 14,000 cells/well and incubated for another 24 hours. After 30 minutes of MitoTracker staining as stated in 2.5.1, cells were treated with the indicated cell death inducers and inhibitors. After 5 hours of treatment, cells were put into the incubation chamber and imaged immediately.

488 nm and 640 nm laser lines were used to excite LifeAct-GFP and MitoTracker Deep Red FM, respectively, and light was collected through a 63x1.4 NA oil immersion objective. Full confocal z-stacks with a section depth of 0.23 µm were acquired and processed with IMARIS (8.3.1, Bitplane, Zurich, Switzerland) by Matthias Plessner. 15x15x5 µm regions were cropped and smoothened by a Gaussian filter (filter size of 0.0673 µm) to reconstruct mitochondrial surfaces using automated settings.

2.8 Protein analysis

2.8.1 Protein sample preparation

For protein analysis, cells were seeded in a 6-well format at a density of 100,000-200,000 cells. After ~24 hours cells were treated for the indicated amount of time and harvested by scratching and centrifugation for 5 minutes at 1,000-2,000 rpm at 4 °C. Cells were washed once with ice-cold PBS and re-suspended in an appropriate volume of cold Western blot lysis buffer (Table 21) (70-500 µL).

Table 21. Western blot lysis buffer, pH 7.8

D-Mannitol	0.25 M
Tris	0.05 M
EDTA	1 mM
EGTA	1 mM
DTT 100 mM	1:100
Triton® X-100	1:100
PhosSTOP	1 tablet
Complete Mini Protease Inhibitor Cocktail	1 tablet
Bidest. H_2O	ad 10 mL

Complete Mini Protease Inhibitor Cocktail and PhosSTOP were obtained from Roche (Penzberg, Germany). After mixing, the Western blot lysis buffer was stored at 4 °C until usage.

After re-suspension of the cell pellet, the lysate was put into liquid nitrogen to disrupt cell membranes and either stored at -80 °C or directly thawed on ice and centrifuged for 15 minutes at 10,000 rpm at 4 °C to eliminate cell debris. The supernatant was transferred into a fresh tube and kept on ice for the determination of protein content by BCA assay and subsequent Western blot analysis.

2.8.2 BCA assay: Determination of protein content

For the analysis of protein amount in cell lysates, the bicinchoninic acid assay (BCA) (Pierce® BCA Protein Assay Ki; Perbio Science, Bonn, Germany) was used. The BCA assay is a colorimetric method to quantitatively determine protein content exploiting purple Cu^{+}-bichinoninic acid complex formation. Cu^{2+} is reduced to Cu^{+} by peptide bonds of proteins in a temperature-dependent ratiometric manner and forms a chelate with two molecules of bicinchoninic acid assessed as a color change from green to purple by measuring absorbance at 562 nm with FluoStar OPTIMA. For the BCA reaction, 2.5 µL of the respective protein sample was mixed with 100 µL of BCA mix (1:50 reagent A: reagent B) and shaken at 60 °C for 30 minutes. After transferring the purple-colored mix to a 96-well plate, absorbance was measured and protein amount calculated using a protein standard curve of 0-190 µg/100 µL bovine serum albumin (Perbio Science, Bonn, Germany).

2.8.3 Polyacrylamide gel electrophoresis (PAGE)

Protein electrophoresis, described as the movement of proteins in an electric field, is used to separate proteins for the purpose of analysis and purification. In an electric field proteins move to the electrode of the opposite charge depending on a variety of biophysical determinants, for instance pH, temperature, ion size, shape/charge of the protein. Electrophoresis performed in polyacrylamide gels is used to separate proteins depending on their size. The gel structure and pore size allows smaller proteins to move faster than larger proteins and thereby provides a technique to separate proteins according to their molecular mass. Sodium dodecyl sulfate (SDS) is used to turn proteins into a state, where only its length and mass-to-charge ratio determines mobility. SDS is negatively charged and binds to proteins in a set ratio so that all proteins get a uniform charge-to-mass ratio independently of their original differences in charged amino acids. Through binding of SDS proteins also lose their spatial structure and will be fractionized in an electric field only by their molecular mass. Gels were prepared in a Bio-Rad gel caster (Munich, Germany) with a concentration of bisacrylamide of 3.5 % in the stacking gel (Table 26) and 12.5 % in the running gel (Table 27) and. The materials and buffers used for gel preparation, electrophoresis and Western blot are provided in Table 22 – Table 34.

Table 22. 1.5 M Tris pH 8.8

Tris-HCl	23.6 g
HCl	q.s. for pH adjustment
Bidest. H_2O	ad 100 mL

Table 23. 0.5 M Tris pH 6.8

Tris-HCl	7.88 g
HCl	q.s. for pH adjustment
Bidest. H_2O	ad 100 mL

Table 24. 10 % Sodium dodecyl sulfate (SDS)

SDS	1 g
Bidest. H_2O	ad 10 mL

Table 25. 10 % Ammonium persulfate (APS)

APS	1 g
Bidest. H_2O	ad 10 mL

Table 26. Stacking gel 3.5 %

Acrylamide/bisacrylamide (37.5:1) 30 %	0.58 mL
Sodium dodecyl sulfate solution 10 %	0.05 mL
0.5 M Tris-HCl buffer pH 6.8	1.2 mL
Ammonium persulfate solution 10 %	0.03 mL
Tetramethylethylenediamine (TEMED)	0.008 mL
Phenol red	q.s.
Bidest. H_2O	ad 5 mL

Table 27. Running gel 12.5 %

Acrylamide/bisacrylamide (37.5:1) 30 %	4.17 mL
Sodium dodecyl sulfate solution 10 %	0.1 mL
1.5 M Tris-HCl buffer pH 8.8	2.5 mL
Ammonium persulfate solution 10 %	0.0625 mL
Tetramethylethylenediamine (TEMED)	0.0125 mL
Bidest. H_2O	ad 10 mL

Table 28. 5x SDS-sample buffer

1.5 M Tris-HCl pH 6.8	2 mL
Glycerol	5 mL
SDS	1 g
β-Mercaptoethanol	2.5 mL
1 % Bromophenol blue	0.5 mL

Table 29. 10x SDS-PAGE buffer

Tris base	30 g
SDS	10 g
Glycine	144 g
Bidest. H_2O	ad 1 L

For SDS-PAGE 10x buffer was diluted 1:10 with bidest. H_2O.

Table 30. 10x Western blot transfer buffer

Tris base	30 g
Glycine	144 g
HCl	q.s. for pH adjustment
Bidest. H_2O	ad 1 L

For Western blot 10x buffer was diluted 1:10 with bidest. H_2O and 20 % methanol.

Table 31. 10x TBS pH 7.5

NaCl	292 g
Tris base	24.2 g
HCl	q.s. for pH adjustment
Bidest. H_2O	ad 1 L

Table 32. 1x TBST

10x TBS	100 mL
Tween® 20	0.5 mL
Bidest. H_2O	ad 1 L

Table 33. 5 % Blocking milk

Skim milk powder	5 g
Bidest. H_2O	ad 100 mL

Table 34. 0.2 % I-Block blocking solution

I-Block™	100 mg
TBS	50 mL
Tween® 20	50 µL

I-Block was dissolved in TBS under heating to ~55 °C and afterwards cooled down to RT prior to Tween® 20 addition.

For SDS-PAGE samples were prepared as follows: 50-80 µg of protein were mixed with an appropriate volume of 5x SDS-sample buffer and heated up to 95 °C for 2 minutes while shaking at 600 rpm. After cooling, samples and protein standard (PageRuler™ Prestained Ladder, ThermoFisher Scientific, Schwerte, Germany, Figure 31) were loaded onto an SDS-gel and electrophoresis performed at 60 V until the samples reached the separation gel. Voltage was then switched to 100-120 V until separation was achieved appropriately.

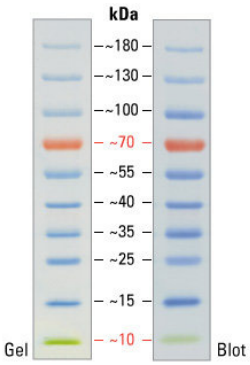

Figure 31. PageRuler™ Prestained Protein Ladder, 10 to 180 kDa [129]

2.8.4 Western blot

Western blotting is defined as the transfer of proteins to a solid-phase membrane followed by immuno-detection. After protein separation by SDS-PAGE, proteins can be bound to membranes where they are accessible for immunological or biochemical analysis, quantitative staining or identification of protein-protein interaction.

Following protein separation by SDS-PAGE, proteins were blotted onto a polyvinylidene fluoride membrane (PVDF, Bio-Rad, Munich, Germany), which was activated by incubation in methanol for 2 minutes and in 1x Western blot transfer buffer for at least 10 minutes. Western blot was performed according to the wet-blot Bio-Rad protocol in a Mini-Trans-Blot Cell tank (Bio-Rad, Munich, Germany) for 75-120 minutes at 300-350 mA submerged with ice-cold 1x Western blot transfer buffer.

After protein transfer, the membrane was blocked for 1 hour with either 5 % blocking milk (Table 33) or I-Block (Table 34) at RT. Thereafter, the membrane was incubated over night at 4 °C with the primary antibody in 5 % milk or I-Block while shaking. On the next day, the membrane was put on RT and incubated with the primary antibody (Table 35) for another hour, before washing three times with TBST (Table 32) for 15 minutes each. After this, the membrane was incubated with the corresponding secondary HRP-antibody (Table 37) for 1 hour at RT and again washed three times with TBST for 15 minutes each. Subsequently, the membrane was put for 1-2 minutes in 1:1 HRP-Juice (PJK GmbH, Kleinblittersdorf, Germany) as a chemi-luminescent substrate for HRP and Western blot signals were detected with semi-automated Chemidoc-XRS Imaging system and Quantity One software package(Bio-Rad, Munich, Germany).

Equal protein loading was controlled for by washing the membrane once in TBST for 10 minutes and re-probing with an appropriate antibody against a house-keeping protein (Table 36) and its corresponding secondary HRP-antibody.

2.8.5 Antibodies

2.8.5.1. Primary antibodies

All primary antibodies used were diluted in either 5% blocking milk (Table 33) or I-Block (Table 34). For Western blot analysis the antibodies were purchased and diluted as given in Table 35:

Table 35. Primary antibodies

Antibody	Company	Diluted in	Dilution	Host
12-LOX	Biorbyt	Milk	1:500	rabbit
AIF D20	Santa Cruz	Milk	1:1000	goat
Bid	Cell signaling	Milk	1:1,000	rabbit
GFP	Rockland	I-Block	1:500	goat
GPX4	Abcam	I-Block	1:500-1:750	rabbit
xCT (mono)	Abcam	Milk	1:1000	rabbit

Table 36. Primary antibodies for house-keeping proteins

Antibody	Company	Diluted in	Dilution	Host
Actin C4	MP Biomedicals	Milk	1:1,000-1:10,000	mouse
Tubulin	Cell signaling	Milk	1:2,000	mouse
Vinculin	Sigma Aldrich	Milk	1:20,000	mouse

2.8.5.2. Secondary antibodies

All secondary antibodies were purchased from Vector Labs (Burlingame, US) if not stated otherwise. Horse radish peroxidase (HRP) labeled anti-mouse IgG (H+L), anti-goat IgG (H+L) and anti-rabbit IgG (H+L) secondary antibodies were utilized for Western blot analysis as illustrated in Table 37.

Table 37. Secondary antibodies

Antibody	Solvent	Dilution
HRP-anti-mouse	5% blocking milk	1:2,500-1,3000
HRP-anti-rabbit	5% blocking milk	1:2,500-1,3000
HRP-anti-goat	5% blocking milk	1:2,500-1,3000

2.8.6 Coomassie protein staining

For the purpose of visualizing purity or recombinant proteins (2.10.3), SDS-PAGE was followed by Coomassie Blue R-250 staining. Coomassie Brilliant Blue R-250 (ThermoFisher Scientific, Schwerte, Germany) binds to proteins in an unspecific manner *via* electrostatic, non-covalent complex formation exhibiting blue color and thus providing a reliable method to optically analyze proteins in SDS gels.

For Coomassie staining, gels were heated in Coomassie solution (Table 38) for 10-20 minutes in the microwave. Thereafter, gels were discolored in acidic methanol solution (Table 39) overnight at room temperature and images taken using white transmission light at the Chemidoc-XRS System (Bio-Rad, Munich, Germany).

Table 38. Coomassie Brilliant Blue R-250 solution

Coomassie Blue R-250	1 g
Methanol	450 mL
100 % Acetic acid	100 mL
Bidest. H_2O	ad 1 L

Table 39. Coomassie staining solution

Methanol	300 mL
100 % Acetic acid	100 mL
Bidest. H_2O	ad 1 L

2.9 DNA/RNA analysis

2.9.1 PCR primer

For PCR and RT-PCR all primers were synthesized by EurofinsGenomics (Ebersberg, Germany). Primer sequences were used as listed in Table 40:

Table 40. Primers for PCR/RT-PCR

Primer	Sequence	Length of gene product
Bid fwd	5´-GGGAACTGCCTGTGCAAGCTTAC-3´	1250 bp
Bid rev	5´-CAGTGAGGCCTTGTCTCTGAA-3´	
GAPDH fwd	5′-CGTCTTCACCACCATGGAGAAGGC-3′	399 bp
GAPDH rev	5′-AAGGCCATGCCAGTGAGCTTCCC-3′	
Bid1028 fwd	5′-AGCCCTGAACGGAAACATGG-3′	1028 bp
Bid1028 rev	5′-CAGGCGGATCTCTGAGTTCG-3′	
Trpc4 fwd	5′-GTCAGCACCTAACGTGTC-3′	707 bp
Trpc4 rev	5′-CGTGGGGCTTAAGTCATAG-3′	
Grm3 fwd	5′-CACTGTGACAGGAAGCTTC-3′	587 bp
Grm3 rev	5′-GTGAGCCACACATCACAG-3′	
Syngr1 fwd	5′-GGAACTCCTTTGGGGTATG-3′	666 bp
Syngr1 rev	5′-GTACCAGAAGAGCAAGTCTG-3′	
Hprt fwd “new”	5′-AATCCTCTGGGAGACGAC-3′	
Hprt rev	5′-GCCTGATCCTTCCTGAAG-3′	728 bp
Hprt rev “new”	5′-TTCTAGAGGTGTTCCCTGG-3′	809 bp
Kcne1 fwd	5′-TGCTGGAATTAGCCAATCAG-3′	593 bp
Kcne1 rev	5′-GGTGCCCCTACAATAAAGAC-3′	
Hivep3 fwd	5′-CTCTACAAGCACAGGAAGTC-3′	721 bp
Hivep3 rev	5′-GATCTCACTGGTGTCCAC-3′	

2.9.2 RNA sample preparation

RNA from frozen cell pellets (-80 °C) was isolated using the InviTrap® Spin Universal RNA Mini Kit (Stratec Molecular GmbH, Berlin, Germany) according to the manufacturer’s protocol.

Briefly, cells were thawed on ice and lysed with 350-700 µL Lysis Solution TR containing 1 % β-mercaptoethanol. The lysate was transferred immediately onto a DNA-Binding Spin Filter and incubated for at least 1 minute at RT to allow contaminating DNA to bind to the filter. Afterwards, the sample was centrifuged for 1 minute at 11,000 rpm. The DNA-Binding Spin Filter was discarded and 350-700 µL 70 % ethanol added to the flow-through to adjust RNA-binding conditions. The sample was then transferred on the RNA-RTA Spin filter, incubated for at least 1 minute to facilitate RNA binding to the filter and centrifuged for 2 minutes at 11,000 rpm. The flow-through was discarded. The RNA-RTA Spin filter was now washed with 600 µL Wash Buffer R1 and 700 µL Wash Buffer R2 with subsequent centrifugation at 11,000 rpm for 1 minute each to remove residual contaminants. In order to eliminate any traces of ethanol, the filter was centrifuged with an open lid for 4 minutes at maximum speed. After transferal of the filter into an RNAse free Elution Tube, 25-40 µL of Elution Buffer R was pipetted onto the membrane, incubated for at least 2 minutes to resolve purified RNA and centrifuged for 1 minute at 11,000 rpm. Eluted RNA was placed on ice and stored at -80 °C for further experiments.

2.9.3 NanoDrop: Photometric determination of DNA/RNA amount

For quantitative determination of RNA/DNA amounts absorbance at 260 nm was measured using the NanoPhotometer™ (Implen, Munich, Germany). To analyze contamination absorbance at 230 nm and 280 nm was measured simultaneously and the ratio of 260/230 nm and 260/280 nm calculated. A 260/280 ratio of ~2.0 was accepted as sufficiently pure RNA, for DNA the 260/280 ratio should be greater than 1.8 and the 260/230 ratio between 2.0 and 2.2.

2.9.4 (Reverse transcriptase) polymerase chain reaction: (RT)-PCR

For the amplification of DNA, the polymerase chain reaction (PCR) was exploited. In the case of RNA samples, first RNA had to be transcribed into complimentary DNA (cDNA) using reverse transcriptase and subsequent amplification *via* PCR.

For DNA amplification, REDTaq® ReadyMixTM PCR Reaction Mix (Sigma Aldrich, Taufkirchen, Germany) and for RT-PCR of RNA samples the SuperScript III One Step RT-PCR System with Platinum® Taq (Invitrogen, Karlsruhe, Germany) were used. Primer were obtained from Eurofins (EurofinsGenomics, Ebersberg, Germany) and listed in Table 40.

Table 41. RT-PCR

2x reaction buffer	12.5 µL
RNA sample	100-300 ng
Fwd primer	1 µL
Rev primer	1 µL
SuperScript III enzyme	0.5 µL
Nuclease free water	ad 25 µL

2.9.5 Agarose gel electrophoresis

After PCR amplification, according to section 2.9.4, the PCR samples were mixed with an appropriate amount of 10x loading dye and loaded onto a 1 % agarose gel stained with ethidium bromide. For comparative analysis of product size 5 µL of GeneRuler 100 bp Plus DNA ladder (ThermoFisher Scientific, Schwerte, Germany) or 1 kb Plus DNA ladder (NEB, Frankfurt, Germany) was placed next to the samples on the gel. Electrophoresis was performed at 80 V for 30-45 minutes and UV light with Chemidoc-XRS Imaging system (Bio-Rad, Munich, Germany) was used for visualization of the respective PCR products.

2.10 Protein X-ray crystallography

2.10.1 Materials for recombinant protein expression

Commercially available equipment used for the recombinant expression, purification and concentration of proteins are provided in Table 42. Materials for crystallographic methods are listed in Table 43.

Table 42. Materials for protein expression, purification and concentration

Materials	**Company**
0.22 µm Whatman Puradisc™ sterile filter	Whatman, Dassel, Germany
10 cm dishes for agar plates	Greiner, Frickenhausen, Germany
3 kDa Amicon® Ultra Centrifugal Filter Units, 15 mL	Millipore, Schwalbach, Germany
Collection tubes 14 mL, 105 x 16.8 mm, Polystyrene	Sarstedt, Nümbrecht, Germany
Cryo vials 2 mL	Sarstedt, Nümbrecht, Germany
Glutathione HiCap Column, 20 mL/10 mL	Qiagen, Düsseldorf, Germany
HiLoad 16/1600 Superdex 75 prep grade	GE Healthcare Freiburg, Germany
HisTrap™ FF, 5 mL	GE Healthcare Freiburg, Germany
HiTrap Q HP, 5 mL	GE Healthcare Freiburg, Germany
trUView™; single-use cuvettes	Bio-Rad, Munich, Germany
Ultra-centrifugation tubes	Beckmann, Krefeld, Germany
Zeba™ Desalt Spin Columns	ThermoFisher Scientific, Schwerte, Germany

Table 43. Equipment for protein crystallization

Materials	Company
MRC2 2-drop-chamber 96-well crystallization plate	JenaBioscience, Jena, Germany
96-deep-well plate Masterblock	Greiner, Frickenhausen, Germany
ViewSeal™	Greiner, Frickenhausen, Germany

2.10.2 Bid vectors and construct cloning

In order to crystallize BID several constructs were used as described in Table 44. From the NMR structure of BID it became evident that the mobile N-terminus and loop would hinder crystallization, for which reason in construct Bid 1 and Bid 3 the loop and N-terminus was removed. To prevent covalent GSH binding to the protein during purification both thiol-containing cysteines were replaced with serines (CCSS).

Table 44. Bid vectors for crystallization

Construct	Tag	Resistance	Source	Molecular weight (g/mol)
pET15b-Bid-p22	His_6	Amp	Addgene plasmid 8784	21,951.7
pET15b-Bid-p22 CCSS	His_6	Amp	Site-directed mutagenesis by Cornelius Krasel	21,919.6
pGEX Δ12-Y47 (Bid 1)	GST	Amp	As described in [132]	17,626.2
pGEX Δ13-Y47 (Bid 3)	GST	Amp	As described in [132]	17,569.2
pGEX Δ13-Y47 CCSS (Bid 3 CCSS)	GST	Amp	Site-directed mutagenesis by Cornelius Krasel	17,537.0

2.10.3 Recombinant protein expression

2.10.3.1. Bacteria for protein expression

For protein expression the vectors were transformed in *Escherichia coli* Rosetta2 (DE3) Singels™ Competent Cells (Novagen/Merck, Darmstadt Germany) carrying chloramphenicol resistance gene. Rosetta2 (DE3) host strains are BL21 derivatives with high transformation efficiency suitable for expression of eukaryotic proteins that contain codons rarely used in *Escherichia coli*. Rosetta2 provide tRNAs for 7 rare codons (AGA, AGG, AUA, CUA, GGA, CCC, and CGG) on a compatible chloramphenicol-resistant plasmid and the tRNA genes are driven by their native promoters. T7 expression strains are lysogens of bacteriophage (λ) DE3, as indicated by the (DE3). These hosts carry a chromosomal copy of the T7 RNA polymerase gene under control of the lacUV5 promoter. Such strains are suitable for production of protein from target genes cloned in appropriate T7 expression vectors using Isopropyl β-D-1-thiogalactopyranoside (IPTG) as an inducer.

2.10.3.2. Transformation for recombinant protein expression

Transformation of Rosetta2 (DE3) was performed according to the protocol recommended by Novagen. In brief, for transformation bacteria and plasmids were thawed on ice for 2-5 minutes. Afterwards, 20-50 µL of Rosetta2 (DE3) were mixed with 1 µg of purified plasmid DNA and gently stirred. The tubes were incubated on ice for 5 minutes and heated for 30 seconds to 42 °C without shaking to allow transformation. Thereafter, the tubes were put on ice for another 2 minutes before adding 250 µL of autoclaved LB (Table 45) or SOC medium (provided with Rosetta2) to each tube. The mixtures were shaken at 37 °C for 30 min in a thermocycler and then plated on LB-Amp agar plates (Table 46), which were treated with 50 µL of chloramphenicol (30 mg/mL in ethanol) beforehand. Then the transformation mix was spread on the LB agar plates. The agar plates were incubated at 37°C overnight until bacterial colonies were grown and visible as single dots.

Table 45. Autoclaved LB medium

Tryptone	10 g
Yeast extract	5 g
NaCl	5 g
Bidest. H2O	ad 1 L

Table 46. Autoclaved agar plate mixture

LB medium	500 mL
Ampicillin 100mg/mL in H_2O	0.5 mL
Agar powder	7.5 g

2.10.3.3. Protein expression and long-term cryo-conservation

Single clones were picked for protein expression in liquid culture and an overnight culture of 2.5-20 mL LB supplemented with 1:1000 ampicillin (100 mg/mL in H_2O) and chloramphenicol (30 mg/mL in ethanol) was inoculated.

After overnight incubation at 37 °C a cryo-stock for long-term-storage was prepare. To do so, 930 µL of the overnight culture were mixed with 70 µL DMSO as cryo-protectant and transferred to cryo-vials for storage at -80 °C.

For expression of recombinant proteins 4x 300 mL LB medium (with 1:1000 ampicillin and chloramphenicol) were inoculated with the overnight culture of single clones or from cryo-stocks, respectively. Cultures were shaken at 37 °C for 4 to 5 hours until an optical density of OD_{600} ~0.6 determined using single use cuvettes with the Bio-Rad SmartSpec™ Plus spectrophotometer (Bio-Rad laboratories, Munich, Germany). Prior to that, the spectrophotometer was blanked with sterile LB medium. At OD_{600} of ~0.6 1:1000 IPTG (1 M in H_2O) was added to each culture to induce protein expression. IPTG mimics allolactose, a lactose metabolite, which triggers transcription of the *lac* operon through binding to the lac repressor and releasing it from the *lac* operator. After IPTG addition, protein expression was induced for 5 hours and bacteria harvested by centrifugation for 15 minutes at 5000 rpm and 4 °C. All 4 pellets were pooled in 20 mL GSH binding buffer (Table 52) in case of GST-tagged proteins or HisTrap FF binding buffer (Table 48) in case of His_6-tagged full-length BID each supplemented with 2 tablets of Complete Mini Protease Inhibitor Cocktail and stored at -80 °C.

2.10.3.4. Protein expression as heavy atom derivatives

Having obtained diffracting protein crystals, the bottleneck in protein-structure determination is to solve the phase problem, which occurs as the x-ray detector can only record amplitudes but not phases of the electromagnetic waves. Molecular replacement (MR) is the method of choice to attain the phases but requires a protein structure with high sequence similarity to be available. If there is no such structure, other methods are used, for example introduction of heavy atom diffraction labels into the crystal (multiple isomorphous replacement, MIR) combined with multi-wavelength anomalous dispersion (MAD) method. Heavy atoms act as anomalous scatterers and multiple data sets of one single crystal can be collected using different wavelengths. Their variation in measured intensities at the different wavelengths can be used to extract the anomalous scatterer's substructure to solve the phase problem.

Selenium (Se) atoms act as anomalous scatterers and can be incorporated into proteins by replacement of methionines with selenomethionine (SeMet) during protein expression in bacteria to aid the structure elucidation. Ideally, the structure of the SeMet-substituted crystal is isomorphous to the native protein crystals, so that the native data can be included into data processing.

To replace methionine with selenomethionine in Bid 3 CCSS the SelenoMet *Dream*™ Media Kit was utilized providing minimal growth medium for selenomethionine incorporation. The SelenoMet Dream Nutrient Mix is formulated for lactose-based or IPTG induction of the target protein. When *E.coli* is cultured in the presence of two carbon sources (glucose and lactose), the bacterium first utilizes glucose and then lactose. Thus, expression of proteins of target gene under control of a *lac* operon will be induced only when glucose as a carbon source is exhausted and the bacterium starts to consume lactose or when IPTG is added. The SelenoMet Dream Nutrient Mix lacks methionine as an amino acid and suppresses methionine biosynthesis in bacteria while providing selenomethionine instead.

Table 47. SelenoMet growth medium

SelenoMet Dream Base	4 sachets
SelenoMet Dream Nutrient Mix	4 sachets
Bidest. H_2O	ad 4 L
Glycerol	2 % (w/v) (optional)
Ampicillin 100 mg/mL /Chloramphenicol 30 mg/mL	4 mL each (1:1000)
SelenoMet Solution 10 mg/mL	16 mL

SelenoMet Dream Base and Nutrient Mix were solved in bidest. water and autoclaved. Glycerol (optional), antibiotics and SelenoMet solution were added freshly before protein expression.

Small-scale expression was done in order to determine optimal bacterial growth and protein expression conditions. For this reason, supplementation with 2 % glycerol and induction with or without IPTG were tested. 200 µL of an overnight culture in standard LB medium were used to inoculate 10 mL of SelenoMet growth medium (± 2 % glycerol, ± IPTG 1mM) and harvested after 22 hours by centrifugation for 15 minutes at 5,000 rpm and 4 °C. Pellets were re-suspended in 50 µL of 2.5x Western blot sample buffer (Table 28), lysed by sonication and run on a 12.5 % SDS-gel. After electrophoresis proteins were stained using Coomassie staining according to 2.8.6.

For large-scale Bid 3 CCSS SeMet expression, 100 mL of SelenoMet growth medium (Table 47) was inoculated with Bid 3 CCSS cryo-stock bacteria and incubated at 37 °C as an overnight culture. Further protein expression was carried out in 4 L SelenoMet growth medium according to 2.10.3.3.

2.10.4 Protein purification

2.10.4.1. Buffers for protein purification

All buffers for protein purification were made according to Table 48-Table 54, sterile-filtered through a 0.22 µm filter and degassed under vacuum for at least 2 hours at RT. Sodium azide was added to avoid bacterial growth.

Table 48. Nickel affinity binding buffer for HisTrap™ FF column 5 mL, pH 7.5

20 mM Tris base	2.42 g
250 mM NaCl	14.6 g
10 mM β-Mercaptoethanol	0.78 g (~ 22 drops)
20 mM Imidazole	1.36 g
Bidest. H_2O	ad 1 L
HCl	q.s. for pH adjustment
0.03 % Na-azide	1 mL (30% aqueous solution)

Table 49. Nickel affinity elution buffer for HisTrap™ FF column 5 mL, pH 7.5

20 mM Tris base	2.42 g
20 mM NaCl	1.17 g
10 mM β-Mercaptoethanol	0.78 g (~ 22 drops)
400 mM Imidazole	27.24 g
Bidest. H_2O	ad 1 L
HCl	q.s. for pH adjustment
0.03 % Na-azide	1 mL (30% aqueous solution)

Table 50. Ion exchange binding buffer for HiTrap Q HP column 5 mL, pH 8.0

20 mM Tris base	2.42 g
10 mM β-Mercaptoethanol	0.78 g (~ 22 drops)
Bidest. H_2O	ad 1 L
HCl	q.s. for pH adjustment
0.03 % Na-azide	1 mL (30% aqueous solution)

Table 51. Ion exchange elution buffer for HiTrap Q HP column 5 mL, pH 8.0

20 mM Tris base	2.42 g
500 mM NaCl	29.22 g
10 mM β-Mercaptoethanol	0.78 g (~ 22 drops)
Bidest. H_2O	ad 1 L
HCl	q.s. for pH adjustment
0.03 % Na-azide	1 mL (30% aqueous solution)

Table 52. GSH binding buffer for GSH HiCap column 20 mL, pH 7.6

20 mM Tris base	2.42 g
100 mM NaCl	5.84 g
1 mM EDTA	0.29 g
1 mM DTT	1 mL (1 M stock)
Bidest. H_2O	ad 1 L
HCl	q.s. for pH adjustment
0.03 % Na-azide	1 mL (30% aqueous solution)

Table 53. GSH elution buffer for GSH HiCap column 20 mL, pH 8.0

50 mM Tris base	6.06 g
10 mM Reduced L-glutathione	3.07 g
1 mM EDTA	0.29 g
1 mM DTT	1 mL (1 M stock)
Bidest. H_2O	ad 1 L
HCl	q.s. for pH adjustment
0.03 % Na-azide	1 mL (30% aqueous solution)

Table 54. Gel filtration buffer for HiLoad™ 16/600 Superdex 75 pg gel filtration column 120 mL, pH 7.4

20 mM Tris base	2.42 g
50 mM NaCl	2.92 g
TCEP	1 g (optional)
Bidest. H_2O	ad 1 L
HCl	q.s. for pH adjustment
0.03 % Na-azide	1 mL (30% aqueous solution)

2.10.4.2. ÄKTA prime plus

ÄKTA prime plus (GE Healthcare, Freiburg, Germany) is a small-scale liquid chromatography system for simple protein purification and includes a system pump, fraction collector, valves for buffer selection, sample injection, gradient formation and flow diversion, and monitors for UV, conductivity and pH. Methods were programmed, results monitored and results presented using PrimeView 5.0 software (GE Healthcare, Freiburg, Germany).

Before each protein purification, the system was pre-equilibrated to remove 20 % ethanol, in which the system was stored. All components were purged three times with degassed bidest. water using system wash and the columns were rinsed with 2 volumes water of the respective column by manual run (flow rate 0.5-1.5 mL/min). Afterwards, the system was prepared for the respective purification method by purging it with 2 column volumes of the required binding buffer by manual run and system wash. At the end of each purification, the system was again purged with water as described above and stored in 20 % ethanol. The maximum pressure was fixed to 0.3-0.5 MPa for all purification columns.

Purification was monitored for protein content by UV/Vis detection using PrimeView 5.0 software. Elution fractions were always analyzed for purity by SDS-gel electrophoresis and subsequent Coomassie staining in order to decide which fractions to pool for further purification steps.

2.10.4.3. Lysis of bacterial cells

Bacterial protein lysates produced according to 2.10.3 were lysed prior to purification with ÄKTA prime plus liquid chromatography. For this, the 20 mL lysate was sonicated on ice using the Branson Sonifier Cell Disrupter S-450D (Branson Ultrasonics, Dietzenbach, Germany) with a macro-tip at 20 % maximum power. To prevent overheating, sonication was performed with an interval of 1 second followed by 1 second without sonication for a total duration of 20 minutes. Afterwards, the lysate was centrifuged in ultra-centrifugation tubes for 60 minutes at 35,000 rpm and 4 °C (Beckman Optima XE-90, Ti70.1 rotor, Beckman Coulter, Krefeld, Germany). The supernatant was kept on ice and sterile-filtered through a 0.22 µm filter to avoid particles clogging the chromatography system.

2.10.4.4. Purification of His_6-tagged full-length BID

Purification of His_6-tagged BID and BID CCSS was performed using three subsequent chromatography steps including nickel-affinity chromatography, ion exchange chromatography and size-exclusion gel chromatography.

For nickel affinity chromatography two connected HisTrap™ FF columns 5 mL (GE Healthcare, Freiburg, Germany) containing Ni sepharose were used. Immobilized metal ion affinity chromatography (IMAC) is exploited to bind histidine-tagged proteins to metal ions and retain them in a column. Elution of the desired protein is achieved by competitive binding of excess imidazole.

For purification two HisTrap™ FF columns were connected to the ÄKTA prime plus system and pre-equilibrated with nickel affinity binding buffer (Table 48) as described above. The sterile-filtered protein lysate of recombinant full-length BID (CCSS) with an N-terminal hexa-histidine tag was purified using the following automated program with a pressure limit of 0.5 MPa:

Table 55. Method #9 for Ni-affinity chromatography

	Break-point	Volume (mL)	Concentration Buffer B (%)	Flow rate (mL/min)	Fraction size (mL)	Inject valve position
Equilibration	1	0	0	1	0	Load
Sample injection 1	2	5	0	1	8	Inject
Wash Buffer A	3	13	0	1	0	Load
Sample injection 2	4	15	0	1	8	Inject
Wash Buffer A	5	23	0	1	0	Load
Sample injection 3	6	25	0	1	8	Inject
Wash Buffer A	7	33	0	1	0	Load
Sample injection 4	8	35	0	1	8	Inject
Wash Buffer A	9	43	0	1	0	Load
Sample injection 5	10	55	0	1	8	Inject
Wash Buffer A	11	63	0	1	5	Load
Start Elution	12	83	5	1	1	Load
Elution	13	103	75	1	1	Load
Elution	14	123	75	1	5	Load
Elution	15	128	100	1	5	Load
Elution wash out	16	133	100	1	0	Load
Re-equilibration	17	143	0	1	0	Waste

Protein samples were loaded by repeated injections (4-5 times) in a 5 mL sample injection loop while collecting flow-through in 8 mL volume fractions. Elution of histidine-tagged proteins was performed using an imidazole gradient with nickel affinity elution buffer (Table 49) and 1-5 mL elution fractions were collected and stored at 4 °C until further use.

After the first purification by Nickel-affinity chromatography, the histidine-tag had to be removed. Therefore, the protein was cleaved using thrombin as described in 2.10.4.6. After cleavage the protein samples had to be de-salted to be suitable for ion exchange chromatography by efficient ionic binding. Therefore, either 5 mL Zeba™ Desalt Spin Columns (ThermoFisher Scientific, Schwerte, Germany) were used according to the manufacturer's protocol or the protein samples were concentrated using 3 kDa cut-off Amicon filters at 4,000 rpm and 4 °C (Merck Millipore, Darmstadt, Germany) and subsequently diluted in ion exchange binding buffer (Table 50).

Ion exchange chromatography (IEX) was accordingly performed using an anionic HiTrap Q HP column 5 mL (GE Healthcare, Freiburg, Germany) with cross-linked agarose beads with quaternary ammonium (Q) anions. Anionic IEX is commonly used to separate molecules based on their net positive surface charge in buffers with a pH above their isoelectric point and is applicable for protein purification. Positive charged proteins will competitively bind to the anionic column in ion exchange binding buffer (Table 50) and can be eluted with ion exchange elution buffer (Table 51) containing a high amount of positive charged sodium ions. The program with a pressure limit of 0.5 MPa used with ÄKTA prime plus is as follows:

Table 56. Method #10 for ion exchange chromatography

	Break-point	**Volume (mL)**	**Concentration Buffer B (%)**	**Flow rate (mL/min)**	**Fraction size (mL)**	**Inject valve position**
Equilibration	1	0	0	5	0	Load
Sample injection 1	2	25	0	5	5	Inject
Wash Buffer A	3	32	0	5	2	Load
Sample injection 2	4	39	0	5	5	Inject
Wash Buffer A	5	46	0	5	2	Load
Sample injection 3	6	53	0	5	5	Inject
Wash Buffer A	7	58	0	5	5	Load
Start Elution	8	85	0	5	2.5	Load
Elution	9	185	100	5	2.5	Load
Elution wash out	10	205	100	5	2.5	Load
Re-equilibration	11	210	0	5	0	Load
End method	12	235	0	5	0	Load

Protein samples were loaded by repeated injections (2-3 times) in a 5 mL sample injection loop while collecting flow-through in 2-5 mL volume fractions. Elution of proteins was performed using a sodium ion gradient with ion exchange elution buffer (Table 51) and 2.5 mL elution fractions were collected and stored at 4 °C until further use.

As a final purification step, size-exclusion chromatography (gel filtration) was performed using a HiLoad™ 16/600 Superdex 75 pg gel filtration column 120 mL (GE Healthcare, Freiburg, Germany). Therefore, the desired protein sample is given onto a column with dextran covalently bound to highly cross-linked agarose. Dextran determines the separation properties as it traps small molecules and lets bigger molecules pass by depending on its pore size. The column used allowed for separation of molecules in a range of 3-70 kDa.

In order to reduce the sample size to 5 mL so that the whole sample can be injected into the sample loop at once and separation efficiency is thus maximized, the protein sample was washed with gel filtration buffer (Table 54), concentrated using 3 kDa cut-off Amicon filters at 4000 rpm and 4 °C and subsequently sterile-filtered through a 0.22 µm filter. For purification the following method was used with a pressure limit of 0.3 MPa:

Table 57. Method #14 for gel filtration

	Break-point	**Volume (mL)**	**Concentration Buffer B (%)**	**Flow rate (mL/min)**	**Fraction size (mL)**	**Inject valve position**
Equilibration	1	0	0	0.8	0	Load
Sample injection	2	10	0	0.8	0	Inject
Elution Start	3	16	0	0.8	5	Load
Elution	4	20	0	0.8	2	Load
Elution	5	45	0	0.8	2	Load
Elution Wash-Out	6	160	0	0.8	2	Load

Protein samples were loaded by one injection in a 5 mL sample injection loop. Elution of proteins was performed using gel filtration buffer (Table 54) and 2-5 mL elution fractions were collected and stored at 4 °C until further use.

For crystallization, the pooled fractions containing pure BID (CCSS) were concentrated to ~5-14 mg/mL using 3 kDa cut-off Amicon filters at 4000 rpm and 4 °C, subsequently sterile-filtered through a 0.22 µm filter and kept at 4 °C until crystallization.

2.10.4.5. Purification of GST-tagged BID proteins

GST-tags are commonly used for protein purification as they support protein solubility, expression efficiency and UV/Vis protein detection especially in case of small proteins, which can be purified in a two-step chromatography of successive glutathione affinity and size-exclusion chromatography.

In order to purify GST-tagged proteins glutathione affinity chromatography using a GSH HiCap column 20 mL (Qiagen, Düsseldorf, Germany) with glutathione sepharose was utilized. Glutathione-S-transferase (GST) binds with high affinity to immobilized glutathione in the column, thus retaining N-terminal GST-tagged BID protein constructs. Elution of the desired protein is achieved by competitive binding of excess reduced L-glutathione.

For purification a GSH HiCap column 20 mL was connected to the ÄKTA prime plus system and pre-equilibrated with glutathione binding buffer (Table 52) as described above. The sterile-filtered protein lysate of recombinant BID constructs with an N-terminal GST-tag was purified using the following automated program with a pressure limit of 0.1 MPa:

Table 58. Method #27 GSH affinity chromatography

	Break-point	**Volume (mL)**	**Concentration Buffer B (%)**	**Flow rate (mL/min)**	**Fraction size (mL)**	**Inject valve position**
Pre-equilibration	1	0	0	1	0	Load
Equilibration	2	10	0	1	0	Load
Sample injection 1	3	12	0	1	5	Inject
Wash Buffer A	4	17	0	1	2	Load
Sample injection 2	5	19	0	1	5	Inject
Wash Buffer A	6	24	0	1	2	Load
Sample injection 3	7	26	0	1	5	Inject
Wash Buffer A	8	31	0	1	2	Load
Sample injection 4	9	33	0	1	5	Inject
Wash Buffer A	10	38	0	1	2	Load
Sample injection 5	11	40	0	1	5	Inject
Wash Buffer A	12	45	0	1	2	Load
Sample injection 6	13	47	0	1	5	Inject
Wash Buffer A	14	52	0	1	2	Load
Start Elution	15	132	0	1	2	Load
Elution	16	134	100	1	2	Load
Elution	17	174	100	1	2	Load
Elution wash out	18	180	0	1	2	Load
Re-equilibration	19	190	0	1	0	Load

Protein samples were loaded by repeated injections (5-6 times) in a 5 mL sample injection loop while collecting flow-through in 2-5 mL volume fractions. Elution of proteins was performed using a reduced glutathione gradient with glutathione elution buffer (Table 53) and 2 mL elution fractions were collected and stored at 4 °C until further use. Fractions containing the respective GST-tagged BID construct were pooled and subjected to thrombin cleavage according to 2.10.4.6.

In order to reduce the sample size to 5 mL, the protein sample was washed with gel filtration buffer (Table 54), concentrated using 3 kDa cut-off Amicon filters at 4000 rpm and 4 °C and subsequently sterile-filtered through a 0.22 µm filter. Subsequent gel filtration was performed as described in 2.10.4.4.

For crystallization the pooled fractions containing pure BID constructs (CCSS) were concentrated to ~5-13 mg/mL using 3 kDa cut-off Amicon filters at 4000 rpm and 4 °C subsequently sterile-filtered through a 0.22 µm filter and kept at 4 °C until crystallization.

2.10.4.6. Quantification of protein content

The concentration of protein content during the purification process was determined by either Bradford assay or using the NanoPhotometer™ (Implen, Munich, Germany).

Bradford assay was performed according to the manufacturer's protocol (AppliChem, Darmstadt, Germany) to estimate tagged protein constructs prior to thrombin cleavage. Similar to 2.8.6 Coomassie Brilliant Blue G-250 is binding to proteins in an unspecific manner while showing a deep blue color. In particular, the absorbance maximum is shifted from 465 nm to 595 nm and can be quantitatively determined using a spectrophotometer (Bio-Rad, Munich, Germany), which was blanked to zero using protein buffer. A standard curve was calculated by means of serial BSA stock (10 mg/ml) dilution with the respective protein buffer to concentrations of 0-10 µg/mL BSA. 100 µL of the respective sample (diluted at least 1:10 in protein buffer) were mixed with 1 mL of Bradford reagent and transferred to single-use cuvettes (trUView™, Bio-Rad, Munich, Germany) to measure absorbance at 595 nm wavelength.

Amino acids containing aromatic rings, such as tyrosine, tryptophan and phenylalanine, have an absorption maximum at ~280 nm, so that protein content can be quantified measuring absorbance at 280 nm wavelength. As the absorption greatly depends on the relative content of these amino acids in a specific protein, extinction coefficients (molecular weight/molar extinction coefficient) for each protein construct had to be calculated from the amino acid sequence data according to [65].

Table 59. Molar extinction coefficients and A280 factors

Protein	**Molecular weight (g/mol)**	**Molar extinction coefficient (mol/L·cm^{-1})**	**A_{280} factor**
Full-length His_6-Bid (CCSS)	24,115 (24,147)	8250	2.923
Bid1	17,626	2560	6.885
Bid3 (CCSS)	17,569 (17,601)	2560	6.863

For determination of protein content with the NanoPhotometer™ the system was blanked with pure protein buffer and 4 µL of the respective protein sample were quantified at 280 nm absorbance corrected with A_{280} factor.

2.10.4.7. Thrombin-cleavage of His_6- and GST-fusion proteins

For the purpose of cleaving the His_6- or GST-tag from the protein to avoid disturbing protein crystallization, the protease thrombin (Novagen/Merck, Darmstadt, Germany) was used. The protein expression vectors pET15b and pGEX include the thrombin recognition sequence LVPR/GS to enable site-specific cleavage to remove tags from the respective recombinant protein.

His_6-tags from full-length Bid constructs were removed after Nickel-affinity chromatography and GST-tag after GSH affinity chromatography, respectively. In order to calculate the appropriate amount of thrombin for cleavage, the protein amount was estimated using the Bradford assay (2.10.4.6). For cleavage, 1 unit thrombin was used for 1 mg of protein in the presence of 12 mM $CaCl_2$ to enhance cutting efficiency. The thrombin solution was incubated at 37 °C for 16-18 hours and stopped by the addition of 1 mM PMSF phenylmethylsulfonyl fluoride. Cleavage was controlled for by SDS-PAGE and Coomassie staining.

2.10.4.8. Mass spectrometry

Mass spectrometry was exploited to analyze identity and purity of the purified proteins. Therefore, Jörg Kahnt (Max-Planck-Institute of Terrestrical Microbiology, Marburg, Germany) kindly performed MALDI-TOF analysis and checked for protein mass and potential contamination with cleavage byproducts or remaining purification chemicals.

2.10.5 Protein crystallization

For the structural analysis and deeper understanding of molecular BID function and interaction in cell death cascades, purified full-length BID and various constructs were crystallized and analyzed by means of X-ray crystallography to obtain electron density data for structure calculation.

All crystallization attempts were performed at the MarXtal crystallization lab (SYNMICRO, University of Marburg, Germany) using high-throughput crystallization robotics (Digilab Honeybee 963™, Cartesian Microsys™ SQ 4000; Formulatrix Rock Imager™ documentation) with the kind support of Dr. Vasundara Srinivasan and Ralf Pöschke.

2.10.5.1. Crystallization techniques

The most common crystallization technique is vapor diffusion as sitting or in fewer cases hanging drops. Vapor diffusion utilizes a dynamic equilibration process to dehydrate a drop of protein, buffer and precipitant, thus driving it gently into a state of oversaturation. The protein drop is sealed air-tight in a chamber with a reservoir solution of higher precipitant concentration forcing water to evaporate towards the reservoir solution. As the drop and the reservoir solution equilibrate, precipitant and protein concentration constantly increase and allow for protein crystallization in case an appropriate concentration ratio is reached. However, identification of optimal crystallization conditions needs extensive testing.

Vapor diffusion can be performed as hanging or sitting drops. Hanging drops are placed on an inverted cover slip suspended above the reservoir, whereas sitting drops are placed on a pedestal separate from the reservoir (Figure 32).

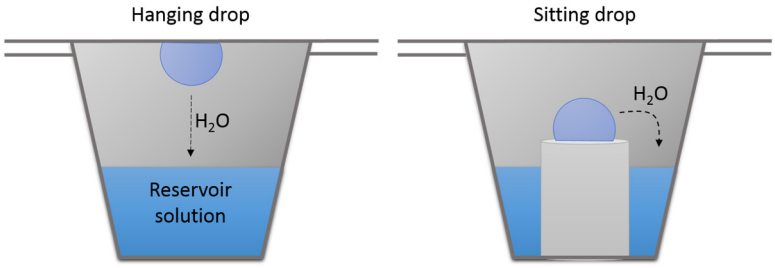

Figure 32. Vapor diffusion techniques

For extensive screening, 96-well plates with micro-chambers and two-drop wells were used with volumes of 100-500 nL/drop. Protein-precipitant solutions were automatically pipetted using MarXtal robots, incubated and imaged at 4 °C in Formulatrix Rock Imager™ and screened for crystal growth by eye using RockImager Web Interface. Imaging was performed using normal visible light and in addition with polarized light to distinguish between salt crystals (no color) and protein crystals (colors due to anisotropic double refraction).

The following ready-to-use screens were available at MarXtal crystallization lab to screen a huge variety of crystallization conditions, such as precipitant concentration, pH, buffer composition, presence of salt anions and additives. Each screen provides 96 different buffers to ensure maximum diversity with limited effort.

Table 60. MarXtal crystallization screens

1	JCSG Core I	Qiagen GmbH, Düsseldorf, Germany
2	JCSG Core II	Qiagen GmbH, Düsseldorf, Germany
3	JCSG Core III	Qiagen GmbH, Düsseldorf, Germany
4	JCSG Core IV	Qiagen GmbH, Düsseldorf, Germany
5	JCSG+	Qiagen GmbH, Düsseldorf, Germany
6	PACT	Qiagen GmbH, Düsseldorf, Germany
7	Classics	Qiagen GmbH, Düsseldorf, Germany
8	Classics Lite	Qiagen GmbH, Düsseldorf, Germany
9	Cryo Suite	Qiagen GmbH, Düsseldorf, Germany
10	$AmSO_4$	Qiagen GmbH, Düsseldorf, Germany
11	Anions	Qiagen GmbH, Düsseldorf, Germany
12	JB Penta	JenaBioscience, Jena, Germany
13	Morpheus	Molecular Dimensions, Suffolk UK
14	Morpheus II	Molecular Dimensions, Suffolk UK
15	MBC I-II	Qiagen GmbH, Düsseldorf, Germany
16	MEMGold	Molecular Dimensions, Suffolk UK
17	MEMStart/Sys	Molecular Dimensions, Suffolk UK
a	Additive Screen HT	Hampton Research, Aliso Viejo, USA
Opti	Morpheus A5/8 Opti	Self-made
OptiSeed	Morpheus A5/8 Opti + Seeding crystals BID3 CCSS	Self-made
A5	Morpheus A5	Self-made
A8	Morpheus A8	Self-made

Screens were automatically filled in 2.2 mL 96-deep-well plates (Greiner, Frickenhausen, Germany) with Lissy-system (Zinsser Analytic GmbH, Frankfurt, Germany), and 80 µL transferred to the reservoirs of an MRC2 2-drop-chamber 96-well crystallization plates (JenaBioscience, Jena, Germany). Using the robot system 300 nL of protein and reservoir solution, respectively, were transferred in the wells as a sitting drop and sealed with ViewSeal™ (Greiner Bio-one, Frickenhausen, Germany).

Optimization of promising original crystallization screens, addition of additives, nanoparticles and seeding with small splitters of crystals (no nucleation energy required) were performed to increase crystal size/quality and resolution of diffraction data.

Morpheus A5/8 Opti Screen was designed as shown in Figure 33 and manually prepared with stock solutions according to Table 61-Table 64 in order to vary salt and precipitant concentration. 1 mL of each reservoir solution was filled in a 96-deep-well plate.

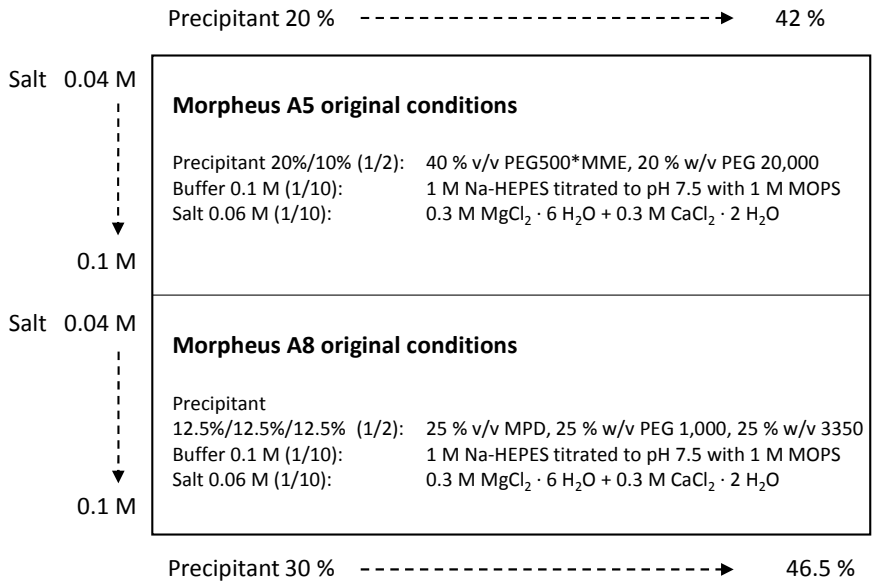

Figure 33. Morpheus A5/8 Opti Screen

Table 61. Salt stock solution for Opti Screen

0.25 M $CaCl_2 \cdot 2\ H_2O$	11.03 g
0.25 M $MgCl_2 \cdot 6\ H_2O$	15.25 g
Bidest. H_2O	ad 300 mL

Table 62. Buffer stock solution for pH 7.5

1 M Na-HEPES	7.8 g in 30 mL
1 M MOPS	31.39 g in 150 mL
Titrate to pH 7.5 with 1 M MOPS	

Table 63. A5 Precipitant stock solution for Opti Screen

40 % PEG500*MME	20 mL
20 % PEG 20,000	10 g
Bidest. H_2O	ad 50 mL (solve in 37 °C water bath)

Table 64. A8 Precipitant stock solution for Opti Screen

25 % MPD	12.5 mL
25 % PEG 1,000	12.5 g
25 % PEG 3,350	12.5 g
Bidest. H_2O	ad 50 mL (solve in 37 °C water bath)

Morpheus A5 and Morpheus A8 screens were mixed manually using original stock solutions (Molecular Dimensions, Suffolk, UK) as shown in and 0.5 mL transferred into a 96-deep-well plate.

Additives were used in this thesis to optimize crystal growth of promising "hit-conditions" Morpheus A5 and A8. A pre-defined commercially available screen (Additive Screen HT™) from Hampton Research was used (Table 60) including multivalent cations, salts, amino acids, dissociating agents, linker, polyamines, chaotropes, co-factors, reducing agents, chelators, polymers, carbohydrates, polyols, detergents, non-detergents, amphiphiles, osmolytes and organics. In case of an additive screen, 90 µL of reservoir solution were mixed with 10 µL additive solution in the reservoir wells of the respective crystallization plate and additionally used for protein drop preparation (0.3 µL protein + 0.3 µL reservoir solution containing 1:10 additives).

An overview of all purified protein constructs and crystallization screens tested in this thesis is depicted in Table 65:

Table 65. Crystallization screens

Screen #	1	2	3	4	5	6	7	8	9	10
Protein construct	**Bid 3**	**Bid 1**	**Bid 3 CCSS**	**Bid 3 CCSS**	**Bid 3 CCSS**	**Bid 22**	**Bid 22 CCSS**	**Bid 3 CCSS**	**Bid 3 CCSS SeMet**	**Bid 3 CCSS SeMet**
Drop 1		+ 2 % NP	10.7	+BI283 19 27 mM	+BI283 19 1 mM		+BI283 19 0.07 mM	+BI283 19		
Drop2			5.3			+BI283 19 0.8 mM			+ BI6c9 0.25 mM	+ BI6c9 0.25 mM
Conc. (mg/mL)	9.5	12.7 +TCEP	10.7	5.3	12.3	4.75	14	12.3	13.2	13.2
Buffer	20 mM Tris. 50 mM NaCl, 0.03 % Na-Azid (Gel filtration buffer)									
Temp.	18 °C	18 °C	18 °C	18 °C	18 °C	18 °C	18 °C	4 °C 18 °C	18 °C	18 °C
Screens (Table 60)	1-3,13	5,9,13	1-11,13,15	10,13,16,17	Opti, Opti w/o reservoir	Opti	1-13,15-17	A5a, A8a, OptiSeed	13,Opti, A5a, A8a	A5a, A5aD3

2.11 X-ray crystallography

High energy x-ray beams are used to obtain diffraction patterns caused by crystalline atoms. By computational analysis of angles and intensities of diffracted beams a three-dimensional picture of electron densities within a protein crystal can be calculated and ideally converted in a 3D protein structure in case of sufficient resolution. Protein crystals are regularly shaped bio-macromolecules with a set of flat faces comprising constant angles and they are built from a unit cell of protein molecules symmetrically arranged in a three-dimensionally periodic manner. In total, 65 space groups are described for chiral molecules, such as for instance orthorhombic with the space group P222 ($\alpha = \beta = \gamma = 90°$):

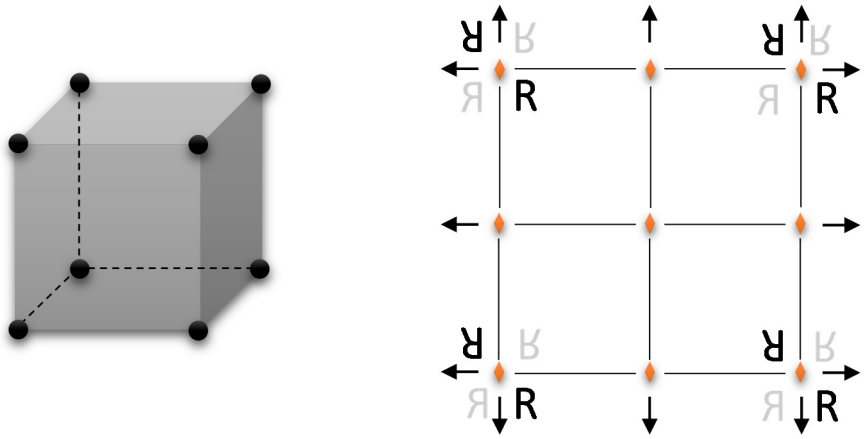

Figure 34. Orthorhombic space group P222

X-rays are produced when a high-energy electron beam accelerated through a voltage in vacuum hits a target. Mostly, a rotating copper anode is used in x-ray sources and produces synchrotron radiation when electrons are kept under the influence of magnetic fields and travel in a pseudocircular trajectory. Synchrotron radiation is then focused by reflectors before the beam is directed onto a mounted shock-frozen crystal, which is rotated around its center. X-ray diffraction is registered using a detector. Crystals are isolated from the crystallization drop using a cryo-loop and stored in cryo-protectant containing mother liquor in liquid nitrogen until measured at a beam-line.

Many macromolecular crystals suffer from radiation damage upon high energy x-ray exposure. For this reason, crystals are mostly cooled to low temperatures allowing for example collection of several data sets from one crystal as the lifetime is dramatically increased. After collecting a complete data set, data have to be processed: Therefore, raw data are visualized and diffraction patterns indexed. Crystal and detector parameters are refined and diffraction spots subsequently integrated. Afterwards, the relative scale factors have to be identified and crystal parameters have to be refined precisely using the whole data set and measurements related by space-group symmetry are merged and analyzed.

X-ray data in this thesis were collected at a microfocus beamline in Grenoble (ESRF Grenoble, France) using cryo-crystallography to avoid radiation damage during data collection. Therefore, crystals were picked with a cryo-loop (Hampton Research, Aliso Viejo, USA), flash-frozen and stored in mother liquor containing cryo-protectant until the day of measurement. Crystal preparation, data collection and processing was kindly performed by Dr. Vasundara Srinivasan (Core facility Structural Biology, MarXtal Crystallization Lab, LOEWE-Center, SYNMIKRO, Marburg, Germany).

2.12 Statistical analysis

2.12.1 Data presentation and tests of statistical significance

All data are presented as mean + or ± standard deviation (SD). Statistical analysis of treatment groups was performed using analysis of variance (ANOVA) followed by Scheffé's post-hoc test to correct for multiple comparison. Calculations were done using Winstat standard statistical software (R. Fitch Software, Germany).

2.12.2 Concentration-response curves and EC50 values

Half-maximal effect concentrations (EC50 values) were calculated from normalized (stretched to 0-100 %) dose-response curves of at least three independent MTT assays using GraphPad Prism Software 6.05 (GraphPad Software Inc., La Jolla, USA) as non-linear fit (log(inhibitor) vs. response, variable slope) following the equation:

$$Y = Bottom + \frac{(Top - Bottom)}{1 + 10^{(\log IC50 - X) \cdot HillSlope}}$$

2.12.3 Quantification of RNA/Western blot bands

To quantify and compare intensity of RNA or Western blot bands, Image Lab 4.0.1 Software (Bio-Rad, Munich, Germany) was used. Using rectangles, bands were selected and intensity (with background subtraction) calculated as percent of the intensity of the respective band of a housekeeping gene/protein.

3 Results

3.1 Oxidative cell death in HT22 and MEF cells

3.1.1 Glutamate-induced cell death in HT22 cells is circumvented by BI-6c9

Spindle-shaped mouse hippocampal HT22cells respond to ~2-10 mM glutamate by competitive system X_c^- blockage resulting in detrimental oxidative stress and injured mitochondria [185]. In the following, rapid cell death becomes visible through rounding up and detaching from the plate's bottom.

In HT22 cells treated with different concentrations of glutamate, this oxidative form of cell death occurred in a concentration-dependent manner starting at 2-3 mM glutamate assessed by loss of metabolic activity with the MTT assay (Figure 35a). Notably, also the amount of seeded cells per well determined sensitivity towards glutamate as conditions with less cells responded to even 1 mM glutamate (Figure 35b).

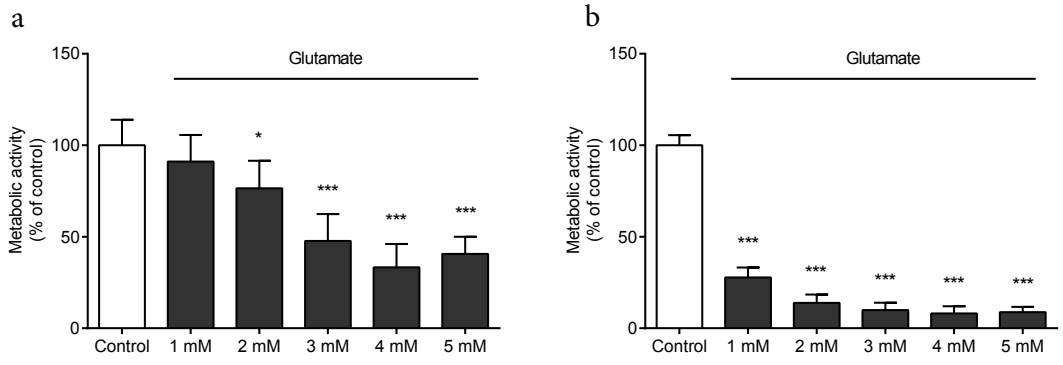

Figure 35. Glutamate-induced cell death in HT22 cells

a, b: MTT assay in HT22 cells reveals dose- and cell number-dependent glutamate sensitivity (**a:** 8K cells/well seeded, **b:** 4K/well; n=16/treatment condition, 16 hours treatment). Data are shown as mean + SD. *p<0.05, ***p<0.001 compared to untreated control (ANOVA, Scheffé's test).

The pro-apoptotic protein BID was shown to mediate fatal mitochondrial demise upon oxytosis induction in HT22 cells which is commonly referred to as *the point of no return* in cells undergoing regulated cell death [103]. The influence of diverse insults on mitochondrial function can be assessed as alterations in the o*xygen consumption rate* (OCR) using Seahorse XF96 extracellular flux measurements, where oxygen consumption indicates the rate of mitochondrial respiration. The subsequent application of ATP-synthase inhibitor oligomycin, respiratory chain uncoupling agent FCCP and complex I/III inhibitors antimycin A/rotenone, allows for assessing parameters of basal respiration, spare respiratory capacity, ATP production and maximum respiration.

The analysis of OCR in HT22 cells treated with glutamate revealed a time-dependent loss of mitochondrial respiration and respiratory capacity starting approximately 8 hours after the glutamate challenge (Figure 36a). Consequently, the well-established BID inhibitor BI-6c9 protected metabolic activity of HT22 cells until at least 8 hours post-treatment of glutamate exposure (Figure 36b) suggesting mitochondrial damage as the critical step in the cell's commitment to die. In xCELLigence real-time impedance analyses, BI-6c9 prevented the loss of cell index until 6 hours after glutamate exposure (Figure 36c) owing to higher glutamate concentrations (10 mM) compared to the MTT assay (6 mM) which shifted detrimental mitochondrial demise to earlier time-points.

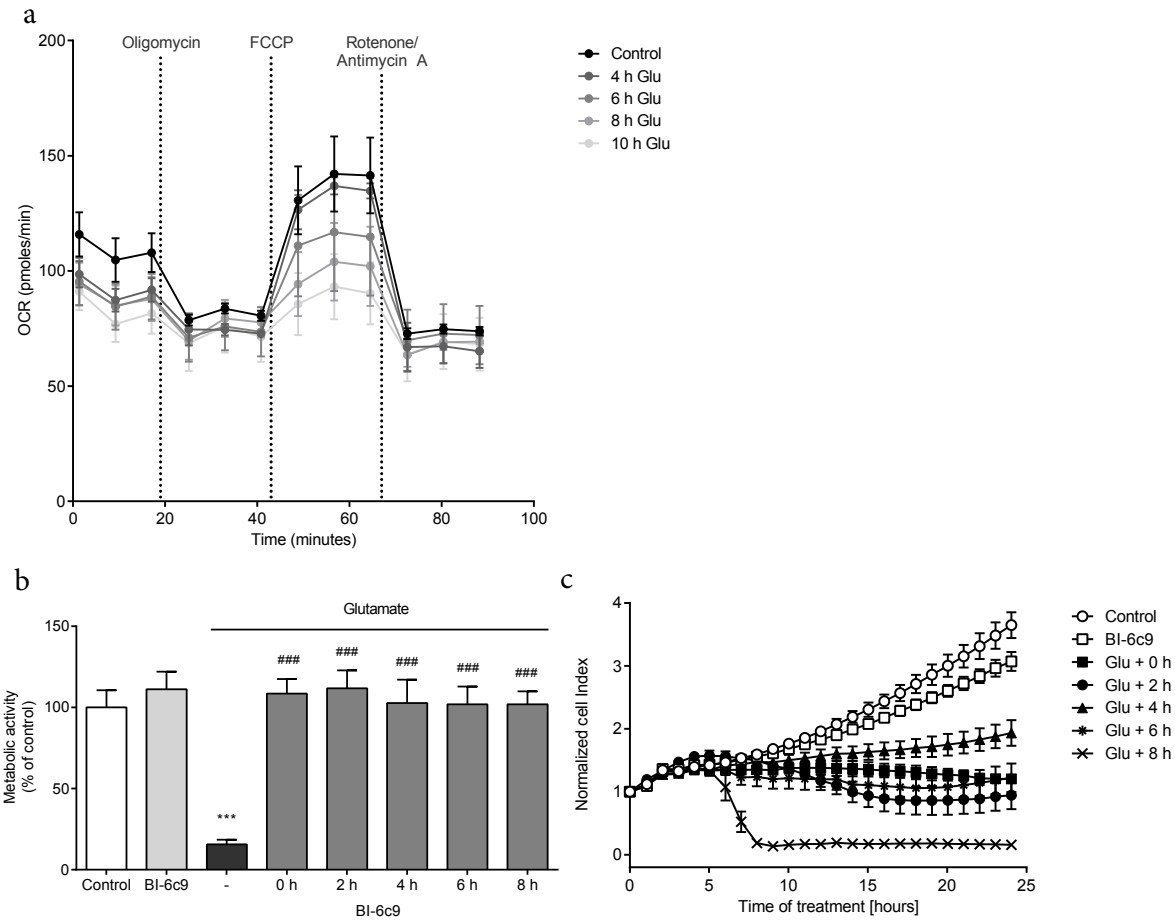

Figure 36. Glutamate induces mitochondrial damage attenuated by BID inhibitor BI-6c9

a: Seahorse OCR measurement (oligomycin: 3 µM, FCCP 0.5 µM, antimycin A 1 µM, rotenone 100 nM) demonstrates time-dependent loss of mitochondrial respiration upon glutamate challenge (6 mM) in HT22 cells (n=4-5/treatment condition). **b:** MTT assay of HT22 cells treated with glutamate (6 mM) ± BI-6c9 (10 µM, 0-8 hours post-treatment) (n=8/treatment condition) reveals protection until 8 hours after glutamate exposure. **c:** xCELLigence impedance measurement shows time-dependent protection of HT22 cells treated with glutamate (10 mM, 24 hours) ± BI-6c9 (10 µM, 0-8 hours post-treatment) until 6-8 hours after treatment (n=5-8/treatment condition). Data are shown as mean + or ± SD. ***p<0.001 compared to untreated control, ###p<0.001 compared to treated control (ANOVA, Scheffé's test).

3.1.2 Comprehensive analysis of erastin-induced cell death in HT22 and MEF cells

Erastin-induced ferroptosis has been generally described in non-neuronal cells [38]. In these cells, similar to glutamate, erastin inhibits X_c^- [39] thereby provoking depletion of glutathione, impaired GPX4 function, and thus, strong lipid peroxidation. However, the detailed biochemical mechanism in neurons and cell death execution downstream of lipid peroxidation remain to be clarified.

Due to apparent mechanistic similarity of cell death induction by glutamate and erastin through X_c^- inhibition, erastin-induced cell death was evaluated according to commonly known features in oxytosis. As ferroptosis was investigated mostly in non-neuronal cells so far, here, erastin-induced cell death in neuronal HT22 cells was compared to MEF cells to control for cell type specific effects.

In MTT assays erastin induced dose-dependent loss of metabolic activity in low micromolar concentrations (Figure 37a) which was prevented by BI-6c9 with an EC50 value of 1.4 µM (Figure 37b). In post-treatment experiments BI-6c9 was able to rescue HT22 cells until 4 hours after erastin challenge demonstrated in MTT (Figure 37c) and in xCELLigence impedance measurements (Figure 37d) indicating that erastin-induced direct X_c^- inhibition is accelerated compared to glutamate.

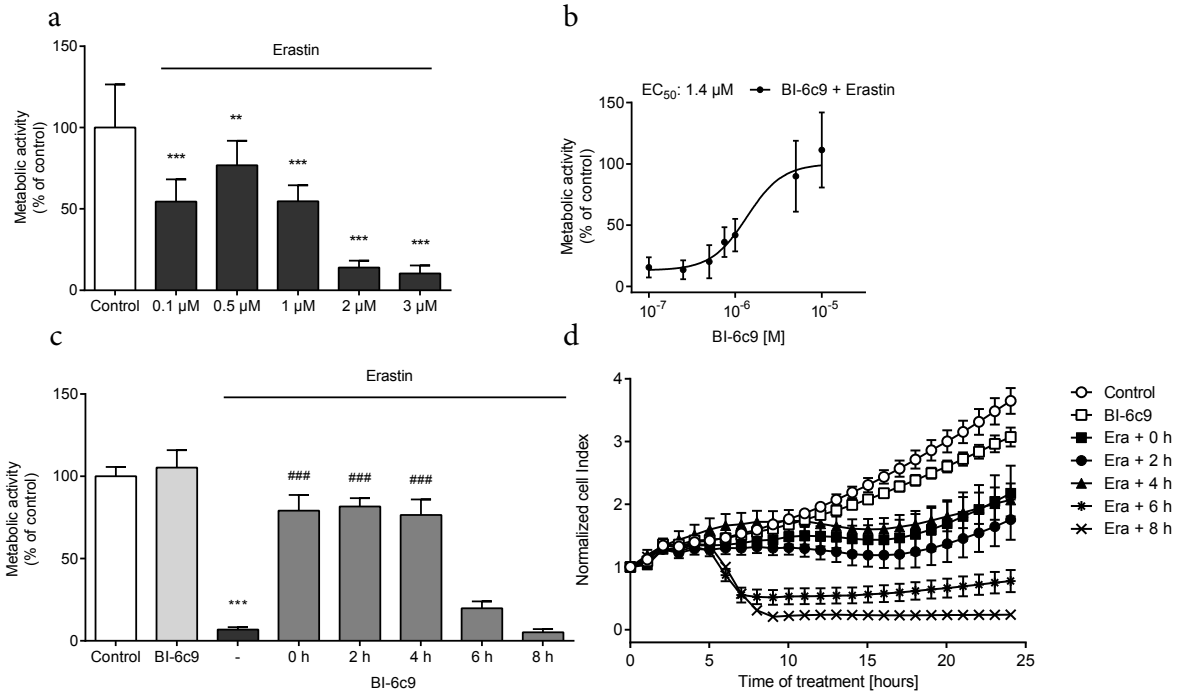

Figure 37. Erastin-induced cell death is circumvented by BI-6c9

a: Increasing erastin-concentrations indicate dose-dependent loss of metabolic activity in HT22 cells (MTT, n=16/treatment condition, 16 hours treatment). **b:** EC50 calculation of MTT experiments reveals protection of BI-6c9 against erastin-induced cell death (1.5 µM) in HT22 cells with an EC50 value of 1.4 µM (n=28/treatment condition, 16 hours treatment). **c:** MTT assay of HT22 cells treated with erastin (2 µM) ± BI-6c9 (10 µM, 0-8 hours post-treatment) (n=8/treatment condition) shows protection until 4 hours after erastin exposure. **d:** xCELLigence impedance measurement depicts time-dependent protection of HT22 cells treated with erastin (1 µM, 24 hours) ± BI-6c9 (10 µM, 0-8 hours post-treatment) until 4 hours after treatment (n=5-8/treatment condition). Data are shown as mean + or ± SD. $^{**}p<0.01$, $^{***}p<0.001$ compared to untreated control, $^{\#\#\#}p<0.001$ compared to treated control (ANOVA, Scheffé's test).

To investigate the chronology of erastin-mediated events, time-course experiments of successive lipid peroxidation, mitochondrial ROS formation, loss of membrane potential and cell death were carried out in HT22 and MEF cells using FACS analyses. In both cell lines, significant lipid peroxidation started at 6 hours (Figure 38a, b) followed by mitochondrial ROS formation (Figure 38c, d) and cell death at 8 hours (Figure 38e, f) after onset of erastin exposure. In HT22 cells loss of mitochondrial membrane potential assessed by TMRE FACS analysis started already 4 hours after erastin treatment (Figure 38g) presumably owing to early lipid peroxidation at the mitochondrial membrane and disruption of membrane morphology.

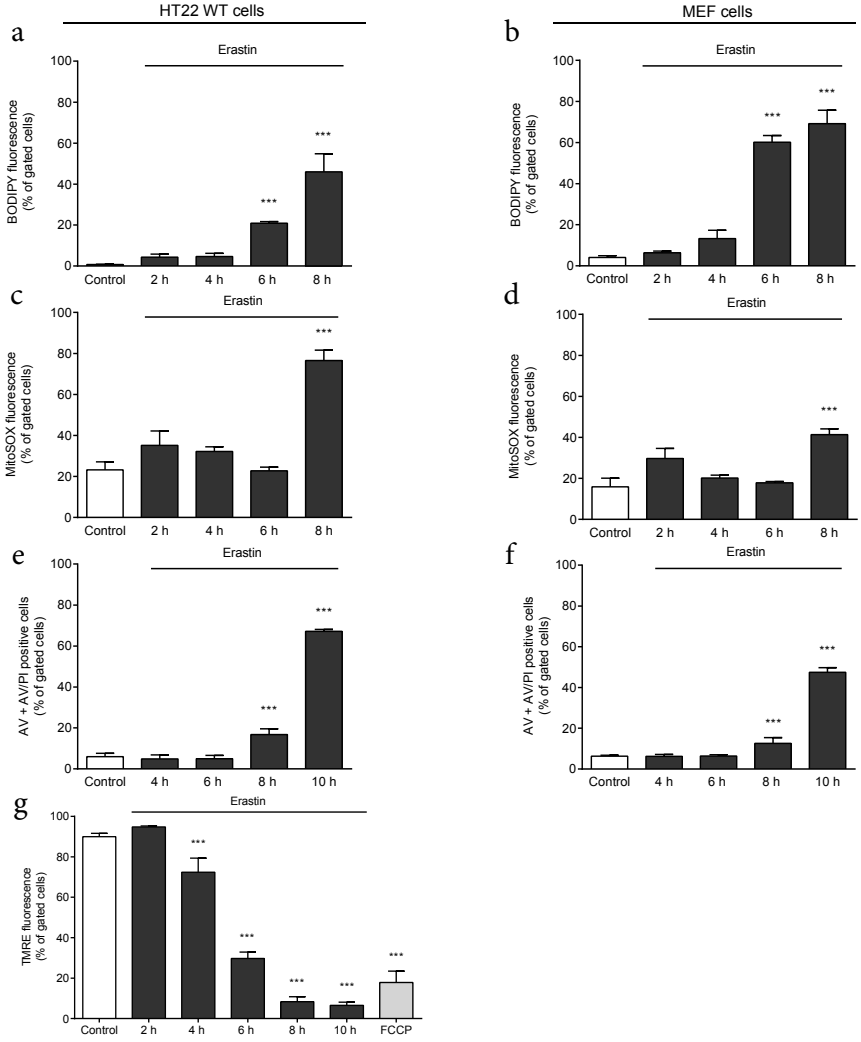

Figure 38. Time-course analysis of erastin-induced cell death

a, b: BODIPY FACS analyses show time-dependent increase in lipid peroxidation starting 6 hours after erastin treatment (1 µM) in HT22 (**a**) and MEF cells (**b**) (n=3/treatment condition). **c, d:** MitoSOX FACS analyses reveal time-dependent mitochondrial ROS formation after 8 hours of erastin treatment (1 µM) in HT22 (**c**) and MEF cells (**d**) (n=3/treatment condition). **e, f:** FACS analyses for Annexin V/PI stained cells demonstrate cell death after 8 hours of erastin challenge (1 µM) in HT22 (**e**) and MEF cells (**f**) (n=3/treatment condition). **g:** TMRE staining and subsequent FACS analysis indicates loss of membrane potential after 4 hours of erastin treatment (1 µM) in HT22 cells (positive control: FCCP, 5 min 50 µM) (n=3/treatment condition). Data are shown as mean + SD.***p<0.001 compared to untreated control (ANOVA, Scheffé's test).

For the purpose of investigating the specific impact of erastin on mitochondrial morphology and function in HT22 and MEF cells, cellular ATP levels were assessed by luminescence measurements, OCR with Seahorse XF96 and mitochondrial morphology by staining with MitoTracker DeepRed and subsequent optical analysis using fluorescence microscopy. As previously described [72], cells were categorized into three subclasses according to their mitochondrial morphology. In brief, cells with elongated mitochondria, organized in a long tubular network represent category I. Cells with predominantly large dotted mitochondria equally distributed in the cytosol were assigned to category II, whereas cells with completely fragmented mitochondria accumulating around the nucleus were classified as category III. In order to re-validate this classification system, the results were compared using ImageJ software-based automated quantification. Quantification of the average perimeter of mitochondria was performed using a custom macro for NIH ImageJ software in order to measure mitochondrial fragmentation as described previously by R. K. Dagda and C. Chu [33].

Measurements of ATP revealed a significant loss of cellular ATP levels 6 hours after erastin treatment in HT22 cells which was well in line with the significantly reduced OCR and impaired maximal respiration after 6 hours of erastin challenge detected in the Seahorse experiments (Figure 39).

The detrimental loss of mitochondrial function occurred at time-points of mitochondrial ROS formation and loss of mitochondrial membrane potential as an additional hallmark of mitochondrial damage and, interestingly, succeeded loss of morphological integrity, which was already apparent 2 hours after erastin exposure in epifluorescence microscopy (Figure 40) indicating morphological damage to be a prerequisite to mitochondrial dysfunction.

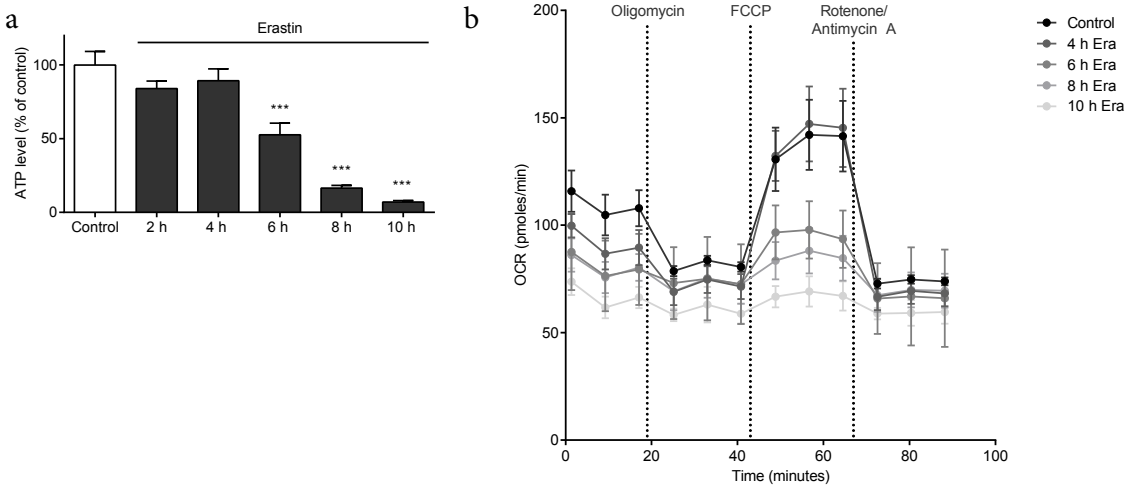

Figure 39. Erastin impairs mitochondrial function

a: ATP luminescence assay reveals loss of cellular ATP levels 6 hours after erastin treatment (1 µM) (n=6/treatment condition). **b:** Time-course analysis of oxygen consumption rate (oligomycin 3 µM, FCCP 0.5 µM, antimycin A 1 µM, rotenone 100 nM) of erastin-treated (1 µM) HT22 cells shows time-dependent decrease of oxygen consumption and maximum respiration (n=3-5/treatment condition). Data are shown as mean + or ± SD. ***p<0.001 compared to untreated control (ANOVA, Scheffé's test).

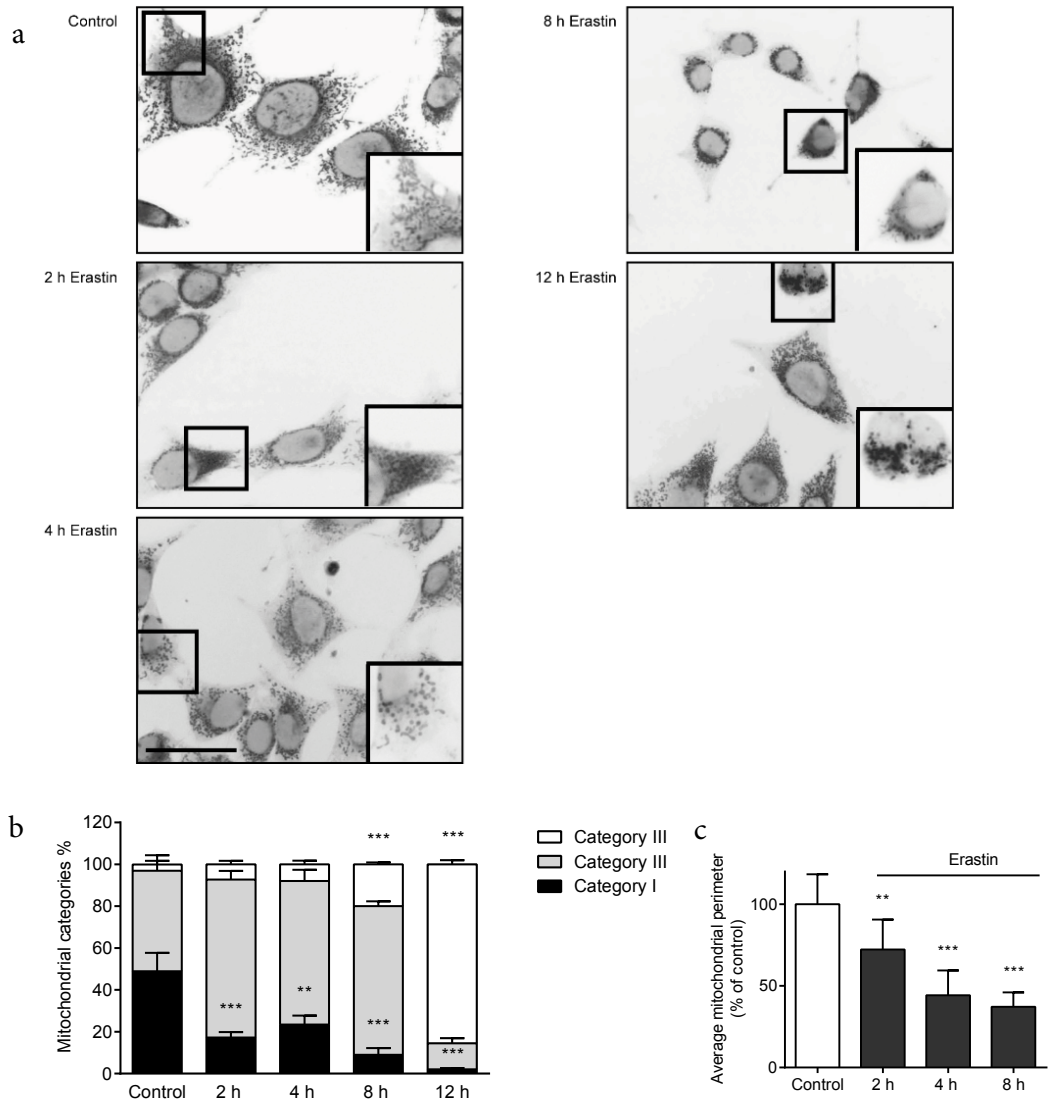

Figure 40. Erastin impairs mitochondrial morphology

a: Representative epifluorescence pictures (63x objective) of Mitotracker-stained (200 nM) HT22 cells depict time-dependent mitochondrial fragmentation and accumulation around the nucleus upon erastin treatment (1 µM). Scale bar 50 µm. **b:** Quantification of mitochondrial morphology categories of at least 500 cells/condition counted blind to treatment demonstrates early occurrence of fragmented mitochondria upon erastin treatment (1 µM) (n=3/treatment condition). **c:** Automated calculation of average mitochondrial perimeter with ImageJ macro of Mitotracker-stained (200 nM) HT22 cells confirms mitochondrial fragmentation starting 2 hours after erastin exposure (1 µM) (n=10 cells/treatment condition). Data are shown as mean + SD. ***p<0.001 compared to untreated control (ANOVA, Scheffé's test).

3.1.3 AIF depletion abrogates glutamate- and erastin-induced cell death

Based on the assumption that oxytosis and ferroptosis share common mechanistic hallmarks, such as AIF translocation, which is critical for cell death in oxytosis [133], was anticipated to be required in also ferroptosis. To test this hypothesis, AIF was depleted in HT22 cells by siRNA (siAIF) and cell viability evaluated by real-time impedance measurements. Here, siAIF was found to protect against glutamate- and erastin-induced cell death compared to control siRNA indicating a common cell death execution mechanism (Figure 41).

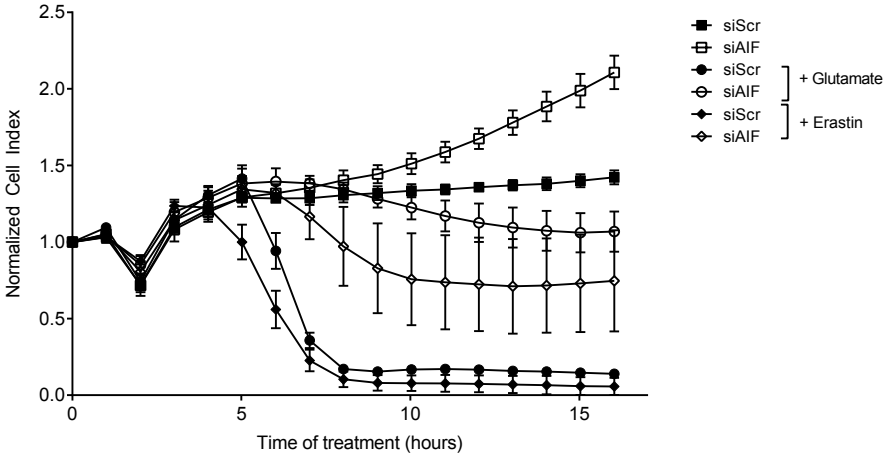

Figure 41. AIF depletion by siRNA prevents glutamate and erastin toxicity
XCELLigence real-time impedance measurement demonstrates protection of cell viability by AIF siRNA (20 nM, 48 hours) against glutamate- (5.5 mM) or erastin-induced toxicity (0.5 μM) in HT22 cells compared to control siRNA (n=5-8/treatment condition). Data are shown as mean ± SD.

3.1.4 H_2O_2-induced oxidative death

To ensure that commonly used oxytosis and ferroptosis inhibitors BI-6c9 and ferrostatin-1, respectively, are not protective due to mere antioxidant capacity, the metabolic activity of HT22 cells was assessed upon oxidative stress induction by H_2O_2. MTT assay revealed that neither BI-6c9 nor ferrostatin could protect cells from H_2O_2-induced oxidative injury (Figure 42).

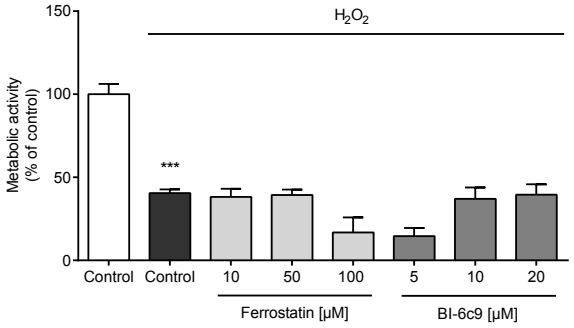

Figure 42. BI-6c9 and ferrostatin do not prevent H_2O_2-induced toxicity
MTT assay of HT22 cells treated with H_2O_2 (1 mM, 16 hours) ± BI-6c9 (10 µM) or ± ferrostatin-1 (10 µM) shows no protection of the oxytosis and ferroptosis inhibitors against oxidative stress challenge. Data are shown as mean + SD. ***p<0.001 compared to untreated control (ANOVA, Scheffé's test).

3.2 BID links ferroptosis to mitochondrial cell death pathways

In order to address the role of BID in oxidative stress induced cell death, BID was depleted by either siRNA approach or CRISPR/*Cas9* knockout to assess alterations in mitochondrial parameters and cell death after glutamate- or erastin exposure.

3.2.1 BID deletion by siRNA knockdown

In order to specifically deplete the protein levels of BID, two different siRNAs targeting *Bid* mRNA were used. Protein analysis on Western blot confirmed significant knockdown of BID protein with siRNA#1 and #2 48 hours after transfection compared to control siRNA (Figure 43a, b). On a functional level, *Bid* siRNA #2 but not #1 significantly reduced the glutamate-induced loss of metabolic activity (Figure 43c) and slightly attenuated cell death assessed by Annexin V/PI FACS analysis (Figure 43d) indicating a critical role for BID in mediating mitochondrial damage and cell death in oxidative stress induced cell death. However, as siRNA #1 and #2 gave differing results and the siRNAs did not lead to a complete knockdown of BID protein, full knockout of the protein was desirable.

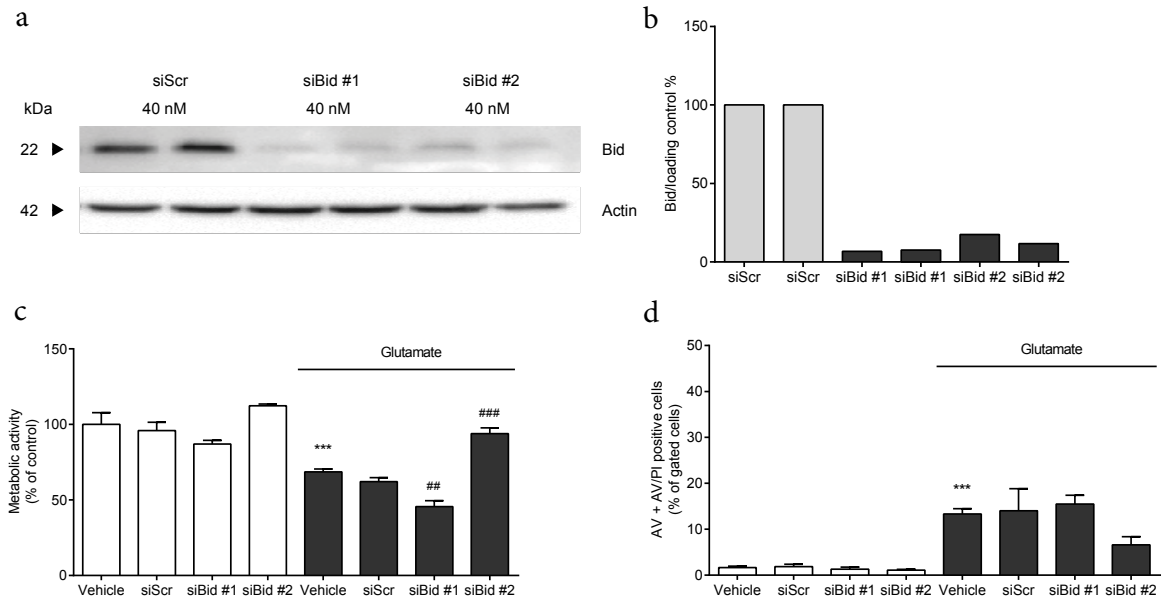

Figure 43. BID siRNA knockdown partly protects against glutamate toxicity

a, b: Western blot (**a**) and subsequent quantification (**b**, normalized to actin protein levels) of HT22 cells transfected with two different siRNAs (40 nM, 48 hours) against *Bid* mRNA demonstrates strong reduction of BID protein levels compared to control siRNA conditions. **c:** MTT assay in *Bid* siRNA transfected (40 nM, 48 hours) HT22 cell reveals protection against glutamate (6 mM, 16 hours) by siRNA #2 compared to control siRNA (n=3/treatment condition). **d:** Annexin V/PI FACS analysis in *Bid* siRNA transfected (40 nM, 48 hours) HT22 cell depicts a trend towards protection for *Bid* siRNA #2 against glutamate treatment (6 mM, 16 hours) (n=3/treatment condition). Data are shown as mean + SD. ***$p<0.001$ compared to untreated vehicle control, $^{\#\#}p<0.01$, $^{\#\#\#}p<0.001$ compared to treated vehicle control (ANOVA, Scheffé's test).

3.2.2 CRISPR/*Cas9 Bid* knockout in HT22 cells

3.2.2.1. Generation of HT22 Bid knockout cells

With the aim of achieving a full knockout of BID protein, the emerging CRISPR/*Cas9* technique was utilized to create HT22 *Bid* knockout cells. CRISPR/*Cas9* induces targeted DNA double-strand breaks leading to error-prone genetic repair and, by this, to insertion/deletion or frameshift mutations that ideally cause a functional protein knockout. In this study, a pre-designed ready-to-use CRISPR *Bid* plasmid from Sigma Aldrich (Taufkirchen, Germany) was transfected in HT22 cells and the cells were screened for *Bid* knockout. The plasmid contained the genetic material for the *Cas9* endonuclease enzyme, a tracrRNA guiding the enzyme to the target site, and a guideRNA (gRNA) specifically designed to recognize the mouse *Bid* gene (Figure 44a, b). In addition, *Cas9* was coupled to GFP (green-fluorescent protein) to facilitate sorting of successfully transfected cells (Figure 44b).

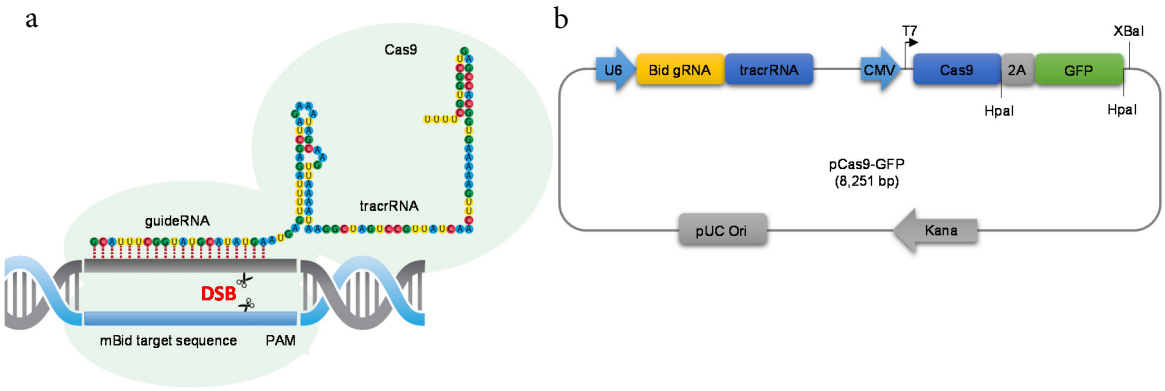

Figure 44. CRISPR/Cas9 plasmid design

a: CRISPR/Cas9 targeting *Bid* at genomic DNA level (modified from [137]). **b:** Commercially available ready-to-use *Bid* CRISPR/Cas9 plasmid from Sigma Aldrich (Taufkirchen, Germany) with *Bid* guideRNA, tracrRNA and GFP-labelled Cas9 endonuclease.

In order to test whether the correct plasmid was obtained from the company, a restriction digest with XbaI enzyme was performed to check for the plasmid size, which was 8.3 kb as expected (Figure 45a). After 48 hours of transfection, HT22 cells were sorted by FACS to enrich GFP-positive cells indicating successful transfection with the CRISPR plasmid. Fluorescence microscopy revealed a sufficient transfection efficiency of about 10-20 % (Figure 45b). Subsequently, cells were seeded in 96-well plates with either 1 cell, 2 cells or 5 cells per well and were constantly screened for colony growth. Each individual colony was subjected to Western blot and genetic sequence analysis to screen for *Bid* knockout. In addition to Western blot analysis, the resulting clonal colonies were sequenced to detect mutations in the CRISPR target region using site-specific primer sequences. A PCR protocol was established to amplify the genomic DNA around the CRISPR *Bid* target site resulting in a 1028 bp PCR product (Figure 45c).

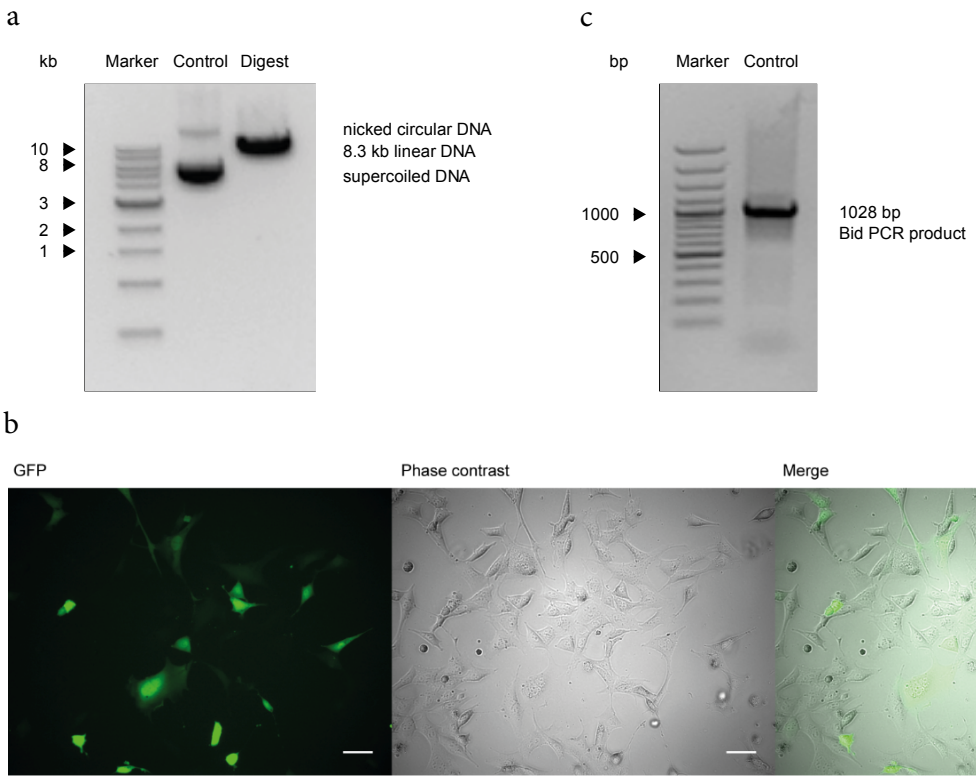

Figure 45. CRISPR/Cas9 establishment

a: Agarose gel (1 % with EtBr) of XbaI digest (1.5 hours, 37 °C) for testing the correct CRISPR/Cas9 plasmid size reveals a correct size of ~ 8 kb and nicked and supercoiled DNA in the undigested sample. **b:** Fluorescence light microscopy pictures (20x objective) depict ~10-20 % transfection efficiency of GFP-labelled CRISPR/*Cas9* in HT22 cells (48 hours, 5 µg plasmid DNA). Scale bar 50 µm. **c:** Agarose gel (1 % with EtBr) of PCR amplification of a 1028 bp region around the CRISPR *Bid* target site.

Following the CRISPR/*Cas9* knockout procedure, a total of 38 colonies were obtained. Western blot analysis of the obtained colonies #3-#38 and subsequent quantification (Figure 46) revealed most efficient knockout of *Bid* in colonies #4, #14, #15 and #25 suggesting a full knockout on both alleles in a homogenous population of HT22 cells.

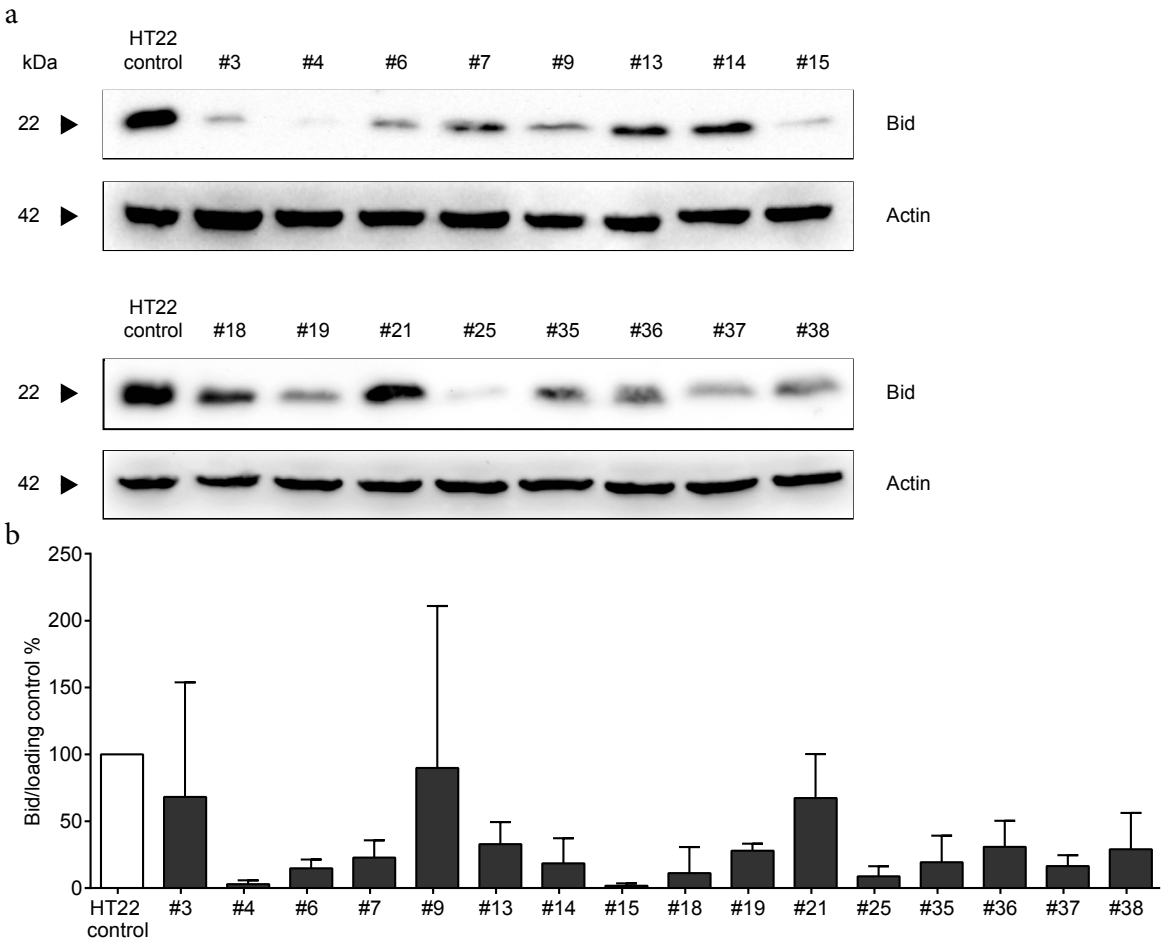

Figure 46. CRISPR Western blot analysis

a, b: Western blot analysis (**a**) and quantification (**b**) of HT22 CRISPR *Bid* colonies depicts efficient knockdown of BID protein in colonies #4, #14, #15 and #25 (normalized to actin as housekeeping protein) (**a:** 80 µg protein, 12.5 % SDS gel, **b:** pooled data from 4 individual Western blots).

In order to detect mutations on the genetic level, the genomic DNA of colonies #4, #14, #15 and #25 was isolated, the CRISPR *Bid* region amplified by PCR and visualized on an EtBr agarose gel (Figure 47). The amplified PCR products were purified and sequenced. Sequencing results demonstrated no mutation in colony #14 and partial mutations and/or deletion in colonies #4, #15 and #25 indicated as multiple peaks in the sequencing plots (Figure 48). Since colony #4 was the most promising knockout colony with a deletion mutation, this colony was chosen for functional experiments and in the following is referred to as *HT22 Bid KO*.

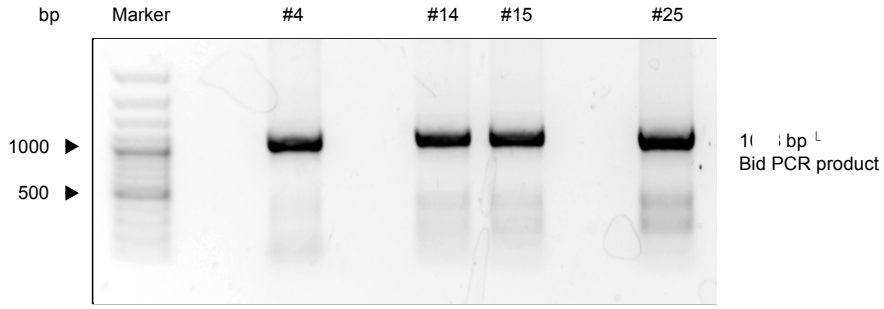

Figure 47. CRISPR target site amplification by PCR

Agarose gel (1 % with EtBr) of CRISPR Bid target site amplification by PCR (200 ng DNA template) visualizes 1028 bp PCR product.

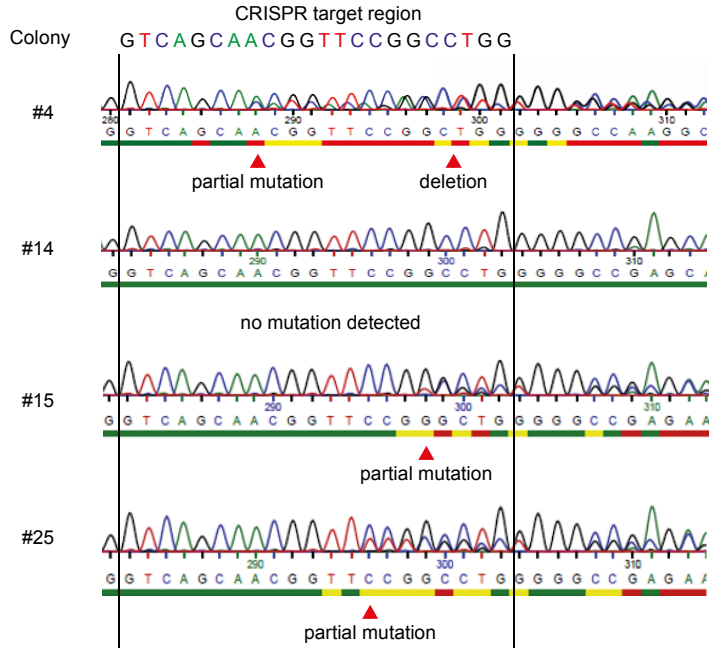

Figure 48. CRISPR sequencing results

Sequencing of genomic CRISPR *Bid* DNA sites in HT22 cells reveals partial mutations and/or deletion in colonies #4, #15 and #25 and no mutation in colony #14 compared to the WT mouse genomic DNA sequence.

The CRISPR/*Cas9* technique is prone to off-targeting as guideRNAs (gRNAs) are limited to 19-24 nucleotides length. In consequence, gRNAs may target resembling DNA sequences in the genome by mistake depending on the order and number of similar nucleotides. In order to reduce off-target probability, gRNAs should be carefully designed by specific web-based design tools using various algorithms to avoid similarity to unspecific genomic DNA sites [179,225].

In this study, these tools were exploited to calculate the most probable off-target sites to sequence the genomic DNA at these specific spots in order to rule out off-target-based functional effects. According to the web-based tools Trpc4, Grm3, Syngr1, Hivep3, Hprt and Kcne1 could be identified as potential off-targets sites. Hence, in HT22 *Bid* KO cells these DNA sites were amplified by PCR and the sequences were analyzed. As depicted in Figure 49, no off-target mutation was found in Trpc4, Grm3, Syngr1, Hivep3 and Hprt compared to mouse genomic WT DNA, however, Kcne1 contained one mutation, which was also found in HT22 WT DNA, for which reason this mutation was not attributed to the CRISPR/*Cas9* knockout procedure.

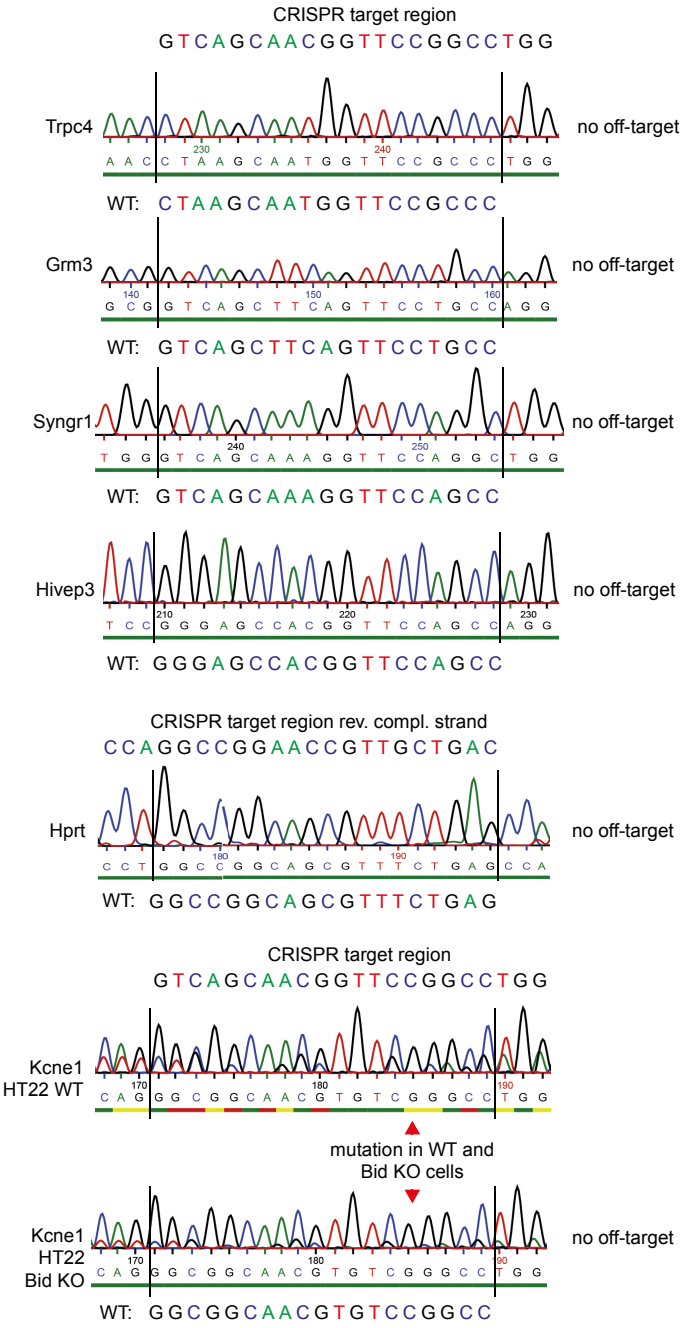

Figure 49 CRISPR off-target sequencing

Sequencing of potential CRISPR off-target sites depicts no mutation in Trpc4, Grm3, Syngr1, Hivep3 or Hprt compared to the respective mouse genomic WT DNA sequence. Kcne1 contained one mutation which was also found in HT22 WT DNA.

In addition to sequencing of potential off-targets in HT22 *Bid* KO cells, Western blot was used to rule out alterations in 12-LOX and xCT protein levels, which would interfere with the cell death process upon glutamate or erastin treatment. The analysis revealed that the according protein levels were comparable to HT22 WT protein levels (Figure 50).

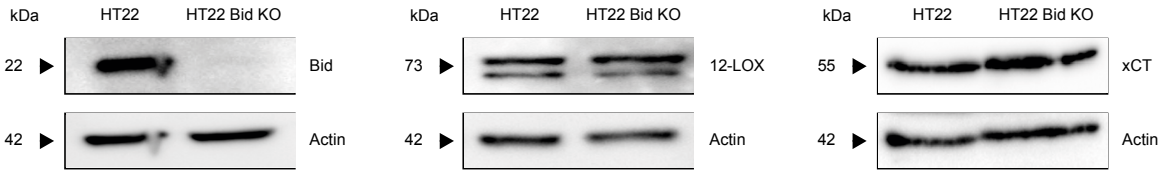

Figure 50. Western blot off-target analysis
Western blot analysis of 12-LOX and xCT protein in HT22 *Bid* KO cells depicts no downregulation compared to HT22 WT protein lysates (12-LOX: 40 µg protein, xCT, Bid: 80 µg protein, 12.5 % SDS gel).

3.2.2.2. Functional analysis of HT22 Bid knockout cells

As a first hint on the influence of CRISPR/*Cas9 Bid* knockout on glutamate-induced oxidative cell death, pooled CRISPR plasmid transfected HT22 cells (referred to as HT22 CRISPR *Bid* stock) were subjected to gentle glutamate treatment and subsequent MTT assay to check for cell viability. Here, the HT22 CRISPR *Bid* stock cells showed protected metabolic activity compared to HT22 WT cells (Figure 51) implying a crucial role for BID in the execution of cell death.

Having identified CRISPR colony #4 as a favorable *Bid* knockout cell line, these cells were analyzed for their ability to undergo cell death upon erastin challenge in order to elucidate the role of BID in ferroptotic cell death. The obtained results were compared to HT22 WT cells and to glutamate-induced oxytosis, where BID could be already identified as a key protein in mediating mitochondrial damage and cell death.

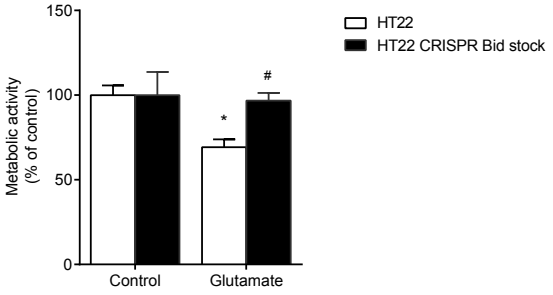

Figure 51. MTT assay in CRISPR Bid stock cells

MTT assay of HT22 CRISPR *Bid* stock cells upon gentle glutamate treatment (4.5 mM, 17 hours) demonstrates protection compared to HT22 WT cells (n=3/treatment condition). Data are shown as mean + SD. *p<0.05 compared to untreated HT22 WT control, #p<0.05 compared to treated HT22 WT control (ANOVA, Scheffé's test).

Therefore, HT22 WT and *Bid* KO cells were exposed to glutamate or erastin, respectively, and cell death was assessed using MTT assay for metabolic activity, Annexin V/PI FACS analysis to estimate cell death induction and xCELLigence measurements for real-time monitoring of cell viability. Remarkably, *Bid* KO led to a full and permanent protection of HT22 cells against glutamate or erastin insults comparable to BI-6c9 mediated rescue (Figure 52).

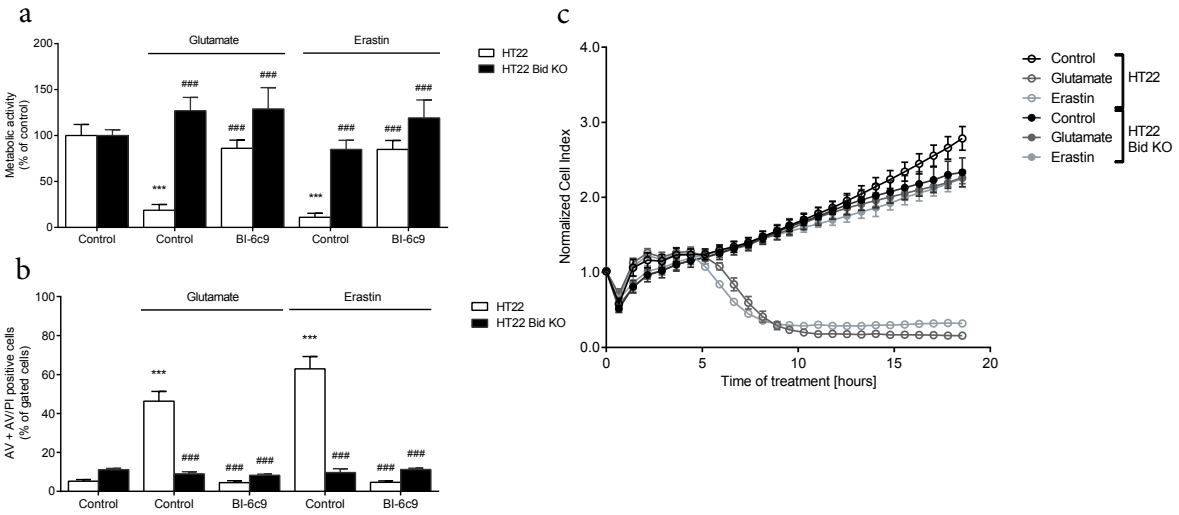

Figure 52. Bid KO protects against glutamate- and erastin-induced cell death

a, b: MTT assay (**a**) and Annexin/PI FACS measurement (**b**) demonstrate *Bid* KO to completely prevent cell death induced by glutamate (**a:** 7 mM, 16 hours; **b:** 8 mM, 17 hours) or erastin (1 µM, **a:** 16 hours, **b:** 17 hours). Protection was comparable to BI-6c9 (10 µM) mediated rescue (**a:** n=8/treatment condition, **b:** n=4/treatment condition). **c:** xCELLigence real-time impedance measurement confirms full protection against glutamate (7 mM) or erastin (1 µM) challenge by *Bid* KO and underlines permanence of cell death prevention (n=5-14/treatment condition). Data are shown as mean + or ± SD. ***p<0.001 compared to untreated HT22 WT control, ###p<0.001 compared to treated HT22 WT control (ANOVA, Scheffé's test).

BID is known to mediate mitochondrial dysfunction downstream of GSH depletion in the model system of oxytosis. Thus, investigations on cellular GSH levels in HT22 *Bid* KO cells upon glutamate or erastin exposure still showed GSH depletion in a time-dependent manner (Figure 53a, b). Fluorescent BODIPY or DCF staining and subsequent FACS analyses were used to evaluate the formation of lipid peroxides and soluble ROS after GSH depletion and successive activation of 12/15-LOX. Increasing levels of lipid peroxides (Figure 53c, d) and ROS (Figure 53e, f) were measured in HT22 WT cells, whereas BID deletion significantly prevented lipid peroxide and ROS formation upon glutamate or erastin treatment indicating a critical role of BID in lipid and soluble ROS formation.

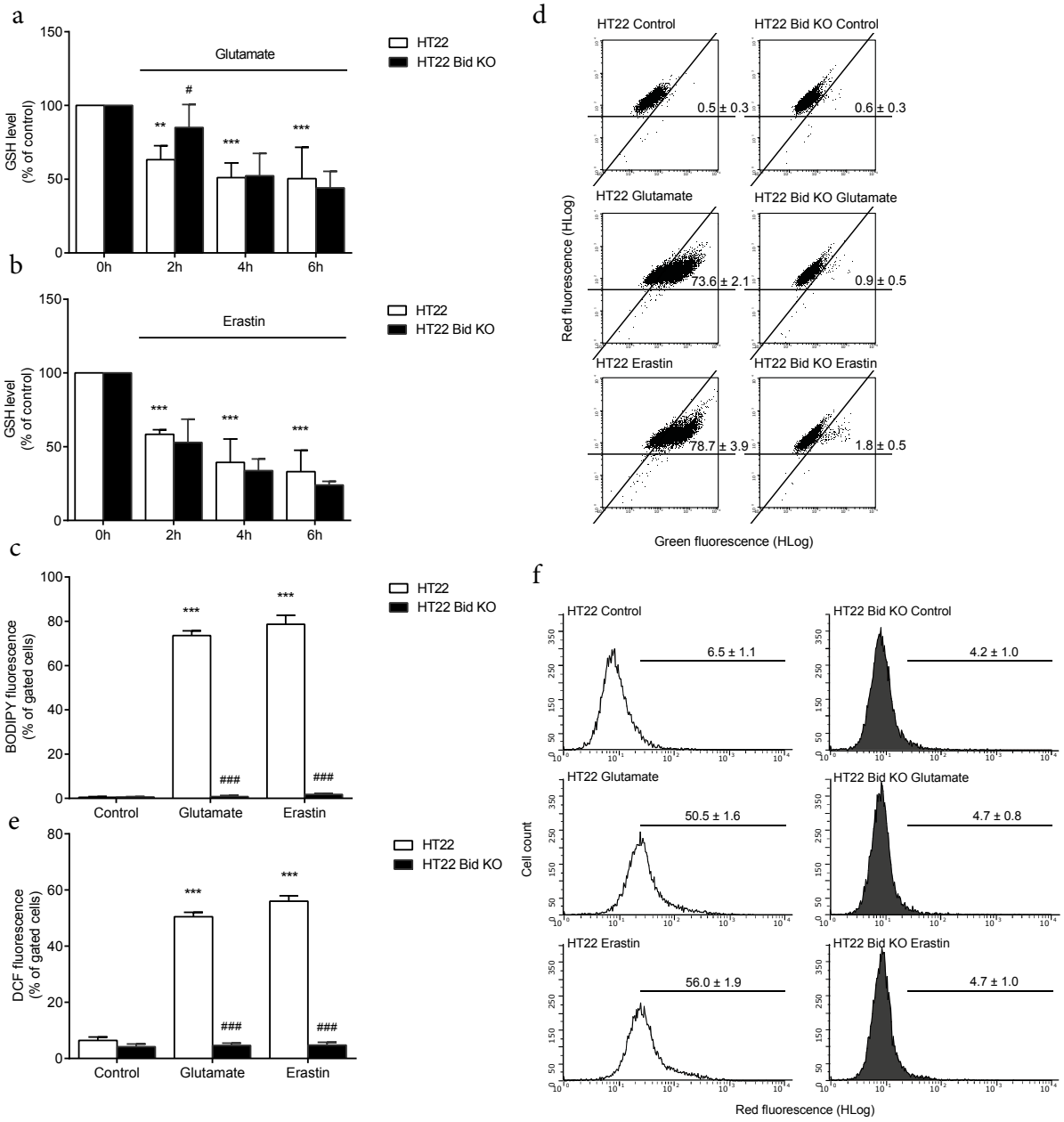

Figure 53. Bid KO does not inhibit GSH depletion but prevents ROS formation

a, b: Measurement of cellular glutathione levels depicts rapid decrease of GSH after glutamate (8 mM, **a)** or erastin (1 µM, **b**) exposure which was not restored by *Bid* KO (n=4-8/treatment condition). **c, d:** Cells were stained with BODIPY 581/591 and changes of fluorescence were detected by FACS analysis after 10 hours of glutamate (7.5 mM) or erastin (1 µM) treatment. Quantification (**c**) and FACS plots (**d**) show that *Bid* KO fully prevents the formation of lipid peroxides compared to WT control cells (n=4/treatment condition). **e, f:** DCF FACS analysis depicts massive accumulation of soluble ROS upon glutamate (7 mM, 17 hours) and erastin (1 µM, 17 hours) challenge in HT22 WT cells, whereas HT22 *Bid* KO cells show constant ROS levels comparable to those in control cells according to quantification (**e**) and representative FACS plots (**f**) (n=4/treatment condition). Data are shown as mean + SD. **p<0.01, ***p<0.001 compared to untreated HT22 WT control, $^{\#}$p<0.05, $^{\#\#\#}$p<0.001 compared to respective treated HT22 WT control (ANOVA, Scheffé's test).

Mitochondrial ROS formation and loss of mitochondrial membrane potential succeeding lipid peroxidation were analyzed by FACS of MitoSOX and TMRE red fluorescence in HT22 *Bid* KO cells upon glutamate and erastin exposure. Notably, *Bid* KO completely abrogated mitochondrial ROS formation (Figure 54a, b) as well as loss of mitochondrial membrane potential (Figure 54c, d) compared to massive ROS and disruption of the mitochondrial membrane potential in WT cells suggesting a key role for BID in mediating mitochondrial damage in both paradigms of oxytosis and ferroptosis.

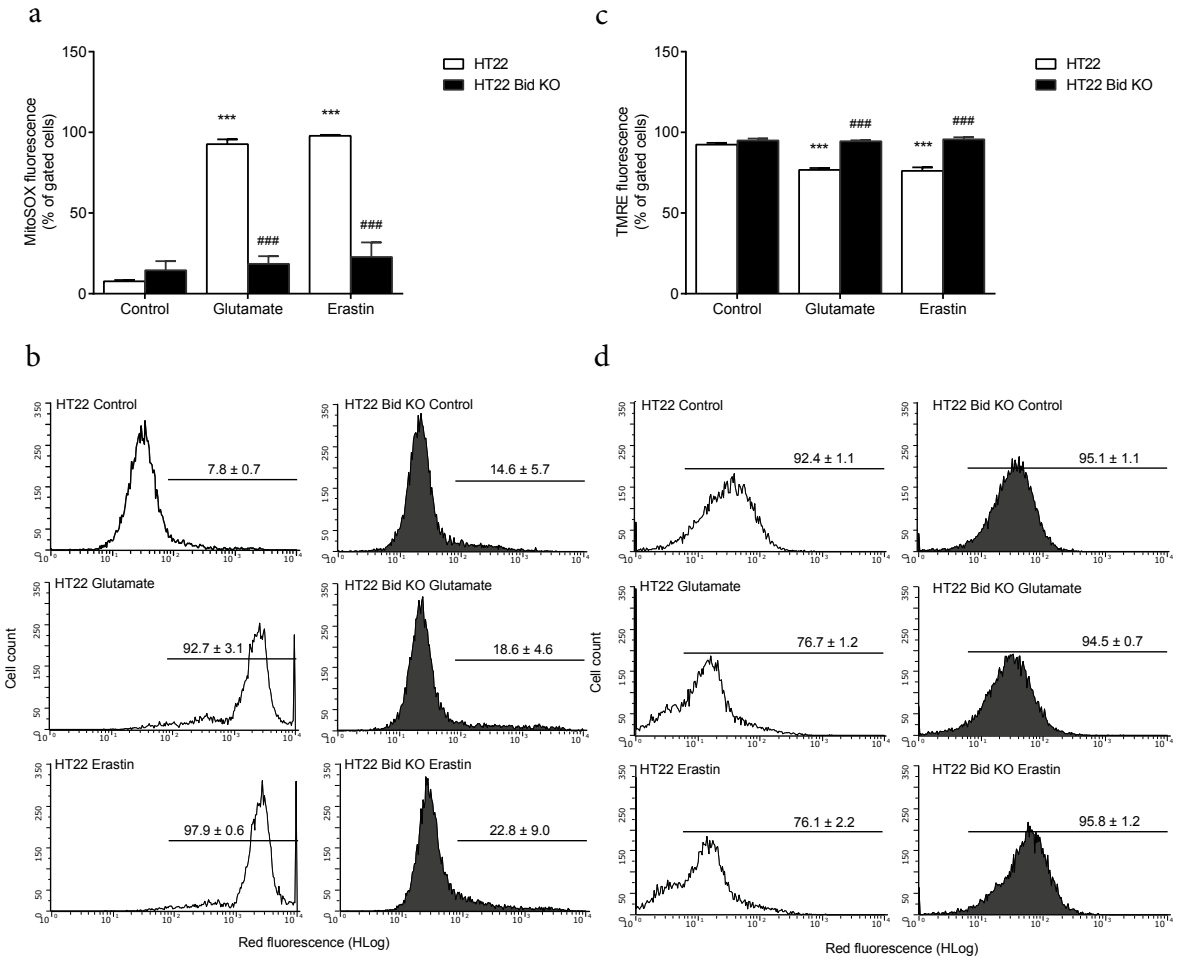

Figure 54. Bid KO prevents mitochondrial damage

a, b: MitoSOX staining and subsequent FACS analysis depicts reduced formation of mitochondrial ROS in HT22 *Bid* KO cells compared to HT22 WT cells after erastin (1 µM, 16 hours) or glutamate (7 mM, 16 hours) challenge according to quantification (**a**) and representative FACS plots (**b**) (n=4/treatment condition). **c, d:** TMRE FACS measurements for assessment of the loss of mitochondrial membrane potential upon erastin (1.2 µM, 16 hours) or glutamate (8 mM, 16 hours) exposure demonstrates rescue by *Bid* KO compared to HT22 WT cells in the quantification (**c**) and representative FACS plots (**d**) (n=4/treatment condition). Data are shown as mean + SD. ***p<0.001 compared to untreated HT22 WT control, ###p<0.001 compared to respective treated HT22 WT control (ANOVA, Scheffé's test).

Furthermore, erastin as well as glutamate treatment led to a significant loss of cellular ATP levels which was circumvented by *Bid* KO (Figure 55a) suggesting that mitochondria of HT22 *Bid* KO cells were also protected at a functional level. In order to further investigate mitochondrial respiration, both HT22 WT and *Bid* KO cells were treated with glutamate (Figure 55b) or erastin (Figure 55c), respectively, and analyzed for OCR in Seahorse XF96 flux analyzer. Interestingly, oxygen consumption of HT22 *Bid* KO cells was completely preserved compared to pronounced reduction in treated HT22 WT cells. Morphological analysis by evaluation of MitoTracker DeepRed stained cells resulted in substantial loss of healthy mitochondria (category I) in HT22 WT cells after 16 hours of glutamate or erastin exposure, respectively, whereas HT22 *Bid* KO cells displayed unchanged mitochondrial morphology with almost no cells of category II or III mitochondria (Figure 55e, f).

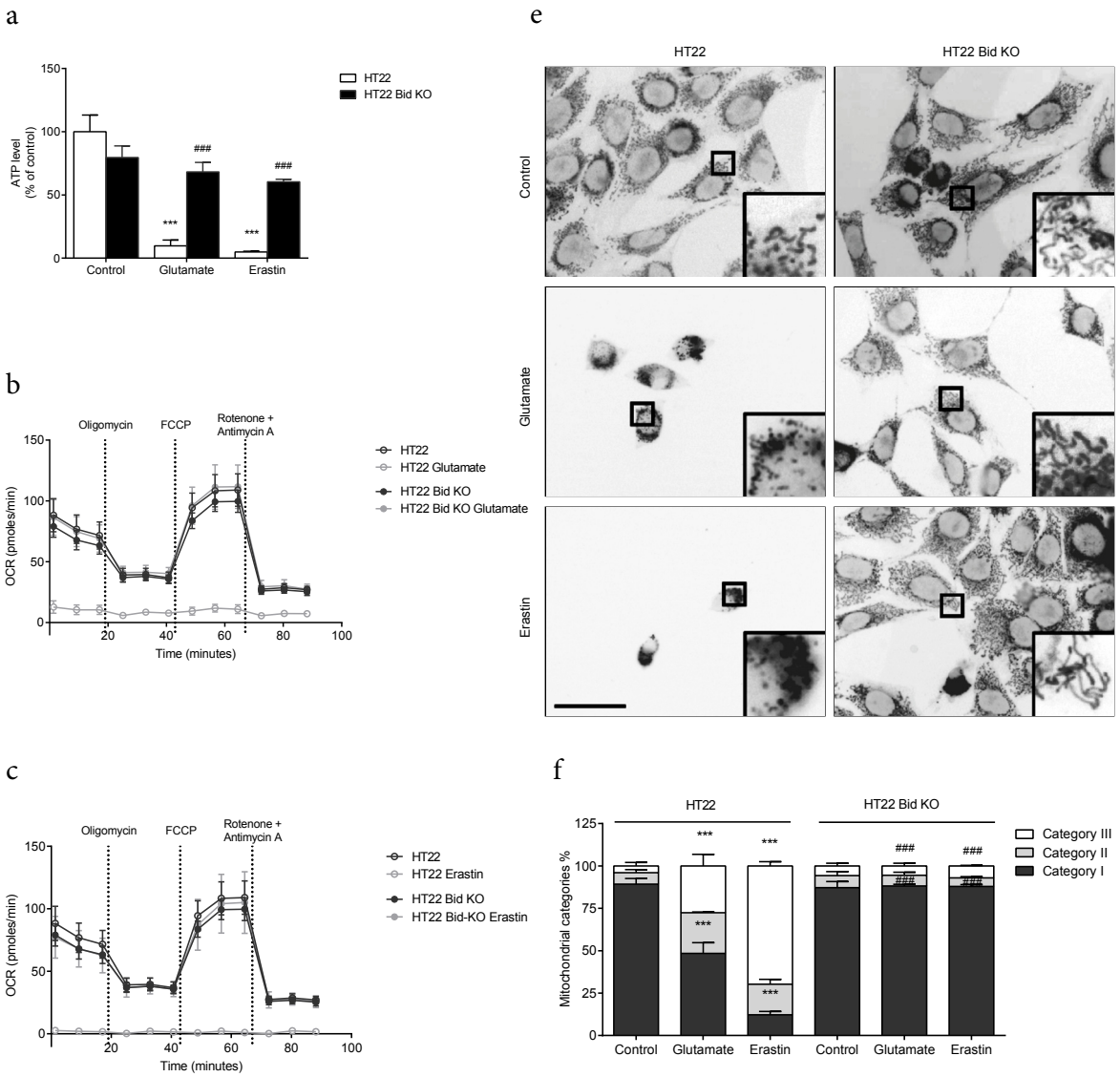

Figure 55. Bid KO preserves mitochondrial morphology

a: After 17 hours of treatment with glutamate (7 mM) or erastin (1 µM) ATP levels are measured. *Bid* KO prevents ATP depletion compared to HT22 WT controls (n=8/treatment condition). **b, c:** Measurement of the oxygen consumption rate (OCR) reveals restored basal and maximal respiration in *Bid* KO cells compared to WT controls after 15 hours glutamate (2 mM; **b**) or erastin (0.25 µM; **c**) exposure (n=6/treatment condition)**.e, f:** Representative microscopy pictures (**e**) and mitochondrial classification (**f**) of Mitotracker (200 nM) stained HT22 WT and *Bid* KO cells which were treated with glutamate (5 mM, 17 hours) or erastin (0.5 µM, 17 hours), respectively. Mitochondrial morphology is massively disturbed with erastin and glutamate in HT22 WT cells, whereas *Bid* KO cells do not show alterations in the morphology (n=3/treatment condition). Scale bar 50 µm. Data are shown as mean + SD. ***p<0.001 compared to untreated HT22 WT

3.2.2.3. *TBID overexpression abrogates protection by Bid KO*

Since *Bid* knockout was shown to protect against cell death and to preserve mitochondrial morphology and function, overexpression of full-length BID or tBID should circumvent the experimental protective effects thereby confirming that the observed outcome specifically resulted from *Bid* knockout. In order to restore BID expression, pcDNA3 Bid p22 was transfected in HT22 *Bid* KO cells which, subsequently, were exposed to glutamate. Cell death was assessed by metabolic activity in MTT assay and compared to the effects of pcDNA3 control vector and HT22 WT cells. HT22 *Bid* KO cells were protected upon transfection with the control vector but regained sensitivity to glutamate when full-length BID was expressed (Figure 56a). Similarly, upon expression of active tBID, HT22 *Bid* KO cells showed reduced cell viability comparable to tBID-expressing HT22 WT cells analyzed by xCELLigence real-time measurements (Figure 56b). Furthermore, tBID expression was able to restore lipid peroxidation in HT22 *Bid* KO cells (Figure 56c).

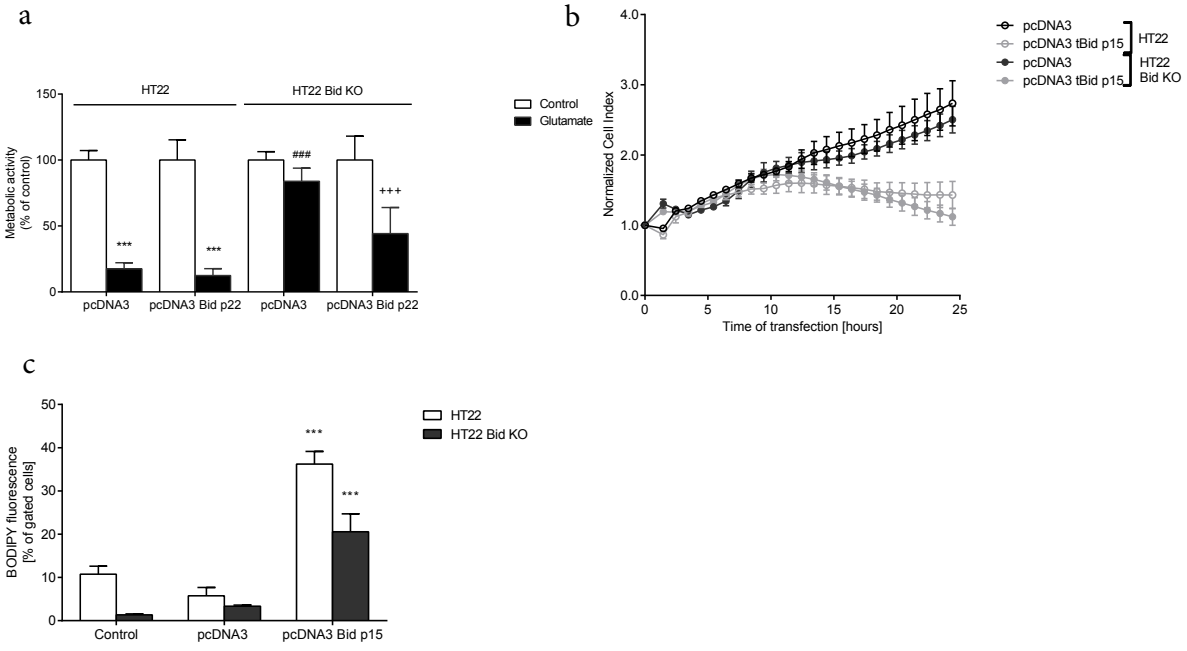

Figure 56. TBID and BID expression reverse protection mediated by Bid knockout

a: MTT assay demonstrates rescue of BID-mediated cell death with glutamate (7 mM, 16 hours) upon transfection of full-length BID (pcDNA3 Bid p22, 48 hours transfection, 200 ng DNA/well) in HT22 *Bid* KO cells compared to HT22 WT cells and control vector (pcDNA3) (n=4/treatment condition). **b:** Real-time analysis of HT22 *Bid* KO cells expressing active tBID (pcDNA3 p15, 0.75 µg DNA/well) reveals cell death induction comparable to HT22 WT cells (n=3-8/treatment condition). **c:** BODIPY FACS analysis in HT22 *Bid* KO cells reveals restoration of lipid peroxidation upon tBID expression (2 µg DNA/well, 10 hours) compared to control vector (pcDNA3) (n=3/treatment condition). Data are shown as mean + or ± SD. ***p<0.001 compared to respective untreated HT22 WT control, $^{###}$p<0.001 compared to treated HT22 WT control, $^{+++}$p<0.001 compared to treated HT22 *Bid* KO control (ANOVA, Scheffé's test).

3.2.2.4. Staurosporine-induced cell death in HT22 Bid KO cells

Staurosporine is a natural alkaloid isolated from *Streptomyces staurosporeus* and is used to induce cell death by ATP-competitive binding to protein kinases. The mechanism of cell death induction by staurosporine is still under debate and differs between various cell lines, however, caspase-3 activation is a generally accepted hallmark [20] and BID independence is discussed. In order to control that HT22 *Bid* KO cells still respond to cell death induction apart from oxidative stress by glutamate or erastin, these cells were subjected to staurosporine treatment. Cell death assessed by MTT assay (Figure 57a) and Annexin V/PI FACS analysis (Figure 57b) was comparable to cell death in HT22 WT cells suggesting a BID-independent pathway of staurosporine induced cell death and underlining that HT22 *Bid* KO cells are still sensitive to other forms of cell death.

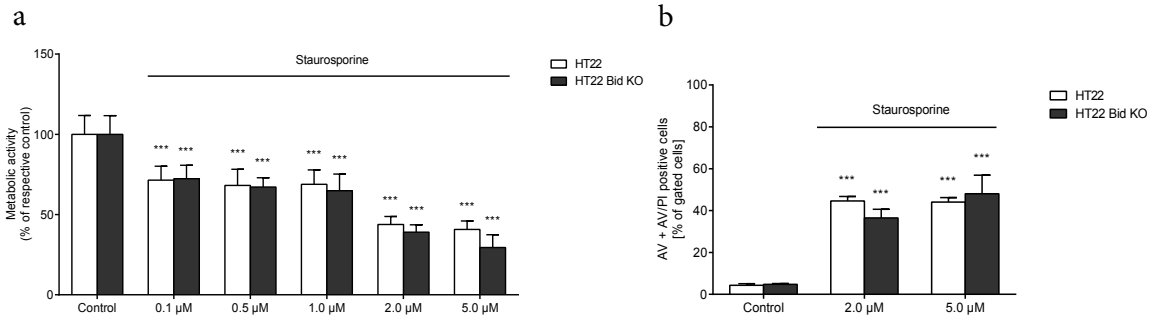

Figure 57. Bid KO does not prevent staurosporine-induced cell death

a, b: MTT assay (**a**) and Annexin V/PI staining and subsequent FACS analysis (**b**) reveals staurosporine sensitivity to be comparable in HT22 WT and *Bid* KO cells (**a:** 17 hours treatment, n=8/treatment condition, **b:** 7 hours treatment, n=3/treatment condition). Data are shown as mean + SD. ***p<0.001 compared to untreated HT22 WT control (ANOVA, Scheffé's test).

3.2.3 Liproxstatin-1 protects against oxytosis and ferroptosis

In order to check for protective effects of ferroptosis inhibition in the paradigm of oxytosis, the recently described ferroptosis inhibitor liproxstatin-1 [53,227] was applied in the present model systems of erastin-induced ferroptosis and glutamate-induced oxytosis in HT22 WT cells. In both paradigms of oxidative death, liproxstatin prevented cell death in a concentration-dependent manner shown by calculated EC50 values of 0.02 µM for glutamate and 0.03 µM for erastin challenge, respectively (Figure 58a, b).

In post-treatment MTT measurements, liproxstatin was able to attenuate loss of metabolic activity up to 4 hours after glutamate or erastin treatment (Figure 58c, d). Similar results were obtained by real-time xCELLigence measurements where liproxstatin preserved cell viability up to 6 hours after glutamate and erastin exposure (Figure 58e, f).

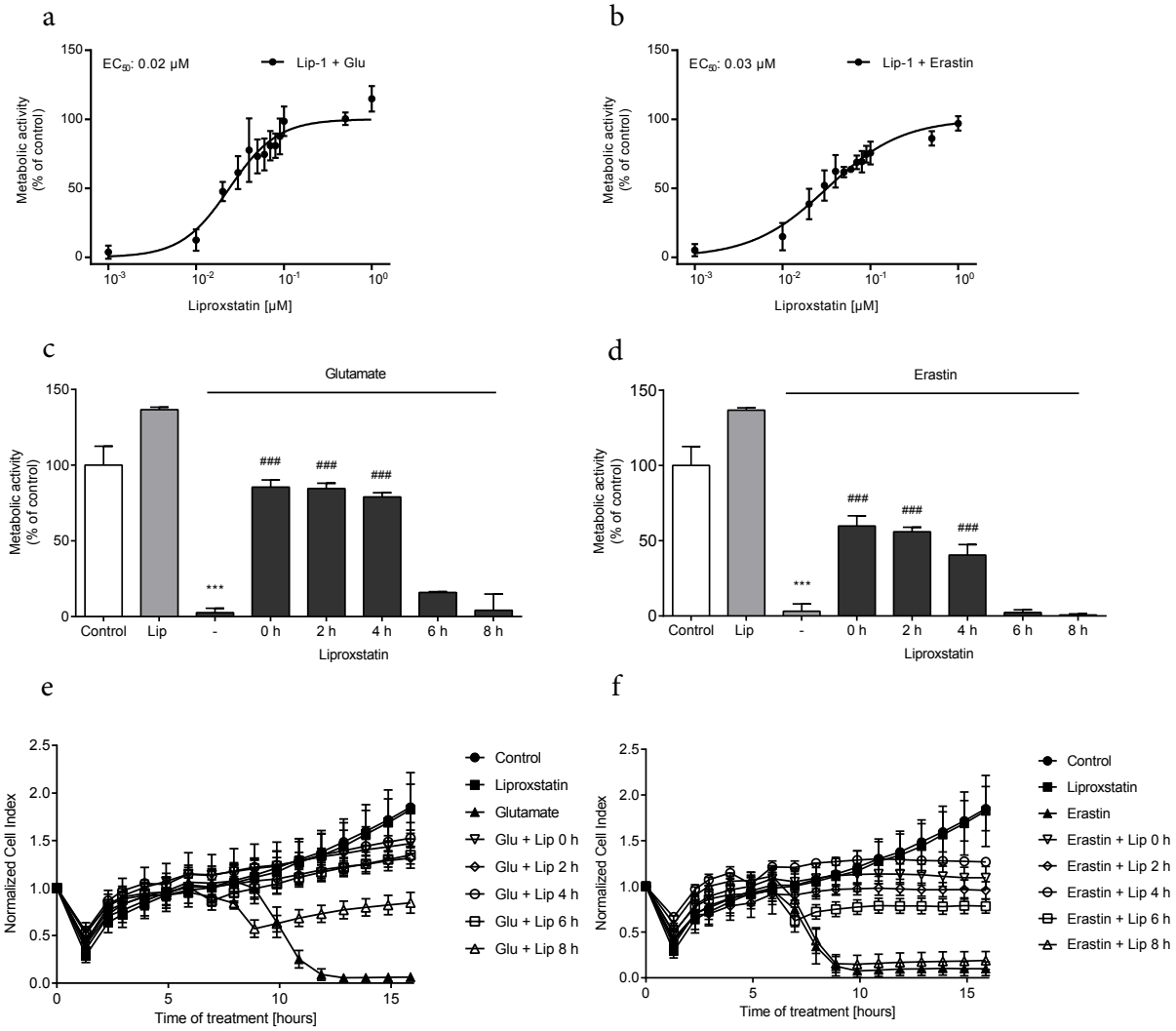

Figure 58. Liproxstatin attenuates glutamate- and erastin-induced toxicity

a, b: Concentration-response curves of liproxstatin upon glutamate (5 mM, 16-17 hours, **a**) and erastin (1 µM, **b**) treatment. Cell viability data were fitted from 0 for glutamate-treated control to 100 for highest protection at 1 µM Lip-1 (n=3/treatment condition). **c, d:** MTT assay reveals protection of liproxstatin (Lip, 150 nM) against glutamate (6 mM, 24 hours, **c**) or erastin (1 µM, **d**) toxicity until 4 hours post-treatment (n=8/treatment condition). **e, f:** Real-time impedance measurements confirm protection of liproxstatin (150 nM) against glutamate (6 mM, **e**) or erastin (1 µM, **f**) toxicity until 6 to 8 hours post-treatment (n=4-8/treatment condition). Data are shown as mean + or ± SD. ***p<0.001 compared to untreated control, ###p<0.001 compared to treated control (ANOVA, Scheffé's test).

In addition, liproxstatin rescued associated hallmarks of glutamate- and erastin-induced mitochondrial damage such as lipid peroxidation (Figure 59c, d), mitochondrial ROS formation (Figure 59e, f), loss of mitochondrial membrane potential (Figure 59g, h) and mitochondrial morphology (Figure 60a-c) in a concentration-dependent and GSH depletion-independent (Figure 59a, b) manner. In conclusion, these results strongly underline the assumption of shared pathways of oxytosis and ferroptosis including BID-mediated mitochondrial damage.

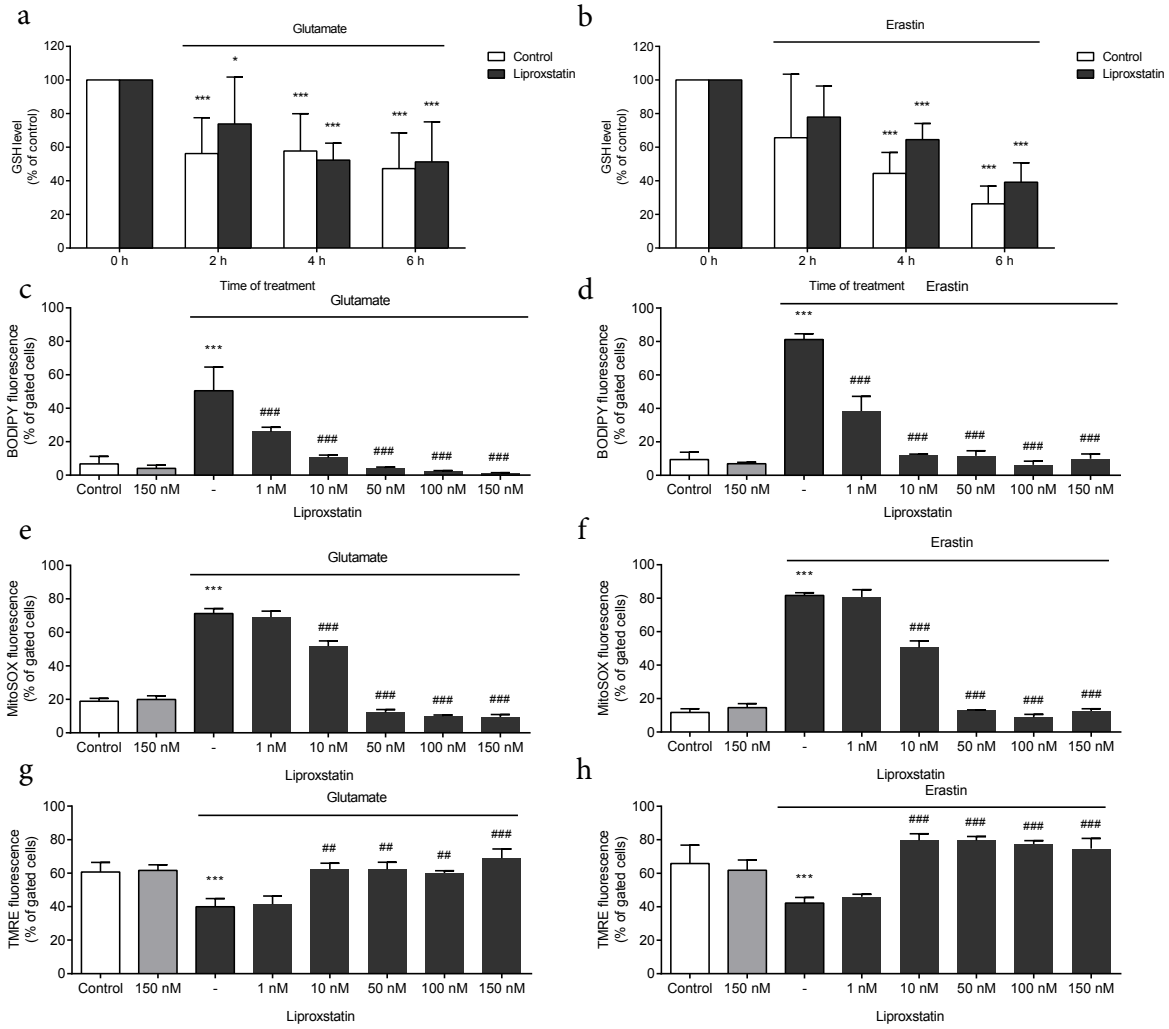

Figure 59. Liproxstatin preserves mitochondrial parameters

a, b: GSH analysis depicts rapid decrease after glutamate (6 mM, **a**) or erastin (1 µM, **b**) which could not be restored upon liproxstatin (150 nM) co-treatment (n=5-6/treatment condition). **c, d:** Glutamate (8 mM, 8 hours, **c**) or erastin (1 µM, **d**) treatment increase lipid peroxide production which is blocked by liproxstatin in a concentration-dependent manner (n=3/treatment condition). **e, f:** Glutamate (7 mM, 16 hours, **e**) or erastin (1 µM, **f**) treatment increases mitochondrial ROS production, which is blocked by co-treatment with liproxstatin in a concentration dependent-manner (n=3/treatment condition). **g, h:** TMRE FACS analysis shows concentration-dependent MMP restoration by liproxstatin after glutamate (8 mM, 16 hours, **g**) or erastin (1 µM, **h**) exposure (n=3/treatment condition). Data are shown as mean + SD. *p<0.05, **p<0.01, ***p<0.001 compared to untreated control, #p<0.05, ##p<0.01, ###p<0.001 compared to treated control (ANOVA, Scheffé's test).

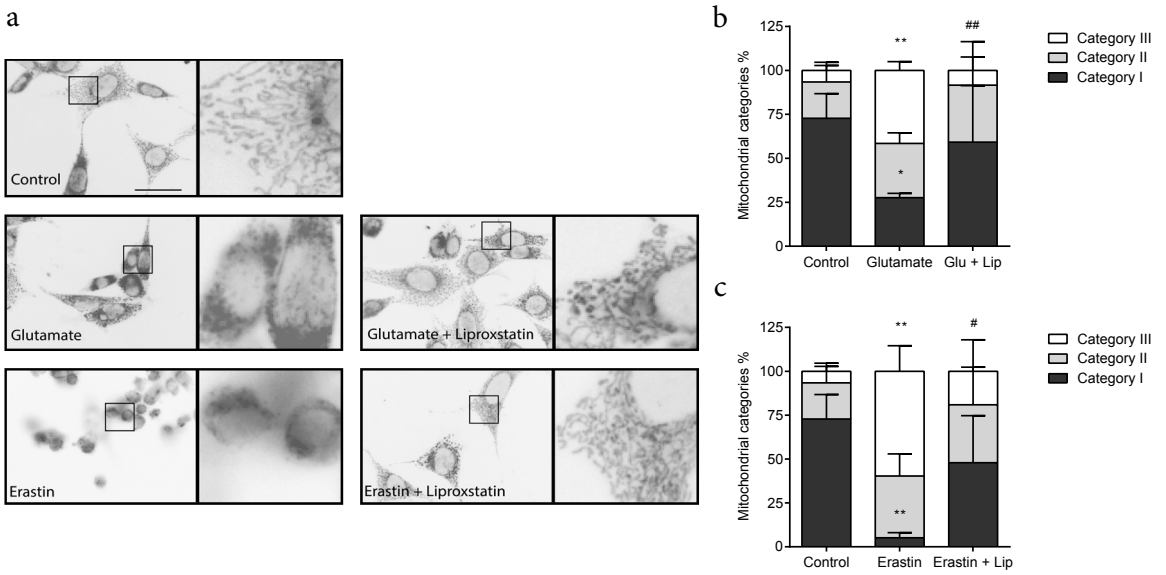

Figure 60. Liproxstatin protects mitochondrial morphology

a: Representative images (63x objective) show mitochondrial morphology with glutamate (4 mM, 16 hours, **j**) or erastin (0.5 µM, **k**) ± liproxstatin (150 nM). **b, c:** Classification of 500 cells (n=3) reveals liproxstatin-dependent reduction of glutamate- or erastin-induced mitochondrial fission. Scale bar 50 µm. Data are shown as mean + SD. *p<0.05, **p<0.01, ***p<0.001 compared to untreated control, $^{\#}$p<0.05, $^{\#\#}$p<0.01, $^{\#\#\#}$p<0.001 compared to treated control (ANOVA, Scheffé's test).

3.3 Characterization of RSL3-induced oxidative death in HT22 and MEF cells

3.3.1 Cell death induction by various isomeric RSL3 forms

Ferroptosis as an oxidative form of regulated necrotic cell death features GSH depletion, disrupted GPX4 redox defense and detrimental lipid ROS formation [38,41,90]. The actual findings so far identified mitochondrial damage in both models of oxidative glutamate toxicity and ferroptosis. Despite knowledge on the signaling pathways of ferroptosis is currently increasing, the particular role of mitochondrial damage requires more in-depth investigation in order to achieve effective treatment options targeting mitochondria. Therefore, in this study, the direct GPX4 inhibitor RSL3 (Figure 61) and its isomers were applied to induce ferroptosis in neuronal HT22 cells and MEFs.

For investigating cell toxicity of the different RSL3 isomers all four compounds were synthesized according to Yang et al. [211] (Figure 13) and their potency to induce cell death was evaluated by MTT assay and EC50 calculation. Yang and co-workers demonstrated that in BJ cells (human foreskin fibroblasts) expressing HRAS the *1S, 3R*-RSL3 isomer was significantly more active than the other isomers lacking selectivity for GPX4 [211].

In line with these previously published results, the EC50 values of 0.004 µM for *1S, 3R*-RSL3 and ~ 5-7 µM for the other three isomers were calculated indicating that the *1S, 3R*-RSL3 was at least 1000-fold more potent in HT22 WT cells than the structural isomers (Figure 62a-d). Apart from HT22 cells, *1S, 3R*-RSL3 was slightly less active in MEF cells and in primary mouse and rat cortical neurons with EC50 values of 0.2 µM, 1.5 µM and 7.2 µM, respectively (Figure 62i-k). Since BID was already identified as a key mediator of oxidative mitochondrial damage and subsequent cell death, the RSL3 isomers were tested in HT22 *Bid* KO cells. In these cells, *1S, 3R*-RSL3 was less potent to induce cell death and unspecific toxicity of the remaining isomers was observed within a similar concentration range as in HT22 WT cells (Figure 62e-h).

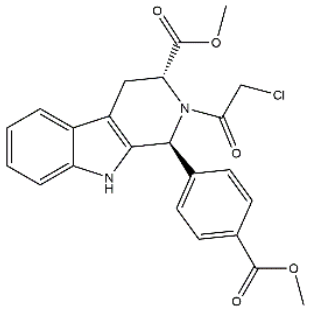

Figure 61. 1S, 3R-RSL3

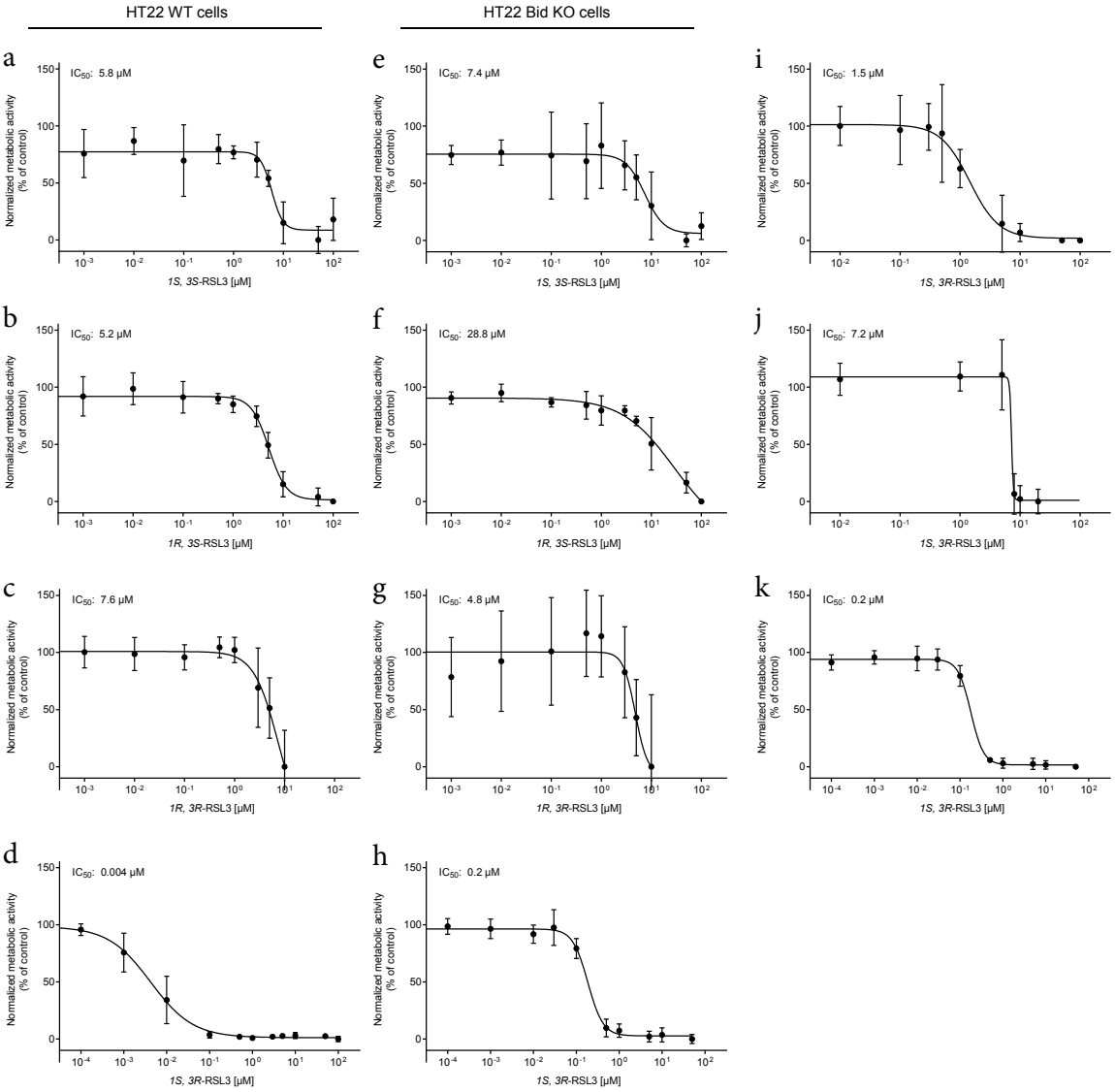

Figure 62. Dose-response curves of RSL3 isomers

a-d: Concentration-response curves in HT22 WT cells derived from MTT experiments depict strong cell death induction of *1S, 3R*-RSL3 and less toxic effects of the isomeric forms of RSL3 (16 hours treatment, n=3-5). **e-g:** Dose-response curves in HT22 *Bid* KO cells show reduced toxicity of *1S, 3R*-RSL3 and unspecific toxicity of the isomers in a similar range as in HT22 WT cells (16 hours treatment, n=3-5). **i, j, k:** Concentration-response curves of *1S, 3R*-RSL3 in primary mouse (**i**) and rat (**j**) cortical neurons and in MEF cells (**k**) (16 hours treatment, n=3-4). Data are shown as mean ± SD. and are fitted to 0-100 %.

As *1S, 3R*-RSL3 was described to directly inactivate GPX4 through covalent binding at its electrophilic chloroacetamide position [212], the effects of the corresponding des-chloro-derivative *1S, 3R*-RSL3-Cl were investigated. In line with the suggested mechanism comprising chlorine as an indispensable chemical feature of RSL3, the inactive *1S, 3R*-RSL3-Cl isoform did not affect cell viability assessed by FACS Annexin/PI and xCELLigence measurement in HT22 WT or MEF cells even when applied at high micromolar concentrations (Figure 63).

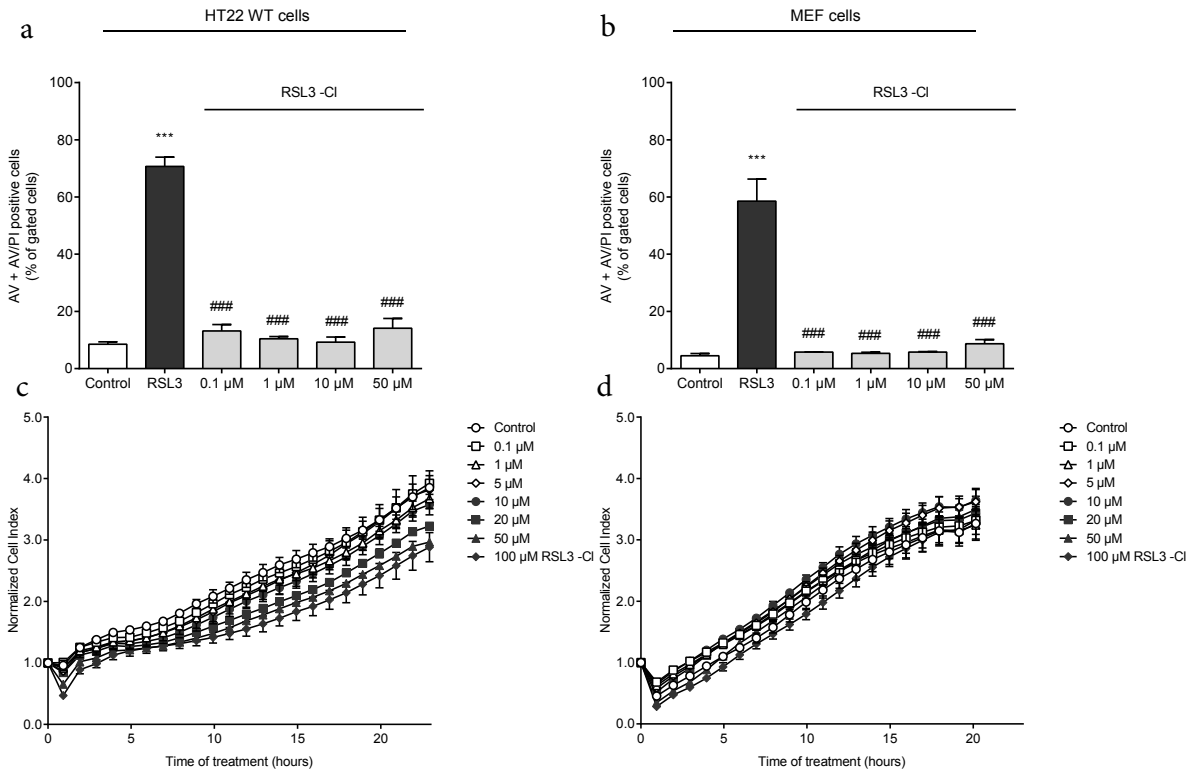

Figure 63. RSL3 -Cl does not induce cell death

a, b: Annexin/PI staining and subsequent FACS analysis reveals no cell death induction by *1S, 3R*-RSL3 –Cl (18 hours treatment) in HT22 (**a**) and MEF cells (**b**) (n=3/treatment condition) compared to *1S, 3R*-RSL3 (1 µM). **c, d:** xCELLigence measurements confirm that *1S, 3R*-RSL3 –Cl is non-toxic in HT22 (**c**) and MEF cells (**d**) (n=5-8/treatment condition). Data are shown as mean + or ± SD. ***p<0.001 compared to untreated control, ###p<0.001 compared to *1S, 3R*-RSL3 treated control (ANOVA, Scheffé's test).

3.3.2 RSL3 induces disruption of the cell's redox defense

To evaluate the effects of *1S, 3R*-RSL3 on GPX4 and the cell's redox defense, intracellular GSH levels were evaluated in HT22 cells after treatment with *1S, 3R*-RSL3 and in co-treatment together with ferrostatin (Figure 64a, b). Neither *1S, 3R*-RSL3 nor *1S, 3R*-RSL3 combined with ferrostatin affected GSH levels 2 to 8 hours after the respective treatment. Interestingly, a significant reduction of GPX4 protein levels was observed after 10 hours of *1S, 3R*-RSL3 exposure in HT22 and MEF cells but not with the inactive des-chloro-derivative (Figure 64c, d). In line with previous findings [90], these results indicate that RSL3 caused rapid proteolysis of inactive GPX4.

1S, 3R-RSL3 provokes sustained lipid peroxidation [212] as a result of GPX4 inhibition, autoxidation and subsequently increased 12/15-LOX activity [162,186,195]. Using BODIPY staining combined with time-course FACS analysis in *1S, 3R*-RSL3-induced ferroptosis in HT22 WT and MEF cells, increased lipid peroxidation was detected early after RSL3 exposure in HT22 and in MEF cells (Figure 64e, f) and was prevented by application of the BID inhibitor BI-6c9 and the commonly used ferroptosis inhibitors liproxstatin, deferoxamine and ferrostatin (Figure 64g, h).

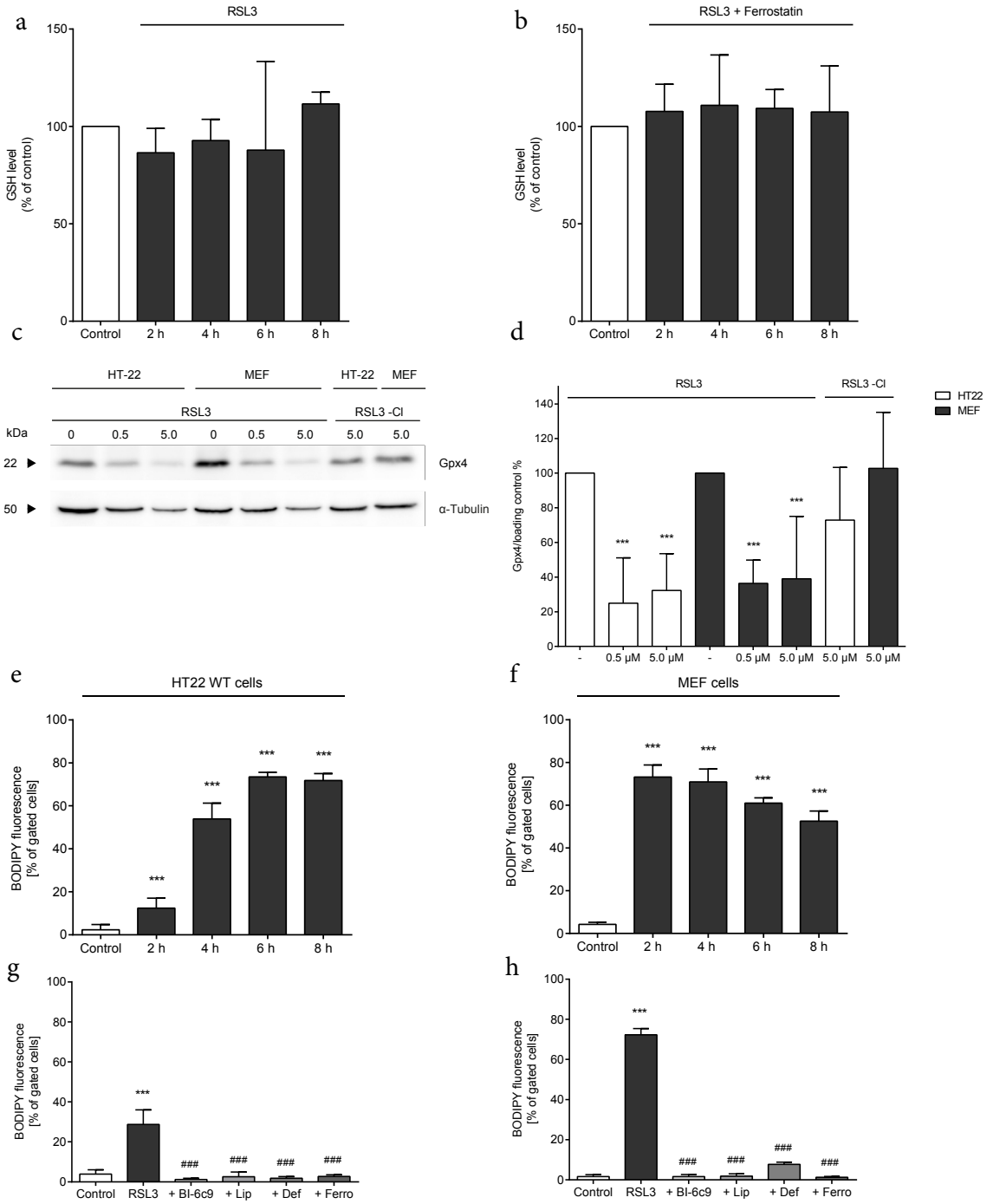

Figure 64. RSL3 impairs the cells' redox homeostasis

a, b: GSH measurements in HT22 cells reveal no alterations after 2-8 hours of RSL3 treatment (**a**, 1 µM) ± ferrostatin (**b**, 10 µM) (n=3/treatment condition, normalized to protein content of the respective sample). **c:** Representative Western blot shows pronounced loss of GPX4 protein levels after 10 hours of *1S, 3R*-RSL3 treatment (0.5 and 5.0 µM) in HT22 WT and MEF cells and sustained GPX4 levels after treatment with 5 µM *1S, 3R*-RSL3 -Cl. **d:** Quantification of Western blot as optical density compared to tubulin as loading control confirms a strong decrease of GPX4 protein upon *1S, 3R*-RSL3 treatment and no significant alteration with *1S, 3R*-RSL3 –Cl (n=3-4/treatment condition). **e, f:** BODIPY FACS analysis for measurement of lipid peroxide formation shows time-dependent increase in the fluorescence after *1S, 3R*-RSL3 (**e**: 100 nM, **f**: 1000 nM, 2-8 hours) exposure in HT22 WT (**e**) and MEF cells f) (n=4/treatment condition). **g, h:** BODIPY analysis reveals protection of BI-6c9 (10 µM) and ferroptosis inhibitors deferoxamine (10 µM), liproxstatin (200 nM) and ferrostatin (10 µM) upon *1S, 3R*-RSL3 (**g:** 50 nM, **h:** 1000 nM, 8 h) treatment in HT22 WT (**g**) and MEF cells (**h**) (n=4/treatment condition). All data are shown as mean + SD. ***p<0.001 compared to untreated control, ###p<0.001 compared to treated control (ANOVA, Scheffé's test).

3.3.3 BID inhibitor BI-6c9 and ferroptosis inhibitors abrogate *1S, 3R*-RSL3 induced cell death in HT22 and MEF cells

In order to further investigate *1S, 3R*-RSL3 (in the following referred to as *RSL3*) induced cell death (Figure 65a, d), loss of cell viability was assessed by means of MTT, depicting cell death 6 hours after RSL3 challenge in HT22 and MEF cells (Figure 65b, e). Real-time impedance measurements using the xCELLigence system demonstrated concentration-dependent induction of ferroptosis in both cell types (Figure 65c, f).

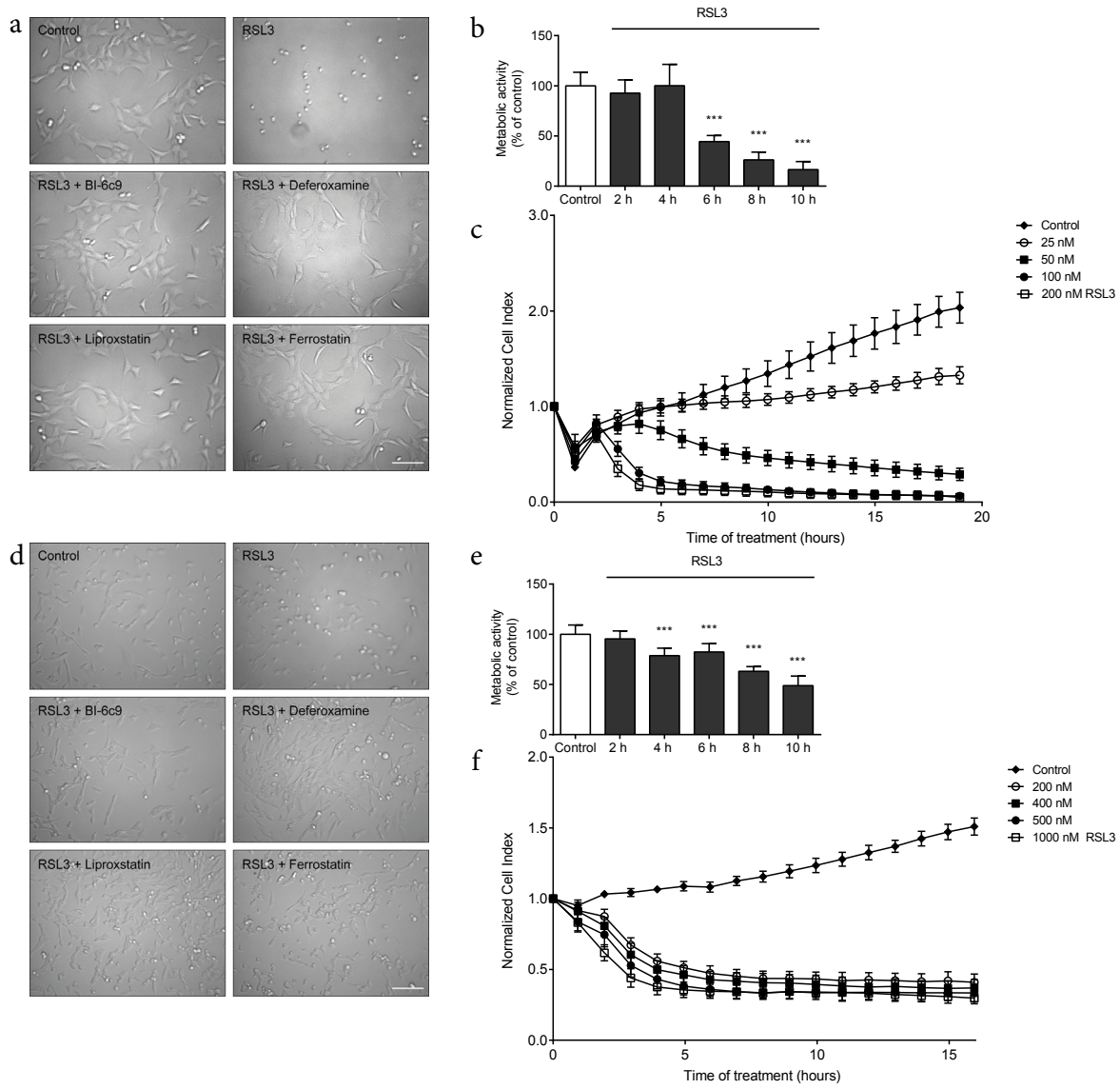

Figure 65. RSL3 toxicity is time- and concentration-dependent

a, d: Representative microscopic pictures of RSL3-treated HT22 (**a**, 24 hours treatment, 500 nM) and MEF cells (**d**, 1000 nM) ± BI-6c9, deferoxamine, ferrostatin (10 µM) or liproxstatin (200 nM). Scale bar 100 µm. **b, e:** MTT assays reveal time-dependent loss of metabolic activity of HT22 (**b**) and MEF cells (**e**) upon *1S, 3R*-RSL3 treatment (**b**: 100 nM, **e:** 200 nM, n=6-8/treatment condition). **c, f:** Real-time impedance measurements shows concentration-dependent toxicity of *1S, 3R*-RSL3 in HT22 (**c**) and MEF cells (**f**) (n=6-8/treatment condition). Data are shown as mean + or ± SD. ***p<0.001 compared to untreated control (ANOVA, Scheffé's test).

To evaluate the significance of BID activation in oxidative stress induced cell death in more detail, the well-established BID inhibitor BI-6c9 [13] was applied upon RSL3 treatment and its effect was compared to the commonly used ferroptosis inhibitors deferoxamine, liproxstatin and ferrostatin. XCELLigence experiments revealed that BI-6c9 preserved cell viability in HT22 and in MEF cells (Figure 66c, f) comparable to the ferroptosis inhibitors in conditions of RSL3 challenge. Most strikingly, BI-6c9 as well as liproxstatin, deferoxamine and ferrostatin rescued HT22 and MEF cells (Figure 66a, b, d, e) even when applied 4 to 6 hours after RSL3 treatment suggesting that the irreversible steps of cell death occurred downstream of early lipid ROS formation.

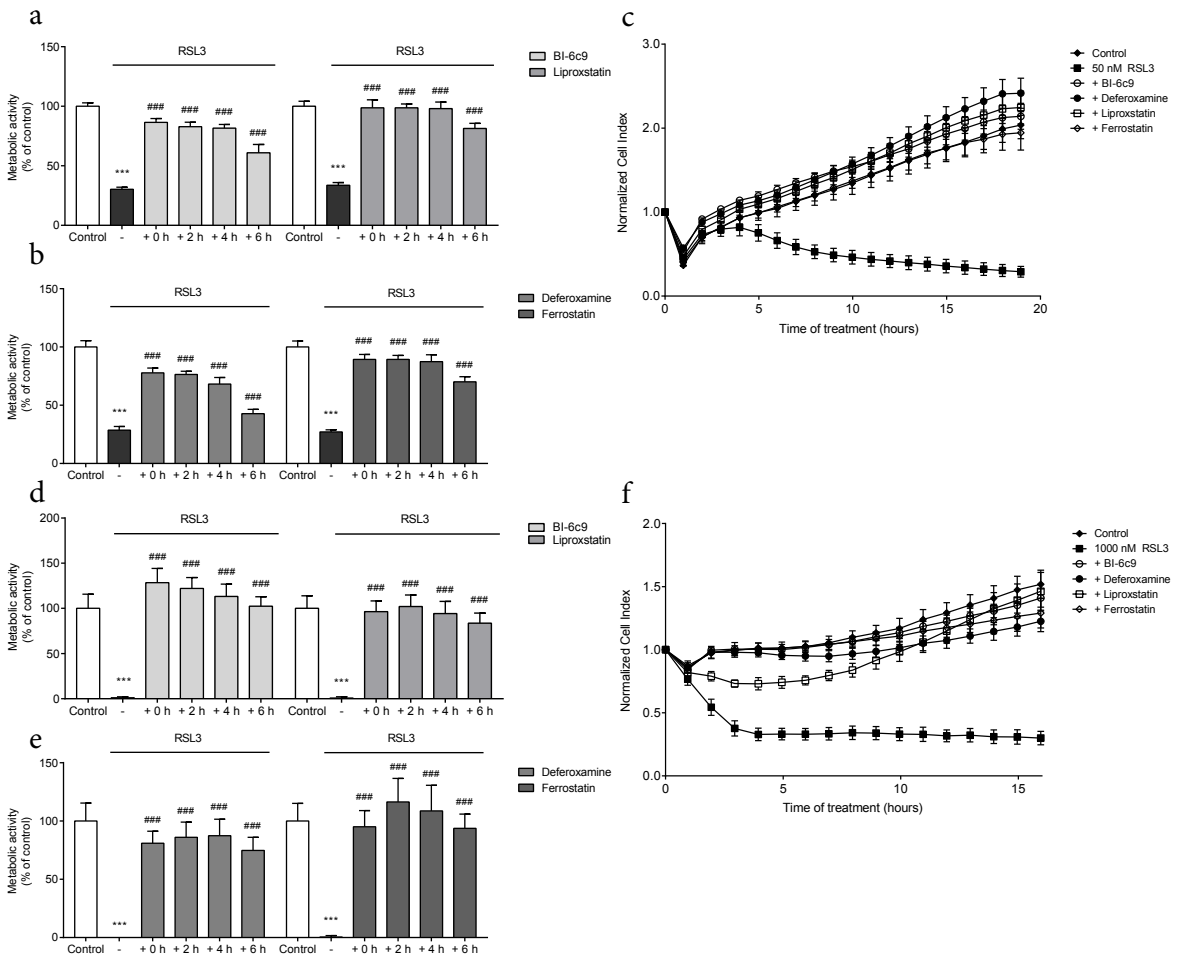

Figure 66. RSL3 toxicity is attenuated by BI-6c9 and ferroptosis inhibitors

a, b, d, e: MTT assays reveal protection of BID inhibitor BI-6c9 (10 µM, **a, d**) and ferroptosis inhibitors deferoxamine (10 µM, **b, e**), liproxstatin (200 nM, **a, d**) and ferrostatin (10 µM, **b, e**) upon **1S, 3R**-RSL3 (**a, b:** 100 nM, **d, e:** 200 nM, 24 h) challenge until 4 to 6 hours post-treatment in HT22 (**a, b**) and MEF cells (**d, e**) (n=6-8/treatment condition). **c, f:** Real-time impedance measurements show protective effects of BID inhibitor BI-6c9 (10 µM) and ferroptosis inhibitors deferoxamine (10 µM), liproxstatin (200 nM) and ferrostatin (10 µM) against *1S, 3R*-RSL3 treatment (**c:** 50 nM, **f:** 1000 nM) in HT22 (**c**) and MEF cells (**f**) (n=5-8/treatment condition). Data are shown as mean + or ± SD. ***p<0.001 compared to untreated control, ###p<0.001 compared to treated control (ANOVA, Scheffé's test).

3.3.4 RSL3 impairs mitochondrial morphology and function

To shed more light on the specific order of events in the induction of RSL3-induced toxicity, FACS measurements were utilized to study mitochondrial ROS formation and loss of mitochondrial membrane potential in HT22 and MEF cells (Figure 67a-h). Using MitoSOX staining and FACS, mitochondrial ROS was evaluated which constantly rose starting at 2 hours after RSL3 exposure and was abolished with the applied inhibitors. Further mitochondrial damage, for instance loss of mitochondrial membrane potential, was assessed by TMRE staining indicating vanishing membrane potential with effect from 4 hours after RSL3 challenge. Consistent with other experiments, the inhibitors were able to completely abolish RSL3-induced mitochondrial damage and to preserve the mitochondrial membrane potential. Functionally, RSL3 provoked strong deficiency in ATP production after 4 hours of treatment (Figure 67i, j). In conclusion, these data imply a chronological order of stepwise lipid peroxidation, mitochondrial ROS formation and succeeding dysfunction of ATP synthesis owing to the loss of mitochondrial membrane potential upon RSL3 treatment.

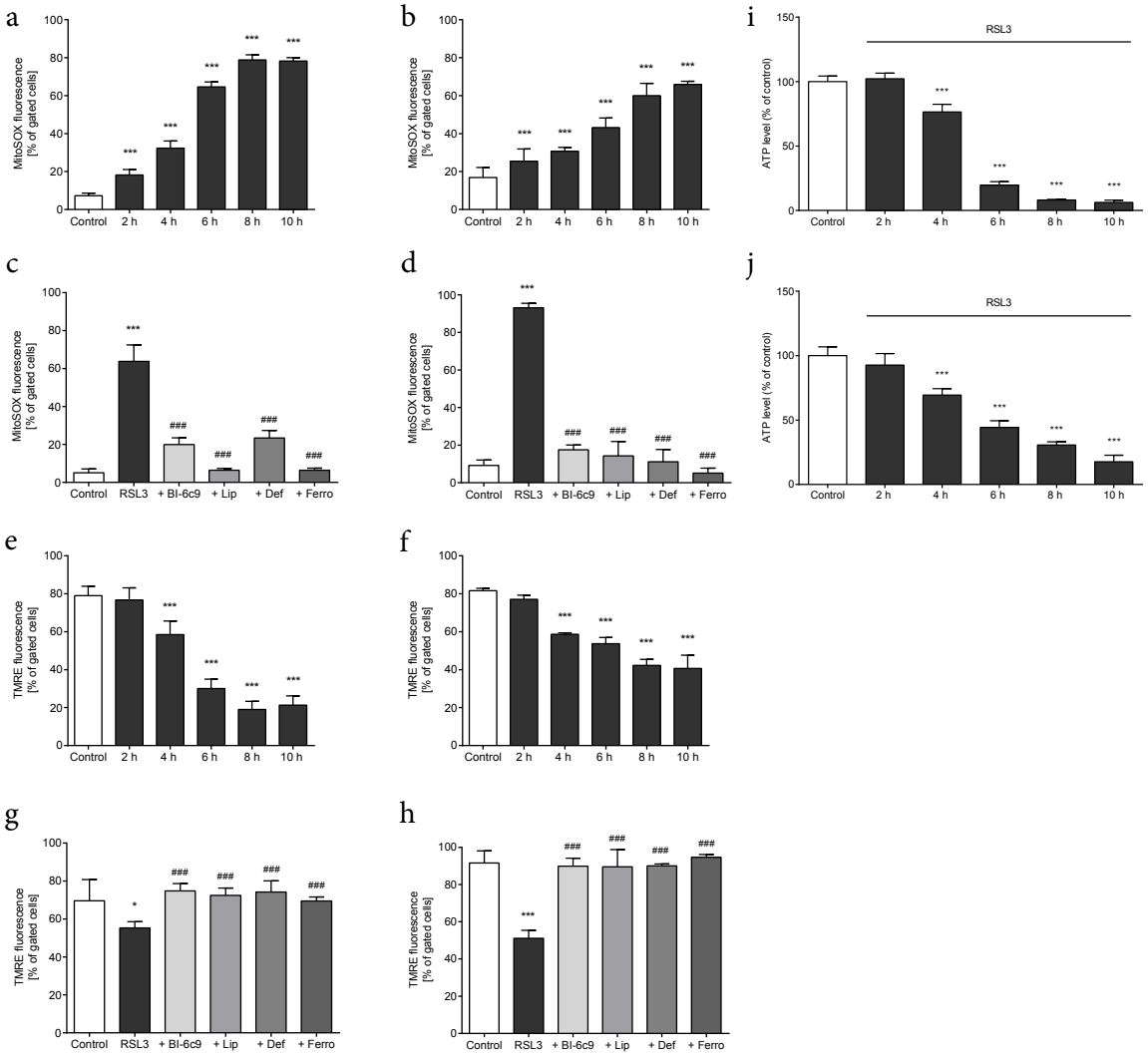

Figure 67. RSL3 induces mitochondrial impairment

a-d: MitoSOX staining shows time-dependent ROS formation after RSL3 exposure (**a:** 100 nM, **b:** 1000nM) and protection of BI-6c9 (10 µM) and ferroptosis inhibitors deferoxamine (10 µM), liproxstatin (200 nM) and ferrostatin (10 µM) upon RSL3 treatment (**c:** 50 nM, **d:** 1000 nM, 6 h) in HT22 (**a, c**) and MEF cells (**b, d**). **e-h:** TMRE staining for mitochondrial membrane potential shows time-dependent loss after RSL3 exposure (**e:** 100 nM, **f:** 1000 nM) and protection of BI-6c9 and ferroptosis inhibitors upon RSL3 treatment (**g:** 50 nM, **h:** 1000 nM, 16 h) in HT22 (**e, g**) and MEF cells (**f, h**) (n=4/treatment condition). **i, j:** ATP assay illustrates time-dependent loss of ATP levels in HT22 (**i**) and MEF (**j**) cells after RSL3 challenge (**i:** 100 nM, **j:** 500 nM) (n=8/treatment condition). Data are shown as mean + SD. ***p<0.001 compared to untreated, ###p<0.001 compared to treated control (ANOVA, Scheffé's test).

3.3.5 AIF executes final cell death in RSL3-induced ferroptosis

In order to investigate death signaling downstream of RSL3-induced mitochondrial damage, the potential involvement of AIF was addressed. Assuming that AIF mediates mitochondrial damage induced death signaling similar to previous findings in glutamate-induced oxytosis, AIF protein levels were depleted by siRNA and cell death measured by means of MTT and xCELLigence. Knockdown of AIF was confirmed using Western blot (Figure 68a, b). In line with earlier studies demonstrating a role for AIF in oxidative cell death by loss of GPX4 [162], considerable protection against RSL3-induced cell death was detected by AIF gene silencing using siRNA in the HT22 cells (Figure 68c, d). The results confirmed that silencing AIF provides protection against mitochondrial damage in this model of ferroptosis. The observed effect may be attributed to direct loss of death-mediating AIF or to enhanced mitochondrial stability through preconditioning effects by complex I degradation as demonstrated by Öxler et al. [23,24,133].

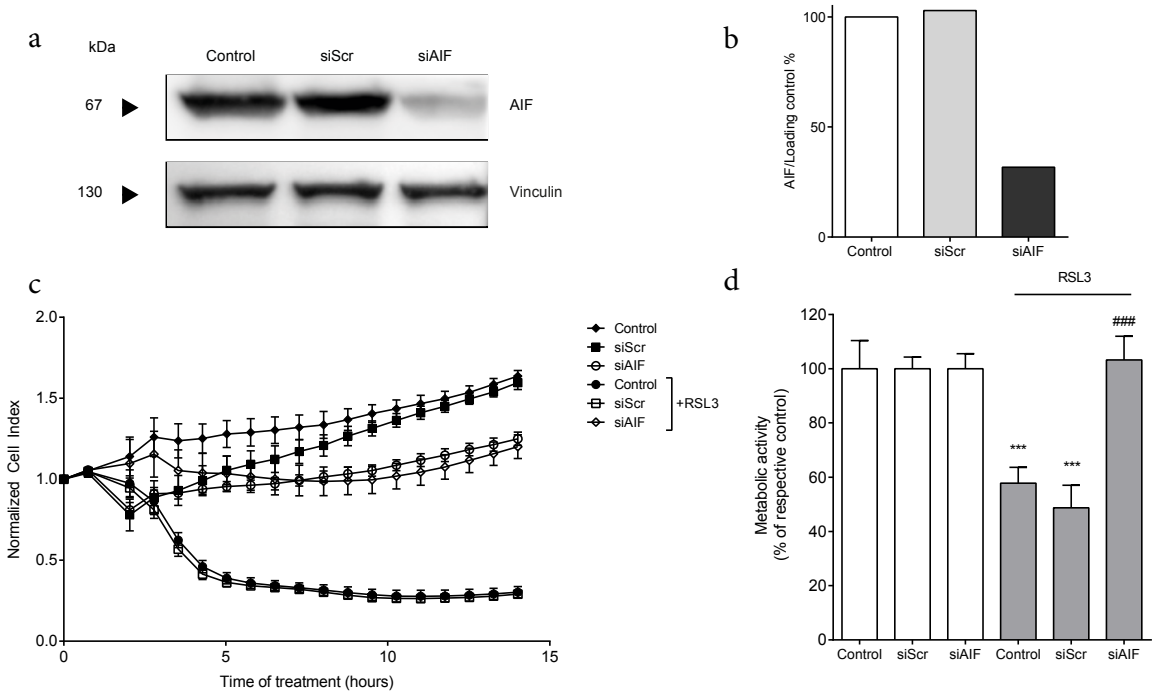

Figure 68. AIF mediates mitochondrial damage induced cell death signals

a: Representative Western blot (**a**) and quantification (**b**) confirm strong knockdown of AIF protein with siAIF (50 µg protein, 72 hours transfection, 20 nM siRNA) in HT22 cells compared to control siRNA. Vinculin was used as loading control. **c:** Real-time impedance measurements demonstrate long-term protection of cell viability of HT22 cells by siAIF (72 hours, 20 nM) against *1S, 3R*-RSL3 challenge (200 nM, n=4-6/treatment condition) compared to control siRNA. **d**: MTT assay of siAIF transfected HT22 cells (72 hours, 20 nM) confirms strong protection against *1S, 3R*-RSL3 treatment (200 nM, 5 hours, n=6/treatment condition) compared to control siRNA. Data are shown as mean + or ± SD. ***p<0.001 compared to untreated control, ###p<0.001 compared to treated control (ANOVA, Scheffé's test).

3.4 Mitochondrial antioxidant MitoQ abrogates GPX4-dependent ferroptosis

3.4.1 MitoQ abrogates RSL3-toxicity

Mitochondrial damage including the organelle's deformation, loss of membrane integrity and extensive ROS formation is considered as *the point of no return* in oxidative stress induced cell death [126] which is essentially why reduction of ROS formation at the mitochondrial site should prevent oxidative cell death. For the purpose of explicitly blocking mitochondrial ROS formation, the potential protective effects of the mitochondria-targeted ubiquinone derivative MitoQ [94] were analyzed in this thesis.

In order to analyze the effects of MitoQ on cell viability MTT, xCELLigence impedance and Annexin/PI FACS measurements were performed. MitoQ preserved cell viability in HT22 and MEF cells in a dose-dependent manner; however, high concentrations of MitoQ alone induced a pronounced reduction in the cell's metabolic activity (Figure 69a, b) and little but significant cell death (Figure 69e, f). Remarkably, protective effects were abolished when HT22 or MEF cells were treated with MitoQ combined with the glycolytic inhibitor 2-desoxyglucose (2-DG) (Figure 69g, h) suggesting that a shift from mitochondrial oxidative phosphorylation towards glycolysis is needed for the observed protective effect. FACS analysis revealed that high doses of MitoQ completely eliminate lipid peroxidation (Figure 70a, b) as well as mitochondrial ROS formation (Figure 70c, d), and preserve the mitochondrial membrane potential (Figure 70e, f) in HT22 and MEF cells exposed to RSL3.

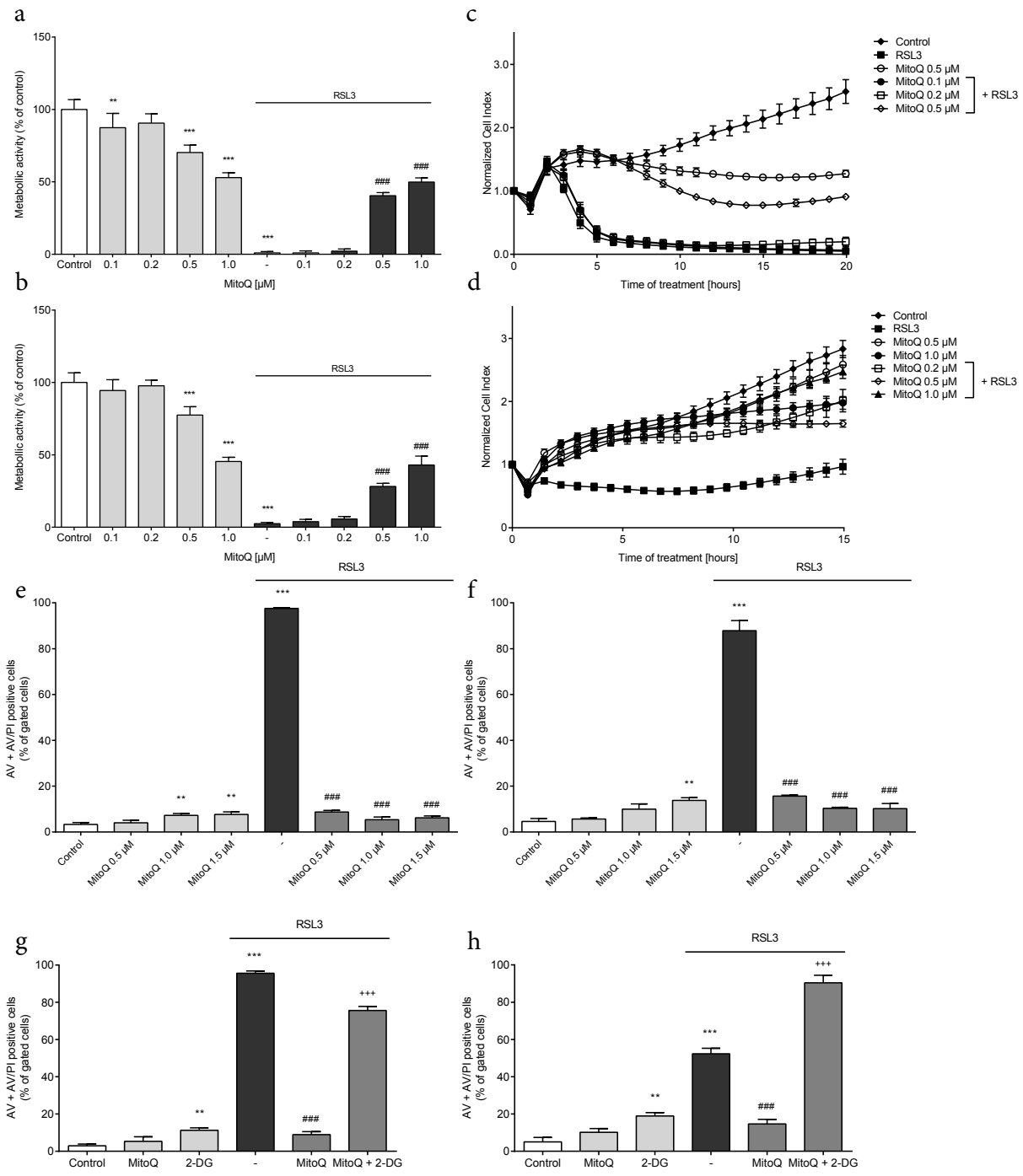

Figure 69. MitoQ abrogates RSL3-induced cell death

a, b: MTT assay reveals dose-dependent protection of MitoQ against RSL3 treatment (**a:** 200 nM, **b:**500 nM) in HT22 (**a**) and MEF cells (**b**) (16 hours treatment, n=8/treatment condition). **c, d:** xCELLigence real-time measurements illustrate concentration-dependent protection by MitoQ upon RSL3 challenge (**c**: 200 nM, **d:** 1000 nM, n=4-6/treatment condition) in HT22 (**c**) and MEF cells (**d**). **e, f:** Annexin/PI FACS analysis demonstrates strong inhibition of cell death by MitoQ upon RSL3 challenge (**e:** 400 nM, **f:** 800 nM, 16 hours treatment, n=3/treatment condition) in HT22 (**e**) and MEF cells (**f**). **g, h:** Annexin/PI FACS analysis reveals loss of protection by MitoQ (1 µM) upon 2-desoxyglucose (2-DG) co-treatment (150 mM) against RSL3 challenge (**g:** 500 nM, **h:** 1000 nM, 16 hours treatment) in HT22 (**g**) and MEF cells (**h**) (n=3/treatment condition). Data are shown as mean + or ± SD. **p<0.01 , ***p<0.001 compared to untreated control, $^{###}$p<0.001 compared to treated control, $^{+++}$p<0.001 compared to MitoQ+RSL3 treated condition (ANOVA, Scheffé's test).

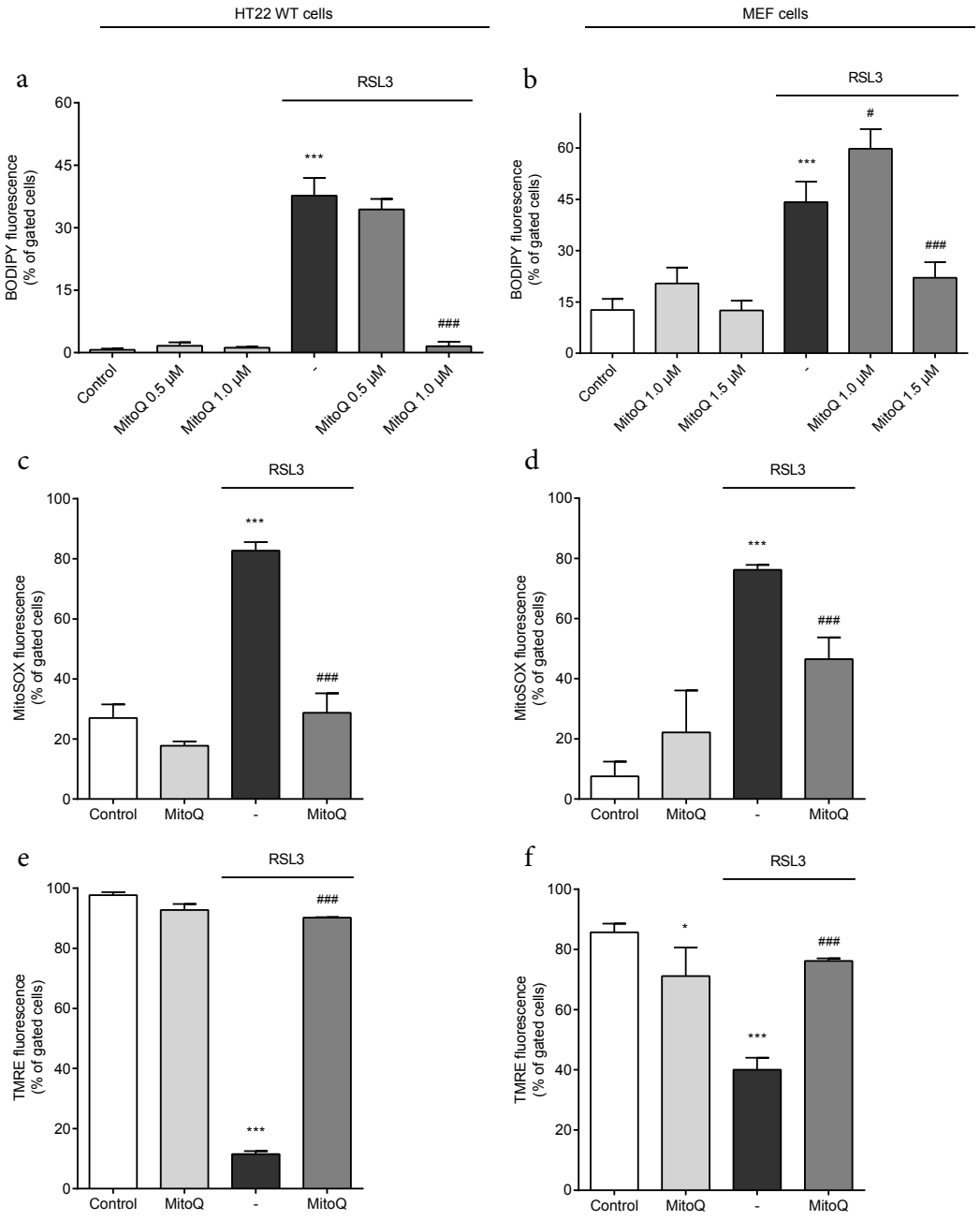

Figure 70. MitoQ abolishes RSL3 toxicity

a, b: BODIPY 581/591 staining and subsequent FACS analysis for measurement of lipid peroxide formation shows protection by high MitoQ concentrations (HT22: 1.0 µM, MEF: 1.5 µM) after RSL3 exposure (**a:** 200 nM, **b:** 1500 nM, 6 hours, n=3/treatment condition) in HT22 cells (**a**) and MEF cells (**b**). **c, d**: MitoSOX staining and subsequent FACS analysis for mitochondrial ROS formation shows a reduction of the fluorescence with MitoQ (0.5 µM) after RSL3 treatment (**c**: 200 nM, **d:** 700 nM, 16 hours, n=3/treatment condition) in HT22 cells (**c**) and MEF cells (**d**). **e, f:** TMRE FACS analysis for mitochondrial membrane potential demonstrates that MitoQ (0.5 µM) preserves the MMP after RSL3 (**e:** 200 nM, **f:** 700 nM, 16 hours, n=3/treatment condition) in HT22 cells (**e**) and MEF cells (**f**). Data are shown as mean + or ± SD. *p<0.05, ***p<0.001 compared to untreated control, $^{\#}$p<0.05, $^{\#\#\#}$p<0.001 compared to treated control (ANOVA, Scheffé's test).

3.4.2 MitoQ preserves mitochondrial morphology and function through a glycolytic shift

In order to further address mitochondrial changes due to RSL3-induced oxidative stress, mitochondrial morphology of HT22 and MEF cells stained with LifeAct-GFP for actin and MitoTracker DeepRed for mitochondria was studied after RSL3 exposure (Figure 71). Mitochondrial fragmentation and accumulation around the nucleus was observable after 5 hours in response to RSL3 treatment shown by quantification according to the recently established classification system [72,126]. Mitochondrial shape judged as 3D mitochondrial reconstructions of stacked confocal images after RSL3 challenge revealed a pronounced loss of category I healthy cells and an equivalent increase in category III cells after 5 hours (Figure 71). This is in line with the above-mentioned rise in mitochondrial ROS formation and loss of mitochondrial membrane potential as an additional indicator of mitochondrial damage. Remarkably, MitoQ alone induced mitochondrial fragmentation quantified as an increase in category II but did not harm the cells as judged by the cell shape and cell viability measurements. Conversely, in combination with RSL3 MitoQ reduced strong mitochondrial damage and prevented cell damage.

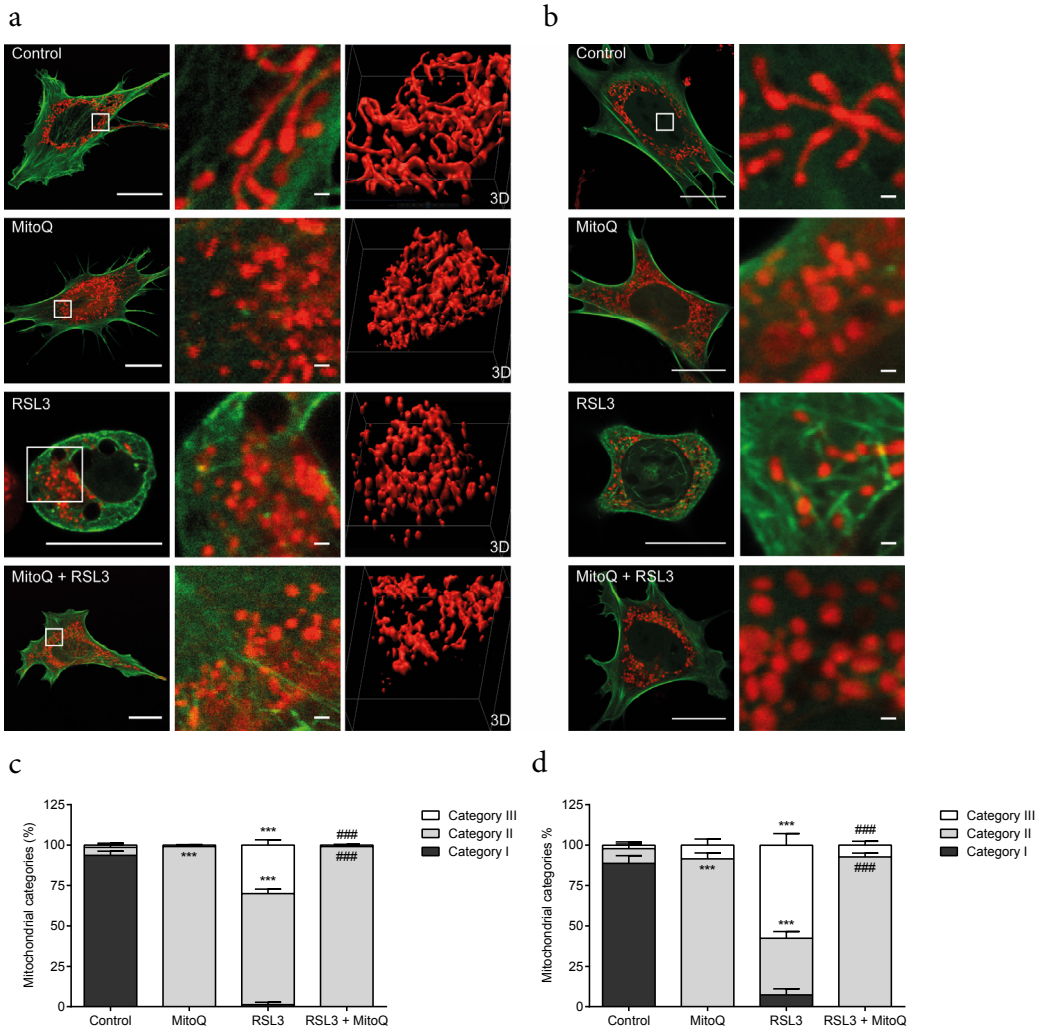

Figure 71. Mitochondrial morphology is preserved by MitoQ

a, b: Representative confocal microscopy images (63x objective) and 3D mitochondrial reconstructions of HT22 (**a**) and MEF cells (**b**) stained with LifeAct-GFP and MitoTracker DeepRed (200 nM) with RSL3 (**a:** 250 nM, **b:** 500 nM, 5 h) ± MitoQ (1.0 µM, 5 h). Scale bars: 20 µm, zoom 1 µm. **c, d:** Quantification of 500 cells demonstrates time-dependent mitochondrial fission and translocation to the nucleus in HT22 (**c**) and MEF (**d**) cells after RSL3 exposure (n=3/treatment condition). MitoQ treatment reveals strong shift to category II when applied alone but rescues mitochondrial phenotype after RSL3 treatment. Data are shown as mean + SD. ***p<0.001 compared to untreated control, $^{###}$p<0.001 compared to treated control (ANOVA, Scheffé's test).

To characterize RSL3 and MitoQ treatment functionally, Seahorse XF96 measurements were performed and mitochondrial respiration (oxygen consumption rate, OCR) and glycolysis (extracellular acidification rate, ECAR) were assessed. In line with the detected mitochondrial damage upon RSL3 treatment, both OCR and ECAR were concomitantly reduced in HT22 cells over time (Figure 72). However, cells did not die completely as spare respiratory capacity was still present after injection of the uncoupling agent FCCP. Interestingly, MitoQ reduced mitochondrial respiration to such an extent that the cells no longer reacted to the uncoupling agent FCCP suggesting no spare respiratory capacity, however, cells shifted their energy metabolism towards ATP production through glycolysis to meet their energy demands. In sharp contrast, RSL3 treated cells could not increase the glycolytic activity suggesting their energy metabolism to be substantially harmed. In conclusion, RSL3 provokes a tremendous disruption of mitochondrial morphology and function, which can be reduced to a non-fatal state by MitoQ.

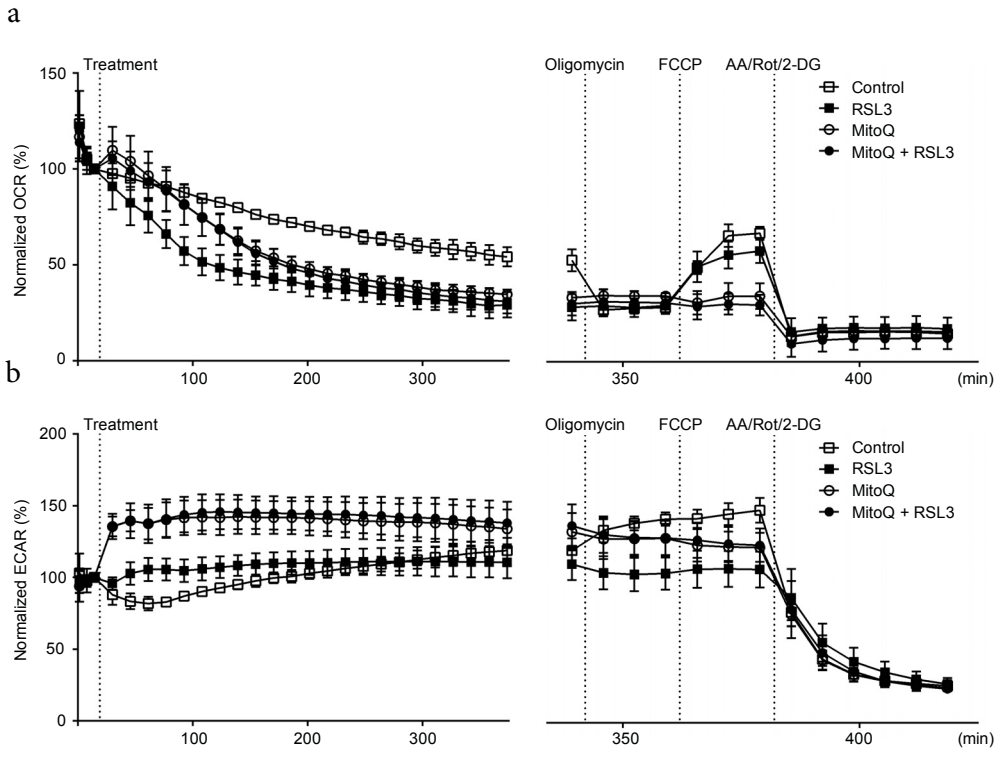

Figure 72. MitoQ protects against RSL3 by shift to glycolysis

a, b: Normalized Seahorse measurements show inhibition of mitochondrial respiration (**a**, OCR) and no further decrease with oligomycin by RSL3 (1.5 µM) or MitoQ (1 µM) in HT22 cells compared to untreated control. After FCCP injection, MitoQ treated cells do not exhibit a spare respiratory capacity compared to control or RSL3 treated cells. ECAR measurements (**b**) as an indicator for glycolytic activity reveal glycolytic switch with MitoQ ± RSL3 in HT22 cells and reduced glycolysis with RSL3 alone. Data are shown as mean ± SD.

3.4.3 MitoQ does not prevent tBID-induced toxicity

In order to further define the scope of protection by MitoQ, tBID toxicity was investigated, which directly mediates mitochondrial membrane disruption and release of death-promoting factors such as Cytc and AIF. For this purpose, active tBID was overexpressed in HT22 cells and cell viability monitored by xCELLigence measurement (Figure 73). Here, tBID induced a significant reduction in cell viability, and MitoQ co-treatment could not prevent tBID toxicity. In fact, MitoQ increased the toxic effects of tBID expression. These findings suggested that upon tBID challenge mitochondrial ROS formation is not the major cause of cell death and that MitoQ acts upstream of BID-mediated mitochondrial release of pro-apoptotic factors. In contrast, the BID inhibitor BI-6c9 was shown to prevent tBID-induced cell death [103]suggesting that it was able to bind to tBID and prevent cell death at advanced stages of death signaling, where mitochondrial antioxidants are not effective anymore.

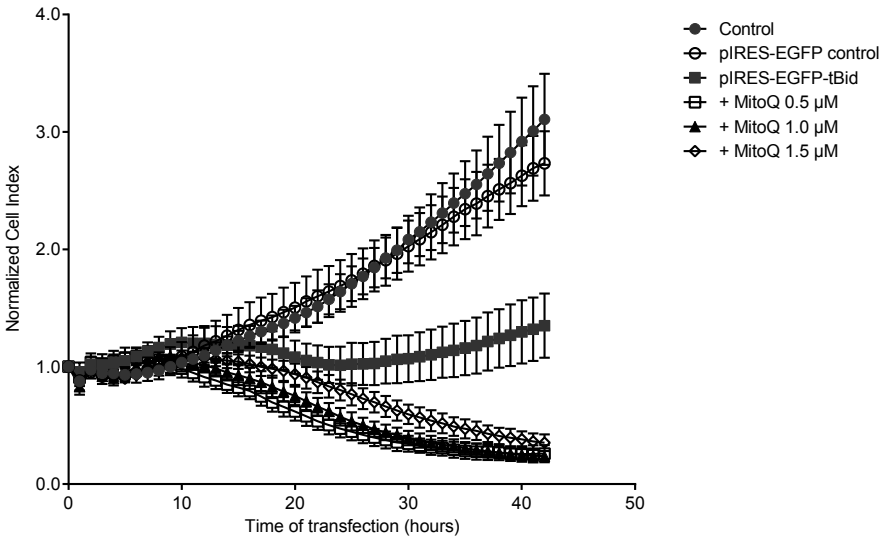

Figure 73. MitoQ does not prevent tBID toxicity

XCELLigence measurement demonstrates significant reduction of cell viability after tBID overexpression (pIRES-EGFP-tBid: 0.3 µg DNA/well) in HT22 cells, which cannot be circumvented by MitoQ co-treatment (n=5-8/treatment condition). Data are shown as mean ± SD.

3.5 Elucidating the structure of BID by crystallization: towards structure-based design of BID inhibitors

Programmed cell death is associated with different human pathologies, such as neurodegenerative diseases (AD or PD) and ischemic brain damage. If brain tissue is degenerating, this ultimately results in cognitive impairment and physical disabilities. As demonstrated in the first part of this thesis, neuronal cell death is tightly connected to BID transactivation and, therefore, impeding BID function should be an auspicious chance to protect brain tissue in neurodegenerative processes.

Functional BID studies and the development of novel small molecule BID inhibitors to provide therapeutic perspectives could be facilitated by structure-guided ligand design requiring high-resolution protein structures. So far, two solution NMR structures for BID have been identified [26,120], however, high-resolution X-ray data are still desirable for precise *in silico* modeling. In previous attempts [132], the expression and purification of a variety of recombinant Bid constructs was established and first crystallization conditions were identified providing the starting point for further optimization. In this work, several modified Bid constructs (Table 44) were cloned with either GST- or His_6-tag, purified and subjected to vapor diffusion crystallization in order to obtain crystals for x-ray structural analysis. As the previously published NMR structures of BID suggested 8 core α-helices and additional mobile regions, such as the flexible intramolecular loop and a flittering N-terminus, in constructs Bid 1 and Bid 3 these regions were removed (Figure 74) to potentially facilitate crystallization. Further constructs contained CCSS mutations to reduce the chance of GSH binding to the thiol-containing cysteines during the purification process.

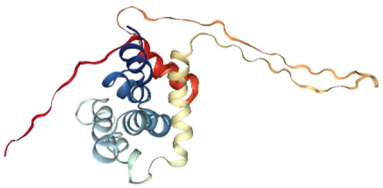

```
Bid22          MDSEVSNGSGLGAEHITDLLVFGFLQSSGCTRQELEVLGRELPVQAYWEADLEDELQTDGSQAS
Bid22 CCSS     MDSEVSNGSGLGAEHITDLLVFGFLQSSGSTRQELEVLGRELPVQAYWEADLEDELQTDGSQAS
Bid 1 12-47                GSGAEHITDLLVFGFLQSSGCTRQELEVLGRELPVQAY----------
Bid 3 13-47                GS---AEHITDLLVFGFLQSSGCTRQELEVLGRELPVQAY----------
Bid 3 CCSS 13-47           GS---AEHITDLLVFGFLQSSGSTRQELEVLGRELPVQAY----------

Bid22                      RSFNQGRIEPDSESQEEIIHNIARHLAQIGDEMDHNIQPTLVRQLAAQFMNGSLSEEDKR
Bid22 CCSS                 RSFNQGRIEPDSESQEEIIHNIARHLAQIGDEMDHNIQPTLVRQLAAQFMNGSLSEEDKR
Bid 1 12-47                ----------SQEEIIHNIARHLAQIGDEMDHNIQPTLVRQLAAQFMNGSLSEEDKR
Bid 3 13-47                ----------SQEEIIHNIARHLAQIGDEMDHNIQPTLVRQLAAQFMNGSLSEEDKR
Bid 3 CCSS 13-47           ----------SQEEIIHNIARHLAQIGDEMDHNIQPTLVRQLAAQFMNGSLSEEDKR

Bid22                      NCLAKALDEVKTAFPRDMENDKAMLIMTMLLAKKVASHAPSLLRDVFHTTVNFINQNLFS
Bid22 CCSS                 NSLAKALDEVKTAFPRDMENDKAMLIMTMLLAKKVASHAPSLLRDVFHTTVNFINQNLFS
Bid 1 12-4                 NCLAKALDEVKTAFPRDMENDKAMLIMTMLLAKKVASHAPSLLRDVFHTTVNFINQNLFS
Bid 3 13-47                NCLAKALDEVKTAFPRDMENDKAMLIMTMLLAKKVASHAPSLLRDVFHTTVNFINQNLFS
Bid 3 CCSS 13-47           NSLAKALDEVKTAFPRDMENDKAMLIMTMLLAKKVASHAPSLLRDVFHTTVNFINQNLFS

Bid22                      YVRNLVRNEMD
Bid22 CCSS                 YVRNLVRNEMD
Bid 1 12-47                YVRNLVRNEMD
Bid 3 13-47                YVRNLVRNEMD
Bid 3 CCSS 13-47           YVRNLVRNEMD
```

Figure 74. Mouse Bid NMR structure (1DDB) and alignment of constructs for crystallization

3.5.1 Initial Bid 1 and Bid 3 purification

Initially, Bid 1 and Bid 3 GST-tagged constructs were transformed and expressed in *Escherichia coli* strain Rosetta2 (DE3) until a suitable optical density was achieved. Subsequently, IPTG was added to induce protein expression for 5 hours before harvesting bacteria. The expression of high amounts of the respective protein construct was verified by SDS-PAGE and Coomassie staining of the total bacterial lysate (TL). Purification of GST-tagged proteins was performed in a two-step chromatography process using the ÄKTA prime plus system. In the first step, proteins were pre-cleaned by GSH affinity chromatography once or twice depending on the amount of total bacterial lysate followed by SDS-PAGE and Coomassie staining to evaluate the resulting protein purity. In addition, the flow-through (FT) was investigated to estimate loss of recombinant BID protein owing to limited column binding capacity. Thereafter, GST-tags were cleaved using thrombin and controlled by SDS-PAGE. In a second step, gel size exclusion chromatography was performed in order to remove cleaved GST-tags and to obtain homogenous protein solutions. Finally, the protein was concentrated on 3 kDa cut-off Amicon filters to a desired concentration of 5-15 mg/mL and sterile-filtered to prevent microbial growth during crystallization. To further investigate the purified proteins, the final protein solution was subjected to MALDI-TOF analysis.

Bid3-GST was purified in two fractions by GSH-affinity chromatography (Figure 76a-d). Chromatograms and corresponding SDS-PAGE analysis revealed adequate protein content in the total lysate (TL), a sufficient initial enrichment of protein in the elution fractions 37-41 and 33-37, respectively, and only a slight loss of protein in the flow-through (FT) due to limited binding capacity of the column. The elution fractions 37-41 and 33-37 were pooled and subjected to thrombin-cleavage (TC) with a cleavage rate of ~ 60-70 %. After concentration with 3 kDa Amicon cut-off filters and subsequent size exclusion gel chromatography (Figure 76a, b) elution fractions 34-39 were pooled as they showed pure Bid3 protein after SDS-gel electrophoresis. Fractions 24-29 containing uncleaved Bid3-GST and GST were discarded. The protein solution was again concentrated to a final concentration of 9.5 mg/mL and sterile-filtered. MALDI-TOF analysis (Figure 76c) revealed multiple and sub-divided split peaks which may be due to partial protein degradation (~ 13-14 kDa, Figure 76d) and GSH disulfide adducts to the proteins' cysteine residues (Δ 307 Da). To prevent these covalent GSH binding, the reducing agent TCEP (tris [2-carboxyethyl] phosphine) was added to the buffers for GSH-affinity chromatography of following Bid1-GST purification and novel constructs were cloned containing serines instead of cysteines (CCSS mutation).

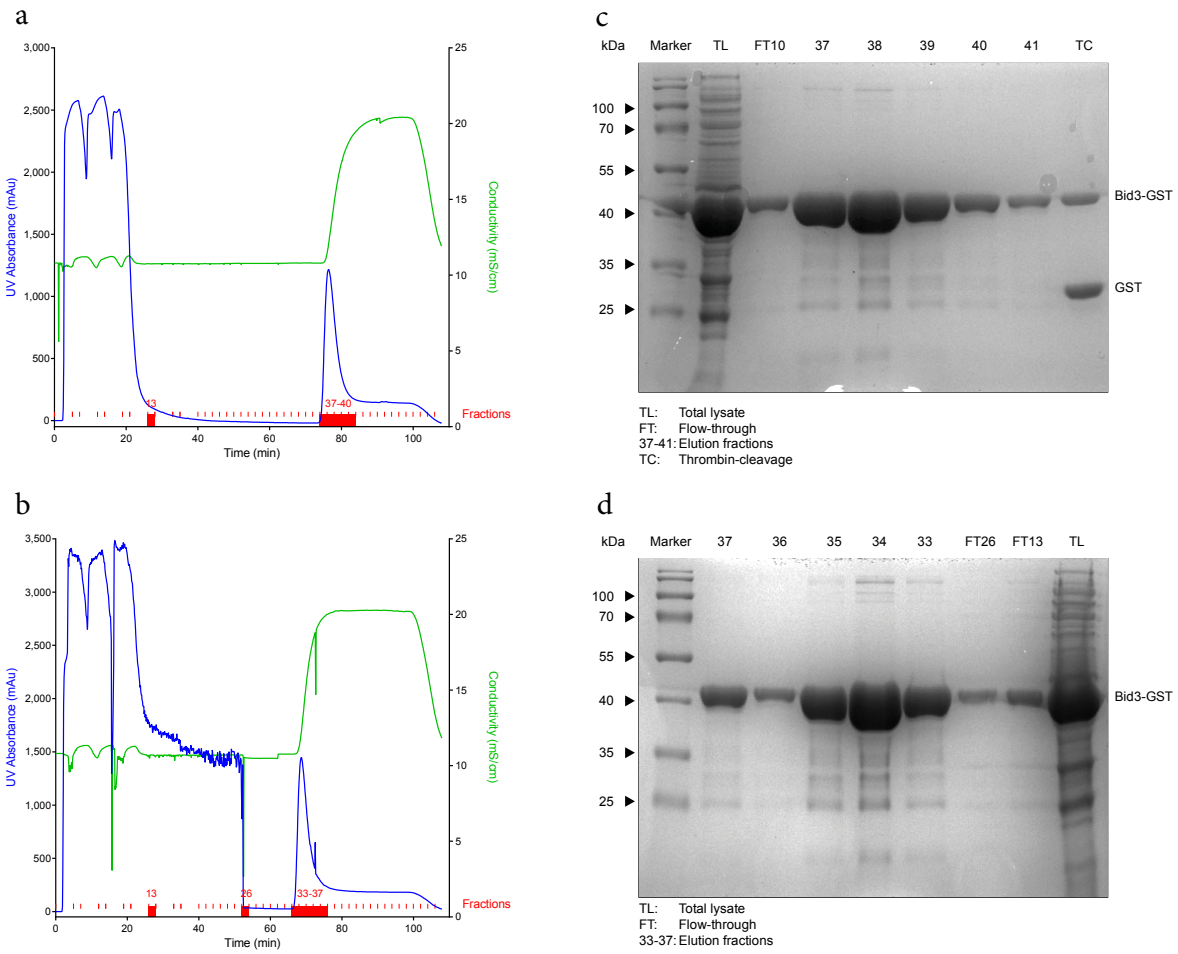

Figure 75. Bid3 purification for screen #1 I

GSH affinity chromatography: Chromatograms of two runs (**a, b**) on Glutathione HiCap 10 mL column and corresponding Coomassie-stained SDS-gels (c**, d**). Total-lysate (TL, **c, d**) depicts sufficient recombinant protein expression. In both runs, UV absorption shows a clear peak for Bid3-GST (~ 44 kDa) (**a, b:** fractions 37-41 and 33-37, respectively) which was confirmed by SDS-PAGE (**c, d**). Flow-through (FT) analysis reveals limited binding capacity inside the column leading to a slight loss of Bid3-GST protein (**c, d**). A sample after thrombin-cleavage (TC, **c**) reveals that a large amount of Bid3-GST was cleaved into GST (~ 26 kDa) and Bid3 (17.5 kDa, missing on gel).

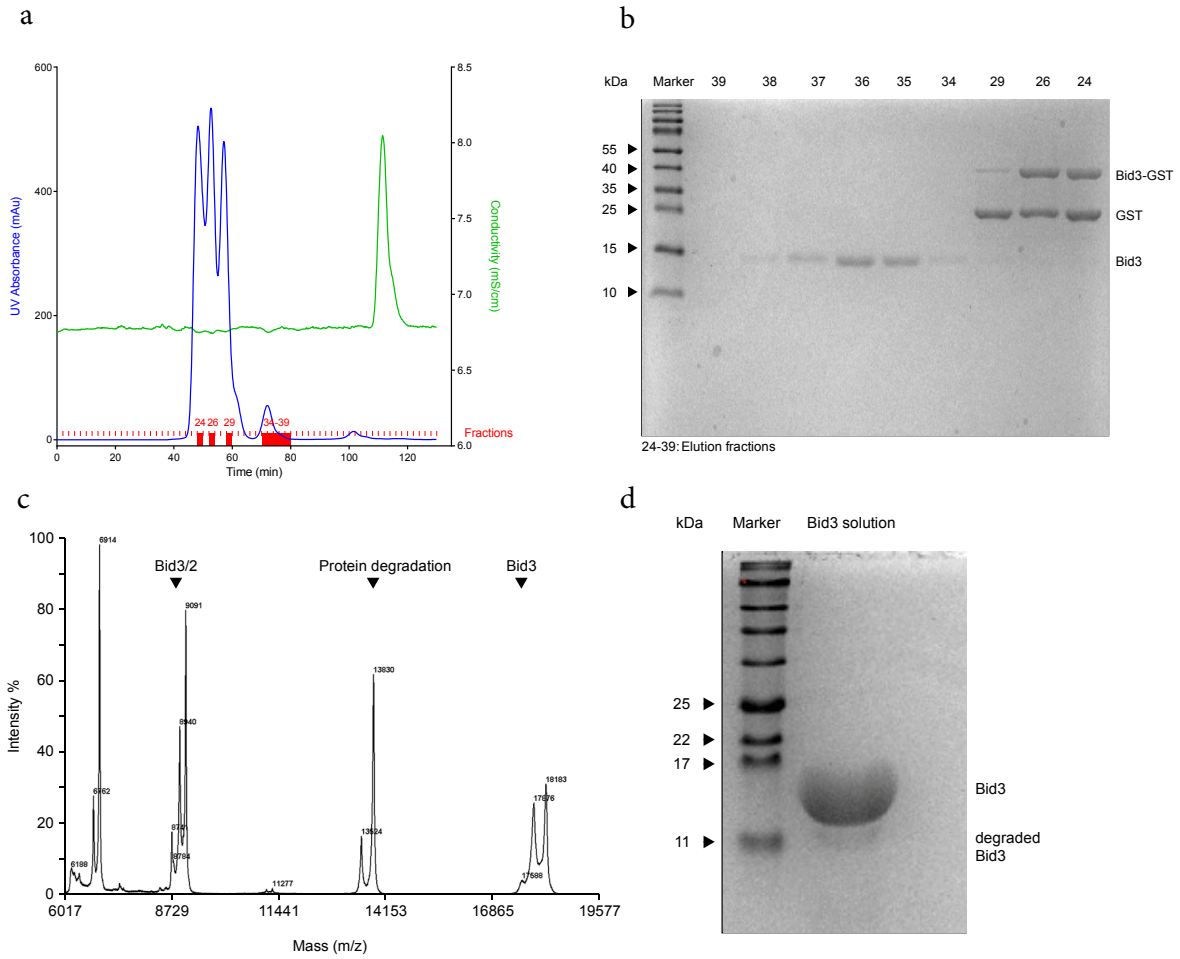

Figure 76. Bid3 purification for screen #1 II

Size exclusion gel chromatography: Chromatogram of a HiLoad 16/1600 Superdex 75 run depicts pronounced UV absorption peaks for GST and Bid3-GST in the beginning (**a**) confirmed by SDS-PAGE (**b**) and a smaller peak for Bid3 in fractions 34-39 (**a**) due to lower amount of aromatic amino acids. Elution fractions after gel chromatography demonstrate successful purification of Bid3 (**b**). **MALDI-TOF analysis** after 6 weeks (**c**) reveals multiple peaks for Bid3 presumably due to GSH covalent binding and protein degradation which was further confirmed by SDS-PAGE (**d**).

After purification Bid3 was subjected to extensive crystallization screening (Table 65) at the MarXtal crystallization lab (SYNMICRO, University of Marburg, Germany) using high-throughput crystallization robotics. Within 1 week, in the *Morpheus* screen (well A8-1) a very small crystal was obtained (Figure 77) providing the basis for the further optimization of crystallization conditions comprising Na-HEPES/MOPS pH7.5 buffer and MPD, PEG1,000 and PEG3,350 as precipitants as well as $MgCl_2$ and $CaCl_2$ as divalent cation salt additives.

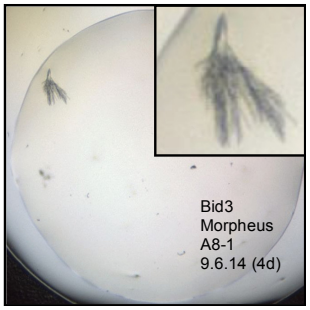

Figure 77. Bid3 crystal

Next, Bid1-GST was purified by GSH-affinity chromatography (Figure 78a, b) in the presence of TCEP to prevent covalent GSH binding to cysteine residues. Chromatograms and SDS-PAGE demonstrated sufficient protein amount in the total lysate (TL), a clean initial enrichment of protein in the elution fractions 68-98 and very little loss of protein in the flow-through (FT) as this time a larger column with 20 mL GSH matrix instead of 10 mL was used. The elution fractions 68-98 were pooled and cleaved by thrombin (TC). After protein concentration with 3 kDa Amicon cut-off filters and size exclusion gel chromatography (Figure 78c, d) elution fractions 36-40 were pooled as they displayed the Bid1 protein with the highest purity as confirmed by SDS-gel electrophoresis. The protein solution was further concentrated to a final concentration of 12.7 mg/mL and sterile-filtered. MALDI-TOF analysis (Figure 78e) depicted single peaks indicating pure protein and no GSH disulfide adducts or degradation. With the obtained protein solution several screens were performed according to Table 65 with the addition of 2 % nanoparticles in drop 1 to facilitate nucleation for crystallization. After several weeks very fine protein needles were obtained (Figure 78f) in *Morpheus* A8-1 and in A9-1 (Tris/BICINE buffer pH 8.5, PEG500 MME and PEG20,000 as precipitants and $MgCl_2$ and $CaCl_2$ as salt additives) suggesting that divalent cations and PEGs (polyethylene glycols) may assist BID crystal growth.

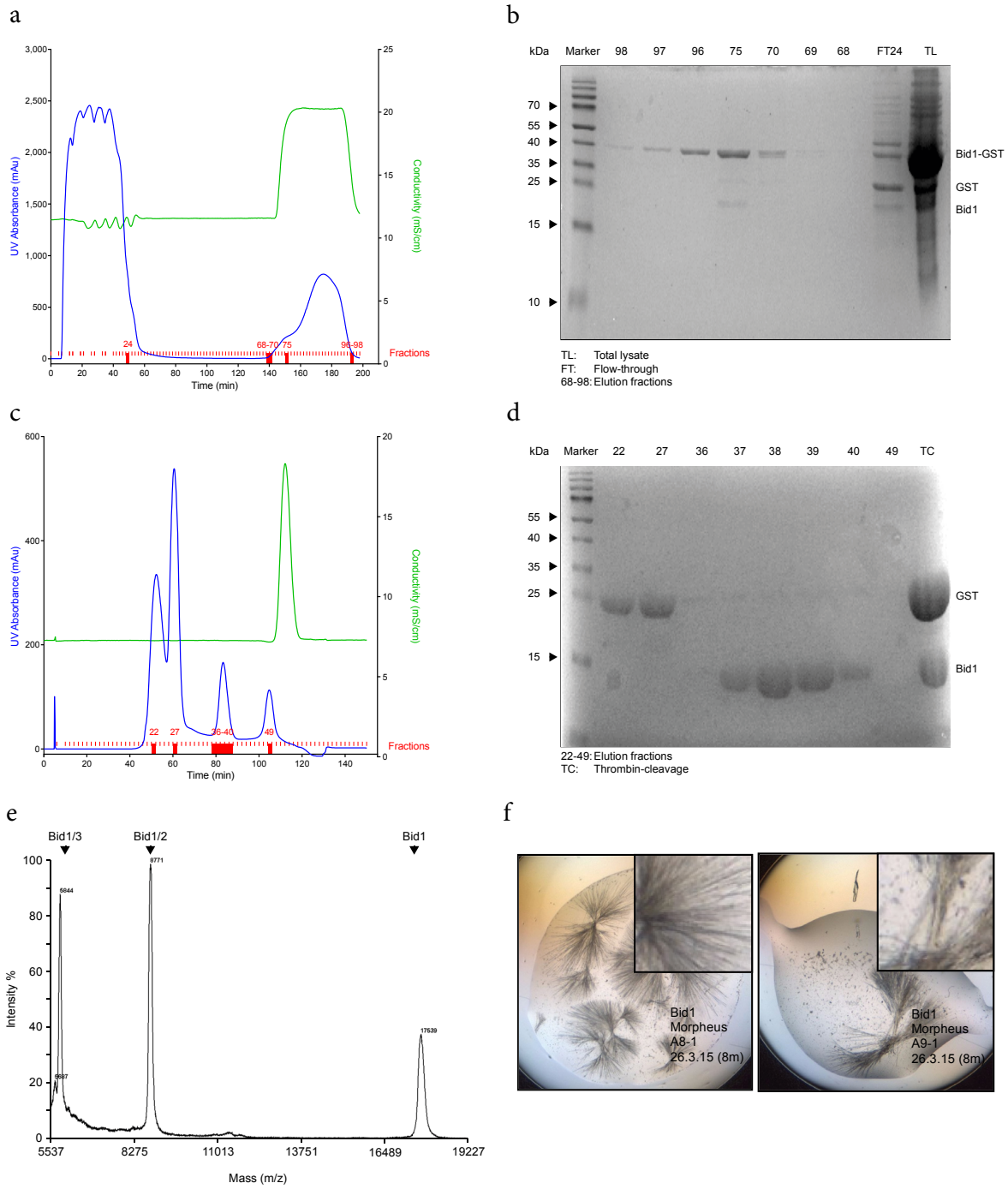

Figure 78. Bid1 purification for screen #2

GSH affinity chromatography: Chromatogram (**a**) of a Glutathione HiCap 20 mL column run and corresponding Coomassie-stained SDS-gel (**b**). Total-lysate (TL, **b**) depicts high recombinant protein expression. UV absorption shows a clear peak for Bid1-GST (~ 44 kDa) (**a:** fractions 68-98) which was confirmed by SDS-PAGE (**b**). Flow-through (FT) analysis reveals very little loss of Bid1-GST protein (**b**). A sample after thrombin-cleavage (TC, **d**) reveals complete cleavage into GST (~ 26 kDa) and Bid1 (17.5 kDa) protein. **Size exclusion gel chromatography:** Chromatogram of a HiLoad 16/1600 Superdex 75 run depicts pronounced UV absorption peaks for GST in the beginning (**e**) confirmed by SDS-PAGE (**d**) and a smaller peak for Bid1 in fractions 36-40 (**c**) due to lower amount of aromatic amino acids. Elution fractions after gel chromatography demonstrate very successful purification of Bid1 (**d**). **MALDI-TOF analysis** directly after purification (**e**) reveals single peaks for Bid1 indicating no GSH covalent binding or protein degradation. Representative Bid1 crystals (**f**).

3.5.2 Bid 3 construct optimization by CCSS mutation

As a second strategy to circumvent undesirable GSH binding to the BID protein, both cysteines of Bid3 were mutated to serines (Bid3 CCSS) using site-directed mutagenesis. The protein was again expressed and purified according to section 3.5.1. In a first step of GSH affinity chromatography (Figure 79a, b, d) remarkably high amounts of Bid3-GST CCSS protein were obtained in fractions 68-78, while very little protein was lost with the flow-through (FT). After thrombin-cleavage (TC) of pooled fractions 68-78, which was almost complete, size exclusion gel chromatography was successful so that excessive Bid3 CCSS protein was obtained according to SDS-PAGE analysis. Notably, in gel fractions 31-37 a small quantity of residual GST was detected which was hardly found in MALDI-TOF analysis. Elution fractions 31-37 were pooled as they displayed the highest Bid3 CCSS protein content as confirmed by SDS-gel electrophoresis. The protein solution was then concentrated to a final concentration of 10.7 mg/mL and sterile-filtered.

The protein solution was subjected to a great variety of crystallization screens (Table 65) with 10.7 mg/mL and a 1:2 dilution to 5.3 mg/mL protein content (screen #3). In the *Morpheus* screen (well A5-1, and A8-1) as well as in the *AmSO$_4$* screen (well D1-1: NaCl and ammonium sulfate) larger crystals were obtained (Figure 80, upper panel). Red-marked crystals were analyzed at the synchrotron microfocus beamline in Grenoble (ESRF Grenoble, France) using cryo-crystallography.

Remaining Bid3 CCSS was used for additional screens (#4) with 5.3 mg/mL concentration protein either alone or supplemented with a novel water-soluble BID inhibitor (BI-28319, 27 mM) in an attempt to obtain co-crystals (Table 65). Again, in *Morpheus* (well A8-1) and also in *MemGold* (well A4-1: NaCl, Na_3PO_4 buffer pH 7.0, PEG4,000, NaN_3) small crystals were obtained (Figure 80 lower panel).

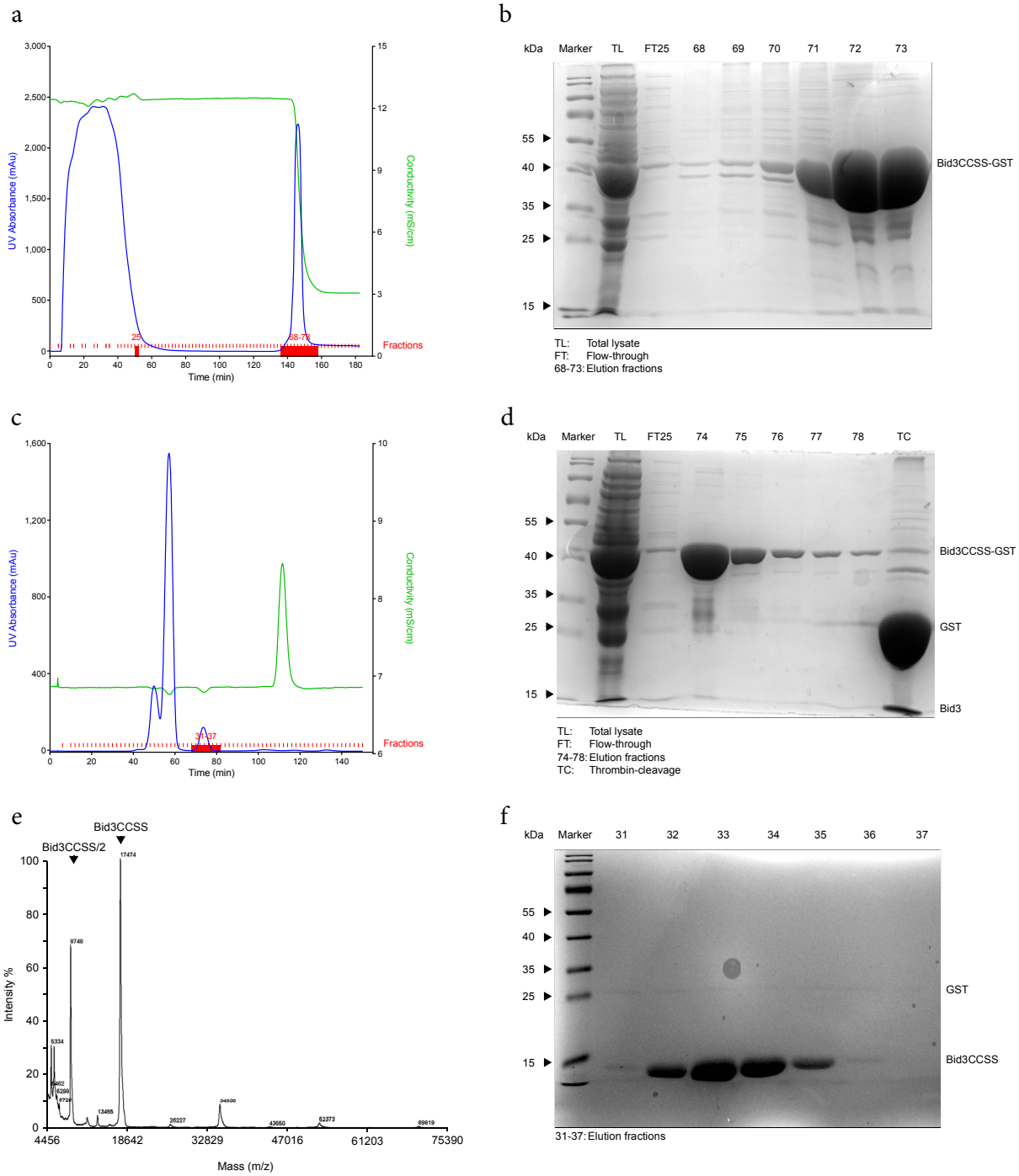

Figure 79. Bid3 CCSS purification for screen #3 and #4

GSH affinity chromatography: Chromatogram (**a**) of a Glutathione HiCap column run and corresponding Coomassie-stained SDS-gels (**b, d**). Total-lysate (TL, **b, d**) depicts high recombinant protein expression. UV absorption shows a clear peak for Bid3 CCSS-GST (~ 44 kDa) (**a:** fractions 68-78), which was confirmed by SDS-PAGE (**b, d**). Flow-through (FT) analysis reveals very little loss of Bid3 CCSS-GST protein (**b, d**). A sample after thrombin-cleavage (TC, **d**) reveals almost complete cleavage into GST (~ 26 kDa) and Bid3 CCSS (17.5 kDa) protein. **Size exclusion gel chromatography:** Chromatogram of a HiLoad 16/1600 Superdex 75 run depicts pronounced UV absorption peaks for GST in the beginning (**c**) and a smaller peak for Bid3 CCSS in fractions 31-37 (**c**). Elution fractions after gel chromatography demonstrate purification of Bid3 CCSS (**f**), however, a faint band at the size of GST is still observable. MALDI-TOF analysis directly after purification (**e**) reveals single peaks for Bid3 CCSS indicating no GSH covalent binding.

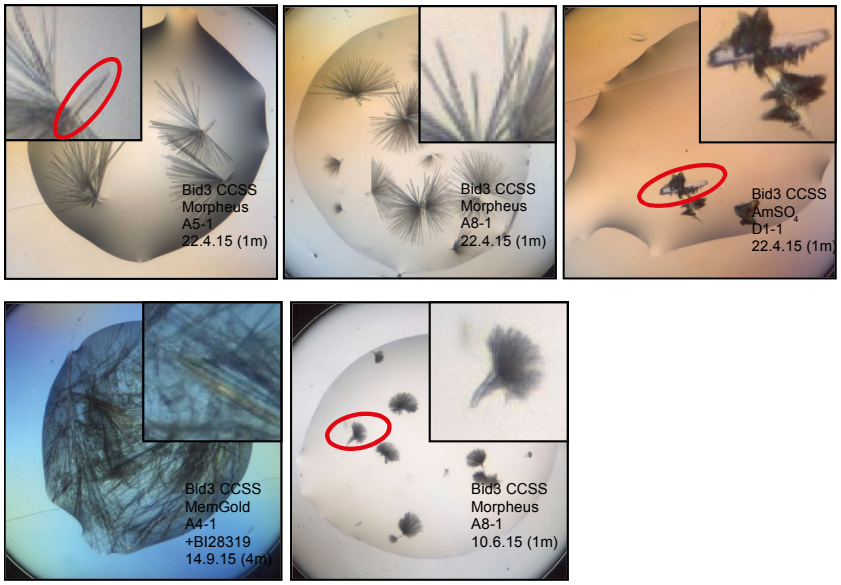

Figure 80. Bid3 CCSS crystals of screen #3 and #4
Bid3 CCSS crystals obtained in screen #3 (upper panel) and #4 (lower panel).

In order to further optimize the most promising *Morpheus* conditions, additional Bid3 CCSS protein was required, for what reason a second purification was performed (Figure 81). In GSH affinity chromatography again high amounts of relatively pure Bid3-GST CCSS protein were obtained in fractions 71-77, while very little protein was lost with the flow-through (FT). After thrombin-cleavage (TC) of pooled fractions 71-77, which was almost complete, size exclusion gel chromatography was successful so that pure Bid3 CCSS protein was obtained according to SDS-PAGE analysis. Elution fractions 32-36 were pooled as they displayed the highest amount of Bid3 CCSS protein. The protein solution was then concentrated to a final concentration of 12.3 mg/mL and sterile-filtered.

Subsequently, the protein solution was subjected to a variety of optimization screens with conditions similar to *Morpheus* A5 and A8 and the protein was again supplemented with BI-28319 (1 mM) to allow co-crystal growth (screen #5). Remaining protein was used for a seeding screen, where old crystals were smashed and used as seeding crystals, and an additive screen, where several chemical substances so-called *additives* were tested whether they may improve crystal growth (screen #8). A large crystal was obtained in the *Opti* screen well C9-1 (similar conditions as *Morpheus* A5) (Figure 81e), in the *additive* screen with *Morpheus* A5 conditions (well B4-1 with $CoCl_2$ * 6 H_2O and B5-1 with LiCl) and in the additive screen with *Morpheus* A8 conditions (well B4-1 with $CoCl_2$ * 6 H_2O and C6-1 with 6-Aminohexanoic acid). In conclusion, these conditions further underline a better crystal growth in the presence of divalent cations such as magnesium, calcium and cobalt.

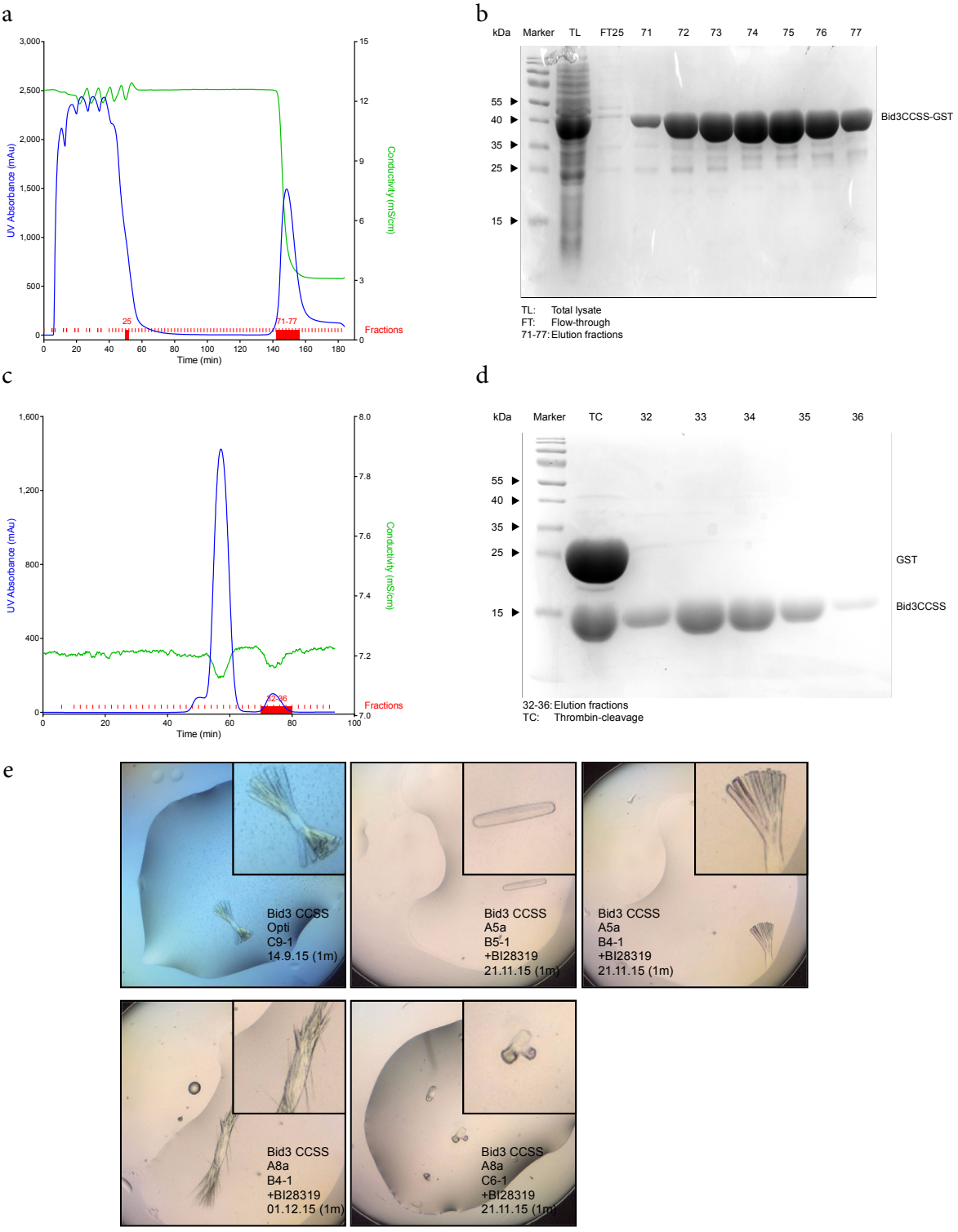

Figure 81. Bid3 CCSS purification for screen #5 and #8

GSH affinity chromatography: Chromatogram (**a**) of a Glutathione HiCap column run and corresponding Coomassie-stained SDS-gel (**b**). Total-lysate (TL, **b**) depicts high recombinant protein expression. UV absorption shows a clear peak for Bid3 CCSS-GST (~ 44 kDa) (**a:** fractions 71-77), which was confirmed by SDS-PAGE (**b**). Flow-through (FT) analysis reveals very little loss of Bid3 CCSS-GST protein (**b**). A sample after thrombin-cleavage (TC, **d**) reveals complete cleavage into GST (~ 26 kDa) and Bid3 CCSS (17.5 kDa) protein. **Size exclusion gel chromatography:** Chromatogram of a HiLoad 16/1600 Superdex 75 run depicts pronounced UV absorption peaks for GST in the beginning (**c**) and a smaller peak for Bid3 CCSS in fractions 32-36 (**c**). Elution fractions after gel chromatography demonstrate purification of Bid3 CCSS (**d**). Representative Bid3 CCSS crystals (**e**) of screen #5 (upper left) and screen #8 (remaining pictures).

3.5.3 Selenomethionine heavy atom exchange in Bid 3 CCSS

Having obtained diffracting protein crystals, the major difficulty of elucidating protein structures is to solve the phase problem which occurs as x-ray detection only records amplitudes but not the phases of electromagnetic waves. Besides molecular replacement (MR), introduction of heavy atom diffraction labels into the crystal (multiple isomorphous replacement, MIR) combined with multi-wavelength anomalous dispersion (MAD) is used. Heavy atoms like selenium (Se) can act as anomalous scatterers and multiple data sets of one single crystal can be collected using different wavelengths. Their variation in recorded intensities at the different wavelengths can be used to extract the anomalous substructure of the scatterer to solve the phase problem.

In light of this, to aid structure elucidation, selenium was incorporated into Bid3 CCSS protein by replacement of methionines with selenomethionine (SeMet) during recombinant protein expression according to section 2.10.3.4. A preliminary small scale expression test was performed to check whether selenomethionine exchanged protein expression principally works and to decide whether the selenomethionine expression media should be supplemented with glycerol as the manufacturer's protocol suggested. For this reason, supplementation with 2 % glycerol was tested compared to normal protein expression in IPTG-induced LB medium and samples run on an SDS-gel with subsequent Coomassie staining for visualization (Figure 82). Since expression worked best in conditions without glycerol (Figure 82) further large-scale SeMet Bid3 CCSS expression was performed without the supplement.

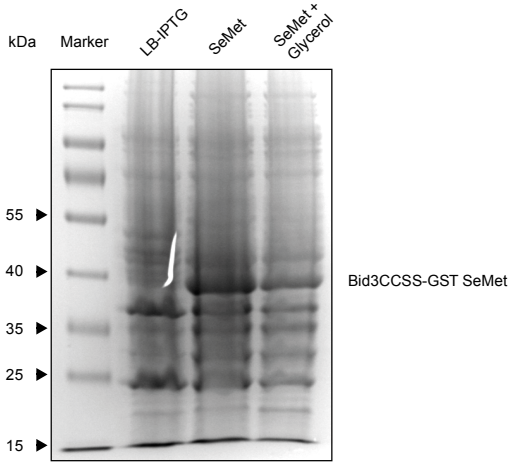

Figure 82. Small-scale SeMet Bid3 CCSS expression test on SDS-gel
Coomassie-stained SDS-gel of preliminary small-scale protein expression test reveals best Bid3 CCSS-GST SeMet expression in SeMet media without addition of 2 % glycerol.

SeMet Bid3 CCSS was purified similarly to regular Bid3 CCSS recombinant protein using GSH affinity and size exclusion chromatography. In GSH affinity chromatography excessive amounts of highly purified SeMet Bid3-GST CCSS protein were obtained in fractions 67-84, while little protein was lost with the flow-through (FT) (Figure 83a, b). After thrombin-cleavage (TC, Figure 83c) of pooled fractions 67-84 size exclusion gel chromatography was effective so that pure SeMet Bid3 CCSS protein was obtained according to SDS-PAGE analysis (Figure 83d, e). Elution fractions 31-37 were pooled as they displayed pure SeMet Bid3 CCSS protein. The protein solution was then concentrated to a final concentration of 13.2 mg/mL and sterile-filtered.

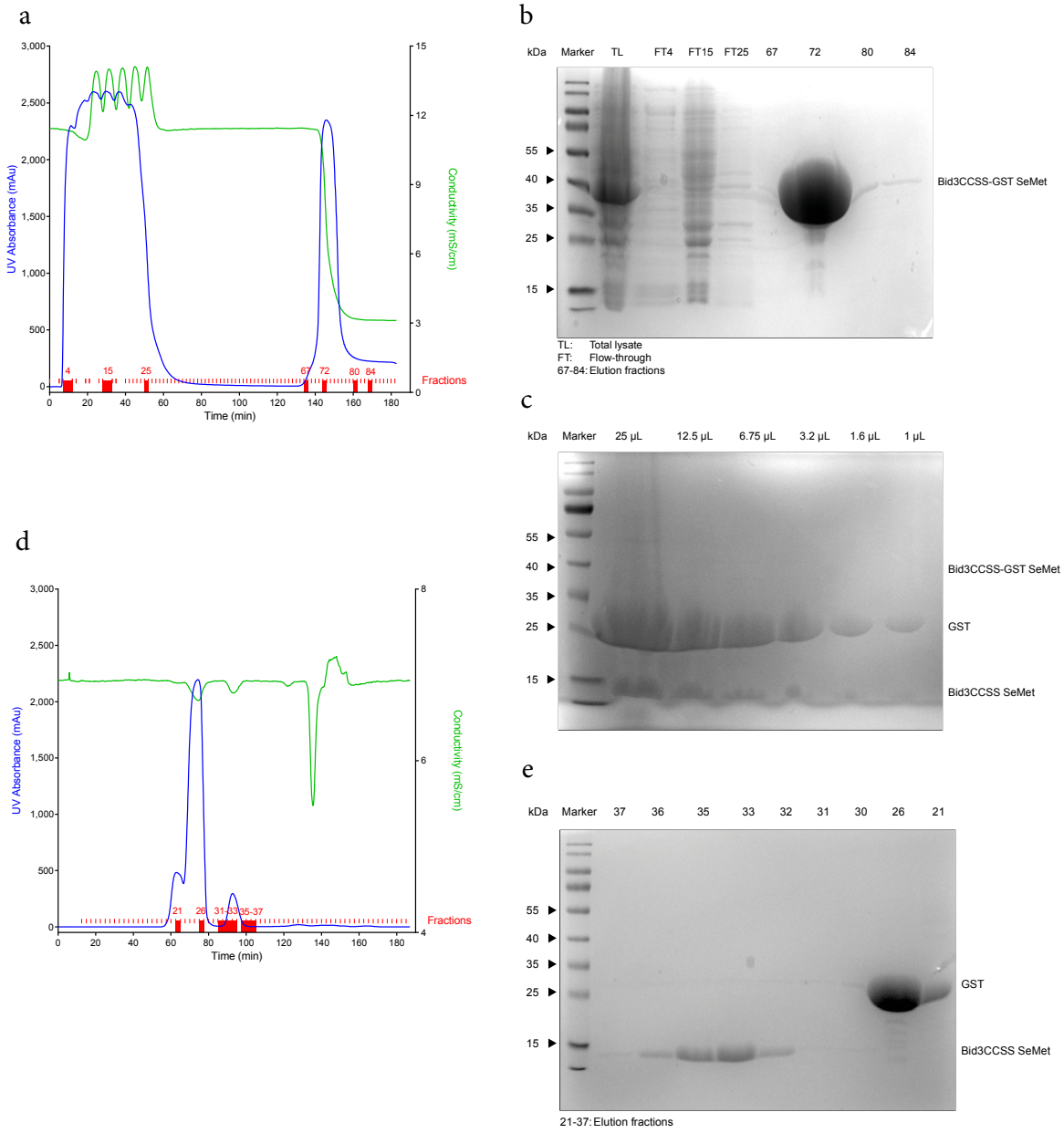

Figure 83. Bid3 CCS SeMet purification for screen #9 and #10

GSH affinity chromatography: Chromatogram (**a**) of a Glutathione HiCap column run and corresponding Coomassie-stained SDS-gel (**b**). Total-lysate (TL, **b**) depicts sufficient recombinant protein expression. The UV absorption graph shows a clear peak for Bid3 CCSS SeMet-GST (~ 44 kDa) (**a:** fractions 67-84), which was confirmed by SDS-PAGE (**b**). Flow-through (FT) analysis reveals very little loss of Bid3 CCSS SeMet-GST protein (**b**). Samples after thrombin-cleavage (TC, **c**) reveal complete cleavage into GST (~ 26 kDa) and Bid3 CCSS SeMet (~18 kDa) protein. **Size exclusion gel chromatography:** Chromatogram of a HiLoad 16/1600 Superdex 75 run depicts pronounced UV absorption peaks for GST in the beginning (**e**) and a small peak for Bid3 CCSS SeMet in fractions 31-37 (**f**). Elution fractions after gel chromatography demonstrate successful purification of Bid3 CCSS SeMet (**f**).

MALDI-TOF analysis confirmed increased protein mass of Bid3 CCSS SeMet (Δ 282 Da) by selenium incorporation compared to Bid3 CCSS suggesting 6 sulfur atom exchanges by selenium (Δ 47 Da) per protein molecule on average (Figure 84a). After purification, the protein solution was subjected to *Morpheus* screen and various optimization screens with conditions similar to *Morpheus* A5 and A8 and the protein was supplemented with BI-6c9 (0.25 mM) to allow co-crystal growth (screen #8). The remaining protein was used for another round of screening with optimization of *Morpheus* A5 and *Morpheus* A5 well D3 (screen #9). Several crystals were obtained including a large crystal in the *Morpheus* A5 *Opti* screen well D3-2 (Figure 84b) which was analyzed by x-ray diffraction.

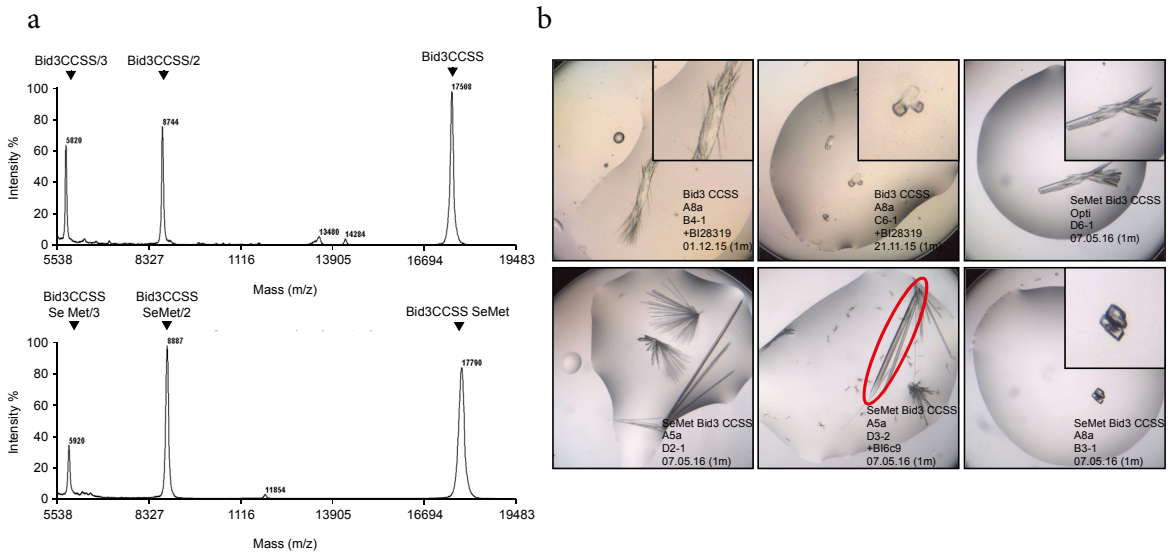

Figure 84. MALDI-TOF analysis and crystals of Bid3 CCSS SeMet

a: MALDI-TOF analysis directly after protein purification reveals single peaks for Bid3 CCSS SeMet indicating successful protein purification. A difference in protein mass of Δ 282 Dalton of Bid3 CCSS compared to Bid3 CCSS without selenium incorporation indicates an average incorporation of 6 selenium atoms per protein molecule. **b:** Representative Bid3 CCSS SeMet crystals of screen #8 (upper left and middle) and screen #9 (remaining pictures).

3.5.4 Full-length Bid 22 purification and construct optimization by CCSS mutation

Since the major aim was to identify the 3D protein structure of full-length BID, Bid 22 was recombinantly expressed, purified and subjected to crystallization screens which were already identified as potentially helpful regarding reproducible crystal growth. As the Bid 22 construct contains a His_6-tag for purification instead of GST the protein purification process was modified accordingly (see section 2.10.4.4).

Briefly, purification of His_6-tagged BID was performed by three independent chromatography steps comprising nickel-affinity, ion exchange and size-exclusion gel chromatography. Importantly, after the nickel affinity chromatography step, the protein solution had to be desalted for ion exchange chromatography. As CCSS mutation already improved Bid construct purification also a full-length Bid construct with CCSS mutation was generated and purified similarly for crystallization screening.

Bid22-His_6 was expressed as stated in 2.10.3 and purified by Nickel affinity chromatography as a first step. According to the UV absorption spectrum (Figure 86a) and the Coomassie-stained SDS-gel (Figure 86b) fractions 33-48 contained relatively pure Bid22-His_6 protein (~ 23 kDa). These fractions were pooled and after the subsequent desalting procedure (see 2.10.4.4) the protein solution was applicable for ion exchange chromatography (Figure 86c) to further purify the protein, which was successful according to SDS-gel analysis although two peaks were apparent in the UV absorption spectrum (Figure 86d).

Pooled fractions 41-53 were subjected to thrombin-cleavage (see 2.10.4.7) to remove the His_6-tag and finally loaded on a gel column for size exclusion chromatography to remove the cleaved protein parts. Interestingly, SDS-gel analysis revealed a second unexpected purification product of ~ 14-15 kDa in size which was not removed after gel chromatography (Figure 86a, b). The fragment likely was a Bid22 fragment due to unspecific thrombin cleavage which could not be removed by a second ion exchange chromatography step (Figure 86c) suggesting that the fragments are cleaved but do not separate from each other. Subsequent Western blot analysis showed that the Bid antibody recognized this fragment confirming that it indeed was an unspecific BID cleavage product (Figure 86d). MALDI-TOF analysis revealed full-length BID with 22.3 kDa and unspecific cleavage products of 14.9 and 7.5 kDa size (Figure 87). After purification the protein solution was concentrated to 4.75 mg/mL. Crystallization attempts with the *Morpheus* A5/A8 *Opti* Screen (screen #6) ± BI-28319 (0.8 mM) did not result in crystal growth presumably due to heterogeneous protein solution or due to low protein concentration.

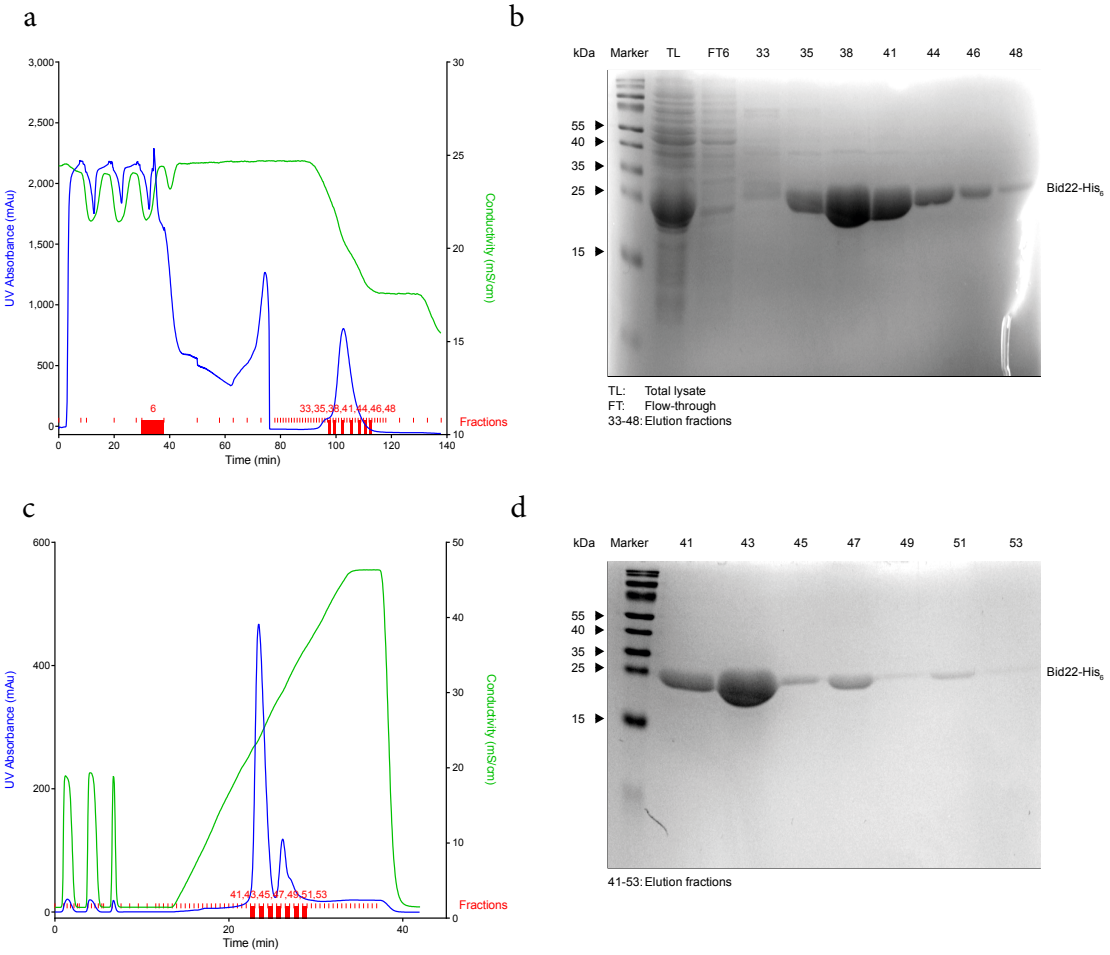

Figure 85. Bid22 purification for screen #6 I

Nickel affinity chromatography: Chromatogram (**a**) of a Nickel HisTrap FF column run and corresponding Coomassie-stained SDS-gel (**b**). Total-lysate (TL, **b**) depicts sufficient recombinant protein expression. The UV absorption graph shows a clear peak for Bid22-His_6 (~ 23 kDa) (**a:** fractions 33-48) which was confirmed by SDS-PAGE (**b**). Flow-through (FT) analysis reveals almost no loss of Bid22-His_6 protein (**b**). **Ion exchange chromatography:** Chromatogram of a run on an ion exchange HiTrap Q HP column shows two elution peaks of Bid22-His_6 (**c**) confirmed by SDS-gel analysis of fractions 41-53 (**d**).

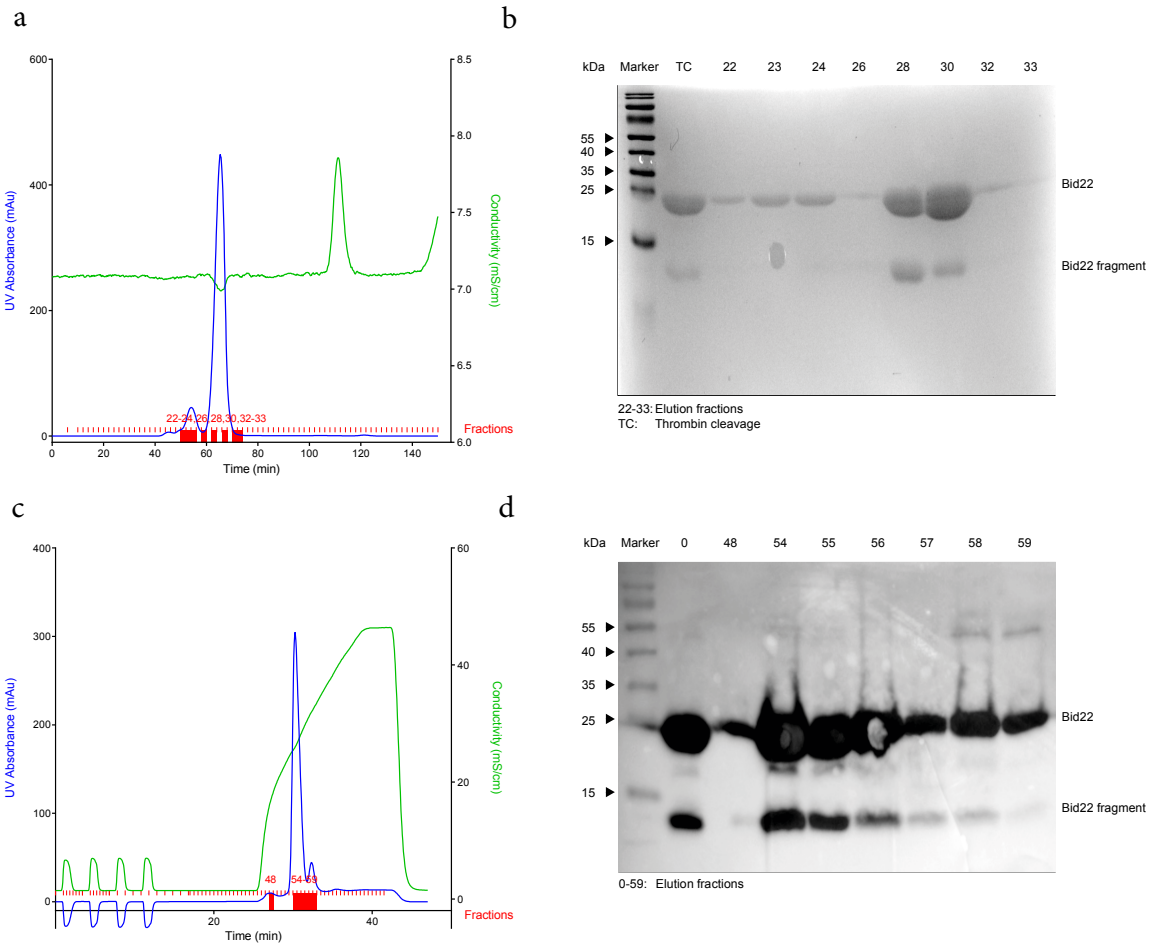

Figure 86. Bid22 purification for screen #6 II

A sample after thrombin-cleavage (TC, **b**) reveals an unspecific cleavage product of ~ 14 kDa size. **Size exclusion gel chromatography:** Chromatogram of a HiLoad 16/1600 Superdex 75 run depicts two UV absorption peaks for Bid22 in fractions 22-33 (**a**). Elution fractions after gel chromatography demonstrate purification of Bid22 and a smaller fragment (**b**). **Ion exchange chromatography:** Second ion chromatography results in two peaks of fractions 48-59 (**c**) containing Bid22 and a Bid fragment which is confirmed by Western-blot demonstrating detection of both bands by Bid antibody (**d**).

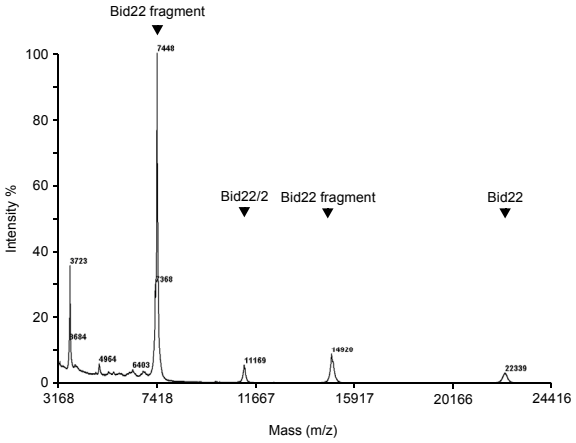

Figure 87. MALDI-TOF analysis of Bid22 purification product
MALDI-TOF analysis shows full-length BID of 22.3 kDa and reveals unspecific thrombin cleavage products of 14.9 and 7.5 kDa size.

In addition, purification of Bid22 CCSS was performed similar to Bid22 purification. According to the UV absorption spectrum (Figure 88a) and the Coomassie-stained SDS-gel (Figure 88b) fractions 34-45 contained relatively pure Bid22 CCSS-His_6 protein (~ 23 kDa). These fractions were pooled and the His_6-tag cleaved by thrombin. However, again SDS-gel analysis revealed a second purification product of ~ 14-15 kDa size. After the subsequent desalting procedure (see 2.10.4.4) the protein solution was applicable for ion exchange chromatography (Figure 88c) to further purify the protein. According to SDS-gel analysis much protein remained in the flow-through (Figure 88d) which is why a second ion exchange chromatography step was performed with fractions 1-14 (Figure 88e). Elution fractions of both runs (first: 36-47, second: 42-47) were subsequently pooled and subjected to gel chromatography (Figure 88f). MALDI-TOF analysis of pooled fractions 27-33 revealed full-length BID with 22.2 kDa and unspecific cleavage products of 14.9 and 7.4 kDa in size (Figure 89). After the purification process the protein solution was concentrated to 14.0 mg/mL. Crystallization attempts with various conditions (screen #7) ± BI-28319 (0.07 mM) did not result in crystal growth presumably due to heterogeneous protein.

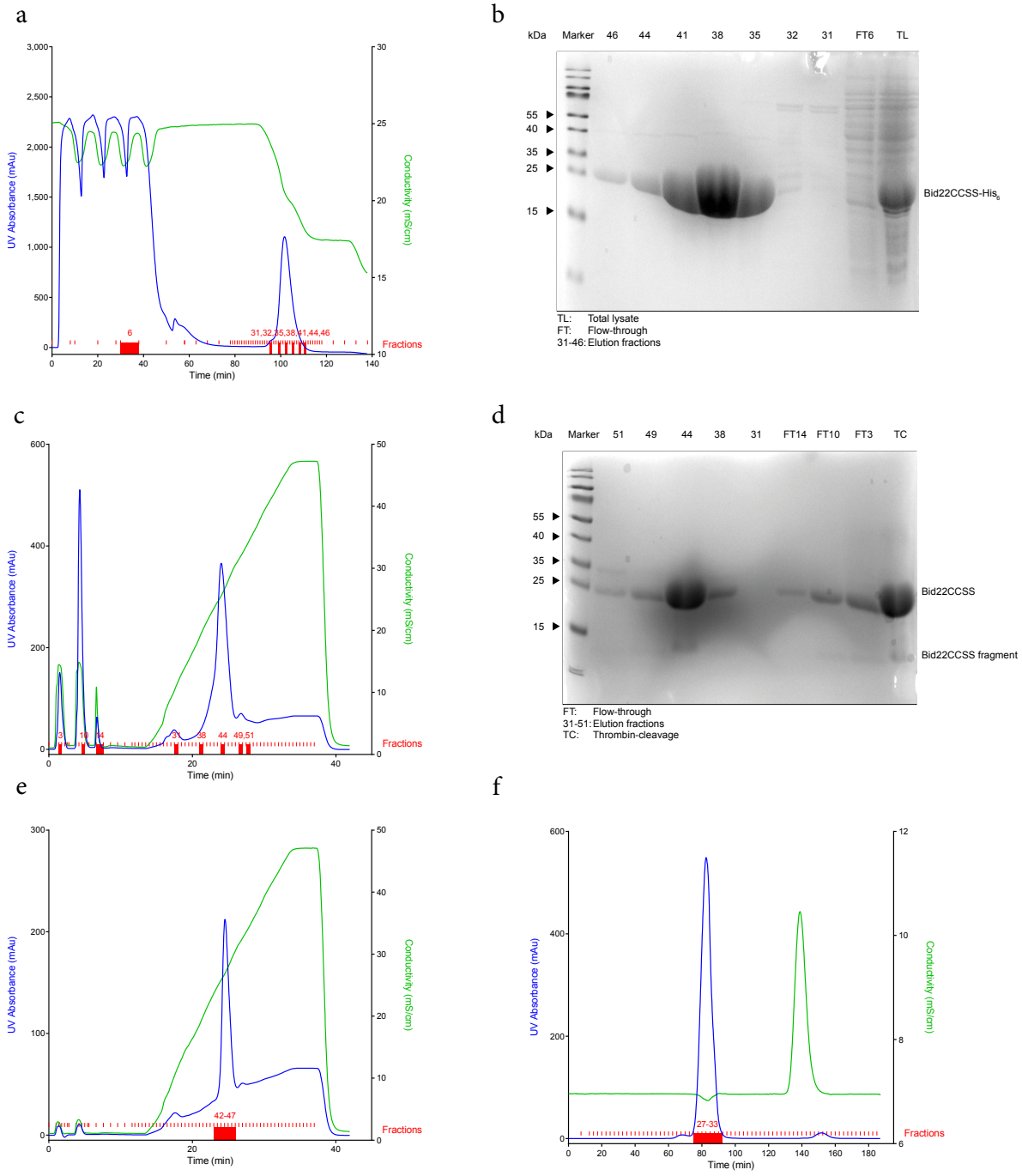

Figure 88. Bid22 CCSS purification for screen #7

Nickel affinity chromatography: Chromatogram (**a**) of a Nickel HisTrap FF column run and corresponding Coomassie-stained SDS-gel (**b**). Total-lysate (TL, **b**) depicts sufficient recombinant protein expression. The UV absorption graph shows a clear peak for Bid22 CCSS-His_6 (~ 23 kDa) (**a:** fractions 31-51) which was confirmed by SDS-PAGE (**b**). Flow-through (FT) analysis reveals almost no loss of Bid22-His_6 protein (**b**). A sample after thrombin-cleavage (TC, **d**) reveals an unspecific cleavage product of ~ 14 kDa size. **Ion exchange chromatography:** Chromatogram of a run on an ion exchange HiTrap Q HP column shows a peak of Bid22 CCSS-His_6 (**c**) confirmed by SDS-gel analysis of fractions 31-51 (**d**), however, the flow-through (FT) still contains much protein. Chromatogram of a second ion exchange run of flow-through fractions 1-14 (**e**). **Size exclusion gel chromatography:** Chromatogram of a HiLoad 16/1600 Superdex 75 run depicts a clear UV absorption peak for Bid22 CCSS in fractions 27-33 (**f**).

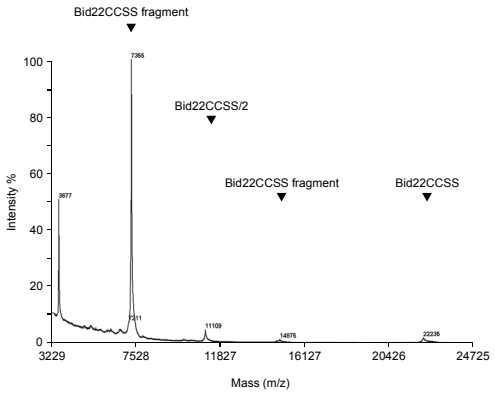

Figure 89. MALDI-TOF analysis of Bid22CCSS purification product
MALDI-TOF analysis shows full-length BID CCSS of 22.2 kDa and reveals unspecific thrombin cleavage products of 14.9 and 7.4 kDa size (**g**).

In conclusion, novel recombinant BID protein constructs were successfully expressed and optimized to improve the purity and to enhance the probability of crystal growth. For the first time, crystallization conditions for reproducible crystal growth were identified and optimized to obtain larger crystals. In order to solve the phase problem, selenomethionine protein expression resulting in reproducible crystal growth was established. Despite relatively large crystals, first x-ray analyses could not solve the 3D structure due to insufficient diffraction resolution but the improved protocols provide a promising basis for further crystallization attempts.

4 Discussion

Disturbed cellular homeostasis and cell death owing to the accumulation of ROS and subsequent mitochondrial damage are well-established features of pathologic processes in the course of neurodegeneration. Despite some evidence for the involvement of the pro-apoptotic protein BID, the underlying mechanisms driving mitochondrial demise in the course of oxidative programmed neural cell death remain poorly defined. Therefore, the aim of the present thesis was to elucidate the role of BID in oxidative cell death pathways affecting mitochondrial integrity and function. In addition, effects of mitochondria-targeted antioxidants were evaluated according to the potential role in preserving mitochondrial function upon RSL3-induced cell death. Finally, the protein BID was recombinantly expressed and purified for X-ray crystal structure analysis and potential *in silico* modeling for the optimization of BID inhibitors.

The first part of this thesis highlights a pivotal role for BID-induced mitochondrial damage in shared pathways of glutamate-induced oxytosis and erastin-induced ferroptosis, both of which were accompanied by BID transactivation to mitochondria and their subsequent fatal damage. In addition, CRISPR/*Cas9* BID knockout in neuronal HT22 cells revealed sustained protection against glutamate- or erastin-induced cell death by protein deletion, thereby supporting a crucial involvement of BID in ROS-induced cell death. The protective effects mediated by the well-established BID and ferroptosis inhibitors in the respective other model system of oxytosis and ferroptosis, confirmed common mechanistic hallmarks of these two cell death modalities and highlighted the crucial involvement of mitochondrial pathways in these paradigms of cell death.

The second part of the actual study addressed the detailed mechanism of RSL3-induced ferroptosis and the chronological sequence of biochemical hallmarks. RSL3 induced ROS-dependent cell death similar to glutamate and erastin, and involved BID-mediated loss of mitochondrial function and morphological alterations. The detailed analysis of RSL3 isomeric forms revealed a specific inhibitory effect on GPX4 only by *1S, 3R*-RSL3 which was accompanied by GPX4 protein degradation and demonstrated that the chloroacetamide moiety of RSL3 was responsible for covalent GPX4 binding. Not only BI-6c9 and ferroptosis inhibitors prevented RSL3-induced cytotoxicity, but also the mitochondria-specific ROS scavenger MitoQ was identified as a potent inhibitor of ferroptotic mitochondrial damage and successive cell death by scavenging ROS and shifting energy metabolism towards glycolysis. These data suggest BID-mediated mitochondrial demise as *the point of no return* in the cell's commitment to die while at the same time providing a novel therapeutic strategy to treat oxidative cell death-related neurodegenerative diseases.

Finally, recombinant BID constructs were optimized for X-ray protein crystallography and crystallization conditions for reproducible crystal growth were established. Despite considerable progress in the optimization of protein constructs and crystallization conditions, electron density data of crystals measured at the microfocus beamline did not have a sufficient resolution to finally elucidate the 3D structure but provided a promising basis for further optimization.

4.1 A key role for BID in glutamate- and erastin-induced oxidative cell death

Oxytosis in HT22 cells is a well-established model system to study neuronal oxidative cell death [125,183–185] and was therefore used to confirm already established concepts on the involvement of BID and mitochondrial damage in ROS-induced cellular demise. In this thesis, these observations were significantly extended by time-course analyses of ROS-mediated mitochondrial dysfunction. Prior work has documented alterations in mitochondrial morphology and function to be implicated in a variety of ROS-dependent neuropathological processes in Alzheimer's disease, Parkinson's disease, and in brain injuries caused by ischemic stroke, trauma or hemorrhagic insults [109,152]. In the model system of oxytosis, glutamate application mimics these pathophysiological conditions by provoking 12/15-lipoxygenase-mediated increases in soluble and lipid ROS [184,186], which were shown to provoke fatal mitochondrial damage mediated by BID transactivation to the outer mitochondrial membrane [72,103].

Consistent with earlier studies on glutamate-induced oxytosis [36,103,125,186], glutamate toxicity by inhibition of system X_c^- was shown to depend on the cell density at the time of treatment and on the glutamate concentration applied to the cells. Variable sensitivity towards glutamate can be explained as a reason of differing extents of system X_c^- blockage depending on how dense the cells are at the time of treatment.

Mitochondrial impairment or dysfunction has been observed in a variety of neuropathological conditions and was identified as a major hallmark of glutamate-induced oxytosis. To address the question of when exactly mitochondrial function is impaired in the course of oxidative cell death, mitochondrial respiration was assessed. By the subsequent application of the ATP-synthase inhibitor oligomycin, uncoupler FCCP and complex I and III inhibitors rotenone and antimycin A, it became evident that mitochondrial respiration was compromised and the respiratory capacity was reduced after 8 hours of glutamate challenge in HT22 cells. Recent publications suggested mitochondrial damage to be mediated by the transactivation of BID to the mitochondria [103,186]. Consequently, inhibition of BID by the well-established BID inhibitor BI-6c9 [13,14] successfully rescued HT22 cells until 6 to 8 hours post-treatment after cell death induction. Taken together, these data imply mitochondrial damage *as the point of no return* in oxidative cell death given the fact that cells cannot be rescued once their mitochondria are no longer functional.

The recently coined term *ferroptosis* describes a form of oxidative cell death very similar to the previously established models of glutamate-induced oxytosis. Common features established so far are the induction of oxidative death by X_c^- inhibition with glutamate or erastin [42], GSH depletion, impaired GPX4 activity or direct inhibition by *1S, 3R*-RSL3 [211] and subsequent burst of mainly lipid ROS [38,41,90,211]. The formation of lipid ROS, mostly involving oxidized arachidonic [20:4] and adrenic [22:4] phosphatidylethanolamines, is based on iron-dependent autoxidation processes [164] as well as enhanced 12/15-lipoxygenase activity [170,212]. However, common mechanisms downstream of lipid ROS occurrence leading to cell death, in particular mitochondrial and BID contribution, were not entirely clear in the context of ferroptosis and, therefore, remained to be further analyzed. Due to apparent mechanistic analogy, erastin-induced cell death in HT22 cells was investigated with respect to well-known biochemical hallmarks of oxytosis and compared to MEF cells to exclude cell-line specific effects.

Similar to glutamate-induced oxytosis, erastin-induced cell death in HT22 cells occurred in a concentration-dependent manner and could be rescued by BID inhibitor BI-6c9 application. Notably, BI-6c9 was not able to rescue H_2O_2-induced oxidative death excluding unspecific antioxidant effects of this compound. Combined XCELLigence measurements and BI-6c9 post-treatment revealed that erastin-induced cell death required lower concentrations of the X_c^- inhibiting compound and appeared about 2 hours earlier than glutamate-induced death. In addition, the fact that cell death could be rescued by BI-6c9 only until 4 hours post-treatment underlines the potency of erastin to induce rapid and strong cell death.

In contrast to glutamate, erastin was described to mediate direct detrimental effects at the mitochondria apart from glutamate/cystine-antiporter inhibition. Yagoda et al. [208] suggested that erastin acts through mitochondrial voltage-dependent anion channels 2/3 (VDAC 2/3), appearance of oxidative species and mitochondrial outer membrane permeabilization in tumor cells. Of note, Dixon and co-workers detected erastin-induced alterations of mitochondrial morphology, however, they could not observe BID-dependence or mitochondrial ROS while Yuan et al. described CDGSH iron sulfur domain 1 (CISD1)-dependent mitochondrial lipid peroxidation [220]. Analyses of lipid peroxidation, mitochondrial ROS formation, mitochondrial membrane potential and cell death established a well-ordered erastin-induced cell death pathway in HT22 and MEF cells. While alterations in mitochondrial morphology, loss of mitochondrial membrane potential, lipid ROS and loss of mitochondrial function consecutively appeared 2 to 6 hours after erastin treatment, mitochondrial ROS and cell death were detected rising after 8 to 10 hours post-treatment implying harmed mitochondria as the source of ROS production being responsible for succeeding cell death applying to both neuronal and non-neuronal cells.

In conclusion, these data indeed confirm shared mitochondrial cell death pathways of oxytosis and ferroptosis in neuronal HT22 cells. Hence, ferroptosis was supposed to involve apoptosis inducing factor (AIF) being an essential player in oxytosis [103,162]. Similar to oxytosis AIF knockdown provided protection against glutamate or erastin-induced cell death by either direct effects of AIF as a pro-death factor or by indirect preconditioning effects [23,24,133].

To address the role of the pro-apoptotic protein BID in these mutual oxidative cell death paradigms, the protein was depleted by two different siRNA sequences and CRISPR/*Cas9* to achieve full knockout. Transfection of BID siRNAs for 48 hours resulted in 80-90 % reduction of BID protein levels. Despite this efficient knockdown, functional effects on cell death were hardly detectable and were only found for BID siRNA #2 significantly reducing cell death assessed by MTT assay and showing a trend towards protection in Annexin V/PI FACS measurements. Thus, these data did not completely match the results of robust protection by BID siRNA shown by Landshamer et al. [103] and imply strong contribution of residual BID after knockdown for what reason a complete knockout of the protein was desirable. Therefore, a pre-designed CRISPR/*Cas9* plasmid targeting *Bid* was transfected in HT22 cells and subsequently screened for knockout colonies. On protein level, several colonies were identified as potential knockout colonies (#4, #15, #25) as the *Bid* antibody detected almost no protein. However, lacking a protein band on Western-blot level may also result from protein mutations at the antibody recognition site. Therefore, genomic DNA sequencing additionally confirmed mutations in the CRISPR *Bid* target region of colonies #15 and #25, while colony #4 additionally displayed a nucleotide deletion, hence being the most promising candidate for successful BID protein knockout. As the CRISPR guideRNAs are limited to 19-24 nucleotides in length, CRISPR targeting is prone to off-target mutations due to unspecific DNA binding. As control, the most probable off-target sites were identified using web-based algorithms [179,225] and subsequently analyzed by sequencing of colony #4 genomic DNA. In addition, 12/15-LOX and xCT protein levels were determined to exclude alterations in these proteins as they are essentially involved in oxidative death signaling. Having excluded off-target effects, CRISPR BID colony #4 was chosen for further experiments on the role of BID in oxidative cell death paradigms.

Remarkably, *Bid* KO in HT22 cells led to a full and sustained protection against glutamate- or erastin-induced cell death comparable to BI-6c9-mediated rescue demonstrated by MTT assay, Annexin V/PI FACS analysis and real-time impedance measurements. However, this protection by *Bid* knockout was independent of GSH depletion which occurred upstream of BID transactivation. In contrast, *Bid* KO led to the complete abrogation of lipid peroxidation and mitochondrial ROS formation. Moreover, *Bid* knockout preserved the mitochondrial membrane potential, mitochondrial energy metabolism as well as healthy morphology, thus exposing BID as a key link of death signaling pathways starting with disrupted GPX4 redox homeostasis and culminating in mitochondrial damage in neuronal cells. Since the effects of *Bid* knockout were circumvented by reintroduction of either full-length or active truncated BID and the fact that the CRISPR knockout cells were still susceptible to cell death induction by staurosporine, the protection against glutamate and erastin toxicity can be specifically attributed to *Bid* knockout while excluding general resistance to cell death.

Taken together, these results strongly suggest BID being transactivated in the course of glutamate- and erastin-mediated oxidative death in neuronal cells, thus contrasting the previous observations in cancer cells by Dixon et al., where BID was not involved in erastin-induced ferroptosis demonstrated by using an shRNA library targeting most known genes encoding mitochondrial proteins [38]. In addition, the presented involvement of BID is in good agreement with earlier studies providing evidence for a key role of BID in models of oxytosis, glutamate excitotoxicity and oxygen glucose-deprivation, and in *in vivo* models of cerebral ischemia and brain trauma [14,15,31,72,103,140,186], where BID was shown to mediate mitochondrial fragmentation, ROS production and release of apoptosis inducing factor. Hence, the concept of BID-mediated mitochondrial damage is transferrable to mechanisms of ferroptosis in neuronal cells.

For further clarification of merged pathways of oxytosis and ferroptosis, the commonly used ferroptosis inhibitor liproxstatin-1 [53,167,227] was analyzed with respect to potential protection against glutamate-induced cell death in HT22 cells. Liproxstatin-1, a spiroquinoxalinamine derivative initially believed to act through LOX inhibition, is now recognized as a radical-trapping antioxidant (RTAs) in lipid bilayers being able to suppress ferroptosis *in vitro*, in *Gpx4*$^{-/-}$ mice and in a pre-clinical model of ischemia/reperfusion-induced hepatic damage [53].

In HT22 cells, liproxstatin-1 completely prevented cell death by both erastin and glutamate up to 6 hours post-treatment independent of GSH depletion, suggesting a critical amount of accumulating lipid peroxides reached at this time-point. In addition, liproxstatin-1 was effective in rescuing lipid peroxidation, mitochondrial ROS formation, loss of mitochondrial membrane potential and alterations of mitochondrial morphology when applied in combination with glutamate or erastin, respectively providing compelling evidence for joint cell death pathways of oxytosis and ferroptosis.

In conclusion, these data suggest that ferroptosis in neurons is merged with previously separated pathways of oxytosis through BID transactivation to mitochondria, thereby underlining mitochondrial damage as the crucial point of decision for neuronal function and survival. Such BID-dependent mitochondrial death pathways involve fragmentation of the organelles, impaired ATP synthesis, and loss of mitochondrial membrane potential and mitochondrial membrane integrity. Subsequently, mitochondrial damage results in the release of pro-apoptotic factors such as AIF and Cytc providing potential new therapeutic intervention strategies in preventing neuronal death at different levels of cellular stress. Such approaches may include ferroptosis inhibitors, inhibitors of lipid peroxidation and strategies of mitochondrial protection through inhibition of BID.

In light of this discussion, the exact mechanisms underlying BID activation by ROS and the precise biochemical pathway of BID-mediated mitochondrial damage upon oxidative stress require further investigation. During apoptosis, BID is activated to tBID by cleavage *via* caspases or calpains. However, this potential mechanism of BID activation was excluded in oxidative death in HT22 cells, as pan caspase inhibitors, such as z-VAD-fmk, or calpain inhibitors were not able to rescue the cells from glutamate toxicity [54,103,194]. In addition, to date, tBID was not detectable following glutamate challenge by Western blot analysis. Instead, full-length BID was observed translocating to the mitochondria after glutamate or erastin challenge, suggesting a cleavage-independent activation machinery already proposed by König et al. in excitotoxic death in hippocampal rat neurons [99]. Therefore, ROS seem to activate BID in a different way than in apoptosis. Garcia-Perez et al. previously revealed involvement of ROS in the progression of tBID-induced Cytc release by sensitizing the mitochondria for OMM permeabilization [61]. *Vice versa*, tBID stimulated mitochondrial ROS production to coordinate the permeabilization of mitochondria using an *inter-mitochondrial amplification mechanism* to propagate Cytc release and to establish an all-or-none response of OMM permeabilization. Similarly, Ding et al. linked BID to mitochondrial ROS generation by demonstrating that BID-deficient hepatocytes exhibited significantly less mitochondrial ROS upon induction of apoptosis [37].

In this context, several *BID-receptors* at the mitochondria have been suggested, such as BAX [18], cardiolipin ([68,112]) or MTCH2 [92,146], all of which are not sufficiently analyzed yet regarding their specific contribution to oxidative death in HT22 cells. At least for BAX an upregulation after glutamate-induced cell death in HT22 cells has been described [107,224], however, the necessity of BAX for oxidative death in HT22 cells is still not settled. On the other hand, mechanisms of tBID directly re-arranging the inner mitochondrial membrane associated with mobilization of Cytc are known, which do not depend on BAK [161].

In summary, BID was exposed as a key mediator of mitochondrial damage in neuronal ROS-associated regulated cell death, however, the exact underlying biochemical pathways inducing BI transactivation and mitochondrial damage require further research.

4.2 Mitochondrial rescue prevents GPX4-dependent ferroptosis

Ferroptosis is defined to occur as a consequence of lethal lipid peroxidation owing to disrupted GPX4 redox homeostasis [180]. Glutamate and erastin indirectly mediate such oxidative cell death by GSH depletion and have been intensively studied in HT22 cells in particular in the context of mitochondrial damage. However, ferroptosis induction by direct GPX4-inhibition has not yet been reported in this neuronal cell-line. Therefore, *1S, 3R*-RSL3 was exploited as a validated GPX4-inhibiting compound. In recent publications, *1S, 3R*-RSL3 was established as a potent inactivator of GPX4 in a variety of cells through covalent binding by its electrophilic chloroacetamide moiety to selenomethionine being specific for this isomeric form [211,212].

Analogous to these findings, the *1S, 3R*-RSL3 isomer induced cell death in HT22 cells in a very low nanomolar range whereas the RSL3 isomers exhibited unspecific toxicity with 1000-fold less potency which underlines the specific toxicity of RSL3 attributed to its unique spatial conformation and which is in general agreement with earlier reports by Yang and co-workers [211]. Interestingly, MEF cells and primary murine and rat cortical neurons were less sensitive to *1S, 3R*-RSL3 treatment requiring low micromolar concentrations for cell death induction, which may be attributed to cell-specific oxidative stress vulnerability by individual redox defense mechanisms and different levels of proteins involved in redox homeostasis. Notably, *1S, 3R*-RSL3 treatment not only inactivated GPX4 but also led to a remarkable reduction in GPX4 protein levels after 9-10 hours of treatment which may be caused by protein-degradation *via* proteases once GPX4 is inactivated [53]. More interestingly, even at high micromolar concentrations, the corresponding des-chloro-derivative *1S, 3R*-RSL3-Cl was no longer active, supporting the conclusion that chlorine is an indispensable chemical feature for covalent GPX4 active site binding and subsequent inactivation.

Analyzing the detailed time-course of biochemical events following RSL3-induced disruption of the redox homeostasis, it was shown that lipid peroxidation as well as mitochondrial ROS formation already occur 2 hours after RSL3 treatment in HT22 and MEF cells, underlining the potent redox homeostasis disruption following GPX4 inhibition. The observed ROS production was closely followed by loss of mitochondrial membrane potential, reduced energy metabolism, excessive mitochondrial fragmentation, and cell death occurred 6-8 hours after RSL3 challenge. These data match those of erastin by demonstrating mitochondrial damage as a prerequisite for cell death, however, cell death by RSL3 is much faster than by erastin given the fact that RSL3 directly targets GPX4 while erastin targets xCT-mediated cystine import, which is necessary for GSH synthesis, thereby indirectly affecting GPX4 activity which is essential for maintenance of the cell's redox defense by catalyzing the detoxification of oxidative 12/15-LOX products and inhibition of 12/15-LOX activity. The observed results confirm findings from prior work in various different cell types which documented specific hallmarks of erastin, RSL3 or GPX4 KO induced ferroptosis, such as toxic iron overload, disturbed GSH/GPX4 redox homeostasis and lipid peroxidation through 12/15-LOX or autoxidation [38,41,90].

In order to verify BID involvement in this additional paradigm of oxidative cell death, CRISPR *Bid* knockout cells were exposed to RSL3 and the BID inhibitor BI-6c9 was tested. *Bid* KO cells were at least 1000-fold less sensitive compared to HT22 wildtype cells and the BID inhibitor was again able to abrogate cell death and mitochondrial damage-associated parameters, such as lipid peroxidation, mitochondrial ROS formation and loss of the mitochondrial membrane potential, suggesting a vital role for BID in the execution of RSL3-induced cell death. The BID inhibitor and the commonly known ferroptosis inhibitors liproxstatin-1, ferrostatin and deferoxamine, were potent in preventing RSL3-induced cell death until 4 to 6 hours of post-treatment, rendering them promising therapeutics in future approaches against ferroptosis. However, these results also imply *the point of no return* to occur earlier than in glutamate- or erastin-induced oxidative death.

Seiler et al. already demonstrated AIF to be crucially involved in GPX4-mediated oxidative cell death [162], which was supposed to apply to RSL3-induced GPX4 disruption as well. Indeed, siRNA-mediated knockdown of AIF led to a significant reduction of RSL3-toxicity in HT22 cells. Similar to other pathways of caspase-independent programmed cell death, mitochondrial damage and the subsequent AIF release is considered a hallmark of the ultimate steps leading to lethal signaling cascades. The present finding on protective effects of AIF siRNA is, thus, well in line with earlier studies demonstrating cell death involving AIF after oxidative damage induced by X_c^- inhibition or genetic GPX4 deletion and AIF depletion-mediated preconditioning effects at the mitochondrial site [31,103,162]. In line with Öxler et al. [133], in RSL3-induced mitochondrial damage it can be assumed that preconditioning by siRNA-mediated AIF knockdown also protects from oxidative cell death through stabilized mitochondria and reduced complex I activity.

Oxidative stress induced mitochondrial damage has been described as a key decision point in neuronal cells undergoing cell death. Assuming that protecting mitochondria, similar to what has been shown for AIF depletion, might prevent ferroptosis, significant protection was found by application of the radical scavenger MitoQ which is targeted to the mitochondria [94,95]. This mitochondrial accumulation is facilitated *via* the positive charge which is spread over a large, hydrophobic surface area, allowing these cations to pass easily through membranes and to accumulate in the mitochondrial matrix in response to the membrane potential [151]. This accumulation was revealed to be 1000-fold more efficient than with the more hydrophobic molecule coenzyme Q10, which has received increasing attention as therapeutic and preventive intervention for neurodegenerative disorders [214]. However, in the treatment of Parkinson's patients, Q10 did not improve motor symptoms although well-tolerated and safe as assessed by meta-analysis of randomized controlled trials [226]. In addition, a clinical study of Q10 in Huntington's disease also failed to slow the progressive functional decline [121].

Despite a considerable amount of studies investigating MitoQ [94,95], no evidence was available for the detailed protective mechanism in regulated oxidative cell death. The results presented here show that the cytoprotective effect of MitoQ was indeed mediated by selective attenuation of mitochondrial ROS formation during oxidative cell death through reduced mitochondrial respiration and concomitantly enhanced glycolytic function, which has been already described by Fink et al. in isolated mitochondria and in bovine aortic endothelium cells (BAE) [52]. It was further revealed that MitoQ significantly protected from RSL3-induced lipid peroxidation, mitochondrial ROS formation, loss of mitochondrial membrane potential and cell death, and that its protective potential was lost upon glycolysis inhibition by 2-desoxyglucose. Notably, at low cytoprotective concentrations MitoQ rescued only mitochondrial parameters of oxidative cell death but did not affect RSL3-mediated increases in lipid peroxidation detected upstream of mitochondrial damage which proves selective ROS scavenging within the mitochondria. This finding thereby implies a mechanism of action through increased tolerance to oxidative stress at the level of mitochondria without affecting non-mitochondrial ROS formation, which the cells can overcome. Such mitochondrial protection by MitoQ was sufficient for cell survival despite GPX4 inhibition and pronounced lipid peroxidation. Of note, MitoQ application alone rapidly led to a modest mitochondrial fragmentation which may be attributed to architectural changes of the mitochondrial membrane upon absorption of MitoQ to the matrix surface of the inner membrane and might contribute to reduced respiratory chain function which has been established by Roginsky and co-workers [150]. The reduced respiratory chain function and simultaneously enhanced glycolysis might also contribute to a preconditioning effect rendering mitochondria resistant to oxidative stress.

Notably, the neuroprotective concentrations of commercially available MitoQ were limited to a small range of 0.5 to 1 μM. Concentrations below 0.5 μM did not provide protection, while concentrations higher than 1.0 μM had cytotoxic effects which limited the maximum protection during oxidative stress in the model system of cultured neuronal HT22 cells. Although at low protective concentrations, the ROS scavenger MitoQ rescued mitochondrial morphology, respiratory function and cell viability, MitoQ treatment induced opposite effects at higher concentrations, i.e. enhanced ROS production and accelerated loss of mitochondrial membrane potential [141]. Pro-oxidant properties of MitoQ can be explained by redox cycling with superoxide production by its semiquinone form at two sites of the mitochondrial complex I, which has been observed by several groups [44,130], and has been eliminated in optimized molecules SkQ_n [172] with a greater therapeutic window. Increased ROS production upon MitoQ application has been published to cause the upregulation of autophagy in several cancer cell lines in an ATG7- and KEAP1/NRF2-dependent manner, thereby sensitizing cancer cells to MitoQ-induced cell death. *Vice versa,* autophagy acted as an antioxidant feed-back triggered by toxic levels of MitoQ [67,148]. The findings on reduced mitochondrial respiration and the according increases in glycolysis activity after MitoQ exposure are in line with earlier findings showing MitoQ mediated mtDNA damage in MDA-MB-231 and H23 cancer cells, thereby decreasing expression of mitochondrial-encoded respiratory chain subunits, which was also compensated by increased glycolytic activity [141]. As a consequence of glycolytic shift, MitoQ displayed chemotherapeutic effects in combination with 2-DG, which synergistically sensitized cancer cells to cell death as they, to some extent, already shifted their energy metabolism towards glycolysis (Warburg effect), which can be intensified by MitoQ [22].

In this thesis, further investigation on the potential mechanism of MitoQ revealed no rescue activity against tBID-induced cell death. TBID overexpression, which mediates mitochondrial disruption and release of pro-apoptotic factors to the cytosol in HT22 cells, was unaffected by MitoQ which rather harmed the cells even more.

In the development of MitoQ as a pharmaceutic drug for human application, it passed through conventional animal toxicity and oral bioavailability was determined at about 10% [173]. In human phase I trials MitoQ was demonstrated to have adequate pharmacokinetic properties with oral dosing at 80 mg (1 mg/kg) resulting in a maximum plasma concentration of ~33 ng/mL after one hour. Currently, oral MitoQ supplementation with 40- 80 mg per day is evaluated in clinical phase II studies on Parkinson's disease [174], hepatitis C virus (HCV) mediated rise in liver enzymes [60], non-alcoholic fatty liver disease (NAFLD), fatigue in multiple sclerosis (MS), chronic kidney disease, and ageing. The study on PD included newly diagnosed untreated patients in a double-blind study of 40 and 80 mg doses of MitoQ over 12 months, however, no difference between MitoQ and placebo on any measure of PD progression was found. This might not necessarily imply ineffectiveness of MitoQ but rather result from insufficient accumulation in the brain and/or the fact that upon diagnosis of PD more than 50 % of dopaminergic neurons are already lost so that treatment at this stage fails. In contrast, in non-responder or unsuitable standard-of-care HCV patients a significant effect of 40 and 80 mg oral MitoQ for 28 days with respect to serum alanine transaminase (ALT) was found.

Unfortunately, the remaining studies have been either terminated due to poor participant recruitment or they are still in the recruitment process. Importantly, these studies provide safety data for the long-term administration of MitoQ in humans. Despite mild dose-dependent nausea, no severe adverse events were reported in either study. However, these studies present heterogeneous results requiring more in-depth investigation for targeted therapy of oxidative mitochondrial diseases.

In conclusion, the present study provides convincing evidence for the substantial involvement of mitochondrial impairment in GPX4-dependent oxidative death (Figure 90) and exposes the protection upstream of mitochondria by BID inhibition or by targeted mitochondrial antioxidants as essential therapeutic strategies for diseases featuring ferroptosis as an underlying mechanism of cell death. However, the exact molecular mechanisms orchestrating mitochondrial damage in the respective pathologic conditions, such as AD, PD or ischemic stroke, have to be elucidated first before predicting the response to targeted mitochondrial therapy. In particular, the activation of BID triggered by oxidative stress and the mode of action how exactly BID mediates mitochondrial damage require further investigation.

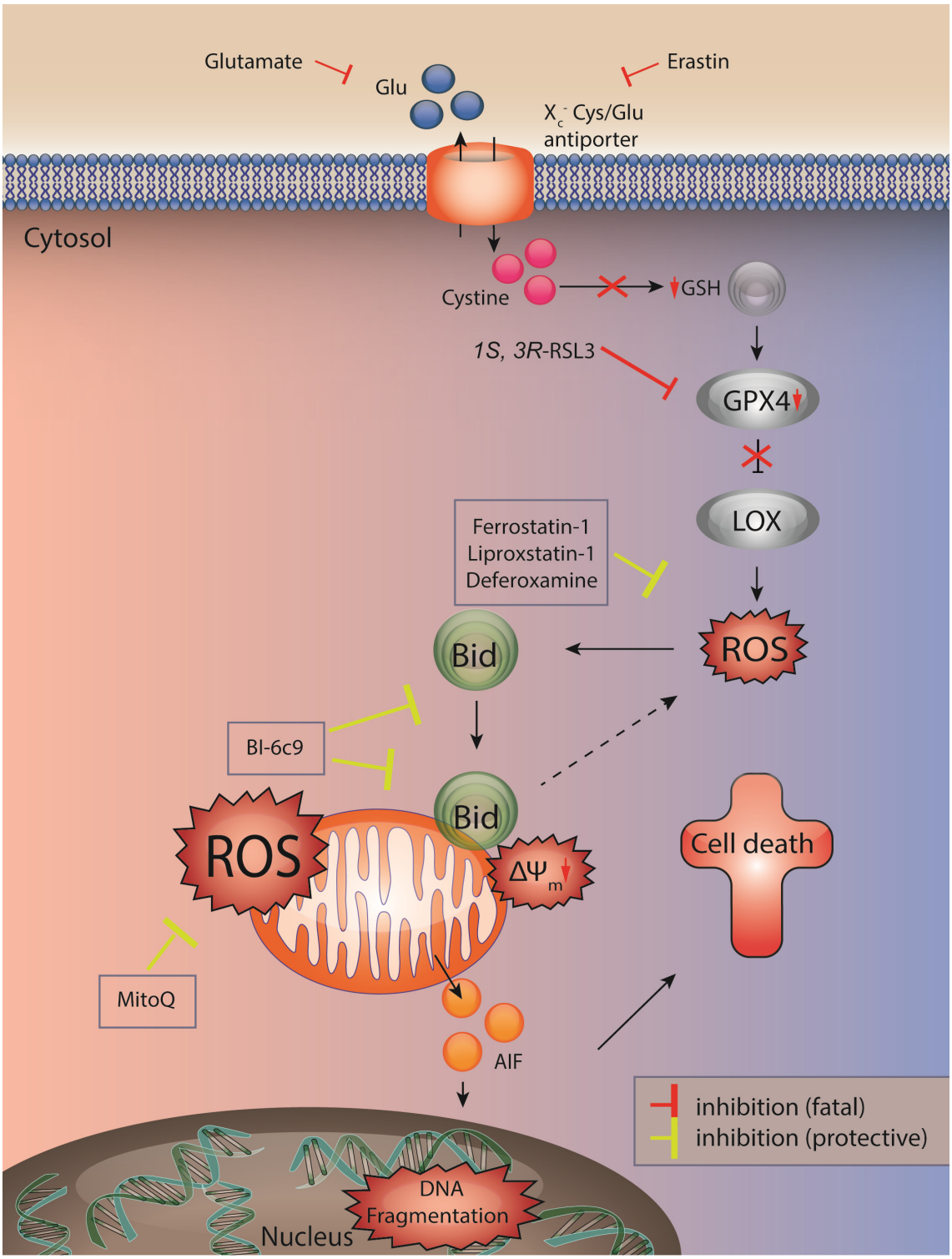

Figure 90. GPX4-dependent oxidative cell death

4.3 BID crystallization for structure-based design of BID inhibitors

Having outlined the great significance of BID transactivation during oxidative cell death mechanisms, BID inhibition became a sensible therapeutic option for treating neurodegenerative disorders involving oxidative stress. To date, solution NMR structures for human and mouse BID have been presented [26,120] suggesting eight α-helices arranged in a compact fold of which helices H6 and H7 are arranged in an antiparallel manner in the core of the protein. The remaining six helices are amphipathic and packed around the two core helices. In addition, a flexible unstructured intramolecular loop and N-terminus were observed sharing significant similarity with other BCL2 family members, such as BCL-XL [124]. Despite these NMR structures, crystal structures of just the BID BH3 peptide in complex with BCL-XL [147] or BAX [32] are available. However, high-resolution atomic X-ray data of full-length BID are still desirable for *in silico* optimization of existing lead structures of BID inhibitors [10,13,14,131,131] improving specificity and application as future therapeutics.

In the course of this thesis, a variety of BID constructs and crystallization screens were performed based on previously established protocols [132]. Initial crystals obtained of purified Bid3 lacking the flexible N-terminus and intracellular unstructured loop were optimized by cysteine-to-serine mutations (CCSS) thereby preventing unspecific GSH binding and increasing protein homogeneity after purification. Indeed, Bid3 CCSS crystals grew larger and in a reproducible fashion. Crystallization conditions comprising PEGs or MPD and divalent cations, such as magnesium, cobalt and calcium, facilitated crystal growth and led to an improvement of crystal size. Unfortunately, crystal analysis at the synchrotron microfocus beamline in Grenoble displayed insufficient resolution for solving the atomic structure and molecular replacement did not work with the electron density data either. Although additional heavy-atom exchange approaches were successful in terms of reliable purification and crystal growth, these data could not aid structural elucidation of Bid3 crystals. These results might be attributed to insufficient crystal quality which should be optimized for future structural analyses. As purification and crystallization condition optimization has been almost exhausted and is reaching its limits, strategies for improving crystal growth quality would comprise altering Bid constructs by mutation rather than testing further crystallization conditions. Ideally, the constructs should be mutated back in the direction of full-length Bid including parts of the flexible loop as this would reduce the chance of artificially altered protein folding.

Co-crystallization attempts of BID constructs with different BID inhibitors mostly resulted in precipitation of BID inhibitors alone or Bid-inhibitor complex at the time of adding the inhibitor to the protein solution, however, some small crystals were obtained, which might be composed of the respective Bid construct and the inhibitor in a co-crystal. Unfortunately, these crystals need further improvement in their quality as their diffraction properties with ~3 Å were insufficient to solve their 3D structure. Hence, a diffraction resolution of less than 2-3 Å would be ideal.

Full-length BID purification, which was desirable to prevent artificial protein crystal structures, unfortunately, did not result in any crystal growth presumably due to unspecific cleavage resulting in a heterogeneous protein solution of BID fragments. As crystal growth is more likely in conditions of homogeneous proteins, future approaches should aim at preventing unspecific protein cleavage by cloning of full-length Bid constructs that do not require thrombin cleavage. For instance, TEV proteases could be used to remove His- or GST-tags by insertion of TEV protease cleavage sites (ENLYFQ\S motifs) into the protein constructs [136].

In addition to mouse Bid constructs, using human Bid constructs would be a reasonable strategy to obtain altered and ideally well-diffracting crystals. Another approach for improving diffraction properties by stabilizing protein crystals is to fuse T4 lysozyme to the flexible N-terminus of the protein by cloning as Zou et al. described for facilitating crystallogenesis of the β2 adrenergic receptor [230]. T4 lysozyme is a well-folded protein forming crystals under a variety of conditions thus stabilizing flexible protein regions upon fusion. Other fusion partners for the stabilization and crystallization of G protein-coupled receptors, such as rubredoxin, xylanase, flavodoxin and thermostabilized apocytochrome b562 (BRIL), have been described by Chun et al. [27] and would be worthwhile in testing for the purpose of stabilizing the Bid protein during crystallization. These fusion techniques for crystallization in the presence of detergent could be used for tBID crystallization, which has not been successful to date owing to low bacterial expression and due to hydrophobicity leading to amorphous protein precipitation.

In conclusion, a promising basis for further optimization of Bid crystallography has been established in this thesis, thus facilitating future approaches in solving the 3D structure of BID.

5 Summary

Age-related neuropathologies, such as Alzheimer's and Parkinson's disease as well as acute brain injury commonly involve oxidative stress-induced disruption of the intracellular calcium homeostasis, disturbed redox balance and impaired energy metabolism attributed to mitochondrial damage which eventually drives neuronal cells to death. Thus, identifying biochemical features underlying the detrimental impairment of mitochondrial integrity and function is key to develop therapeutic strategies preventing neuronal loss. To date, a great variety of regulated cell death modalities has been established in neuronal death. In particular, apoptosis, excitotoxicity and regulated necrosis were shown to play a prominent role, and tight crosstalk between these paradigms of cell death exists, especially via convergence at the mitochondria. Despite increasing knowledge on cell death pathways, for many neurodegenerative diseases no curative treatment is available, so far.

Over the last decades, a number of publications proposed the involvement of BCL-2-family proteins like BID and BAX in mediating mitochondrial cell death. For the protein BID, the contribution to neuronal apoptosis during ischemia has been widely established *in vivo*, exposing BID inhibition as a promising future therapy option. However, in non-apoptotic models of oxidative cell death, for instance ferroptosis, the role of BID and involvement of mitochondrial damage in cell death execution remained to be elucidated. In addition, the exact mechanisms how lipid ROS formation triggers BID activation and mitochondrial demise are still unknown. Due to high energy utilization for the maintenance of the membrane potential, neurotransmitter synthesis and restoring intracellular ion pools after action potentials, neurons strongly rely on oxygen and functional energy metabolism, thus being vulnerable to loss of mitochondrial function.

The aim of this study was to determine hallmarks of regulated oxidative cell death pathways with respect to their time-dependent progression, involvement of BID as well as mitochondrial damage. Therefore, CRISPR/*Cas9* technology was applied to generate neuronal HT22 cell lines lacking BID in order to analyze their sensitivity to oxidative stress induced by erastin and RSL3. Further, protective effects of MitoQ were investigated to evaluate the therapeutic potential of this mitochondria-targeted ROS scavenger in models of ferroptosis. Additionally, this work aimed to improve BID crystallization with novel recombinant protein constructs and optimized crystallization conditions.

The first part of the thesis reports on the involvement of mitochondrial damage in oxidative death signaling in neuronal HT22 cells and mouse embryonic fibroblasts. In the model of glutamate-induced oxytosis, which is concentration- and cell density-dependent, impairment of mitochondrial respiration occurred in a time-dependent manner. In this cell death paradigm mitochondrial damage was represented the point of no return in the cell's commitment to die as the well-established BID inhibitor BI-6c9 could rescue the cells within a time window of up to 8 hours after onset of glutamate exposure when massive mitochondrial damage was observed. The comprehensive analysis of erastin-induced oxidative death revealed a close interconnection of the previously separated cell death pathways of oxytosis and ferroptosis. In a time-dependent manner, erastin induced loss of mitochondrial membrane potential and lipid peroxidation followed by cell death 8 to 10 hours after treatment onset. Mitochondrial ROS production and loss of mitochondrial function was observed after 6 hours, and was tightly connected to severe mitochondrial fission thereby underlining the major finding of mitochondrial damage as the converging point of death signaling in neural and MEF cells in this paradigm of erastin-induced ferroptosis. In addition, siRNA-mediated AIF knockdown mitigated cell death in HT22 cells exposed to erastin, revealing a significant role for AIF release from mitochondria in ferroptosis similar to earlier findings in glutamate-induced oxytosis.

The second part of the thesis focused on the involvement of BID in mitochondrial cell death pathways. SiRNA approach and CRISPR/*Cas9 Bid* knockout in HT22 cells revealed a significant contribution of BID in mediating mitochondrial demise upon oxidative stress. BID deprived cells were not only protected against glutamate- or erastin-induced cell death but also their mitochondrial parameters, such as membrane potential, ROS production and morphology were preserved at control levels. In contrast, tBID overexpression in *Bid* KO cells reversed the protective effects of BID absence and led to a significant increase in lipid ROS formation and cell death. In addition to shared BID involvement, mechanistic overlap of oxytosis and ferroptosis could be shown by the comparable cell protection against glutamate and erastin challenge by the ferroptosis inhibitor liproxstatin. Direct GPX4 inhibition by *1S, 3R*-RSL3 and protection mediated by the mitochondria-targeted antioxidant MitoQ further established significant contribution of ROS formation to mitochondrial damage and again highlighted a role for BID as *Bid* KO cells were less sensitive to RSL3-mediated ferroptosis. Overall, these findings highlight a key role for BID in both paradigms of oxytosis and ferroptosis and expose BID transactivation to the mitochondria, mitochondrial oxidative damage and AIF-release as common mechanistic hallmarks linking these pathways.

Finally, the 3D structure of BID should be elucidated by X-ray crystallography and, therefore, novel recombinant Bid constructs were established. For the first time, BID crystals could be obtained in a reproducible manner and were optimized by improving protein constructs and crystallization conditions. In order to solve the phase problem, selenomethionine crystals were grown, however, the resolution of electron density data was not sufficient to solve the molecular 3D structure of BID but provide a promising basis for further optimization.

6 Zusammenfassung

Altersbedingte neuronale Erkrankungen, wie Alzheimer oder Parkinson sowie akute Hirnschädigungen nach Schlaganfall oder Schädel-Hirn-Trauma sind durch nachhaltige Störungen der zellulären Homöostase in Neuronen gekennzeichnet. Dies ist in der Regel verbunden mit einer Entgleisung der intrazellulären Calciumhomöostase, einem gestörten Redoxgleichgewicht und Energieverlust, was über die Schädigung der Mitochondrien weiter verstärkt wird und schließlich zum Zelltod führt. Folglich ist die Aufklärung biochemischer Signalkaskaden des neuronalen Zelltods eine wesentliche Voraussetzung dafür, neue und effektive therapeutische Konzepte zu entwickeln. Bislang konnten verschiedene Modalitäten des regulierten Zelltods in Neuronen identifiziert werden, darunter Mechanismen der Apoptose, Exzitotoxizität sowie regulierten Nekrose. Diese verschiedenen Mechanismen münden wahrscheinlich alle in einer Schädigung der Mitochondrien, die damit in der Regulation des neuronalen Zelltods eine entscheidende Rolle einnehmen. Trotz zunehmender Erkenntnisse über spezifische Signalwege des regulierten Zelltods steht bislang keine kurative Therapie für neurodegenerative Erkrankungen zur Verfügung.

Frühere Arbeiten haben aufgezeigt, dass pro-apoptotische BCL-2 Proteine wie BID und BAX eine entscheidende Rolle bei mitochondrialen Mechanismen des Zelltods spielen. *In vivo* konnte nachgewiesen werden, dass BID an der neuronalen Apoptose entscheidend beteiligt ist, so dass die Hemmung dieses Proteins einen vielversprechenden Ansatz für zukünftige Therapien darstellt. Hingegen sind die Beteiligung von BID und die Schädigung der Mitochondrien in nicht-apoptotischen Zelltodmodellen, wie z.B. der Ferroptose, weitgehend unklar. Neurone sind auf einen funktionierenden Energiestoffwechsel angewiesen, da sie für die Aufrechterhaltung des Membranpotentials, die Neurotransmittersysnthese sowie für die Wiederherstellung der Ionenhomöostase nach einem Aktionspotential viel Energie brauchen, was sie wiederum für Schäden durch Sauerstoff- und Energiemangel anfällig macht.

Das Ziel dieser Studie war es, die Schlüsselmechanismen des regulierten oxidativen Zelltods aufzuklären sowie den Zeitverlauf entsprechend darzustellen und hier insbesondere die Rolle von BID bei der Schädigung der Mitochondrien zu charakterisieren. Dafür wurden mithilfe der CRISPR/*Cas9* Technik *Bid* knockout Zellen generiert und deren Empfindlichkeit gegen die Ferroptose-Induktoren Erastin und RSL3 untersucht. Als weitere therapeutische Strategie wurde die Behandlung mit MitoQ analysiert, das reaktive Sauerstoffmoleküle spezifisch in den Mitochondrien abfängt. Ferner sollte die BID Kristallisation durch Entwicklung neuer rekombinanter Bid Konstrukte und Kristallisierungskonditionen optimiert werden.

Im ersten Teil der Studie wurde die Regulation des oxidativen Zelltods in MEF und neuronalen HT22 Zellen untersucht. Im Modell der Glutamat-induzierten Oxytose konnte ein zeitabhängiger Verlust der mitochondrialen Atmung beobachtet werden. In diesem Modell konnte mithilfe des BID-Inhibitors BI-6c9 nachgewiesen werden, dass die mitochondriale Schädigung durch BID den kritischen Punkt im oxidativen Zelltod darstellt. Nach funktioneller und struktureller Schädigung der Mitochondrien kann der Zelltod nicht mehr aufgehalten werden. Die Analyse des Erastin-induzierten Zelltods ergab mechanistische Überschneidungen der bislang separat betrachteten Zelltod-Modalitäten von Oxytose und Ferroptose. Erastin verursachte ähnlich zur Oxytose den Verlust des mitochondrialen Membranpotentials und die Produktion von Lipidperoxiden. Diesen folgte der Zelltod innerhalb von ca. 8-10 Stunden. Das Auftreten mitochondrialer reaktiver Sauerstoffspezies und der Verlust der mitochondrialen Funktion wurde 6 Stunden nach Erastinexposition beobachtet, und trat zeitgleich mit morphologischen Veränderungen der Mitochondrien auf. Des Weiteren konnte gezeigt werden, dass der Apoptose-induzierender Faktor AIF ebenfalls eine wichtige Rolle in der Erastin-induzierten Ferroptose spielt. Die siRNA-vermittelte Depletion von AIF verminderte den ferroptotischen Zelltod analog zu früheren Befunden aus dem Modell der Glutamat-induzierten Oxytose.

Der zweite Teil befasste sich mit der Beteiligung des BCL-2 Proteins BID in mitochondrialen Prozessen des oxidativen Zelltods. Die Depletion von BID mittels siRNA oder CRISPR/*Cas9* schützte die Zellen vor einer Schädigung der Mitochondrien und Ferroptose. Dies unterstreicht die entscheidende Rolle der BID-Aktivierung bei den Schlüsselmechanismen der Mitochondrienschädigung im oxidativen Zelltod. Folgerichtig führte die Reexpression von aktiviertem tBID zu einer Auslöschung des protektiven Effekts durch die BID-Depletion und induzierte wiederum Lipidperoxidation, mitochondriale Schädigung und Zelltod.

Abgesehen von der gemeinsamen Beteiligung von BID in Oxytose und Ferroptose konnten die mechanistischen Übereinstimmungen zudem dadurch nachgewiesen werden, dass der Ferroptoseinhibitor Liproxstatin HT22 Zellen auch gegen Oxytose schützte. Die direkte Inaktivierung des Enzyms GPX4 mithilfe von *1S, 3R*-RSL3 und die gleichzeitige Protektion der Mitochondrien mithilfe von MitoQ belegen ebenfalls die signifikante Bedeutung der Mitochondrienschäden im Zelltod durch oxidativen Stress. Dieser Teil der Studien untermauerte auch die entscheidende Rolle von BID, da *Bid* KO Zellen auch hier weniger sensibel auf die RSL3-Behandlung reagierten. Zusammengefasst unterstreichen diese Ergebnisse eine besondere Beteiligung von BID in den beiden Zelltodmodellen Oxytose und Ferroptose und belegen, dass die Aktivierung von BID, die Mitochondrienschädigung und AIF-Abhängigkeit in diesen bislang getrennt betrachteten Zelltodmodalitäten identisch sind.

Abschließend sollte die 3D-Struktur von BID mittels Röntgenstrukturanalyse untersucht werden. Dazu wurden neuartige rekombinante Bid Konstrukte und deren Reinigung etabliert. Zum ersten Mal konnten Kristalle reproduzierbar erzeugt und optimiert werden, in dem die Bid Konstrukte und Kristallisationsbedingungen sukzessive verbessert wurden. Um das Phasenproblem zu lösen, wurden Selenomethionin-Kristalle gezüchtet, deren errechnete Elektronendichten am Ende nicht ausreichten, um die molekulare Struktur abschießend zu klären. Dennoch bieten die erhobenen Daten eine vielversprechende Grundlage für weitere Optimierungsversuche.

7 Abbreviations

°C	Degree Celsius
µL	Microliter
µM	Micromolar
12/15 LOX	12/15 Lipoxygenase
2-DG	2-Desoxyglucose
AA	Antimycin A
ACSL4	Long-chain-fatty-acid—CoA ligase 4
AD	Alzheimer's Disease
AIF	Apoptosis inducing factor
ALS	Amyotrophic lateral sclerosis
AMPA	α-amino-3-hydroxy-5-methyl-4-isoxazolepropionic acid
AMR	ATP monitoring reagent
ANOVA	Analysis of variance
APAF-1	Apoptotic protease-activating factor 1
APOE	Apolipoprotein E
APP	Amyloid precursor protein
ATP	Adenosinetriphosphate
BAD	Bcl-2 antagonist of cell death
BAK	Bcl-2 antagonist killer 1
BAX	Bcl-2 associated x protein
BCA	Bicinchonic acid
BCL-2	B-cell lymphoma-2
BCL-XL	Bcl-2 related gene, long isoform
BH	Bcl-2 homology
BI	BID inhibitor
BID	Bcl-2 interacting domain death antagonist
BIK	Bcl-2-interacting killer
BIM	Bcl-2-interacting mediator of cell death
BODIPY	4,4-Difluoro-5-(4-phenyl-1,3-butadienyl)-4-bora 3a,4a-diaza-s-indacene-3-undecanoic acid
BOK	Bcl-2 related ovarian killer
Bp	Base pairs
BSA	Bovine serum albumin
Ca^{2+}	Calcium
Cas9	CRISPR associated protein 9
Casp	Caspase
cBid	Caspase-8 cleaved Bid

CCCP	Carbonyl cyanide chlorophenyl hydrazone
CCI	Controlled cortical impact
CD95	Cluster of differentiation 95
CL	Cardiolipin
Cl^-	Chloride
CLSM	Confocal laser scanning microscopy
CNS	Central nervous system
CO_2	Carbon dioxide
COX	Cyclooxygenase
CRISPR	Clustered regularly-interspaced short palindromic repeats
Cu^+	Copper
Cytc	Cytochrome C
DAMP	Damage-associated molecular pattern
DAPI	4',6-Diamidino-2-phenylindole
DCF	Dichlorodihydrofluoresceinediacetate
Def	Deferoxamine
DMEM	Dulbecco's Modified Eagle Medium
DMSO	Dimethyl sulfoxide
DNA	Desoxyribonucleic acid
DRP1	Dynamin-related protein 1
DSB	Double-strand break
DTT	DL- Dithiothreitol
EBSS	Earl's balanced salt solution
EC50	Half maximal effective concentration
ECAR	Extracellular acidification rate
EDTA	Ethylenediamine-tetra-acetic acid
EGFP	Green fluorescent protein
EGTA	Ethylene glycol-bis(2-aminoethylether)-N,N,N',N'- tetraacetic acid
EndoG	Endonuclease G
FACS	Fluorescence-activated cell sorting
FADD	Fas-associated protein with death domain
FasL	Fas ligand
FCCP	Carbonyl cyanide-4-(trifluoromethoxy)phenyl-hydrazone
FCS	Fetal calf serum
Ferro	Ferrostatin-1
FLIP	FLICE-inhibitory proteins
FT	Flow-through
GAPDH	Glyceraldehyde-3-phosphatedehydrogenase
GFP	Green fluorescent protein

Glu	Glutamate
GPX4	Glutathione peroxidase 4
GSH	Hydrochloric acid
h	Hour
H_2O_2	Hydrogen peroxide
HBSS	Hank's balanced salt solution
HCl	Hydrogen chloride
HD	Huntington's disease
HDR	Homology-directed repair
HEPES	4-(2-Hydroxyethyl)piperazine-1-ethanesulfonic acid
HRP	Horseradish peroxidase
IAP	Inhibitors of apoptosis proteins
IMM	Inner mitochondrial membrane
IMS	Mitochondrial intermembrane space
IP3	Inositol trisphosphate
iPSC	Induced pluripotent stem cells
IPTG	Isopropyl-β-D-thiogalactopyranosid
kDa	Kilo Dalton
KO	Knockout
Lip	Liproxstatin-1
LOX	Lipoxygenase
LPCAT3	Lysophospholipid acyltransferase 5
MALDI-TOF	Matrix-assisted laser desorption/ionization time of flight
MCAO	Middle cerebral artery occlusion
MCL-1	Induced myeloid leukemia cell differentiation protein
MEF	Mouse embryonic fibroblast
MEM+	Eagle's minimum essential medium
MIF	Macrophage migration inhibitory factor
min	Minute
mL	Milliliter
mM	Millimolar
MNNG	Methylnitronitrosoguanidine
MOM	Mitochondrial outer membrane
MOMP	Mitochondrial outer membrane permeabilization
MOPS	3-(N-morpholino) propanesulfonic acid
mPTP	Mitochondrial permeability transition pore
mtDNA	Mitochondrial DNA
MTCH2	Mitochondrial carrier homolog 2
MTT	3-(4,5-Dimethylthiazol-2-yl)-2,5-diphenyltetrazolium bromide
N^2	Nitrogen
NAC	N-acetyl-L-cysteine

NADH	Nicotinamide adenine dinucleotide
NADPH	Nicotinamide adenine dinucleotide phosphate
$NaHCO_3$	Sodium hydrogen carbonate
NaOH	Sodium hydroxide
NCX	Na^+/Ca^{2+} exchanger
NHEJ	Non-homologous end joining
nM	Nanomolar
nm	Nanometer
NMDA	N-methyl-D-aspartic acid
NMR	Nuclear magnetic resonance
NO	Nitrogen monoxide
NO^+	Nitrosium ion
NOS	Nitrogen monooxide synthethase
NOXA	Phorbol-12-myristate-13-acetate-induced protein 1
OCR	Oxygen consumption rate
OGD	Oxygen-glucose deprivation
OMI/HrtA2	High temperature acquired protein A2
ORAI1	Calcium release-activated calcium channel protein 1
PAM	Protospacer adjacent motif
PBS	Phosphate buffered saline
PC	Phosphatidylcholin
PCD	Programmed cell death
PCR	Polymerase chain reaction
PD	Parkinson's Disease
PDB	Protein data bank
PE	Phosphatidylethanolamin
PEG	Polyethyleneglycole
PEI	Polyethylenimine
Pen/Strep	Penicillin + Streptomycin
PFA	Paraformaldehyde
pH	Potentia hydrogenii
PI	Propidium iodide
PL	Phospholipid
PLL	Poly-L-Lysine
PMSF	phenylmethylsulfonyl fluoride
PSEN	Presenelin
PTP	Permeability transition pore
PUFA	Polyunsaturated fatty acid
PVDF	Polyvinylidenfluorid

RCD	Regulated cell death
RIP	Receptor-interacting serine/threonine-protein
RNA	Ribonucleic acid
ROS	Reactive oxygen species
Rot	Rotenone
RSL3	RAS-selective lethal compound 3
RT	Room temperature
s	Second
Scr	Scrambled
SD	Standard deviation
SDS	Sodium dodecyl sulfate
SDS-PAGE	Sodium dodecyl sulfate polyacrylamide gel electrophoresis
SeMet	Selenomethionine
siRNA	Small interfering ribonucleic acid
SMAC/DIABLO	Second mitochondria – derived activator of caspase/direct IAP binding protein with low pI
SOD	Superoxide dismutase
STS	Staurosporine
TBE	Tris/borate/EDTA
TBI	Traumatic brain injury
tBID	Truncated BID
TBS	Tris-buffered solution
TBST	Tris-buffered solution with Tween 20
TC	Thrombin-cleavage
TCEP	Tris (2-carboxyethyl) phosphine
TE	Trypsin-EDTA
TEMED	Tetramethylenethylendiamine
TL	Total lysate
TMRE	Tetramethylrhodamin ethyl ester
TNF	Tumor necrosis factor
TRADD	Tumor necrosis factor receptor type 1-associated DEATH domain protein
TRAF2	TNF receptor-associated factor 2
TRAIL	TNF-related apoposis-inducing ligand
U	Unit(s)
UV	Ultra-violet
V	Volt
VDAC	Voltage-dependent anion channel
w/o	Without

WB	Western-blot
WT	Wildtype
xCT	Glutamine-cystine antiporter
XIAP	X-chromosomal linked inhibitor of apoptosis
ZFN	Zinc finger nuclease

8 References

1. Abeti, R. et al. (2015) Targeting lipid peroxidation and mitochondrial imbalance in Friedreich's ataxia. Pharmacological research 99, 344–350
2. Albrecht, P. et al. (2010) Mechanisms of oxidative glutamate toxicity: the glutamate/cystine antiporter system xc- as a neuroprotective drug target. CNS & neurological disorders drug targets 9, 373–382
3. Ankarcrona, M. et al. (1995) Glutamate-induced neuronal death: a succession of necrosis or apoptosis depending on mitochondrial function. Neuron 15, 961–973
4. Aoyama, K. and Nakaki, T. (2013) Impaired glutathione synthesis in neurodegeneration. International journal of molecular sciences 14, 21021–21044
5. Arnoult, D. et al. (2002) Mitochondrial release of apoptosis-inducing factor occurs downstream of cytochrome c release in response to several proapoptotic stimuli. The Journal of cell biology 159, 923–929
6. Artus, C. et al. (2010) AIF promotes chromatinolysis and caspase-independent programmed necrosis by interacting with histone H2AX. The EMBO journal 29, 1585–1599
7. Ashkenazi, A. and Dixit, V.M. (1998) Death receptors: signaling and modulation. Science (New York, N.Y.) 281, 1305–1308
8. Auer, T.O. and Del Bene, F. (2014) CRISPR/Cas9 and TALEN-mediated knock-in approaches in zebrafish. Methods (San Diego, Calif.) 69, 142–150
9. Bannai, S. and Kitamura, E. (1980) Transport interaction of L-cystine and L-glutamate in human diploid fibroblasts in culture. The Journal of biological chemistry 255, 2372–2376
10. Barho, M.T. et al. (2014) N-acyl derivatives of 4-phenoxyaniline as neuroprotective agents. ChemMedChem 9, 2260–2273
11. Baritaud, M. et al. (2012) AIF-mediated caspase-independent necroptosis requires ATM and DNA-PK-induced histone H2AX Ser139 phosphorylation. Cell death & disease 3, e390
12. Basañez, G. et al. (1999) Bax, but not Bcl-xL, decreases the lifetime of planar phospholipid bilayer membranes at subnanomolar concentrations. Proceedings of the National Academy of Sciences of the United States of America 96, 5492–5497
13. Becattini, B. et al. (2004) Targeting apoptosis via chemical design: inhibition of bid-induced cell death by small organic molecules. Chemistry & biology 11, 1107–1117
14. Becattini, B. et al. (2006) Structure-activity relationships by interligand NOE-based design and synthesis of antiapoptotic compounds targeting Bid. Proceedings of the National Academy of Sciences of the United States of America 103, 12602–12606
15. Bermpohl, D. et al. (2006) Traumatic brain injury in mice deficient in Bid: effects on histopathology and functional outcome. Journal of cerebral blood flow and metabolism : official journal of the International Society of Cerebral Blood Flow and Metabolism 26, 625–633
16. Bernardi, P. and Di Lisa, F. (2015) The mitochondrial permeability transition pore: Molecular nature and role as a target in cardioprotection. Journal of molecular and cellular cardiology 78, 100–106
17. Bertram, L. and Tanzi, R.E. (2005) The genetic epidemiology of neurodegenerative disease. The Journal of clinical investigation 115, 1449–1457
18. Billen, L.P. et al. (2008) Bid: a Bax-like BH3 protein. Oncogene 27 Suppl 1, S93-104
19. Cabon, L. et al. (2012) BID regulates AIF-mediated caspase-independent necroptosis by promoting BAX activation. Cell death and differentiation 19, 245–256
20. Chae, H.J. et al. (2000) Molecular mechanism of staurosporine-induced apoptosis in osteoblasts. Pharmacological research 42, 373–381

21. Chen, L. et al. (2008) Lipid peroxidation up-regulates BACE1 expression in vivo: a possible early event of amyloidogenesis in Alzheimer's disease. Journal of neurochemistry 107, 197–207
22. Cheng, G. et al. (2012) Mitochondria-targeted drugs synergize with 2-deoxyglucose to trigger breast cancer cell death. Cancer research 72, 2634–2644
23. Cheung, E.C.C. et al. (2005) Apoptosis-inducing factor is a key factor in neuronal cell death propagated by BAX-dependent and BAX-independent mechanisms. The Journal of neuroscience : the official journal of the Society for Neuroscience 25, 1324–1334
24. Cheung, E.C.C. et al. (2006) Dissociating the dual roles of apoptosis-inducing factor in maintaining mitochondrial structure and apoptosis. The EMBO journal 25, 4061–4073
25. Cheung, N.S. et al. (1998) Micromolar L-glutamate induces extensive apoptosis in an apoptotic-necrotic continuum of insult-dependent, excitotoxic injury in cultured cortical neurones. Neuropharmacology 37, 1419–1429
26. Chou, J.J. et al. (1999) Solution structure of BID, an intracellular amplifier of apoptotic signaling. Cell 96, 615–624
27. Chun, E. et al. (2012) Fusion partner toolchest for the stabilization and crystallization of G protein-coupled receptors. Structure (London, England : 1993) 20, 967–976
28. Colurso, G.J. et al. (2003) Quantitative assessment of DNA fragmentation and beta-amyloid deposition in insular cortex and midfrontal gyrus from patients with Alzheimer's disease. Life sciences 73, 1795–1803
29. Cong, W.-n. et al. (2012) Altered hypothalamic protein expression in a rat model of Huntington's disease. PloS one 7, e47240
30. Conrad, M. et al. (2016) Regulated necrosis: disease relevance and therapeutic opportunities. Nature reviews. Drug discovery 15, 348–366
31. Culmsee, C. et al. (2005) Apoptosis-inducing factor triggered by poly(ADP-ribose) polymerase and Bid mediates neuronal cell death after oxygen-glucose deprivation and focal cerebral ischemia. The Journal of neuroscience : the official journal of the Society for Neuroscience 25, 10262–10272
32. Czabotar, P.E. et al. (2013) Bax crystal structures reveal how BH3 domains activate Bax and nucleate its oligomerization to induce apoptosis. Cell 152, 519–531
33. Dagda, R.K. et al. (2009) Loss of PINK1 function promotes mitophagy through effects on oxidative stress and mitochondrial fission. The Journal of biological chemistry 284, 13843–13855
34. Davis, J.B. and Maher, P. (1994) Protein kinase C activation inhibits glutamate-induced cytotoxicity in a neuronal cell line. Brain research 652, 169–173
35. Deas, E. et al. (2016) Alpha-Synuclein Oligomers Interact with Metal Ions to Induce Oxidative Stress and Neuronal Death in Parkinson's Disease. Antioxidants & redox signaling 24, 376–391
36. Diemert, S. et al. (2012) Impedance measurement for real time detection of neuronal cell death. Journal of neuroscience methods 203, 69–77
37. Ding, W.-X. et al. (2004) Bid-dependent generation of oxygen radicals promotes death receptor activation-induced apoptosis in murine hepatocytes. Hepatology (Baltimore, Md.) 40, 403–413
38. Dixon, S.J. et al. (2012) Ferroptosis: an iron-dependent form of nonapoptotic cell death. Cell 149, 1060–1072
39. Dixon, S.J. et al. (2014) Pharmacological inhibition of cystine-glutamate exchange induces endoplasmic reticulum stress and ferroptosis. eLife 3, e02523
40. Dixon, S.J. et al. (2015) Human Haploid Cell Genetics Reveals Roles for Lipid Metabolism Genes in Nonapoptotic Cell Death. ACS chemical biology 10, 1604–1609
41. Doll, S. et al. (2017) ACSL4 dictates ferroptosis sensitivity by shaping cellular lipid composition. Nature chemical biology 13, 91–98
42. Dolma, S. et al. (2003) Identification of genotype-selective antitumor agents using synthetic lethal chemical screening in engineered human tumor cells. Cancer cell 3, 285–296

43. Doti, N. et al. (2014) Inhibition of the AIF/CypA complex protects against intrinsic death pathways induced by oxidative stress. Cell death & disease 5, e993
44. Doughan, A.K. and Dikalov, S.I. (2007) Mitochondrial redox cycling of mitoquinone leads to superoxide production and cellular apoptosis. Antioxidants & redox signaling 9, 1825–1836
45. Dringen, R. and Hirrlinger, J. (2003) Glutathione pathways in the brain. Biological chemistry 384, 505–516
46. Du, C. et al. (2000) Smac, a mitochondrial protein that promotes cytochrome c-dependent caspase activation by eliminating IAP inhibition. Cell 102, 33–42
47. Elmore, S. (2007) Apoptosis: a review of programmed cell death. Toxicologic pathology 35, 495–516
48. Esposti, M.D. (2002) The roles of Bid. Apoptosis : an international journal on programmed cell death 7, 433–440
49. Fanzani, A. and Poli, M. (2017) Iron, Oxidative Damage and Ferroptosis in Rhabdomyosarcoma. International journal of molecular sciences 18
50. Fayaz, S.M. et al. (2014) Necroptosis: who knew there were so many interesting ways to die? CNS & neurological disorders drug targets 13, 42–51
51. Fineran, P.C. and Dy, R.L. (2014) Gene regulation by engineered CRISPR-Cas systems. Current opinion in microbiology 18, 83–89
52. Fink, B.D. et al. (2009) Mitochondrial targeted coenzyme Q, superoxide, and fuel selectivity in endothelial cells. PloS one 4, e4250
53. Friedmann Angeli, J.P. et al. (2014) Inactivation of the ferroptosis regulator Gpx4 triggers acute renal failure in mice. Nature cell biology 16, 1180–1191
54. Fukui, M. et al. (2009) Mechanism of glutamate-induced neurotoxicity in HT22 mouse hippocampal cells. European journal of pharmacology 617, 1–11
55. Gahl, R.F. et al. (2016) Bcl-2 proteins bid and bax form a network to permeabilize the mitochondria at the onset of apoptosis. Cell death & disease 7, e2424
56. Gaj, T. et al. (2013) ZFN, TALEN, and CRISPR/Cas-based methods for genome engineering. Trends in biotechnology 31, 397–405
57. Galluzzi, L. et al. (2009) Mitochondrial membrane permeabilization in neuronal injury. Nature reviews. Neuroscience 10, 481–494
58. Galluzzi, L. et al. (2012) Molecular definitions of cell death subroutines: recommendations of the Nomenclature Committee on Cell Death 2012. Cell death and differentiation 19, 107–120
59. Galluzzi, L. et al. (2015) Essential versus accessory aspects of cell death: recommendations of the NCCD 2015. Cell death and differentiation 22, 58–73
60. Gane, E.J. et al. (2010) The mitochondria-targeted anti-oxidant mitoquinone decreases liver damage in a phase II study of hepatitis C patients. Liver international : official journal of the International Association for the Study of the Liver 30, 1019–1026
61. Garcia-Perez, C. et al. (2012) Bid-induced mitochondrial membrane permeabilization waves propagated by local reactive oxygen species (ROS) signaling. Proceedings of the National Academy of Sciences of the United States of America 109, 4497–4502
62. García-Sáez, A.J. (2012) The secrets of the Bcl-2 family. Cell death and differentiation 19, 1733–1740
63. Gasiunas, G. et al. (2012) Cas9-crRNA ribonucleoprotein complex mediates specific DNA cleavage for adaptive immunity in bacteria. Proceedings of the National Academy of Sciences of the United States of America 109, E2579-86
64. Gilbert, L.A. et al. (2013) CRISPR-mediated modular RNA-guided regulation of transcription in eukaryotes. Cell 154, 442–451
65. Gill, S.C. and Hippel, P.H. von (1989) Calculation of protein extinction coefficients from amino acid sequence data. Analytical biochemistry 182, 319–326

66. Giménez-Cassina, A. and Danial, N.N. (2015) Regulation of mitochondrial nutrient and energy metabolism by BCL-2 family proteins. Trends in endocrinology and metabolism: TEM 26, 165–175
67. Gonzalez, Y. et al. (2014) Atg7- and Keap1-dependent autophagy protects breast cancer cell lines against mitoquinone-induced oxidative stress. Oncotarget 5, 1526–1537
68. Gonzalvez, F. et al. (2005) tBid interaction with cardiolipin primarily orchestrates mitochondrial dysfunctions and subsequently activates Bax and Bak. Cell death and differentiation 12, 614–626
69. Görlach, A. et al. (2015) Calcium and ROS: A mutual interplay. Redox biology 6, 260–271
70. Gorman, A.M. (2008) Neuronal cell death in neurodegenerative diseases: recurring themes around protein handling. Journal of cellular and molecular medicine 12, 2263–2280
71. Grinberg, M. et al. (2005) Mitochondrial carrier homolog 2 is a target of tBID in cells signaled to die by tumor necrosis factor alpha. Molecular and cellular biology 25, 4579–4590
72. Grohm, J. et al. (2010) Bid mediates fission, membrane permeabilization and peri-nuclear accumulation of mitochondria as a prerequisite for oxidative neuronal cell death. Brain, behavior, and immunity 24, 831–838
73. Gross, A. et al. (1998) Enforced dimerization of BAX results in its translocation, mitochondrial dysfunction and apoptosis. The EMBO journal 17, 3878–3885
74. Gross, A. et al. (1999) Caspase cleaved BID targets mitochondria and is required for cytochrome c release, while BCL-XL prevents this release but not tumor necrosis factor-R1/Fas death. The Journal of biological chemistry 274, 1156–1163
75. Häcker, G. (2000) The morphology of apoptosis. Cell and tissue research 301, 5–17
76. Hara, A. et al. (1998) Evidence for apoptosis in human intracranial aneurysms. Neurological research 20, 127–130
77. Hauser, D.N. et al. (2013) Dopamine quinone modifies and decreases the abundance of the mitochondrial selenoprotein glutathione peroxidase 4. Free radical biology & medicine 65, 419–427
78. Hegde, R. et al. (2002) Identification of Omi/HtrA2 as a mitochondrial apoptotic serine protease that disrupts inhibitor of apoptosis protein-caspase interaction. The Journal of biological chemistry 277, 432–438
79. Hengartner, M.O. (2000) The biochemistry of apoptosis. Nature 407, 770–776
80. Henke, N. et al. (2013) The plasma membrane channel ORAI1 mediates detrimental calcium influx caused by endogenous oxidative stress. Cell death & disease 4, e470
81. Henshall, D.C. et al. (2001) Cleavage of bid may amplify caspase-8-induced neuronal death following focally evoked limbic seizures. Neurobiology of disease 8, 568–580
82. Hsu, P.D. et al. (2013) DNA targeting specificity of RNA-guided Cas9 nucleases. Nature biotechnology 31, 827–832
83. Hsu, P.D. et al. (2014) Development and applications of CRISPR-Cas9 for genome engineering. Cell 157, 1262–1278
84. Hu, J. et al. (2014) Direct activation of human and mouse Oct4 genes using engineered TALE and Cas9 transcription factors. Nucleic acids research 42, 4375–4390
85. Ishino, Y. et al. (1987) Nucleotide sequence of the iap gene, responsible for alkaline phosphatase isozyme conversion in Escherichia coli, and identification of the gene product. Journal of bacteriology 169, 5429–5433
86. Jakobson, M. et al. (2013) Multiple mechanisms repress N-Bak mRNA translation in the healthy and apoptotic neurons. Cell death & disease 4, e777
87. Jinek, M. et al. (2012) A programmable dual-RNA-guided DNA endonuclease in adaptive bacterial immunity. Science (New York, N.Y.) 337, 816–821
88. Joshi, Y.B. et al. (2015) The 12/15-lipoxygenase as an emerging therapeutic target for Alzheimer's disease. Trends in pharmacological sciences 36, 181–186
89. Joung, J.K. and Sander, J.D. (2013) TALENs: A widely applicable technology for targeted genome editing. Nature reviews. Molecular cell biology 14, 49–55

90. Kagan, V.E. et al. (2017) Oxidized arachidonic and adrenic PEs navigate cells to ferroptosis. Nature chemical biology 13, 81–90
91. Kamer, I. et al. (2005) Proapoptotic BID is an ATM effector in the DNA-damage response. Cell 122, 593–603
92. Katz, C. et al. (2012) Molecular basis of the interaction between proapoptotic truncated BID (tBID) protein and mitochondrial carrier homologue 2 (MTCH2) protein: key players in mitochondrial death pathway. The Journal of biological chemistry 287, 15016–15023
93. Kazhdan, I. et al. (2006) Targeted gene therapy for breast cancer with truncated Bid. Cancer gene therapy 13, 141–149
94. Kelso, G.F. et al. (2001) Selective targeting of a redox-active ubiquinone to mitochondria within cells: antioxidant and antiapoptotic properties. The Journal of biological chemistry 276, 4588–4596
95. Kelso, G.F. et al. (2002) Prevention of mitochondrial oxidative damage using targeted antioxidants. Annals of the New York Academy of Sciences 959, 263–274
96. Kerr, J.F. et al. (1972) Apoptosis: a basic biological phenomenon with wide-ranging implications in tissue kinetics. British journal of cancer 26, 239–257
97. Kim, H. and Kim, J.-S. (2014) A guide to genome engineering with programmable nucleases. Nature reviews. Genetics 15, 321–334
98. Köhler, B. et al. (2008) Bid participates in genotoxic drug-induced apoptosis of HeLa cells and is essential for death receptor ligands' apoptotic and synergistic effects. PloS one 3, e2844
99. König, H.-G. et al. (2007) Full length Bid is sufficient to induce apoptosis of cultured rat hippocampal neurons. BMC cell biology 8, 7
100. König, H.-G. et al. (2014) The BCL-2 family protein Bid is critical for pro-inflammatory signaling in astrocytes. Neurobiology of disease 70, 99–107
101. Kuwana, T. et al. (2005) BH3 domains of BH3-only proteins differentially regulate Bax-mediated mitochondrial membrane permeabilization both directly and indirectly. Molecular cell 17, 525–535
102. Kvansakul, M. et al. (2008) Vaccinia virus anti-apoptotic F1L is a novel Bcl-2-like domain-swapped dimer that binds a highly selective subset of BH3-containing death ligands. Cell death and differentiation 15, 1564–1571
103. Landshamer, S. et al. (2008) Bid-induced release of AIF from mitochondria causes immediate neuronal cell death. Cell death and differentiation 15, 1553–1563
104. Li, H. et al. (1998) Cleavage of BID by caspase 8 mediates the mitochondrial damage in the Fas pathway of apoptosis. Cell 94, 491–501
105. Li, P. et al. (1997) Cytochrome c and dATP-dependent formation of Apaf-1/caspase-9 complex initiates an apoptotic protease cascade. Cell 91, 479–489
106. Li, Y. et al. (1997) A role for 12-lipoxygenase in nerve cell death caused by glutathione depletion. Neuron 19, 453–463
107. Li, Z. et al. (2017) Anti-Oxidative Stress Activity Is Essential for Amanita caesarea Mediated Neuroprotection on Glutamate-Induced Apoptotic HT22 Cells and an Alzheimer's Disease Mouse Model. International journal of molecular sciences 18
108. Lim, D. et al. (2008) Calcium homeostasis and mitochondrial dysfunction in striatal neurons of Huntington disease. The Journal of biological chemistry 283, 5780–5789
109. Lin, M.T. and Beal, M.F. (2006) Mitochondrial dysfunction and oxidative stress in neurodegenerative diseases. Nature 443, 787–795
110. Liu, X. et al. (1996) Induction of Apoptotic Program in Cell-Free Extracts: Requirement for dATP and Cytochrome c. Cell 86, 147–157
111. Luo, X. et al. (1998) Bid, a Bcl2 interacting protein, mediates cytochrome c release from mitochondria in response to activation of cell surface death receptors. Cell 94, 481–490
112. Lutter, M. et al. (2000) Cardiolipin provides specificity for targeting of tBid to mitochondria. Nature cell biology 2, 754–761

113. Mali, P. et al. (2013) RNA-guided human genome engineering via Cas9. Science (New York, N.Y.) 339, 823–826
114. Marí, M. et al. (2009) Mitochondrial glutathione, a key survival antioxidant. Antioxidants & redox signaling 11, 2685–2700
115. Markesbery, W.R. and Lovell, M.A. (1998) Four-hydroxynonenal, a product of lipid peroxidation, is increased in the brain in Alzheimer's disease. Neurobiology of aging 19, 33–36
116. Martin, L.J. et al. (1998) Neurodegeneration in excitotoxicity, global cerebral ischemia, and target deprivation: A perspective on the contributions of apoptosis and necrosis. Brain research bulletin 46, 281–309
117. Martin, N.A. et al. (2016) BID Mediates Oxygen-Glucose Deprivation-Induced Neuronal Injury in Organotypic Hippocampal Slice Cultures and Modulates Tissue Inflammation in a Transient Focal Cerebral Ischemia Model without Changing Lesion Volume. Frontiers in cellular neuroscience 10, 14
118. Martinou, J.-C. and Youle, R.J. (2011) Mitochondria in apoptosis: Bcl-2 family members and mitochondrial dynamics. Developmental cell 21, 92–101
119. Mattson, M.P. et al. (1999) Cellular and molecular mechanisms underlying perturbed energy metabolism and neuronal degeneration in Alzheimer's and Parkinson's diseases. Annals of the New York Academy of Sciences 893, 154–175
120. McDonnell, J.M. et al. (1999) Solution structure of the proapoptotic molecule BID: a structural basis for apoptotic agonists and antagonists. Cell 96, 625–634
121. McGarry, A. et al. (2017) A randomized, double-blind, placebo-controlled trial of coenzyme Q10 in Huntington disease. Neurology 88, 152–159
122. Mojica, F.J.M. et al. (2005) Intervening sequences of regularly spaced prokaryotic repeats derive from foreign genetic elements. Journal of molecular evolution 60, 174–182
123. Morimoto, B.H. and Koshland, D.E. (1990) Induction and expression of long- and short-term neurosecretory potentiation in a neural cell line. Neuron 5, 875–880
124. Muchmore, S.W. et al. (1996) X-ray and NMR structure of human Bcl-xL, an inhibitor of programmed cell death. Nature 381, 335–341
125. Murphy, T.H. et al. (1989) Glutamate toxicity in a neuronal cell line involves inhibition of cystine transport leading to oxidative stress. Neuron 2, 1547–1558
126. Neitemeier, S. et al. (2017) BID links ferroptosis to mitochondrial cell death pathways. Redox biology 12, 558–570
127. Newmeyer, D.D. et al. (1994) Cell-free apoptosis in Xenopus egg extracts: Inhibition by Bcl-2 and requirement for an organelle fraction enriched in mitochondria. Cell 79, 353–364
128. Nitatori, T. et al. (1995) Delayed neuronal death in the CA1 pyramidal cell layer of the gerbil hippocampus following transient ischemia is apoptosis. The Journal of neuroscience : the official journal of the Society for Neuroscience 15, 1001–1011
129. Olney, J.W. (1969) Brain Lesions, Obesity, and Other Disturbances in Mice Treated with Monosodium Glutamate. Science 164, 719–721
130. O'Malley, Y. et al. (2006) Reactive oxygen and targeted antioxidant administration in endothelial cell mitochondria. The Journal of biological chemistry 281, 39766–39775
131. Oppermann, S. et al. (2014) Novel N-phenyl-substituted thiazolidinediones protect neural cells against glutamate- and tBid-induced toxicity. The Journal of pharmacology and experimental therapeutics 350, 273–289
132. Oppermann, S. (2014) *Targeting Bid for mitoprotection: Bid crystallization, new mechanisms and inhibitory compounds*
133. Oxler, E.-M. et al. (2012) AIF depletion provides neuroprotection through a preconditioning effect. Apoptosis : an international journal on programmed cell death 17, 1027–1038
134. Pan, G. et al. (1998) Caspase-9, Bcl-X L , and Apaf-1 Form a Ternary Complex. J. Biol. Chem. 273, 5841–5845
135. Paquet, D. et al. (2016) Efficient introduction of specific homozygous and heterozygous mutations using CRISPR/Cas9. Nature 533, 125–129

136. Parks, T.D. et al. (1994) Release of proteins and peptides from fusion proteins using a recombinant plant virus proteinase. Analytical biochemistry 216, 413–417

137. Paul, B.D. et al. (2014) Cystathionine gamma-lyase deficiency mediates neurodegeneration in Huntington's disease. Nature 509, 96–100

138. Peña-Blanco, A. and García-Sáez, A.J. (2017) Bax, Bak and beyond: mitochondrial performance in apoptosis. The FEBS journal

139. Perry, V.H. et al. (2010) Microglia in neurodegenerative disease. Nature reviews. Neurology 6, 193–201

140. Plesnila, N. et al. (2001) BID mediates neuronal cell death after oxygen/ glucose deprivation and focal cerebral ischemia. Proceedings of the National Academy of Sciences of the United States of America 98, 15318–15323

141. Pokrzywinski, K.L. et al. (2016) Therapeutic Targeting of the Mitochondria Initiates Excessive Superoxide Production and Mitochondrial Depolarization Causing Decreased mtDNA Integrity. PloS one 11, e0168283

142. Portera-Cailliau, C. et al. (1997) Excitotoxic neuronal death in the immature brain is an apoptosis-necrosis morphological continuum. The Journal of comparative neurology 378, 70–87

143. Portera-Cailliau, C. et al. (1997) Non-NMDA and NMDA receptor-mediated excitotoxic neuronal deaths in adult brain are morphologically distinct: further evidence for an apoptosis-necrosis continuum. The Journal of comparative neurology 378, 88–104

144. Pourcel, C. et al. (2005) CRISPR elements in Yersinia pestis acquire new repeats by preferential uptake of bacteriophage DNA, and provide additional tools for evolutionary studies. Microbiology (Reading, England) 151, 653–663

145. Qu, J. et al. (2016) The Injury and Therapy of Reactive Oxygen Species in Intracerebral Hemorrhage Looking at Mitochondria. Oxidative medicine and cellular longevity 2016, 2592935

146. Raemy, E. et al. (2016) Cardiolipin or MTCH2 can serve as tBID receptors during apoptosis. Cell death and differentiation 23, 1165–1174

147. Rajan, S. et al. (2015) Bh3 induced conformational changes in Bcl-Xl revealed by crystal structure and comparative analysis. Proteins 83, 1262–1272

148. Rao, V.A. et al. (2010) The antioxidant transcription factor Nrf2 negatively regulates autophagy and growth arrest induced by the anticancer redox agent mitoquinone. The Journal of biological chemistry 285, 34447–34459

149. Rink, A. et al. (1995) Evidence of apoptotic cell death after experimental traumatic brain injury in the rat. The American journal of pathology 147, 1575–1583

150. Roginsky, V.A. et al. (2009) Chain-breaking antioxidant activity of reduced forms of mitochondria-targeted quinones, a novel type of geroprotectors. Aging 1, 481–489

151. Ross, M.F. et al. (2005) Lipophilic triphenylphosphonium cations as tools in mitochondrial bioenergetics and free radical biology. Biochemistry (Moscow) 70, 222–230

152. Ruszkiewicz, J. and Albrecht, J. (2015) Changes in the mitochondrial antioxidant systems in neurodegenerative diseases and acute brain disorders. Neurochemistry international 88, 66–72

153. Saelens, X. et al. (2004) Toxic proteins released from mitochondria in cell death. Oncogene 23, 2861–2874

154. Saito, M. et al. (2000) BAX-dependent transport of cytochrome c reconstituted in pure liposomes. Nature cell biology 2, 553–555

155. Sato, H. et al. (1999) Cloning and expression of a plasma membrane cystine/glutamate exchange transporter composed of two distinct proteins. The Journal of biological chemistry 274, 11455–11458

156. Savitskaya, M.A. and Onishchenko, G.E. (2015) Mechanisms of Apoptosis. Biochemistry. Biokhimiia 80, 1393–1405

157. Sax, J.K. et al. (2002) BID regulation by p53 contributes to chemosensitivity. Nature cell biology 4, 842–849

158. Schaefer, K.A. et al. (2017) Unexpected mutations after CRISPR-Cas9 editing in vivo. Nature methods 14, 547–548

159. Schubert, D. et al. (1992) Growth factros and vitamin E modify neuronal glutamate toxicity. Proceedings of the National Academy of Sciences of the United States of America, 8264–8267

160. Schulze-Osthoff, K. et al. (1998) Apoptosis signaling by death receptors. European journal of biochemistry 254, 439–459
161. Scorrano, L. et al. (2002) A Distinct Pathway Remodels Mitochondrial Cristae and Mobilizes Cytochrome c during Apoptosis. Developmental cell 2, 55–67
162. Seiler, A. et al. (2008) Glutathione peroxidase 4 senses and translates oxidative stress into 12/15-lipoxygenase dependent- and AIF-mediated cell death. Cell metabolism 8, 237–248
163. Sevrioukova, I.F. (2011) Apoptosis-inducing factor: structure, function, and redox regulation. Antioxidants & redox signaling 14, 2545–2579
164. Shah, R. et al. (2017) The Potency of Diarylamine Radical-Trapping Antioxidants as Inhibitors of Ferroptosis Underscores the Role of Autoxidation in the Mechanism of Cell Death. ACS chemical biology
165. Shamas-Din, A. et al. (2013) tBid undergoes multiple conformational changes at the membrane required for Bax activation. The Journal of biological chemistry 288, 22111–22127
166. Sheehan, J.P. et al. (1997) Calcium homeostasis and reactive oxygen species production in cells transformed by mitochondria from individuals with sporadic Alzheimer's disease. The Journal of neuroscience : the official journal of the Society for Neuroscience 17, 4612–4622
167. Sheng, X. et al. (2017) Theoretical insights into the mechanism of ferroptosis suppression via inactivation of a lipid peroxide radical by liproxstatin-1. Physical chemistry chemical physics : PCCP 19, 13153–13159
168. Shimada, K. et al. (2016) Cell-Line Selectivity Improves the Predictive Power of Pharmacogenomic Analyses and Helps Identify NADPH as Biomarker for Ferroptosis Sensitivity. Cell chemical biology 23, 225–235
169. Shimada, K. et al. (2016) Global survey of cell death mechanisms reveals metabolic regulation of ferroptosis. Nature chemical biology 12, 497–503
170. Shintoku, R. et al. (2017) Lipoxygenase-mediated generation of lipid peroxides enhances ferroptosis induced by erastin and RSL3. Cancer science
171. Skouta, R. et al. (2014) Ferrostatins inhibit oxidative lipid damage and cell death in diverse disease models. Journal of the American Chemical Society 136, 4551–4556
172. Skulachev, V.P. (2007) A biochemical approach to the problem of aging: "megaproject" on membrane-penetrating ions. The first results and prospects. Biochemistry (Moscow) 72, 1385–1396
173. Smith, R.A.J. and Murphy, M.P. (2010) Animal and human studies with the mitochondria-targeted antioxidant MitoQ. Annals of the New York Academy of Sciences 1201, 96–103
174. Snow, B.J. et al. (2010) A double-blind, placebo-controlled study to assess the mitochondria-targeted antioxidant MitoQ as a disease-modifying therapy in Parkinson's disease. Movement disorders : official journal of the Movement Disorder Society 25, 1670–1674
175. Speer, R.E. et al. (2013) Hypoxia-inducible factor prolyl hydroxylases as targets for neuroprotection by "antioxidant" metal chelators: From ferroptosis to stroke. Free radical biology & medicine 62, 26–36
176. Starkov, A.A. et al. (2004) Mitochondrial calcium and oxidative stress as mediators of ischemic brain injury. Cell calcium 36, 257–264
177. Stefanis, L. (2005) Caspase-dependent and -independent neuronal death: two distinct pathways to neuronal injury. The Neuroscientist : a review journal bringing neurobiology, neurology and psychiatry 11, 50–62
178. Stemmer, M. et al. (2015) CCTop: An Intuitive, Flexible and Reliable CRISPR/Cas9 Target Prediction Tool. PloS one 10, e0124633
180. Stockwell, B.R. et al. (2017) Ferroptosis: A Regulated Cell Death Nexus Linking Metabolism, Redox Biology, and Disease. Cell 171, 273–285

181. Surmeier, D.J. et al. (2011) The role of calcium and mitochondrial oxidant stress in the loss of substantia nigra pars compacta dopaminergic neurons in Parkinson's disease. Neuroscience 198, 221–231
182. Tait, S.W.G. and Green, D.R. (2008) Caspase-independent cell death: leaving the set without the final cut. Oncogene 27, 6452–6461
183. Tan, S. et al. (1998) Oxidative stress induces a form of programmed cell death with characteristics of both apoptosis and necrosis in neuronal cells. Journal of neurochemistry 71, 95–105
184. Tan, S. et al. (1998) The regulation of reactive oxygen species production during programmed cell death. The Journal of cell biology 141, 1423–1432
185. Tan, S. et al. (2001) Oxytosis: A novel form of programmed cell death. Current topics in medicinal chemistry 1, 497–506
186. Tobaben, S. et al. (2011) Bid-mediated mitochondrial damage is a key mechanism in glutamate-induced oxidative stress and AIF-dependent cell death in immortalized HT-22 hippocampal neurons. Cell death and differentiation 18, 282–292
187. Tompkins, M.M. et al. (1997) Apoptotic-like changes in Lewy-body-associated disorders and normal aging in substantia nigral neurons. The American journal of pathology 150, 119–131
188. Tsujimoto, Y. (1998) Role of Bcl-2 family proteins in apoptosis: apoptosomes or mitochondria? Genes to cells : devoted to molecular & cellular mechanisms 3, 697–707
189. Uo, T. et al. (2005) Neurons exclusively express N-Bak, a BH3 domain-only Bak isoform that promotes neuronal apoptosis. J. Biol. Chem. 280, 9065–9073
190. Urnov, F.D. et al. (2010) Genome editing with engineered zinc finger nucleases. Nature reviews. Genetics 11, 636–646
191. van Chu, T. et al. (2015) Increasing the efficiency of homology-directed repair for CRISPR-Cas9-induced precise gene editing in mammalian cells. Nature biotechnology 33, 543–548
192. van Dommelen, S.M. et al. (2012) Microvesicles and exosomes: Opportunities for cell-derived membrane vesicles in drug delivery. Journal of controlled release : official journal of the Controlled Release Society 161, 635–644
193. van Horssen, J. et al. (2017) Inflammation and mitochondrial dysfunction: A vicious circle in neurodegenerative disorders? Neuroscience letters
194. van Leyen, K. et al. (2005) Proteasome inhibition protects HT22 neuronal cells from oxidative glutamate toxicity. Journal of neurochemistry 92, 824–830
195. van Leyen, K. et al. (2006) Baicalein and 12/15-lipoxygenase in the ischemic brain. Stroke 37, 3014–3018
196. Vanden Berghe, T. et al. (2014) Regulated necrosis: the expanding network of non-apoptotic cell death pathways. Nature reviews. Molecular cell biology 15, 135–147
197. Vis, J.C. et al. (2005) Expression pattern of apoptosis-related markers in Huntington's disease. Acta neuropathologica 109, 321–328
198. Vogt, C. (1842) Untersuchungen über die Entwicklungsgeschichte der Geburtshelferkröte (Alytes obstetricans). Jent und Gassman, Solothurn, 281–284
199. Wang, K. et al. (1996) BID: a novel BH3 domain-only death agonist. Genes & development 10, 2859–2869
200. Wang, Y. et al. (2016) A nuclease that mediates cell death induced by DNA damage and poly(ADP-ribose) polymerase-1. Science (New York, N.Y.) 354
201. Wang, Y. and Qin, Z.-H. (2010) Molecular and cellular mechanisms of excitotoxic neuronal death. Apoptosis : an international journal on programmed cell death 15, 1382–1402
202. Wei, M.C. et al. (2000) tBID, a membrane-targeted death ligand, oligomerizes BAK to release cytochrome c. Genes & development 14, 2060–2071
203. Wei, Q. et al. (2006) Bid deficiency ameliorates ischemic renal failure and delays animal death in C57BL/6 mice. American journal of physiology. Renal physiology 290, F35-42

204. Wenzel, S.E. et al. (2017) PEBP1 Wardens Ferroptosis by Enabling Lipoxygenase Generation of Lipid Death Signals. Cell 171, 628-641.e26

205. Williams, T.I. et al. (2006) Increased levels of 4-hydroxynonenal and acrolein, neurotoxic markers of lipid peroxidation, in the brain in Mild Cognitive Impairment and early Alzheimer's disease. Neurobiology of aging 27, 1094–1099

206. Wolter, K.G. et al. (1997) Movement of Bax from the cytosol to mitochondria during apoptosis. The Journal of cell biology 139, 1281–1292

207. Xie, Y. et al. (2016) Ferroptosis: process and function. Cell death and differentiation 23, 369–379

208. Yagoda, N. et al. (2007) RAS-RAF-MEK-dependent oxidative cell death involving voltage-dependent anion channels. Nature 447, 864–868

209. Yamamoto, A. et al. (2006) Endoplasmic reticulum stress and apoptosis signaling in human temporal lobe epilepsy. Journal of neuropathology and experimental neurology 65, 217–225

210. Yang, H. et al. (2014) Generating genetically modified mice using CRISPR/Cas-mediated genome engineering. Nature protocols 9, 1956–1968

211. Yang, W.S. et al. (2014) Regulation of ferroptotic cancer cell death by GPX4. Cell 156, 317–331

212. Yang, W.S. et al. (2016) Peroxidation of polyunsaturated fatty acids by lipoxygenases drives ferroptosis. Proceedings of the National Academy of Sciences of the United States of America

213. Yang, W.S. and Stockwell, B.R. (2008) Synthetic lethal screening identifies compounds activating iron-dependent, nonapoptotic cell death in oncogenic-RAS-harboring cancer cells. Chemistry & biology 15, 234–245

214. Yang, X. et al. (2016) Neuroprotection of Coenzyme Q10 in Neurodegenerative Diseases. Current topics in medicinal chemistry 16, 858–866

215. Yin, X.M. et al. (1999) Bid-deficient mice are resistant to Fas-induced hepatocellular apoptosis. Nature 400, 886–891

216. Yin, X.-M. et al. (2002) Bid-mediated mitochondrial pathway is critical to ischemic neuronal apoptosis and focal cerebral ischemia. The Journal of biological chemistry 277, 42074–42081

217. Yoritaka, A. et al. (1996) Immunohistochemical detection of 4-hydroxynonenal protein adducts in Parkinson disease. Proceedings of the National Academy of Sciences of the United States of America 93, 2696–2701

218. Youle, R.J. and Strasser, A. (2008) The BCL-2 protein family: opposing activities that mediate cell death. Nature reviews. Molecular cell biology 9, 47–59

219. Yu, H. et al. (2017) Ferroptosis, a new form of cell death, and its relationships with tumourous diseases. Journal of cellular and molecular medicine 21, 648–657

220. Yuan, H. et al. (2016) CISD1 inhibits ferroptosis by protection against mitochondrial lipid peroxidation. Biochemical and biophysical research communications 478, 838–844

221. Yuan, J. et al. (2003) Diversity in the mechanisms of neuronal cell death. Neuron 40, 401–413

222. Zaltsman, Y. et al. (2010) MTCH2/MIMP is a major facilitator of tBID recruitment to mitochondria. Nature cell biology 12, 553–562

223. Zamzami, N. et al. (1996) Mitochondrial control of nuclear apoptosis. The Journal of experimental medicine 183, 1533–1544

224. Zhang, Y. et al. (2003) Equine estrogens differentially inhibit DNA fragmentation induced by glutamate in neuronal cells by modulation of regulatory proteins involved in programmed cell death. BMC neuroscience 4, 32

226. Zhu, Z.-G. et al. (2017) The efficacy and safety of coenzyme Q10 in Parkinson's disease: A meta-analysis of randomized controlled trials. Neurological sciences : official journal of the Italian Neurological Society and of the Italian Society of Clinical Neurophysiology 38, 215–224

227. Zilka, O. et al. (2017) On the Mechanism of Cytoprotection by Ferrostatin-1 and Liproxstatin-1 and the Role of Lipid Peroxidation in Ferroptotic Cell Death. ACS central science 3, 232–243

228. Zinkel, S.S. et al. (2005) A role for proapoptotic BID in the DNA-damage response. Cell 122, 579–591

229. Zou, H. et al. (1997) Apaf-1, a human protein homologous to C. elegans CED-4, participates in cytochrome c-dependent activation of caspase-3. Cell 90, 405–413

230. Zou, Y. et al. (2012) N-terminal T4 lysozyme fusion facilitates crystallization of a G protein coupled receptor. PloS one 7, e46039

9 Index of Tables

10 Index of Figures

11 Publications

11.1 Original Papers

Jelinek, A.; Heyder, L.; Daude, M.; Plessner, M.; Krippner, S.; Grosse, R.; Diederich, W.E., Culmsee, C.; *Mitochondrial rescue prevents glutathione peroxidase-dependent ferroptosis.* (submitted to Free Radical Biology & Medicine, 2017)

Ochs J., **Jelinek A.**, Honrath B., Ganjam G., Culmsee C.; *CRISPR/Cas9 BAX knockout abrogates mitochondrial damage and cell death in neuronal HT22 cells* (in preparation)

Jelinek, A., Neitemeier, S., Laino, V., Hoffmann, L., Eisenbach, I., Eying, R., Ganjam, G.K., Dolga, A.M., Oppermann, S., Culmsee, C., *Bid links ferroptosis to mitochondrial cell death pathways in neurons.* (Redox Biology, 2017)

11.2 Poster presentations

Jelinek, A.; Heyder, L.; Daude, M.; Plessner, M.; Krippner, S.; Grosse, R.; Diederich, W. E..; Culmsee, C.; MitoQ abrogates BID-mediated mitochondrial damage in RSL3-induced ferroptosis, *Neurochemical Conference: Advances in molecular and epigenetic mechanisms in neurodegeneration and neuroinflammation: novel therapeutic approaches*, Warsaw, Poland (**2017**)

Jelinek, A.; Heyder, L.; Daude, M.; Plessner, M.; Krippner, S.; Grosse, R.; Diederich, W. E..; Culmsee, C.; A BID of ferroptosis, *25th Euroconference on Apoptosis (ECDO): Cell death and immunity in disease; from molecules to translational medicine,* Leuven, Belgium (**2017**)

Jelinek, A.; Neitemeier, S.; Hoffmann, L.; Ganjam, G.K.; Culmsee, C.; CRISPR/Cas9 knockout demonstrates a key role for BID as a molecular link in paradigms of oxytosis & ferroptosis, *46th annual meeting of the Society for neuroscience (SfN)*, San Diego, USA (**2016**)

Jelinek, A.; Neitemeier, S.; Hoffmann, L.; Ganjam, G.K.; Culmsee, C.; CRISPR/Cas9 Bid knockout reveals a key role for BID-mediated mitochondrial damage in ferroptosis, *Annual DPHG conference,* Munich, Germany (**2016**)

Jelinek, A.; Neitemeier, S.; Hoffmann, L.; Ganjam, G.K.; Culmsee, C.; CRISPR/Cas9 Bid knockout reveals a key role for BID-mediated mitochondrial damage in ferroptosis, *PhD student day BPC* (**2016**)

Jelinek, A.; Neitemeier, S.; Oppermann, S.; Laino, V.; Ganjam, G.K.; Dolga, A.; Culmsee, C., CRISPR/Cas9 Knockout reveals a Key Role for Bid-mediated mitochondrial Damage in Paradigms of Oxytosis and Ferroptosis, MARA Day, Marburg, Germany **(2015)**

Jelinek, A.; Neitemeier, S.; Oppermann, S.; Laino, V.; Ganjam, G.K.; Dolga, A.; Culmsee, C., CRISPR/Cas9 Knockout reveals a Key Role for Bid-mediated mitochondrial Damage in Paradigms of Oxytosis and Ferroptosis, *23rd Conference of the European Cell Death Organization (ECDO): Death pathways and beyond*, Geneva, Switzerland **(2015)**

Jelinek, A.; Neitemeier, S.; Oppermann, S.; Laino, V.; Ganjam, G.K.; Dolga, A.; Culmsee, C., Bid links Ferroptosis to Mitochondrial Demise in Neuronal Cell Death Pathways, *EMBO workshop: Mitochondria, Apoptosis and cancer (MAC)*, Frankfurt, Germany **(2015)**

11.3 Oral presentations

"A key role for Bid-mediated mitochondrial damage in paradigms of oxytosis and ferroptosis", *82nd Annual Meeting of the German Society for Experimental and Clinical Pharmacology and Toxicology (DGPT)*, Berlin, Germany **(2016)**

"A key role for Bid-mediated mitochondrial damage in paradigms of oxytosis and ferroptosis", *23rd Conference of the European Cell Death Organization (ECDO): Death pathways and beyond*, Geneva, Switzerland **(2015)**

12 Grants

MARA (Marburg University Research Academy) travel grant for 25th Euroconference on Apoptosis (ECDO): *Cell death and immunity in disease; from molecules to translational medicine*, Leuven, Belgium (**2017**)

Marburg International Doctorate travel grant (DAAD) for 23rd Conference of the European Cell Death Organization (ECDO): *Death pathways and beyond*, Geneva, Switzerland **(2015)**